Intricacies of Astrophysical X-ray Spectroscopy and Investigations of Multi-Scale Solar Flares

A thesis submitted in partial fulfillment of

the requirements for the degree of

Doctor of Philosophy

by

Mithun Neelakandan P. S.

(Roll No. 18330012)

Under the supervision of

Prof. Santosh V. Vadawale
Senior Professor
Astronomy and Astrophysics
Physical Research Laboratory, Ahmedabad, India.

DEPARTMENT OF PHYSICS

INDIAN INSTITUTE OF TECHNOLOGY GANDHINAGAR

2024

to

my family & my teachers

DECLARATION

I declare that this written submission represents my ideas in my own words and where others' ideas or words have been included, I have adequately cited and referenced the original sources. I also declare that I have adhered to all principles of academic honesty and integrity and have not misrepresented or fabricated or falsified any idea/data/fact/source in my submission. I understand that any violation of the above will be cause for disciplinary action by the Institute and can also evoke penal action from the sources which have thus not been properly cited or from whom proper permission has not been taken when needed.

(Name: Mithun Neelakandan P. S.)

(Roll No: 18330012)

CERTIFICATE

It is certified that the work contained in the thesis titled **"Intricacies of Astrophysical X-ray Spectroscopy and Investigations of Multi-Scale Solar Flares"** by **Mithun Neelakandan P. S.** (Roll no: 18330012), has been carried out under my supervision and that this work has not been submitted elsewhere for degree.

I have read this dissertation and in my opinion, it is fully adequate in scope and quality as a dissertation for the degree of Doctor of Philosophy.

Santosh V. Vadawale
(Thesis Supervisor)
Senior Professor
Astronomy & Astrophysics Division
Physical Research Laboratory, Ahmedabad

Acknowledgements

At the outset, let me begin by thanking my thesis supervisor and our X-ray astronomy and instrumentation group lead, Prof. Santosh Vadawale. I started working with him in 2014 when I joined PRL, four years before I began my PhD work, and I had the opportunity to learn a lot during all these years. He has been very supportive of my Ph.D. journey from the initial days till the completion of this thesis, and without his support, it would have been even more difficult to manage the thesis work alongside my other assignments in the group. Stimulating discussions with him have guided me through the work presented in this thesis.

The work presented in this thesis uses observations from two instruments: Chandrayaan-2 XSM and AstroSat CZTI. I thank the XSM instrument team at PRL with Dr. M. Shanmugam, Dr. Arpit Patel, Mr. Hiteshkumar L Adalja, Mr. Tinkal Ladiya, Mr. Shiv Kumar Goyal, Mr. Neeraj K Tiwari, Mr. Nishant Singh, and Mr. Sushil Kumar and other teams from various centers of Indian Space Research Organization (ISRO) who contributed in various aspects from testing of instrument to regular in-flight operations. I also acknowledge the discussions with the XSM science team members, Dr. Aveek Sarkar, Prof. Bhuwan Joshi, Prof. P. Janardhan, Prof. Anil Bhardwaj, and Dr. Biswajit Mondal. I thank the CZTI team, including Prof. A. R. Rao, Prof. Dipankar Bhattacharya, Dr. Varun Bhalerao, Dr. Ajay M. Vibhute, Dr. Tanmoy Chattopadhyay, and Prof. Gulab Dewangan along with the technical teams from TIFR, VSSC, IUCAA, and ISRO. I thank IUCAA for the hospitality while carrying out part of the work with CZTI.

I am grateful to my various collaborators: Dr. Giulio Del Zanna, Prof. Helen Mason, Dr. Yamini Rao, Dr. Urmila Mitrakraev from DAMTP, University of Cambridge, and Dr. Sam Krucker, Dr. Ewan Dickson, Dr. Alexander Warmuth, Mr. Andrea Francesco Battaglia, Dr. Erica Lastuka, Dr. Iain G Hannah from the Solar Orbiter STIX team. I acknowledge the support from the Royal Society through an international exchange grant that fostered these collaborations.

I am thankful to my doctoral studies committee members, Dr. Mudit K. Srivastava, Dr. Aveek Sarkar, Dr. Kinsuk Acharya, and Prof. Bhuwan Joshi, for their guidance and suggestions over the years. I thank the current and past members of our X-ray group: Hitesh Adalja, Neeraj Tiwari, C. S. Vaish-

nava, Bharath Saiguhan, Soumya Kohli, Ashish Mondal, Abhay Kumar, Biswajit Mondal, Sandeep K Rout, Aarthy E, Anjali Rao, and Tanmoy Chattopadhyay. Special thanks to the PRL JRF 2018 and 2019 batches with whom I had the joy of attending the courses. I thank all members of the Astronomy and Astrophysics division, academic committee, Dean, Registrar, Director, and the entire PRL family. I also thank the IIT Gandhinagar family.

Lastly, I am forever thankful to my friends and family for their support and my teachers, who have taught me and guided me over the years.

(Mithun Neelakandan P. S.)

Abstract

Observations of astrophysical sources in X-rays provide the opportunity to investigate matter in extreme conditions such as high temperature, high density, and strong gravity, which are not achievable in terrestrial experiments. Energy spectra of these sources are often composed of continuum emission from multiple components arising from different mechanisms. Continuum X-ray spectroscopy is thus a powerful tool that can disentangle the components from different mechanisms and derive the physical conditions in the astrophysical source. However, continuum X-ray spectroscopy is particularly challenging as the observed spectrum is convolved with the response of X-ray spectroscopic instruments, which are often intricate and could be variable over time due to the harsh conditions in space. Thus, accurate modeling of the instrument response and continuous improvements are essential to fully utilize the potential of observatories for spectroscopic investigations of astrophysical sources.

The Sun is the first-detected and the brightest celestial X-ray source. X-rays from the Sun arise from its outer atmosphere, the corona, which is composed of plasma heated to temperatures of a few million Kelvin. The exact mechanism that heats the corona to multi-million Kelvin temperatures still remains elusive. Apart from quiescent X-ray emission from the hot corona, sudden enhancements in fluxes that could be up to several orders of magnitudes are observed, which are known as solar flares. Evidence suggests magnetic reconnection as the underlying mechanism powering the flares, which accelerates particles and heats the plasma. However, the locations and mechanisms of the conversion of magnetic energy to kinetic and thermal energies are in debate. As the flaring plasma and accelerated electrons emit profusely in soft and hard X-rays, X-ray spectroscopic observations offer the most direct diagnostics of the thermal and non-thermal particle populations in flares and, thus, insights into the energy release mechanisms in flares. The presence of flares having energies orders of magnitude smaller than the largest solar flares, termed nanoflares, is believed to be a reason for the heating of the corona. These hypothesized events are too faint to be detectable as individual events, so their presence is inferred from other observations, such as

extrapolating the properties and frequency distributions of the faintest observable events in the microflare regime. Thus, investigations of multi-scale solar flares, from large flares to the smallest microflares, are key to the missing pieces in our understanding of the flaring process and coronal heating.

This thesis includes modeling of the X-ray spectroscopic response of two instruments and investigations of solar flares using X-ray spectroscopy as the primary tool. Various aspects of the instrument response of AstroSat Cadmium Zinc Telluride Imager (CZTI) that observes astrophysical sources in the hard X-ray band and Chandrayaan-2 Solar X-ray Monitor (XSM) measuring solar spectrum in the soft X-ray band are investigated using their in-flight observations and improved responses are derived. The spectroscopic capabilities of both instruments have been significantly enhanced by the work presented in this thesis, such as the methodology for statistically limited background subtraction in CZTI and correction to the energy-dependent angular response of XSM.

Further, X-ray spectroscopic observations with XSM combined with other observations are used to investigate solar flares of different scales. With the detection and characterization of the largest sample of X-ray microflares observed in the quiet Sun, we provide stringent limits for the occurrence of such events and discuss its implications on the contribution of nanoflares to coronal heating. Time-resolved spectroscopic studies of larger solar flares reveal the presence of bimodal temperature distributions for X-ray-emitting plasma, pointing to two distinct sources of plasma heating in flares. Further, with joint modeling of soft and hard X-ray spectra of a solar flare with XSM and Solar Orbiter STIX, we provide improved estimates of thermal and non-thermal energies. Going beyond spectroscopy, we present an instrument concept for hard X-ray polarimetric observations of solar flares that would enable the measurement of properties of the flare-accelerated electrons that cannot be inferred from spectroscopic observations. An extension of this concept for X-ray polarization observations of other astrophysical sources is also presented.

Keywords: X-ray spectroscopy, spectral calibration, solar flares, coronal heating, microflares, non-thermal X-rays, X-ray polarimetry

List of Publications

Publications included in this thesis

1. **N. P. S. Mithun**, Santosh V. Vadawale, Aveek Sarkar, M. Shanmugam, Arpit R. Patel, Biswajit Mondal, Bhuwan Joshi, P. Janardhan, Hiteshkumar L. Adalja, Shiv Kumar Goyal, Tinkal Ladiya, Neeraj Kumar Tiwari, Nishant Singh, Sushil Kumar, Manoj K. Tiwari, M. H. Modi, and Anil Bhardwaj. Solar X-Ray Monitor on Board the Chandrayaan-2 Orbiter: In-Flight Performance and Science Prospects. Sol. Phys., 295(10):139, October 2020.

2. Santosh V. Vadawale, **N. P. S. Mithun**, Biswajit Mondal, Aveek Sarkar, P. Janardhan, Bhuwan Joshi, Anil Bhardwaj, M. Shanmugam, Arpit R. Patel, Hitesh Kumar L. Adalja, Shiv Kumar Goyal, Tinkal Ladiya, Neeraj Kumar Tiwari, Nishant Singh, and Sushil Kumar. Observations of the Quiet Sun during the Deepest Solar Minimum of the Past Century with Chandrayaan-2 XSM: Sub-A-class Microflares outside Active Regions. ApJ, 912(1):L13, May 2021.

3. **N. P. S. Mithun**, Santosh V. Vadawale, Giulio Del Zanna, Yamini K. Rao, Bhuwan Joshi, Aveek Sarkar, Biswajit Mondal, P. Janardhan, Anil Bhardwaj, and Helen E. Mason. Soft X-Ray Spectral Diagnostics of Multithermal Plasma in Solar Flares with Chandrayaan-2 XSM. ApJ, 939(2):112, November 2022.

4. **N. P. S. Mithun** et al., Improved energy estimates of solar flare from X-ray spectroscopy with Chandrayaan-2 XSM and Solar Orbiter STIX, in prep.

5. **N. P. S. Mithun** et al., Hard X-ray Spectroscopy with AstroSat CZT-Imager, in prep.

Other publications

1. **N. P. S. Mithun**, Santosh V. Vadawale, M. Shanmugam, Arpit R. Patel, Neeraj Kumar Tiwari, Hiteshkumar L. Adalja, Shiv Kumar Goyal, Tinkal Ladiya, Nishant Singh, Sushil Kumar, Manoj K. Tiwari, M. H. Modi, Biswajit Mondal, Aveek Sarkar, Bhuwan Joshi, P. Janardhan, and Anil Bhardwaj. Ground calibration of Solar X-ray Monitor on board the Chandrayaan-2 orbiter. Experimental Astronomy, 51(1):33–60, February 2021.

2. **N. P. S. Mithun**, S. V. Vadawale, A. R. Patel, M. Shanmugam, D. Chakrabarty, P. Konar, T. N. Sarvaiya, G. D. Padia, A. Sarkar, P. Kumar, P. Jangid, A. Sarda, M. S. Shah, and A. Bhardwaj. Data processing software for Chandrayaan-2 Solar X-ray Monitor. Astronomy and Computing, 34:100449, January 2021.

3. **N. P. S. Mithun**, Santosh V. Vadawale, M. Shanmugam, Arpit R. Patel, Nishant Singh, Sushil Kumar, Neeraj Kumar Tiwari, Shiv Kumar Goyal, Amit Basu Sarbadhikari, Garima Arora, Yash Srivastava, Hitesh Kumar Adalja, Tinkal Ladiya, Deepak Kumar Painkra, Swaroop B. Banerjee, Vishnubhai R. Patel, and Anil Bhardwaj. Ground calibration of Alpha Particle X-ray Spectrometer (APXS) on-board Chandrayaan-2 Pragyaan rover: An empirical approach. Planet. Space Sci., 187:104923, August 2020.

4. Tanmoy Chattopadhyay, Abhay Kumar, A. R. Rao, Yash Bhargava, Santosh V. Vadawale, Ajay Ratheesh, Gulab Dewangan, Dipankar Bhattacharya, **N. P. S. Mithun**, Varun Bhalerao, High Hard X-Ray Polarization in Cygnus X-1 Confined to the Intermediate Hard State: Evidence for a Variable Jet Component, ApJL, 960:L2, December 2023.

5. Yamini K. Rao, B. Mondal, Giulio Del Zanna, **N. P. S. Mithun**, S. V. Vadawale, K. K. Reeves, Helen E. Mason, Anil Bhardwaj, Multiwavelength Observations of a B-class Flare Using XSM, AIA, and XRT, ApJ, 958:190, November 2023.

6. Suman Bala, Sujay Mate, Advait Mehla, Parth Sastry, **N. P. S. Mithun**, Sourav Palit, Mehul Vijay Chanda, Divita Saraogi, C. S. Vaishnava, Gaurav Waratkar, Varun Bhalerao, Dipankar Bhattacharya, Shriharsh Tendulkar, Santosh Vadawale. Prospects of measuring gamma-ray burst polarization with the Daksha mission, JATIS, 9(4):048002, October 2023.

7. Biswajit Mondal, Santosh V. Vadawale, Giulio Del Zanna, **N. P. S. Mithun**, Aveek Sarkar, Helen E. Mason, P. Janardhan, Anil Bhardwaj. Evolution of Elemental Abundances in Hot Active Region Cores from Chandrayaan-2 XSM Observations, ApJ, 955(2):146, September 2023.

8. Abhijit Kayal, Veeresh Singh, Claudio Ricci, **N. P. S. Mithun**, Santosh Vadawale, Gulab Dewangan, Poshak Gandhi, Multi-epoch hard X-ray view of Compton-thick AGN Circinus Galaxy. MNRAS 522, 4098 – 4115, April 2023.

9. Biswajit Mondal, James A Klimchuk, Santosh V. Vadawale, Aveek Sarkar, Giulio Del Zanna, P. S. Athiray, **N. P. S. Mithun**, Helen E. Mason, Anil Bhardwaj. Role of Small-scale Impulsive Events in Heating the X-Ray Bright Points of the Quiet Sun. ApJ, 945:37 (14pp), March 2023.

10. Vishal Upendran, Durgesh Tripathi, **N. P. S. Mithun**, Santosh Vadawale, and Anil Bhardwaj. Nanoflare Heating of the Solar Corona Observed in X-Rays. ApJ, 940(2):L38, December 2022.

11. Abhay Kumar, Tanmoy Chattopadhyay, Santosh V. Vadawale, A. R. Rao, **N. P. S. Mithun**, Varun Bhalerao, and Dipankar Bhattacharya. Extending the energy range of AstroSat-CZTI up to 380 keV with compton spectroscopy. MNRAS, 516(2):3102–3112, October 2022.

12. Tanmoy Chattopadhyay, Soumya Gupta, Shabnam Iyyani, Divita Saraogi, Vidushi Sharma, Anastasia Tsvetkova, Ajay Ratheesh, Rahul Gupta, **N. P. S. Mithun**, C. S. Vaishnava, Vipul Prasad, E. Aarthy, Abhay Kumar, A. R. Rao, Santosh Vadawale, Varun Bhalerao, Dipankar Bhattacharya, Ajay Vibhute, and Dmitry Frederiks. Hard X-Ray Polarization Catalog

for a Five-year Sample of Gamma-Ray Bursts Using AstroSat CZT Imager. ApJ, 936(1):12, September 2022.

13. G. Del Zanna, B. Mondal, Y. K. Rao, **N. P. S. Mithun**, S. V. Vadawale, K. K. Reeves, H. E. Mason, A. Sarkar, P. Janardhan, and A. Bhardwaj. Multiwavelength Observations by XSM, Hinode, and SDO of an Active Region. Chemical Abundances and Temperatures. ApJ, 934(2):159, August 2022.

14. C. S. Vaishnava, **N. P. S. Mithun**, Santosh V. Vadawale, Esakkiappan Aarthy, Arpit R. Patel, Hiteshku- mar L. Adalja, Neeraj Kumar Tiwari, Tinkal Ladiya, Nilam Navale, Tanmoy Chattopadhyay, A. R. Rao, Varun Bhalerao, and Dipankar Bhattacharya. Experimental verification of off-axis polarimetry with cad- mium zinc telluride detectors of AstroSat-CZT Imager. Journal of Astronomical Telescopes, Instruments, and Systems, 8:038005, July 2022.

15. A. Ratheesh, A. R. Rao, **N. P. S. Mithun**, S. V. Vadawale, A. Vibhute, D. Bhattacharya, P. Pradeep, S. Sreekumar, and V. Bhalerao. A generalized event selection algorithm for AstroSat CZT imager data. Journal of Astrophysics and Astronomy, 42(2):37, October 2021.

16. D. Paul, A. R. Rao, A. Ratheesh, **N. P. S. Mithun**, S. V. Vadawale, A. Vibhute, D. Bhattacharya, P. Pradeep, and S. Sreekumar. Characterisation of cosmic ray induced noise events in AstroSat-CZT imager. Journal of Astrophysics and Astronomy, 42(2):68, October 2021.

17. Ajay Vibhute, Dipankar Bhattacharya, **N. P. S. Mithun**, V. Bhalerao, A. R. Rao, and S. V. Vadawale. Imaging calibration of AstroSat Cadmium Zinc Telluride Imager (CZTI). Journal of Astrophysics and Astronomy, 42(2):76, October 2021.

18. Tanmoy Chattopadhyay, Soumya Gupta, Vidushi Sharma, Shabnam Iyyani, Ajay Ratheesh, **N. P. S. Mithun**, E. Aarthy, Sourav Palit, Abhay Kumar, Santosh V. Vadawale, A. R. Rao, Varun Bhalerao, and Di-

pankar Bhattacharya. Sub-MeV spectroscopy with AstroSat-CZT imager for gamma ray bursts. Journal of Astrophysics and Astronomy, 42(2):82, October 2021.

19. Abhay Kumar, Tanmoy Chattopadhyay, Santosh V. Vadawale, A. R. Rao, Soumya Gupta, **N. P. S. Mithun**, Varun Bhalerao, and Dipankar Bhattacharya. Exploring sub-MeV sensitivity of AstroSat-CZTI for ON-axis bright sources. Journal of Astrophysics and Astronomy, 42(2):67, October 2021.

20. Sujay Mate, Tanmoy Chattopadhyay, Varun Bhalerao, E. Aarthy, Arvind Balasubramanian, Dipankar Bhattacharya, Soumya Gupta, Krishnan Kutty, **N. P. S. Mithun**, Sourav Palit, A. R. Rao, Divita Saraogi, Santosh Vadawale, and Ajay Vibhute. The AstroSat mass model: Imaging and flux studies of off-axis sources with CZTI. Journal of Astrophysics and Astronomy, 42(2):93, October 2021.

21. Biswajit Mondal, Aveek Sarkar, Santosh V. Vadawale, **N. P. S. Mithun**, P. Janardhan, Giulio Del Zanna, Helen E. Mason, Urmila Mitra-Kraev, and S. Narendranath. Evolution of Elemental Abundances during B-Class Solar Flares: Soft X-Ray Spectral Measurements with Chandrayaan-2 XSM. ApJ, 920(1):4, October 2021.

22. R. Ramesh, C. Kathiravan, **N. P. S. Mithun**, and S. V. Vadawale. Radio, X-Ray, and Extreme-ultraviolet Observations of Weak Energy Releases in the "Quiet" Sun. ApJ, 918(1):L18, September 2021.

23. Netra S. Pillai, S. Narendranath, K. Vadodariya, Srikar P. Tadepalli, V. Radhakrishna, Anurag Tyagi, Reena Yadav, Brajpal Singh, Vaishali Sharan, P. S. Athiray, P. Sreekumar, K. Sankarasubramanian, Megha Bhatt, Amit Basu Sarbadhikari, **N. P. S. Mithun**, and Santosh Vadawale. Chandrayaan-2 Large Area Soft X-ray Spectrometer (CLASS): Calibration, In-flight performance and first results. Icarus, 363:114436, July 2021.

24. Santosh V. Vadawale, Biswajit Mondal, **N. P. S. Mithun**, Aveek Sarkar, P.

Janardhan, Bhuwan Joshi, Anil Bhardwaj, M. Shanmugam, Arpit R. Patel, Hitesh Kumar L. Adalja, Shiv Kumar Goyal, Tinkal Ladiya, Neeraj Ku- mar Tiwari, Nishant Singh, and Sushil Kumar. Observations of the Quiet Sun during the Deepest Solar Minimum of the Past Century with Chandrayaan-2 XSM: Elemental Abundances in the Quiescent Corona. ApJ, 912(1):L12, May 2021.

25. B. Mondal, S. V. Vadawale, **N. P. S. Mithun**, C. S. Vaishnava, N. K. Tiwari, S. K. Goyal, S. S. Panini, V. Navalkar, C. Karmakar, M. R. Patel, and R. B. Upadhyay. DarpanX: A python package for modeling X-ray reflectivity of multilayer mirrors. Astronomy and Computing, 34:100446, January 2021.

26. M. Shanmugam, S. V. Vadawale, Arpit R. Patel, Hitesh Kumar Adalaja, **N. P. S. Mithun**, Tinkal Ladiya, Shiv Kumar Goyal, Neeraj K. Tiwari, Nishant Singh, Sushil Kumar, Deepak Kumar Painkra, Y. B. Acharya, Anil Bhardwaj, A. K. Hait, A. Patinge, Abinand han Kapoor, H. N. Suresh Kumar, Neeraj Satya, Gaurav Saxena, and Kalpana Arvind. Solar X-ray Monitor Onboard Chandrayaan-2 Orbiter. Current Science, 118(1):45–52, January 2020.

27. M. Shanmugam, S. V. Vadawale, Arpit R. Patel, **N. P. S. Mithun**, Hitesh Kumar Adalaja, Tinkal Ladiya, Shiv Kumar Goyal, Neeraj K. Tiwari, Nishant Singh, Sushil Kumar, Deepak Kumar Painkra, A. K. Hait, A. Patinge, Abhishek Kumar, Saleem Basha, Vivek R. Subramanian, R. G. Venkatesh, D. B. Prashant, Sonal Navle, Y. B. Acharya, S. V. S. Murty, and Anil Bhardwaj. Alpha Particle X-Ray Spectrometer Onboard Chandrayaan-2 Rover. Current Science, 118(1):53–61, January 2020.

28. Vidushi Sharma, Shabnam Iyyani, Dipankar Bhattacharya, Tanmoy Chattopadhyay, A. R. Rao, E. Aarthy, Santosh V. Vadawale, **N. P. S. Mithun**, Varun. B. Bhalerao, Felix Ryde, and Asaf Pe'er. Time-varying polarized gamma-rays from GRB 160821a: Evidence for ordered magnetic fields. The Astrophysical Journal, 882(1):L10, sep 2019.

29. Tanmoy Chattopadhyay, Santosh V. Vadawale, E. Aarthy, **N. P. S. Mithun**, Vikas Chand, Ajay Ratheesh, Rupal Basak, A. R. Rao, Varun Bhalerao, Sujay Mate, Arvind B., V. Sharma, and Dipankar Bhattacharya. Prompt emission polarimetry of gamma-ray bursts with the AstroSat CZT imager. The Astrophysical Journal, 884(2):123, oct 2019.

30. S. K. Goyal, A. P. Naik, **N. P. S. Mithun**, S. V. Vadawale, N. Nagrani, S. Madhvi, N. K. Tiwari, T. Ladiya, A. R. Patel, H. K. Adalja, T. Chattopadhyay, M. Shanmugam, A Auknoor, P Sharma, and V. R. Patel. Development of position sensitive detector module using scintillator and si photomultiplier for hard x-ray imaging and spectroscopy. Journal of Astronomical Telescopes, Instruments, and Systems, 5:5 – 5– 13, December 2018.

31. A. Basu, B. C. Joshi, D. Bhattacharya, A. R. Rao, A. Naidu, M. A. Krishnakumar, P. Arumugsamy, S. Vadawale, P. K. Manoharan, G. C. Dewangan, A. Vibhute, **N. P. S. Mithun**, and V. Sharma. Timing offset calibration of CZTI instrument aboard ASTROSAT. A&A, 617:A22, September 2018.

List of Figures

1.1 Emission components in X-ray spectra of BH binary, NS binary, and solar flares . . . 17

1.2 X-ray spectra of Perseus cluster with instruments in 1976 and 2016 23

1.3 Spectral redistribution of mono-energetic X-rays in detectors . . . 26

1.4 Effective areas of X-ray observatories . . . 30

1.5 Origin of background in X-ray detectors . . . 32

1.6 Dead time behavior in photon-counting detectors . . . 35

1.7 Modeling spectral redistribution in Silicon Drift Detectors . . . 38

1.8 Entrance window transmission measurement . . . 39

1.9 *AstroSat* mass model in Geant4 . . . 41

1.10 Background correlations in RXTE PCA . . . 45

1.11 Crab spectral parameters with two sets of calibration for RXTE PCA . . . 48

2.1 *AstroSat* CZTI instrument . . . 56

2.2 Ground calibration gain measurements of CZTI detector pixels . . 64

2.3 Calibration source spectra for CZTI quadrant A . . . 65

2.4 Spectral line redistribution function of CZTI detector pixel . . . 67

2.5 Spectral redistribution model parameters of all CZTI pixels . . . 68

2.6 Low gain pixels in CZTI: DPH and spectra . . . 72

2.7 CZTI pixel quality map . . . 73

2.8 Onboard calibration source spectrum fitting . . . 75

2.9 CZTI pixel gain correction: Original peak energies and corrected energies . . . 76

2.10 Detector resolution over time 77
2.11 Low energy and high energy thresholds of detector pixels 78
2.12 Short-term variations in background counts 81
2.13 Veto count rate histogram and thresholds 83
2.14 Long-term variability of CZTI background 84
2.15 Spectral variability in CZTI observations 85
2.16 Background DPH in different energy bands 87
2.17 Detector plane histogram of alpha-tagged events 88
2.18 Schematic showing source and background counts in detector elements in a coded mask instrument. 90
2.19 Efficacy of mask-weighting: Light curves of a blank sky observation 96
2.20 Efficacy of mask-weighting: Spectrum of a blank sky observation . 97
2.21 Systematic uncertainties in background subtraction 97
2.22 Mask-weighted flux profiles for different angular offsets 99
2.23 Measurement of angular offset by fitting mask-weighted flux profile 100
2.24 Angular offsets measured for each detector with respect to the mask. 101
2.25 Crab spectrum fitted with canonical models showing residuals at low and high energies 103
2.26 Low energy effective area correction 104
2.27 Simulation results showing expected additional contributions at higher energies 105
2.28 Crab spectra with different models 108
2.29 High energy response correction factor for each quadrant of CZTI 108
2.30 Crab spectral fits after effective area correction 109
2.31 Crab spectral parameters for different observations 110
2.32 Spectroscopic sensitivity of CZTI 111
2.33 Phase-resolved polarization measurements of Crab 114
2.34 Crab pulse profiles in different energy bins 115
2.35 Spectral parameters of pulsed component in Crab pulsar 116
2.36 Phase-resolved spectral index of Crab including off-pulse phases . 117

3.1 Chandrayaan-2 XSM instrument and its mounting on spacecraft . 125

3.2 Chandrayaan-2 orbital seasons and XSM solar observation opportunity . . . 128
3.3 XSM calibration source spectra . . . 132
3.4 XSM energy resolution and peak energy over time . . . 133
3.5 Variation in calibration source line intensity . . . 134
3.6 XSM FOV validation with solar observations . . . 136
3.7 XSM light curves with and without updates in effective area correction . . . 138
3.8 Effective area corrections to XSM . . . 141
3.9 Differences between event trigger rates and detected rates . . . 146
3.10 Correlation of event trigger and detected rates . . . 147
3.11 XSM light curve showing quiet Sun and background observations 149
3.12 X-ray flux light curve and dynamic spectrum of observations around a B-class flare . . . 150
3.13 Daily average background rates above 6 keV and ULD rates over four years . . . 151
3.14 ULD count rates over four years . . . 152
3.15 Daily average background rates above 6 keV for the first few months 153
3.16 Contribution of Sco X-1 to XSM background . . . 154
3.17 Daily average background rates above 6 keV and ULD rates over four years, excluding times with Sco X-1 in FOV and high ULD rates . . . 155
3.18 XSM background spectra in different observing conditions . . . 156
3.19 XSM spectra of sub-A to X-class flares . . . 157
3.20 XSM spectrum of a B-class flare fitted with isothermal model . . 159

4.1 Coronal X-ray/EUV features and photospheric magnetogram . . . 165
4.2 X-ray Sun over a Solar Cycle with Hinode XRT . . . 166
4.3 Solar flares in X-rays and classification . . . 167
4.4 Phases of solar flare . . . 169
4.5 Schematic of standard flare model scenario . . . 170
4.6 Flare frequency distributions from multiple observatories . . . 174

4.7 Thermal X-ray spectra of solar flares 176

4.8 Non-thermal X-ray spectra of solar flares 178

5.1 EUV and X-ray images during XSM observations and identification of quiet periods 186

5.2 XSM light curve and microflares in the quiet Sun 187

5.3 Selection of flare duration and quiet Sun period 191

5.4 X-ray light curves of representative microflares 193

5.5 EUV counterparts of XSM microflares and flare locations 194

5.6 Spectral fitting of XSM spectra of microflares 195

5.7 Temperature and emission measure of microflares 197

5.8 Flare frequency distribution and energy content 199

5.9 Probability distributions of power law parameters of the flare frequency distribution 200

6.1 X-ray light curves of three C-class flares 209

6.2 Isothermal fits to XSM spectra of the three C-class flares 211

6.3 Isothermal fit results to XSM spectra of the three flares 212

6.4 Investigation of effect of temporal averaging 213

6.5 Demonstration of the presence of multi-thermal plasma in flares . 215

6.6 XSM temperature response and temperature sensitivity of line complexes 217

6.7 EM loci curves for XSM spectrum 218

6.8 Fitting of X-ray spectra with multi-thermal models and best fit DEMs 222

6.9 DEM evolution during flares as inferred from XSM spectra 223

6.10 Evolution of elemental abundances during a solar flare 226

7.1 Sun viewing geometry from Solar Orbiter and Earth view points . 234

7.2 XSM and STIX X-ray light curves of the solar flare 236

7.3 X-ray spectra from XSM and STIX at three phases of solar flare with best-fit models 242

7.4 Flare plasma parameters during the flare 243

7.5 Comparions of XSPEC and OSPEX fitted parameters 246
7.6 Flaring region images from STIX and AIA 247
7.7 Flaring region volume estimates from STIX and AIA 248
7.8 Thermal and non-thermal energy estimates of the flare 250
7.9 Excess Fe line flux and possibility of fluorescence emission 253

8.1 Energy dependant polarization with anisotropy and high energy cutoff from simulations 259
8.2 Prototype focal plane Compton polarimeter 263
8.3 Geant4 rendering and CAD model of proposed polarimeter configuration 264
8.4 Optimal geometry of scatterer from simulation 266
8.5 Modulation amplitude and effective area of flare polarimeter . . . 266
8.6 Model and simulated observed flare spectra with polarimeter . . . 268
8.7 Minimum Detectable Polarization for different flare classes 269
8.8 Observation simulations of energy dependence of polarization . . . 270
8.9 Number of flares over the years and histogram of flares in solar maximum 270
8.10 Concept model of the polarimeter array and effective area 276
8.11 Minimum Detectable Polarization with source flux 277
8.12 Expected MDP for 1 Crab and 100 mCrab sources 278
8.13 Observation simulations for measurement of energy dependant polarization of Crab and Cyg X-1 279
8.14 Expected performance to measure off-pulse polarization variability in Crab pulsar 281

List of Tables

2.1 Summary of pixel quality classification 74

2.2 Threshold count rates in veto for data selection 82

2.3 List of observations used to generate the background non-uniformity model 94

2.4 List of observations of Crab with CZTI used for effective area calibration 102

2.5 List of CZTI sources with significant detections above 100 keV, excluding Crab and Cygnus X-1 113

3.1 Specifications of the XSM. 123

8.1 List of recent X-ray polarimetry missions 273

A.1 List of CZTI observations with signifcant detection of sources . . 306

Contents

Abstract **iii**

List of Publications **v**

List of Figures **xiii**

List of Tables **xix**

1 Intricacies of Astrophysical X-ray Spectroscopy **7**

1.1 X-ray Emission from Astrophysical Sources 8

1.1.1 Astrophysical X-ray sources 9

1.1.2 X-ray emission mechanisms 11

1.1.3 Disentangling emission components with X-ray spectroscopy 15

1.2 X-ray Spectroscopy: Instrumentation 16

1.2.1 Imaging and photon collection 16

1.2.2 Photon detection and energy measurement 19

1.2.3 Polarization measurement 24

1.3 X-ray Spectral Analysis and Challenges 24

1.3.1 What is the energy of the photon? 26

1.3.2 How much fraction of photons did we collect? 28

1.3.3 Is this event a photon from the source? 31

1.3.4 Did we miss to count some photons? 34

1.4 Calibrating X-ray Spectrometers on Ground 36

1.4.1 Spectral redistribution 36

1.4.2 Effective area 38

1.4.3 Background 40

1.4.4 Dead time . . . 42
1.5 Necessity of In-flight Calibration . . . 42
1.5.1 Detector response variations . . . 42
1.5.2 Background modeling . . . 44
1.5.3 Effective area and absolute flux calibration . . . 46
1.6 Thesis Objectives and Outline . . . 49

2 Hard X-ray Spectroscopy with AstroSat CZT-Imager 53
2.1 *AstroSat* Mission . . . 53
2.2 Cadmium Zinc Telluride Imager (CZTI) . . . 55
2.3 A Summary of Ground Calibration . . . 63
2.3.1 Gain calibration . . . 63
2.3.2 Spectral Redistribution and Effective Area . . . 65
2.4 In-flight Detector Characteristics and Gain . . . 70
2.4.1 Disabled and noisy pixels . . . 70
2.4.2 Low-gain pixels . . . 70
2.4.3 Gain parameters of good pixels . . . 74
2.4.4 Low energy and high energy thresholds . . . 77
2.5 Background in CZTI . . . 79
2.5.1 Short Term Variability and Data Selection . . . 80
2.5.2 Long Term Variability . . . 83
2.5.3 Variability Across Detector Plane . . . 85
2.6 Spectral Extraction by Mask-Weighting . . . 89
2.6.1 Background Non-Uniformity Model . . . 93
2.6.2 Efficacy of Background Subtraction . . . 95
2.7 Detector and Coded Mask Alignment . . . 98
2.8 Effective Area Calibration . . . 101
2.9 Spectroscopic Sensitivity and Prospects . . . 109
2.10 Phase-resolved Spectroscopy of the Crab Pulsar and Nebula . . . 114
2.11 Summary . . . 116

3 Soft X-ray Spectroscopy with Chandrayaan-2 XSM 119
3.1 Introduction . . . 119

3.2 *Chandrayaan-2* Solar X-ray Monitor (XSM) . . . 122
3.3 A Summary of Ground Calibration . . . 127
3.4 In-flight Performance and Calibration . . . 131
3.4.1 Energy Resolution and Gain . . . 132
3.4.2 Collimator Response and Effective Area . . . 134
3.4.3 Deadtime Correction . . . 145
3.4.4 Background and Sensitivity . . . 148
3.5 X-ray Spectral Analysis with XSM . . . 158
3.6 Summary and Prospects with XSM . . . 159

4 Multi-Scale Solar Flares: An X-ray Perspective 161
4.1 The X-ray Sun . . . 162
4.1.1 A Historical Overview . . . 162
4.1.2 Coronal X-ray Features . . . 164
4.1.3 Solar flares . . . 166
4.2 Flare Observations and Standard Flare Model . . . 168
4.3 Coronal Heating: Nanoflares and Microflares . . . 172
4.4 X-ray Spectral Investigations of Solar Flares . . . 175
4.4.1 Thermal emission . . . 176
4.4.2 Non-thermal emission . . . 177
4.4.3 Solar observatories . . . 179
4.4.4 Solar X-ray spectral analysis . . . 181

5 Multi-Scale Solar Flares: Microflares and Coronal Heating 183
5.1 Introduction . . . 184
5.2 Microflare Observations and Analysis . . . 185
5.2.1 EUV Counter Parts of Microflares . . . 188
5.2.2 X-Ray Images and Photospheric Magnetograms . . . 189
5.2.3 X-Ray Spectroscopy of Microflares . . . 190
5.3 Results and Discussion . . . 192
5.3.1 Microflare location . . . 192
5.3.2 Temperature and Emission Measure . . . 195
5.3.3 Flare Thermal Energy Distribution . . . 198

5.4 Summary 202

6 Multi-Scale Solar Flares: Heating of Multi-thermal Plasma in Flares 205

6.1 Introduction 206

6.2 Flare Observations 208

6.3 Isothermal Approximation 210

6.3.1 Effect of temporal averaging 213

6.3.2 Range of temperatures in multi-thermal plasma 214

6.4 Multithermal Plasma: Differential Emission Measure Analysis . . 215

6.4.1 XSM temperature response and temperature sensitivity of line profiles 216

6.4.2 Emission measure loci 218

6.4.3 Multi-thermal model fitting 219

6.5 Discussion and Conclusions 225

7 Multi-Scale Solar Flares: Thermal and Non-thermal Energies of Flares 231

7.1 Introduction 231

7.2 Observation of the Flare with XSM and STIX 233

7.2.1 Flare observation geometry 234

7.2.2 Soft and hard X-ray light curves 236

7.2.3 X-ray Spectral Analysis 237

7.2.4 Imaging Analysis 240

7.3 Analysis Results 241

7.3.1 Spectroscopy 241

7.3.2 Imaging 246

7.4 Discussion 248

7.4.1 Thermal and Non-thermal Energy 249

7.4.2 Fe line residuals and Fe fluorescence 251

7.4.3 Directivity and Albedo effects 254

7.5 Conclusions and Summary 254

8 Beyond Spectroscopy: Prospects of X-ray Spectro-Polarimetry 257

8.1 Case for X-ray Polarimetry of Solar Flares 258

8.2 Conceptual Design of Flare Polarimeter 260

8.2.1 Compton X-ray polarimetry 261

8.2.2 A prototype focal plane Compton polarimeter 262

8.2.3 Spectro-Polarimeter Configuration and Geant4 Simulations 263

8.2.4 Expected Performance 267

8.3 Polarimetry of Other Astrophysical Sources 271

8.3.1 Science Cases of Hard X-ray Polarimetry 274

8.3.2 Instrument Concept and Expected Performance 276

8.4 Summary 281

9 Summary and Future Prospects 283

9.1 Summary 283

9.2 Future Prospects 286

A List of observations with source detections in CZTI 291

Chapter 1

Intricacies of Astrophysical X-ray Spectroscopy

Celestial objects have always fascinated humanity. Historical records and remains from ancient civilizations show their interest in studies of celestial objects. The invention of telescopes allowed humans to resolve objects that could not be seen with the naked eye, such as the Moons of Jupiter. Still, the observational capabilities were limited by the 'detector', which was the human eye. The modern era of astronomical observations began with the advent of photographic plates and their use with telescopes. Imaging the sky with longer integration times allowed the discovery of fainter objects and spatial distribution of extended sources, and observations over time allowed measurements of time variability. The development of prisms to disperse visible light into different wavelengths and their use with telescopes added another dimension to astrophysical observations. The discovery of electromagnetic radiation beyond the visible wavelengths prompted astronomers to search for emissions from astrophysical sources at other wavelengths, expanding astronomy to include infrared astronomy, radio astronomy, ultra-violet astronomy, and X-ray and gamma-ray astronomy.

Modern-day astronomical observations use advanced technologies to record the sky location, wavelength (or energy), arrival time, and polarization of photons from astrophysical sources to decipher their geometry and physical processes involved. This is complemented by the parallel advances in theoretical and numerical studies that provide predictions of models that can be compared against observations. Specifically, observations in the high energy end of the electromagnetic spectrum, the X-rays and Gamma-rays, offer the possibility of investigating the matter in extreme conditions such as the plasma with temperatures of millions of Kelvin in the solar atmosphere, the accreting material close to the event horizon in black hole binaries, and highly dense material in fast rotating neutron stars. They also offer the possibility of testing physics in extreme limits such as the strong field limit tests of general relativity (Ayzenberg & Bambi, 2022) and testing quantum electrodynamics (QED) effects in highly magnetized neutron stars (Nättilä & Kajava, 2022).

1.1 X-ray Emission from Astrophysical Sources

It took more than 50 years since the discovery of X-rays in 1895 to detect X-ray emission from astrophysical sources as it required rockets or satellites to carry the instruments above the layers of Earth's atmosphere that absorb the X-rays. Experiments by scientists from Naval Research Laboratory (NRL), USA, using V-2 rockets led to the first detection of X-rays from an astrophysical source - the Sun (Burnight, 1949; Friedman et al., 1951). More than ten years later, rocket experiments looking for X-rays from the Moon resulted in the first detection of X-rays originating outside the solar system, from the source now named as Sco X-1 (Giacconi et al., 1962). Several rocket flights in the years to come discovered a few more X-ray sources, including the Crab Nebula. However, the limited observing windows available with rocket flights restricted significant advances.

X-ray astronomy was revolutionized with the 1970 launch of the first dedicated X-ray observatory satellite *Uhuru* (Giacconi et al., 1971). Observations with *Uhuru* led to the discovery of more than three hundred new X-ray sources (Forman et al., 1978). The opportunity to observe the sources for longer periods with *Uhuru* allowed the detection of pulsations and time variability in the sources. This led to the identification of many X-ray sources as binary systems, with one star being a fast-rotating neutron star or a black hole. *Uhuru* also detected the X-ray emission from the intracluster medium between the galaxies, which also had profound implications in cosmology (Gursky et al., 1972). In parallel, X-ray observations of the Sun were advanced during this period with the experiments on board the series of Orbiting Solar Observatories (OSO) and experiments including imaging X-ray telescopes on the first US space station, Skylab. The *Einstein* observatory, which was the first to employ focusing X-ray telescopes for astrophysical observations, discovered other classes of X-ray sources from the Auroral emission from Jupiter in the solar system to distant Active galaxies and quasars. For a brief account of the early history of X-ray astronomy, interested readers are referred to the Nobel Lecture by Riccardo Giacconi[1]. A chronological history of X-ray astronomy missions is given by Santangelo et al. (2023).

In the last three decades, there have been many more dedicated X-ray and Gamma-ray observatories, such as *RXTE*, *Chandra*, *XMM-Newton*, *INTEGRAL*, *Fermi*, *Swift*, *NuSTAR*, *AstroSat*, *NICER*, *SRG*, and most recently, the X-ray polarimetry mission *IXPE*. Observations with these have contributed significantly to our understanding of various classes of X-ray emitting sources by employing the techniques of X-ray timing, spectroscopy and more recently, polarimetry. A brief overview of astrophysical X-ray sources and X-ray emission mechanisms is given here, and the power of X-ray spectroscopic measurements to disentangle different emission components is brought out.

1.1.1 Astrophysical X-ray sources

Different classes of astrophysical sources of X-ray emission, where the emission arises in extreme conditions, are listed here.

Solar Corona: Corona, the outer atmosphere of the Sun, is rare hot plasma at temperatures of the order of million Kelvin. Solar corona emits profusely in the X-ray and EUV wavelengths. In addition to quiescent emission from the corona, sudden enhancements in emission, called solar flares, are also observed. A recent review on X-ray emission from solar corona is given by Testa & Reale (2023). More details on the X-ray Sun are given in Chapter 4 of this thesis, and X-ray

[1] https://www.nobelprize.org/uploads/2018/06/giacconi-lecture.pdf

spectroscopic investigations of solar flares are part of the thesis.

Black hole binaries: These are binary systems where one object is a stellar mass black hole that accretes matter from its companion and emits profusely in X-rays. Due to the angular momentum of the incoming material, they form an accretion disk around the black hole (Shakura & Sunyaev, 1973). Observations also suggest the presence of a hot inner corona and, in some cases jets (Remillard & McClintock, 2006). Some of the black hole binaries are persistent X-ray sources, while others are transients. A recent review on X-ray spectral and timing properties of black holes is given by Kalemci et al. (2022).

Neutron star binaries: These are binary systems where a neutron star is accreting matter from its companion. Depending on the mass of the companion, they are classified into low-mass X-ray binaries and high-mass X-ray binaries (the same classification applies to black hole binaries as well). The interplay of magnetic fields around the neutron star and accretion causes rich phenomenology in these classes of sources. Reviews of neutron star X-ray binaries with low magnetic fields and high magnetic fields are given by Salvo et al. (2022) and Mushtukov & Tsygankov (2022).

Pulsar Wind Nebulae: They are powered by the energetic pulsars at their center. The emission from PWNs has been detected over the entire electromagnetic spectrum up to very high energy gamma rays, showing the presence of particles accelerated to ultra-relativistic energies. Mitchell & Gelfand (2022) provides a review on pulsar wind nebulae.

Active Galactic Nuclei: AGNs are powered by the accretion of matter into the supermassive black hole at their center. The high energy emission arises from the central region of the AGNs. Based on the unification model of the AGN, the different classes of AGNs arise from the viewing angle effect. Emission processes in the vicinity of supermassive black holes in AGNs are reviewed by Alston et al. (2023).

ISM, IGM, CGM, and ICM: The interstellar medium (ISM) in other galaxies, intergalactic medium (IGM), circumgalactic medium (CGM), and intracluster medium (ICM) are all regions where warm/hot ionized gas is present that emits in predominantly soft X-rays.

Gamma-ray Bursts: Gamma-ray bursts (GRBs) are one of the most energetic events in the universe, observed first as flashes of gamma-rays and hard X-rays. After this 'prompt' GRB emission, afterglow is observed in soft X-rays and other higher wavelength bands. Progenitors of GRBs are identified as the core collapse of massive stars and the merger of neutron stars, depending on whether the GRB emission is long ($\sim> 2s$) or short ($\sim< 2s$), respectively. See Yu et al. (2022) for a recent review on GRBs.

Stellar coronae: Much like the Sun, many of the main sequence Sun-like stars also have a hot corona, which emits X-ray emission. Magnetically active stars produce a corona and stellar flares that are intrinsically brighter than the solar flares are also observed from some of the active stars. A recent review on stellar coronae and their X-ray observations is given by Drake & Stelzer (2023).

In addition to the sources listed above, solar system objects such as planets and satellites have also been observed in X-rays, where the X-ray emission often arises from excitation due to external sources such as solar X-rays or particles and cosmic rays (Bhardwaj, 2022; Dunn, 2022a,b).

1.1.2 X-ray emission mechanisms

When any charged particle undergoes acceleration, electromagnetic radiation is emitted. Larmor's formula provides the power emitted by an accelerating charged particle in the non-relativistic regime, whereas calculations with Liénard–Wiechert potentials give a relativistic generalization (Jackson, 1998). Radiation emitted by a population of charged particles often spans over a wide range of wavelengths, and such emission is referred to as continuum emission. If the particles emitting the radiation are in thermal equilibrium and follow the Maxwell-Boltzmann distribution, we call it 'thermal emission'. On the other hand, if the particles are accelerated to non-Maxwellian distributions such as a power law, then it is referred to as 'non-thermal emission'. Aside from the continuum emission processes, line emission confined to specific wavelengths also arises from the relaxation of atoms from excited states. A brief overview of the major continuum processes and various atomic excitation processes resulting in line emission is provided.

Continuum Emission

Bremsstrahlung: Bremsstrahlung emission occurs when charged particles like electrons decelerate in the Coulomb field of another charged particle, such as atomic nuclei. As the particles emitting the radiation are free (not bound to atoms) before and after the emission, it is also often referred to as free-free emission. The mass difference between electrons and nuclei makes electrons the primary radiators. The emission spectrum by bremsstrahlung depends on the energy/velocity distribution of particles (electrons) in the emitting medium. When the electron population is thermal following Maxwell-Boltzmann distribution, the bremsstrahlung emissivity is:

$$\epsilon_\nu{}^{ff} = 6.8 \times 10^{-38}\ Z^2 n_e n_i T^{-1/2} exp\left[-\frac{h\nu}{kT}\right]\bar{g}_{ff} \tag{1.1}$$

where $\bar{g}_{ff}$ is the velocity averaged Gaunt factor that incorporates quantum mechanical corrections to the classical treatment (Rybicki & Lightman, 1979). From the equation, it can be noted that the thermal bremsstrahlung spectrum is constant at lower energies (frequencies) and has an exponential cut-off at higher energies. When the medium is optically thick to the emitted free-free photons, the lower energy part of the spectrum gets modified, similar to that of black body radiation. The thermal bremsstrahlung process is observed in sources such as the solar corona and intracluster medium. When the population of particles follows a non-thermal distribution such as a power law, the spectrum of non-thermal bremsstrahlung also follows a power law distribution. Non-thermal bremsstrahlung is important in sources such as solar flares.

Synchrotron emission: Acceleration of electrons in magnetic fields results in the emission of electromagnetic radiation. If the electrons are non-relativistic ($v \ll c$), the emission is called gyro radiation. Emission from mildly relativistic electrons ($\gamma \sim 1$) is termed cyclotron radiation, and that from ultra-relativistic electrons ($\gamma \gg 1$) is synchrotron radiation. The synchrotron emission spectrum from a population of non-thermal electrons following a power law distribution is again a power law in some energy ranges. For example, if the electron energy distribution is given by $N(E) \propto E^{-p}$, then the synchrotron emissivity is:

$$I(\nu) \propto \nu^{-(p-1)/2} \tag{1.2}$$

which is again a power law with an index related to the electron index (Longair, 2011). At low frequencies/energies, when Synchrotron-self absorption causes the medium to be optically thick, the spectrum is proportional to $\nu^{(5/2)}$. The synchrotron process is important in the emission from supernova remnants and jets of active galactic nuclei.

Compton Scattering: X-ray scattering processes lead to modification of the emission spectra in astrophysical sources. In Compton scattering, photons are scattered from a stationary electron, and the energy of the scattered photon is less than the incident photon, transferring the energy difference to the electron. When photon energies are much lower than the rest mass energy of the electron ($h\nu \ll m_e c^2$), the scattering process leads to only change in the photon direction without any energy transfer, and the process is called Thomson scattering. The scattering cross-section for the Compton process is given by the Klein-Nishina formula, which reduces to the Thomson scattering cross-section for low energy photons (Longair, 2011; Rybicki & Lightman, 1979). When low-energy photons get scattered from ultra-relativistic electrons, they gain energy, while the electrons lose their kinetic energy. This process is known as inverse Compton scattering. In black hole binaries, the hard X-ray emission from the corona is due to inverse Compton scattering of the accretion disk emission by hot electrons in the corona (e.g., Remillard & McClintock, 2006).

Blackbody radiation: When the emitted photons are in thermodynamic equilibrium with the thermal population of particles emitting the radiation, the emission spectrum follows the Planck function, providing the intensity of emission as a function of frequency (I_ν) for a given temperature (T) as:

$$I_\nu(T) = \frac{2h\nu^3}{c^2}\left[exp\left(\frac{h\nu}{kT}\right) - 1\right]^{-1} \tag{1.3}$$

This happens when the optical depth of the emission region is very high ($\tau \gg 1$), so the photons have to undergo several interactions before leaving the medium. The classic example of blackbody emission is the stellar photospheric emission peaking in optical/NIR/NUV wavelengths. The X-ray emission from accretion disks of blackhole binaries is a multi-color blackbody emission consisting of blackbodies at different temperatures from different annuli of the disk (Frank et al., 2002).

Radiative Recombination: It is the capturing of a free electron by an ion into a bound state, emitting radiation. The continuum emission from this process is often termed free-bound emission. This is the reverse process of photoionization. The emitted photon energy is equal to the kinetic energy of the captured electron and the ionization energy of the bound state to which it was captured, and thus, the photon spectrum is a continuum for a thermal electron population. However, the spectrum has discontinuities at ionization energy levels of different bound states of ionized species. Free-bound emission is dominant compared to free-free emission in some cases, such as in the solar corona at some energy ranges for some ranges of temperatures (see, e.g., Kaastra et al., 2008).

Two-photon emission: This process is important for H-like and He-like ions. Suppose for H-like ions, the electrons in $1s$ shells are collisionally excited to $2s$ level with chances of further collisional excitation to be less due to low densities. In such cases, as the dipole transitions from the $2s$ level to the $1s$ level are forbidden, the electron decays by emission of two photons. The sum of the energy of the two photons is equal to the energy level difference. A similar process is applicable for transitions from $1s^1 2s^1$ state to $1s^2$ state for He-like ions. This process has no significant contribution in most cases in X-ray energies, but it is important to consider in estimating populations of H-like and He-like ions in plasma such as in the solar corona (see Del Zanna & Mason, 2018 and references therein).

Line Emission

In addition to various emission processes resulting in continuum emission, line emissions are important in some astrophysical X-ray sources. Line emission arises from bound-bound transitions of various neutral or ionized species. Electronic transitions from upper levels to lower levels result in the emission of photons corresponding to the energy difference. The power of the spectral line per unit volume for a transition from j to i level is given by:

$$P_{ji} = A_{ji}\, n_j \tag{1.4}$$

where A_{ji} is the Einstein coefficient of the spontaneous transition probability, and n_j is the number density in the excited state. Atoms or ions need to be first excited to higher levels before they can decay with the emission of lines. Various processes are responsible for this, such as collisional excitation, photo-absorption, inner shell ionization by free electron collision, free electron capture to higher levels by radiative recombination or dielectronic recombination, and inner shell ionization by photoelectric effect leading to X-ray fluorescence emission (Kaastra et al., 2008). Line emission intensities are calculated by considering the detailed balance of these processes to determine the equilibrium level populations.

1.1.3 Disentangling emission components with X-ray spectroscopy

Often, the X-ray emission from astrophysical sources arises from more than one of the radiative processes discussed before, and the objective is to identify the contributions of different processes and understand the physical parameters and geometry of the source regions. If we look at the X-ray spectrum of astrophysical sources, we see multiple components superposing to get the total spectrum. As an example, Figure 1.1 presents the model X-ray spectra for Black hole binaries, Neutron star binaries, and solar flares, showing the different components. In black hole binaries, there is multi-color black body emission from the accretion disk, inverse Compton scattered component of the disk emission from the corona, and the so-called reflection component, which is due to irradiation of the disk by the coronal emission resulting in X-ray fluorescence and Compton scattered emissions. In the case of the neutron star binary spectrum, the dominant component is bremsstrahlung. The black body surface of the neutron star, Fe fluorescence emission, and cyclotron resonant scattering feature are the other contributing components. For solar flares, the model spectra show a contribution from thermal bremsstrahlung and line emissions in soft X-rays, non-thermal bremsstrahlung in hard X-rays, and positron, nuclear lines, and pion decay in gamma rays.

In all cases, what we can observe is the total spectrum that reaches us, which is the sum of spectra from all different processes. But, if we can accurately measure the X-ray spectrum over broad energy ranges, then by modeling the observed spectra as the sum of different components, we can infer the contributions from different emission mechanisms as done to get to the models given in Figure 1.1. This is often referred to as continuum X-ray spectroscopy, as in most cases, the continuum processes dominate the emission spectrum, and even when line emission is present, they are on top of the continuum emission. Disentangling the emission components by continuum X-ray spectroscopy is possible only when the spectral measurements have the least uncertainties such that ‘correct’ models can be favored over other possible ‘incorrect’ models. Let us first review the instrumentation used for X-ray spectroscopy.

1.2 X-ray Spectroscopy: Instrumentation

Any X-ray spectroscopic instrument for astrophysical observations consists of two primary components. The first component is the imaging component, which helps in locating the source in the sky and collecting photons from a specific part of the sky while restricting photons from other regions. These may be collimators, indirect imaging techniques such as coded masks, or focusing X-ray telescopes. The other component is the X-ray detector, which detects the X-ray photons, measures their energy, and, in case of use with X-ray imaging elements, measures the photon’s position.

1.2.1 Imaging and photon collection

Collimators: Collimators are the simplest imaging/photon collection system where photons from only a specific solid angle range are allowed to reach the detector. The geometry decides the field of view (FOV) of the collimators. They are made of materials that do not allow X-ray photons within the energy range of

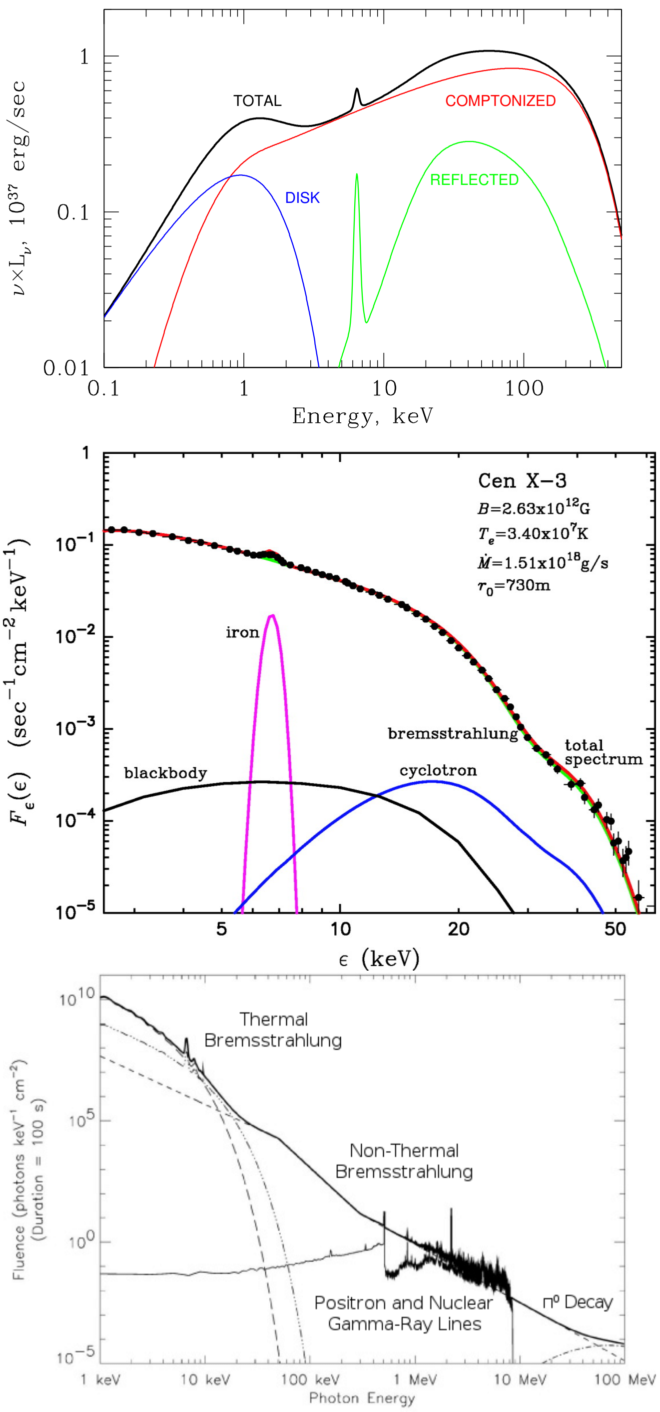

Figure 1.1: Components from different emission processes in X-ray spectra of black hole binaries (top), neutron star binaries (middle), and solar flares (bottom). Figures are taken from Gilfanov (2010), Becker & Wolff (2007), and Lin et al. (2002), respectively.

interest from regions outside the FOV to reach the detector. Often, collimators are made with multiple materials so that X-ray fluorescence from the collimator material reaching the detector is restricted. If there are multiple sources within the FOV, collimated instruments will not be able to distinguish between them. Another drawback is that the detector area determines the effective area, and thus, the background is generally much higher in collimated instruments. However, the advantage is that very large area instruments can be built with collimators, which is especially useful for timing studies, such as the case with *AstroSat* LAXPC.

Indirect imaging: Another class of techniques is indirect imaging, where parts of a position sensitive detector are selectively blocked with opaque material while the source illuminates other parts. This creates spatial modulation of the signal on the detectors, from which the image is reconstructed. One of the most commonly used indirect imaging techniques in X-ray and gamma-ray astronomy is coded aperture mask (Goldwurm & Gros, 2022). In this, random open and closed mask elements are placed on top of a position-sensitive detector plane such that the shadow pattern for sources from various directions differs, and the sky images can be reconstructed from observed counts in detectors and knowledge of the mask pattern. A major advantage of coded mask instruments is that they can have wide FOV and are best suited for transient detections and surveys. Coded masks have been employed in various instruments such as *RXTE* ASM, *INTEGRAL* IBIS, *Swift* BAT, *MAXI*, *AstroSat* SSM, and *AstroSat* CZTI. Another kind of indirect imaging uses multiple sets of detectors (not position sensitive) with grid patterns placed in front and then rotates the instrument so that the counts in the detectors are modulated temporally; these are called rotating modulation collimators (RMC; Smith et al., 2004). This technique is employed in the solar hard X-ray imaging spectrometer RHESSI (Lin et al., 2002). The requirement of rotation can be avoided by having two grid patterns in front of position-sensitive detectors such that spatial modulations are obtained, which can be used to reconstruct images (see Saint-Hilaire et al., 2022 for a review of this technique). This method has been employed for solar X-ray imaging by *Yohkoh* Hard X-ray Telescope (HXT) and more recently by *Solar Orbiter* Spectrometer/Telescope Imaging in X-rays (STIX).

Focusing X-ray telescopes: Both collimated instruments and indirect imaging instruments have the disadvantage of requiring large area detectors, causing the background to be high, which is proportional to the detector volume and hence have lower sensitivity. This can be overcome with telescopes that will focus the flux from the source to a smaller detector area, which also provides high angular resolution imaging. As the refractive index of X-rays is close to unity, X-ray reflection is feasible only at grazing angles and the geometric configuration that is most commonly used in the Wolter-I configuration (Wolter, 1952). The first focusing X-ray optics telescope was flown in the *Einstein* mission, and since then, most of the X-ray telescopes have been limited to the soft X-ray band due to difficulties in reflecting hard X-rays. The first and the only operational hard X-ray telescope is *NuSTAR* (Harrison et al., 2013), employing depth-graded multi-layer coating to enhance reflectivity at higher energies. A recent review of X-ray optics used in astrophysical observations is given by Christensen & Ramsey (2022).

In addition to the photon-collecting elements, the X-ray photons from the source usually have to pass through some entrance window or filter before reaching the X-ray detector. The specific purpose of these X-ray filters may differ from case to case. But in general, X-ray filters block electromagnetic radiation from other bands, such as the optical band, low-energy particles, and low-energy X-rays below the energy range of interest, so they would not interfere with the X-ray measurements (Barbera et al., 2022). For observations of bright X-ray sources, such as the Sun, filters are also used to ensure that the photon flux on the detector is within its operating limits.

1.2.2 Photon detection and energy measurement

High-energy photons interact with matter by four major processes: (i) photoelectric absorption, (ii) Thomson/Rayleigh scattering, (iii) Compton scattering, and (iv) electron-positron pair production. Among these, pair production is feasible for Gamma-rays at energies above 1.022 MeV and thus not relevant in detecting X-rays. Thomson/Rayleigh scattering of photons results in a change in the direction of the incoming photon without any energy deposition in the matter and thus does not help to detect X-ray photons. Compton scattering results in partial deposition of its energy in the matter, so while it can be used to detect photons, it is not the best-suited process to rely on for energy measurement.

Thus, most X-ray spectroscopic detectors rely on the photoelectric absorption process, and it is also the most dominant process for the low energy X-rays where $E = h\nu \ll m_e c^2$. In the photoelectric effect, photons having energy higher than that of an atomic energy level cause the ejection of the electrons from that energy level with the kinetic energy equal to the difference between the photon energy and energy required to eject from the atmoic level. X-ray detectors measure the charge generated due to this deposition of energy by the photon. The vacancy in the ionized atom gets quickly filled by either radiative or non-radiative relaxation. In the case of radiative atomic relaxation with the emission of a characteristic X-ray and it escapes the detector medium, the charge recorded by the detector will correspond to the incident photon energy minus the characteristic photon energy. The cross-section of photo-electric absorption is proportional to Z^n, where Z is the material's atomic number with n varying between 4 and 5 (Knoll, 2000). Thus, materials with higher atomic numbers are more efficient as X-ray detectors compared to materials of lower atomic numbers with the same thickness. Some of the most commonly used X-ray detectors for astrophysical observations are discussed below.

Proportional counters: Gas-filled proportional counter detectors were the earliest used X-ray detectors for astrophysical observations. This consists of a gas-filled chamber with anode wires. Photo-electric interaction in the gas by the incident X-rays results in charge cloud generation, which drifts and multiplies towards the anode wire, and the charge is collected at the anode. The voltage applied to the anode is set such that the chamber operates in the proportional regime where the charge is proportional to the photon energy. Some of the instruments that have employed large area proportional counters for X-ray timing and spectroscopic studies are *Ginga* Large Area Proportional Counter

(LAC), *RXTE* Proportional Counter Array (PCA), and *AstroSat* Large Area Proportional Counters (LAXPC; Agrawal et al., 2017). Position sensitive proportional counters have been used in *RXTE* All Sky Monitor (ASM), *MAXI* Gas Slit Camera (GSC; Mihara et al., 2011), and *AstroSat* Scanning Sky Monitor (SSM; Ramadevi et al., 2017) for all sky monitoring of X-ray transients. An account of proportional counter detectors for X-ray astronomy is provided by Diebold (2022).

Scintillators: X-ray interactions in scintillation detectors result in the generation of optical light. By measuring the intensity of the scintillation light using devices such as photo-multiplier tubes, the energy of the incident photon can be estimated. Inorganic scintillation detectors like CsI and NaI have relatively high-Z constituent elements and can be made into thick crystals, and thus, they can have good detection efficiency for high-energy X-rays. *RXTE* High Energy X-ray Timing Experiment (HEXTE) and *Suzaku* Hard X-Ray Detector (HXD) used scintillation detectors. Iyudin et al. (2022) reviews the use of scintillation detectors in X-ray and gamma-ray astronomy.

X-ray Charge-Coupled Device: Soon after their development, CCDs replaced photographic plates as imaging detectors in optical astronomy. CCDs were also then adapted in X-ray observations as focal plane detectors for focusing telescopes with an increase in the depth of the depletion layer to have good efficiency for X-ray detection. X-ray CCDs are used in various observatories such as *Chandra* ACIS, *Swift* XRT, and *AstroSat* SXT. *XMM-Newton* EPIC-PN uses a special type of CDD with a depletion layer thickness of $\sim$ 300 μm providing higher efficiency for X-ray detection. Bautz et al. (2022) provides an account of X-ray CCDs.

Thick silicon detectors: While X-ray CCDs have the advantage of providing high position resolution, they have limitations in achieving higher efficiencies due to their relatively thin depletion depth. Silicon-based detectors with thicker depletion depths, such as Si-PIN and Si-strip detectors, have also been used in X-ray astronomy missions. *Suzaku* HXD uses a 2 mm thick Si-PIN detector with no position resolution operating in the energy range of 10 – 70 keV, and *Hitomi* SGD uses multiple Si-strip detectors having 0.6 mm thickness with coarse position resolution. The new generation of Si detectors with a unique electrode configuration resulting in lower detector capacitance, named Silicon Drift Detectors (SDD), provide better energy resolution and timing compared to the Si-PIN detectors and, at the same time, provide higher depletion depths than CCDs. SDDs are used in the NICER mission. *Chandrayaan-2* XSM also employs SDD for spectroscopic observations of the Sun (see Chapter 3). SDD is also used in the SoLEXS instrument onboard *Aditya-L1*. See Tajima & Hagino (2022) for more details on Si-strip detectors, and details of SDDs are provided by Vacchi (2022).

CdTe and CZT: Silicon-based detectors have limitations in use for the detection of higher energy X-rays as they have relatively lower photoelectric absorption-cross sections. Thus, semiconductor detectors made of higher-Z materials like Cadmium Telluride (CdTe) and Cadmium Zinc Telluride (CZT) are used as hard X-ray detectors. Single-pixel CZT detectors are used in *Swift* BAT while *NuSTAR* and *AstroSat* CZTI use pixellated CZT detectors. *Hitomi* HXI and SGD employ CdTe double-sided strip detectors. Hard X-ray solar spectrometer HEL1OS onboard *Aditya-L1* employs both CdTe and CZT detectors. Meuris et al. (2022) provides a review of CZT detectors in X-ray and gamma-ray astronomy.

Microcalorimeter: Microcalorimeters are high-resolution X-ray detectors achieving few eV spectral resolution. Unlike the other detectors discussed so far, they do not measure the charge corresponding to the photon but rather measure the change in temperature due to photoelectric interactions. The change in temperature corresponds to the photon energy. To reach such high resolutions, the sensors have to be operated at very low temperatures of the order of a few mK. Microcaloritmer-based spectrometers were part of *Astro-E*, *Suzaku (Astro-E2)* and *Hitomi (Astro-H)* missions, but unfortunately had very limited to no observing opportunity. The Soft X-ray Spectrometer (SXS) onboard *Hitomi*, used a silicon thermistor-based microcalorimeter (Kilbourne et al., 2018), which could make a few very high spectral resolution observations before the mission was lost. It is now flown again on the recently launched *XRISM* mission. Next-generation microcalorimeters based on other technologies, such as transition-edge sensors, are in development (see Gottardi & Smith, 2022 for a recent review).

It may be noted that aside from direct energy measurements by X-ray detectors, as discussed above, dispersive elements such as gratings can also be used to obtain very high-resolution spectra in soft X-rays, similar to the techniques used in optical wavelengths. *Chandra* mission includes two spectrometers that use transmission gratings, HETG and LETG. *XMM-Newton* employs reflection gratings in RGS. Crystal-based spectrographs using Bragg's law also have been employed, specifically in solar observations. *SMM* BCS, *Yohkoh* BCS, and *CORONOS-PHOTON* RESIK were some of the Bragg crystal spectrographs used for high resolution soft X-ray spectral measurements of the Sun.

Over time, since the advent of X-ray astronomy, detector technologies have improved in various aspects, and efforts continue to improve the detectors and develop new kinds of detectors. Figure 1.2 shows the X-ray spectrum of the Perseus cluster observed with proportional counters on *Ariel 5* in 1976 compared to the spectrum from the microcalorimeter instrument on *Hitomi* in 2016, displaying the advancement in X-ray spectroscopic capabilities over the years.

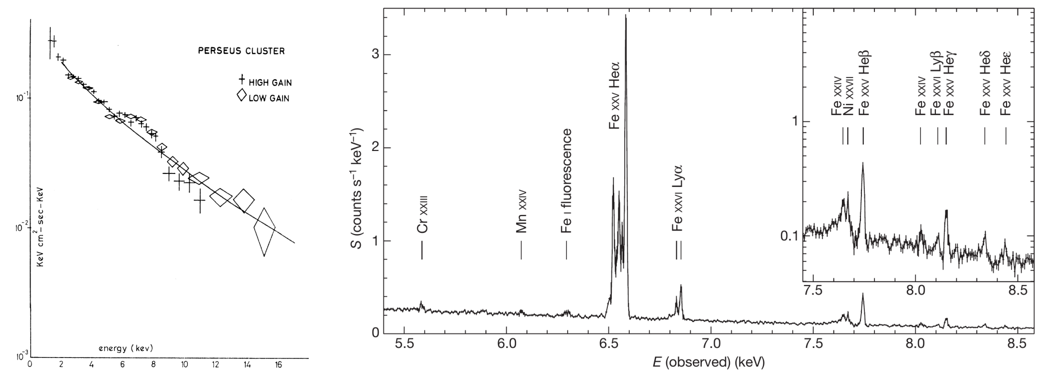

Figure 1.2: X-ray spectrum of the Perseus cluster obtained with proportional counters onboard *Ariel 5* in 1976 (left) and with microcalorimeter onboard *Hitomi* in 2016 (right). The figures are taken from Mitchell et al. (1976) and Hitomi Collaboration et al. (2016).

1.2.3 Polarization measurement

Aside from forming the basis for X-ray spectroscopy, the photoelectric absorption process is also utilized for X-ray polarization measurements. By detecting the tracks of ejected photoelectrons and measuring their azimuthal angle distribution, the polarization degree and angle of incident photons can be measured in the soft X-ray band (Costa et al., 2001). This technique of photoelectric polarimetry is employed in the recent dedicated X-ray polarimetry mission *IXPE* (Weisskopf et al., 2022). Although the Rayleigh and Compton scattering processes are not ideal for X-ray spectroscopy, they are invaluable in X-ray polarization measurements at higher energies. By measuring the azimuthal angle distribution of Rayleigh (Thomson) or Compton scattered photons, polarization properties of the incident X-rays can be determined (see e.g. Del Monte et al., 2023). Rayleigh scattering is best suited in the medium energy X-rays ($\sim 10 - 30$ keV), whereas Compton scattering polarimetry is employed at even higher energies. POLIX onboard the upcoming *XPoSat* mission employs Thomson scattering polarimetry in the energy range of 8 – 30 keV (Paul, 2022). *AstroSat* Cadmium Zinc Telluride Imager (CZTI; Bhalerao et al., 2017b), which is primarily an X-ray spectrometer (see Chapter 2), uses Compton scattering to measure X-ray polarization in the energy range of 100 – 380 keV.

1.3 X-ray Spectral Analysis and Challenges

The objective of X-ray spectral analysis is to infer the incident X-ray photon spectral components arising from different emission mechanisms in the astrophysical sources as discussed in Section 1.1 from the measurements obtained using different kinds of spectroscopic instruments and detectors as discussed in Section 1.2. X-ray instruments operate in event mode and, in general, record the details of each detected event. The charge deposited by the X-ray event in the detector is converted to a digital number, usually referred to as Pulse Height Amplitude (PHA), which is nominally proportional to the incident photon energy. For each event, the arrival time, position (in the case of a position-sensitive detector), and

PHA value are recorded.

From this list of events, the raw X-ray spectrum $C(I)$, i.e., counts as a function of the PHA channel (I), can be obtained (units of counts channel^{-1}). This is related to the incident photon spectrum from the source $S(E)$, which is the number of photons from the source reaching the detector per unit time per unit area per unit energy (units of photons s^{-1} cm^{-2} keV^{-1}), but not the same. It is worth noting that *"not all photons are counted and not all counts are from photons"* [2].

The observed count spectrum is the convolution of the incident photon spectrum with the instrument's response as:

$$C(I) = \left[T_{\text{exp}} \int S(E)\; R(E, I)\; A(E)\; dE\right] + B(I) \tag{1.5}$$

Here, $R(E, I)$ is the probability that a photon of energy E incident on the detector is detected in channel I of the instrument, called the redistribution matrix (RMF), $A(E)$ is the effective area which is the product of geometric area and efficiency, referred to as ancillary response (ARF), $B(I)$ is the background count rate in channel I, and T_{exp} is the exposure time for which the spectrum is acquired. $R(E, I)$ has units of keV channel^{-1} and $A(E)$ has units of cm^2 counts photon^{-1}.

The response of the X-ray spectroscopic instruments is complex, and thus Equation 1.5 cannot be inverted to obtain the photon spectrum $S(E)$ that we are interested in from the observed count spectrum $C(I)$. Thus, a forward folding approach is employed in X-ray spectral analysis. The source spectrum $S(E)$ is defined as an empirical or physics model with a set of model parameters. This model spectrum is convolved with the instrument response and then fitted with the observed spectrum by χ^2-minimization or other techniques to obtain the best-fit source photon model parameters. This forward folding technique is implemented in X-ray spectral fitting packages such as XSPEC (Arnaud, 1996), which is part of HEASOFT distribution, OSPEX (Tolbert & Schwartz, 2020), which is part of SolarSoft, ISIS (Houck & Denicola, 2000), Sherpa (Freeman et al., 2001), and SPEX (Kaastra et al., 1996).

Practically, due to the complexities in the source model and instrument

[2] https://cxc.cfa.harvard.edu/xrayschool/talks/intro_xray_analysis.pdf

response, the integration in Equation 1.5 is evaluated as a summation:

$$C(I) = \left[T_{\rm exp} \sum_j S(E_j)\ R(E_j, I)\ A(E_j)\ dE \right] + B(I) \tag{1.6}$$

where E_j are discrete energies at which model calculation is done, and the redistribution matrix and effective area are defined at these energies. Now, the accuracy of obtaining the source spectrum from the observed count spectrum by forward folding using Equation 1.6 crucially depends on how well the other terms in the equation are known.

We now discuss the intricate details of each of these terms related to the X-ray spectral response and the challenges in determining them.

1.3.1 What is the energy of the photon?

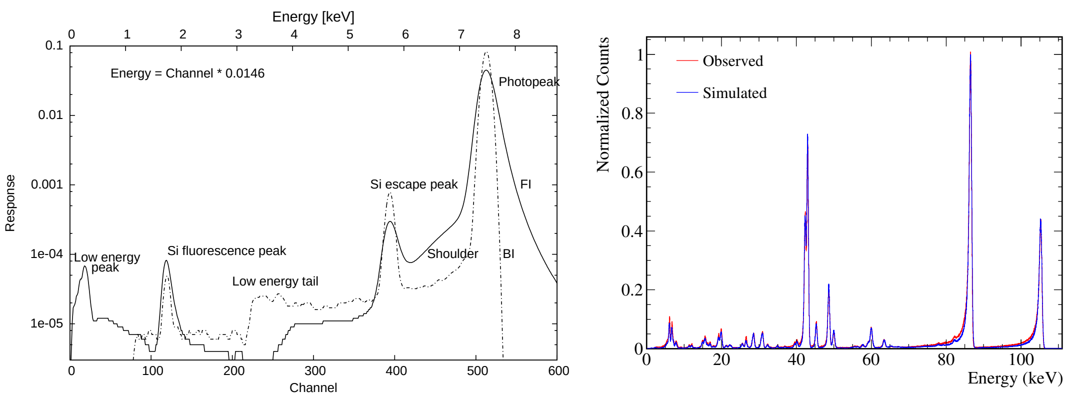

Figure 1.3: Left panel shows *Chandra* ACIS detector response to monoenergetic photons for front illuminated CCD (solid line) and back-illuminated CDD (dashed line) taken from Grimm et al. (2009) and the right panel shows *NuSTAR* CZT detector response from Kitaguchi et al. (2011).

In an ideal scenario, the energy of the incident photon would directly correspond to the channel number in the observed spectrum, and photons of a given energy are all detected as events in the same channel. In that case, the matrix $R(E_j, I)$ in Equation 1.6 will be a diagonal matrix, and it would have been possible to invert the equation to get the incident photon spectrum. The behavior of real X-ray detectors differ from this, and the redistribution matrix is complex.

Figure 1.3 shows the response of two X-ray detectors to mono-energetic X-rays to demonstrate the typical salient features of the spectral redistribution of X-ray detectors. The left panel corresponds to the CCD of *Chandra* ACIS illuminated with photons of a single energy, and the right panel corresponds to the CZT detector of *NuSTAR* when illuminated with mono-energetic X-ray lines from Eu-155 source. As can be seen from the figure, photons of the same energy have a finite probability of getting detected over a range of instrument channels.

The most prominent feature is the photo peak, where most photons are detected. This corresponds to the complete collection of charge deposited by the photo-electric interaction of the photon in the detector. By correlating the positions of photo peaks in the instrument PHA channels with the photon energies, a 'nominal energy' corresponding to the PHA channels is usually defined for ease of representation (as shown in Figure 1.3). This energy-channel relation is defined by the 'gain' parameters of the detector system. The gain-corrected energy bins are often referred to as 'Pulse Invariant' (PI) channels.

The detected events are distributed over a few channels around the photo peak, generally following a Gaussian distribution. The full width at half maximum (FWHM) of this Gaussian distribution around the photo peak is defined as the energy resolution of the instrument. It arises from multiple sources, and the most important factor is the inherent statistical fluctuations in the number of charge carriers produced by photons of the same energy. As the process of generation of charge carriers is not entirely independent, the number of charge carriers does not follow Poisson distribution, and the variance in energy measurement due to the statistical fluctuations of the number of charge carriers (N) is:

$$\sigma^2{}_s = K\ F\ N \tag{1.7}$$

where F is called the Fano factor (Fano, 1947) and K is the proportionality constant. The total variance of the Gaussian peak is the sum of this factor with the contribution from other sources, such as electronic noise.

The second prominent feature is another peak at channels corresponding to nominal energy as the difference between incident photon energy and characteristic line energy of the detector material. This is called an escape peak, as it arises from the escape of characteristic fluorescence emission of the detector atom from the active volume of the detector. If the photoelectric interaction of the incident photon occurs not within the depleted active volume of the detector but the fluorescence emission reaches the active volume, they constitute another peak at the characteristic line energy of the detector material.

In addition to the peaks, the response of semi-conductor detectors often has other components, such as the low energy tails to the peaks extending down to lower channels. These features are the result of incomplete charge collection due to various factors such as trapping of charge carriers in crystal defects, finite mobility lifetime of carriers (especially holes), charge sharing between pixels in pixelated detectors, and photoelectron energy losses in electrode materials. While the specifics may vary from detector system to detector system, in general, the redistribution matrix $R(E_j, I)$ has non-zero elements for channels up to the one corresponding to the nominal energy of the incident photon, with these general features.

1.3.2 How much fraction of photons did we collect?

Effective area, $A(E_j)$ in Equation 1.6, determines how much of the photon flux from the source is recorded by the instrument. One component in the effective area is the geometric area used in photon collection. For instruments with focusing optics, this will be determined by the geometric area of the optics, whereas for collimated or indirect imaging instruments, it would be the geometric area of the detector unobstructed by the imaging system. The geometric area is dictated by the geometric configuration of the elements within the imaging system, the alignment of the imaging system with the detector system, and the angle at which the source is observed. Thus, knowledge of the alignment of various components in the instrument is crucial to computing the geometric area of the instrument. If observations of off-axis sources are planned, the geometric response of the imaging system at different off-axis angles is required. In simpler cases, these may be obtained analytically, and in practice, more complex simulations are required to estimate them, which needs to be validated experimentally.

The other component in the effective area is efficiency, which decides how much fraction of the photons incident over the geometric area make its way to the detector and gets detected, and it depends on various factors in the imaging system and the detector system that the photons encounter. In focusing optics, the energy-dependent reflectivity of each mirror foil will get convolved with the respective geometric area factors to get the total effective area of optics. In the case of collimators and indirect imaging masks or grids, any partial transmission of the X-rays by these elements at higher energies needs to be accounted for. Further, the transmission through entrance windows or filters, top dead layers or electrodes of detectors, and finally, the absorption efficiency within the active detector volume thickness will all contribute to the effective area. The transmission and absorption efficiencies depend on the material and its thickness. Transmission fraction through a material having mass attenuation coefficient μ, density ρ and thickness t is given by:

$$I_{\text{trans}} = e^{-\mu\rho t} \tag{1.8}$$

and the absorption fraction is simply $1 - I_{\text{trans}}$. While computing transmission, the total mass attenuation coefficient is considered with all photon interactions, including the Rayleigh scattering. However, in detector absorption efficiency, the attenuation excluding Rayleigh scattering is only meaningful. The photo-electric absorption cross-sections usually have discontinuities at energies corresponding to the ionization energy of specific shells. usually called as K-edge, L-edge, etc. These would result in discontinuities in the overall effective area as well, as can be seen from the examples shown in Figure 1.4.

In general, the effective area at higher energies is determined by the efficiency of the detector and the reflectivity of optics, and at lower energies, the transmission by the window/filter dictates the effective area. The attenuation coefficients of individual elements are rather well-known from theoretical calculations and verified at least over some energy ranges experimentally. They

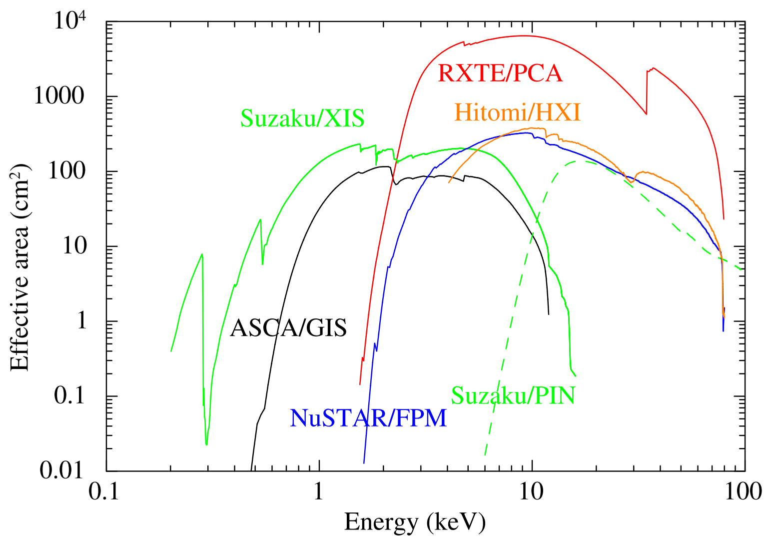

Figure 1.4: Effective areas of some astrophysical observatories. Figure courtesy: Katsuda et al. (2023).

are available in databases such as the NIST database[3]. However, the difficulty is getting the exact composition of the imaging or detector elements, accurate measurements of their thickness, etc. As the transmission or absorption near the edges varies significantly, small uncertainties can lead to significant differences in the overall effective area. Measurement of the absolute effective area over the entire energy range is impractical, and thus, having absolute flux calibration of X-ray spectrometers is a challenging issue, as discussed in the subsequent sections.

In the typical readout chain for X-ray detectors, pulses are considered events if they cross a specific threshold level corresponding to a low energy threshold, usually called lower-level discriminator (LLD). As the pulse heights for the same energy photons would slightly differ, for photons having energy close to the specified low energy threshold, there is a probability that only some events may get detected. This affects the detection efficiency for events near the low energy threshold (e.g., see Figure 10 of Madsen et al., 2022). This effect also needs to be accounted for in the effective area calculations.

[3] https://www.nist.gov/pml/x-ray-mass-attenuation-coefficients

1.3.3 Is this event a photon from the source?

In all X-ray spectroscopic instruments, at least some events get recorded that are not the photons from the source(s) of interest. These 'background' counts, $B(I)$ in Equation 1.6, determine the sensitivity of the instrument to observe fainter sources. Background in X-ray detectors consists of various components, including photon background and particle background, many of which are shown in the top panel of Figure 1.5 and discussed briefly below.

The most significant photon background in X-ray detectors is the diffuse Cosmic X-ray Background (CXB). CXB is nearly isotropic and thus extragalactic in nature. It is now known that it is the integrated emission from numerous unresolved X-ray sources, primarily active galactic nuclei. With *Chandra* deep field surveys, a significant fraction ($\sim 80-90\%$) of the CXB has been resolved into individual sources in soft X-rays, whereas at higher energies, a lower fraction ($\sim 35\%$) of the CXB has been resolved with *NuSTAR* (see (Brandt & Yang, 2022) and references therein). Figure 1.5 middle panel shows the CXB spectrum as estimated from various observatories. It is imperative to note that there are still some uncertainties in the absolute intensity of the CXB, which is coupled with the trouble of having absolute flux calibration of X-ray spectrometers (Campana, 2022). In addition to the isotropic extragalactic CXB, diffuse X-ray emission arising from the unresolved Galactic sources is also present. This spatially non-uniform Galactic diffuse emission peaks along the galactic plane as one would expect.

Aside from the photons, charged particles also act as background in X-ray detectors. High energy charged particles can directly deposit some charge in the detectors, which are detected as events. Particles also interact with the instrument and spacecraft structures, producing secondary particles and X-rays, which also add to the background in the detectors. Cosmic rays are one of the prominent sources of particle background. These are particles (mostly protons) that are accelerated to very high energies in various astrophysical sources. At the Earth's location, the flux of cosmic rays is modulated by the eleven-year Solar Cycle, as the magnetic fields associated with solar winds deflect the incoming

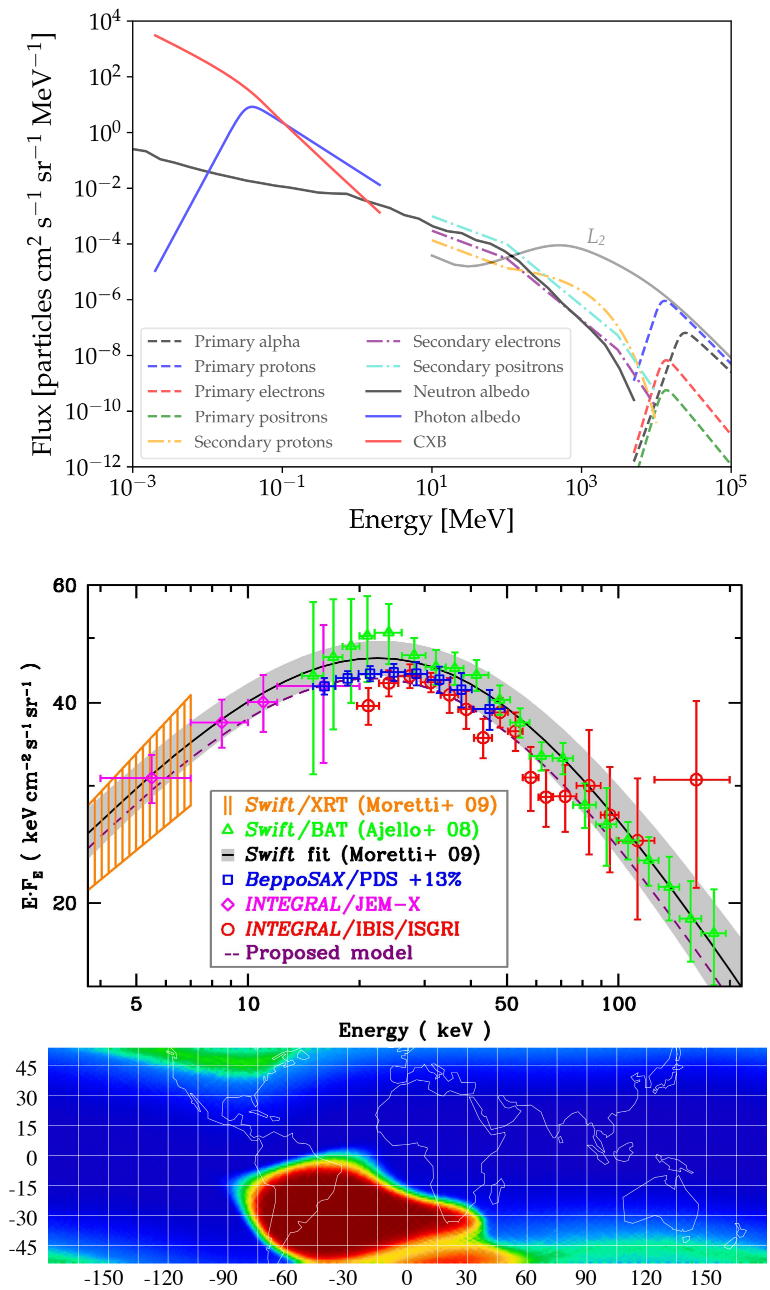

Figure 1.5: Top panel: Various components of background in X-ray detectors, taken from Campana (2022). Middle panel: Cosmic X-ray background spectrum as estimated from different observations, taken from Türler et al. (2010). Bottom panel: Trapped charged particle distribution around Earth as measured by the charged particle monitor onboard ROSAT, showing the South Atlantic Anomaly region, figure taken from Tatischeff et al. (2022)

cosmic rays, resulting in lower cosmic ray fluxes in solar maximum. In addition, for low Earth orbits, only cosmic rays with a minimum energy can reach due to the geomagnetic field. This is usually defined in terms of *cut-off rigidity*, which varies with location in the geomagnetic field. Energetic particles from the Sun also can add to the background. It has limited impact on satellites in low Earth orbits but is important for instruments placed outside the Earth's magnetosphere.

While the magnetosphere provides some shielding from cosmic rays and solar energetic particles, they also cause additional background due to the trapping of charged particles in the Van Allen radiation belts. In the inner radiation belt, the trapped particles are mostly protons, while mostly electrons are trapped in the outer belt. As the magnetic dipole axis and rotation axis of Earth do not coincide, the inner belts reach down to altitudes of ~ 200 km in the regions above the southern parts of the Atlantic Ocean. This region with enhanced particle background for low Earth orbits is called the South Atlantic Anomaly (SAA). The bottom panel of Figure 1.5 shows the map of the charged particle background as measured by the charged particle monitor onboard ROSAT, showing the SAA region. The particle fluxes in the SAA are so high that the X-ray detectors are usually either powered off or brought to low-voltage operation modes during passages near SAA. As can be seen from the figure, the passages through SAA will be shorter for low-inclination orbits, which is preferred to reduce the background contribution from SAA. Observations with X-ray instruments are not usually performed during the passages of the spacecraft through the core of the SAA regions. However, observations just before and after SAA are affected by the particle background in SAA.

Moreover, the irradiation of the detectors and other materials by high flux of charged particles in SAA (as well as high energy cosmic rays) leads to activation. Short and long-term lived isotopes are formed, which decay emitting particles, X-rays, and gamma-rays, which may reach the detectors and add to the background. An enhanced decaying background is usually seen in high energy detectors after exiting from the SAA due to decay of short-lived nuclei. X-ray and gamma-ray emission from the isotopes will show up as background lines in the instruments.

In addition to the direct interaction of X-rays and particles from various sources directly with the spacecraft carrying instruments, secondary emission from the Earth, the Earth Albedo, also adds to the background in X-ray instruments. CXB and galactic diffuse X-ray emission get scattered off the Earth's atmosphere and reach the X-ray spectrometers in orbits around the Earth. Cosmic rays and other high-energy particles also interact with the Earth's atmosphere, producing showers of secondaries that also add the background.

The relative contribution of each of these different components to the actually observed background spectrum for an X-ray spectroscopic instrument depends on the specific instrument design and orbit of the spacecraft and may be highly dynamic due to the locations in the magnetosphere of the Earth. Understanding and having methods to estimate the background spectrum is very crucial in inferring the incident photon spectrum from the source, especially when the background is a significant fraction of the counts from the source itself.

1.3.4 Did we miss to count some photons?

As discussed earlier, X-ray detectors operate in event mode. Any detector system takes finite time in processing the event from one photon interaction, starting with the collection of charge deposited, converting it into an electronic pulse, identifying the peak height of the pulse, and digitizing the peak height. During this period, often termed as the *dead time*, the detector system is incapable of detecting other events, missing to count some of the photons. At high incident photon rates, the probability of having photons incident on the detector within the dead time increases, and thus, more photons will be missed. So, to get accurate incident flux, one must account for the losses due to dead time and correct the exposure time (T_{exp} in Equation 1.6) accordingly.

The dead time behavior of each instrument would depend on the details of their implementation. Often, the dead time behaviors of real systems are close to one of the two models, viz. paralyzable and nonparalyzable (Knoll, 2000). In the nonparalyzable model, events occurring within the dead time of the previous event are lost, and they have no effect on the behavior of the detector. On the other hand, in a paralyzable system, events occurring within the dead time, while not counted by the detector, cause an extension of the dead time. This is illustrated in Figure 1.6.

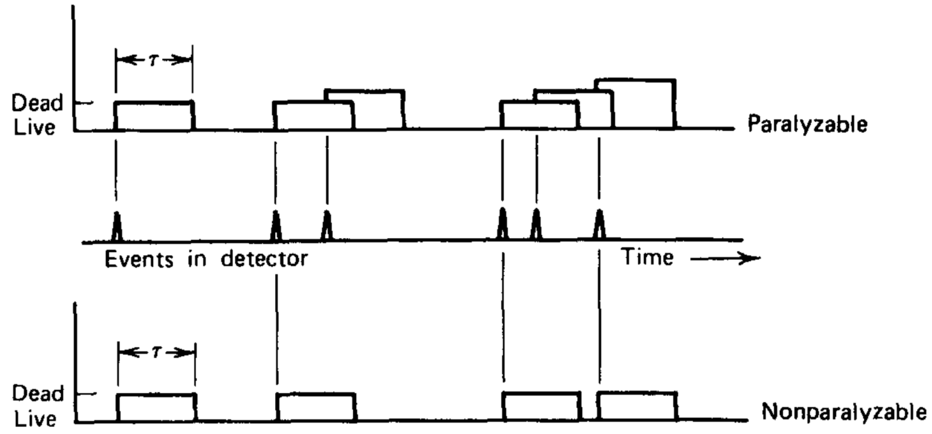

Figure 1.6: Paralyzable and nonparalyzable models of dead time behavior. The illustration is taken from Knoll (2000)

Assuming a fixed dead time τ for each event, the relation between detected count rate n_{det} and true incident rate n_{inc} can be computed for both models (Knoll, 2000). For a nonparalyzable model, they are related as

$$n_{\text{inc}} = \frac{n_{\text{det}}}{1 - n_{\text{det}}\ \tau} \tag{1.9}$$

whereas for a paralyzable model, it is

$$n_{\text{det}} = n_{\text{inc}}\ e^{-n_{\text{inc}}\tau} \tag{1.10}$$

In the case of the nonparalyzable model, the incident rate can be estimated directly from the detected rate, whereas that is not directly possible in the case of the paralyzable model. In either case, knowledge of the actual dead time and which model the detector system follows is essential to apply any dead time correction. Sometimes, the dead time can be known from the design of the system and remain constant, while in other cases, it may be unknown and variable with operating conditions. In both cases, the dead time behavior of the system needs to be investigated with experiments and modeled if the corrections are to be applied for actual observations if the instrument is expected to be operated in count rates where it is essential.

If the second photon arrives within the time when the charge deposited from the first photon is being collected and an electronic pulse is generated, both photons will be counted as a single event with energy of up to the sum of energies of two photons. This is known as *pulse pileup*. In such cases, it is not just that some photons are not counted, but the energy spectrum also gets modified, complicating the instrument response further. In general, it is best to design instruments so that pulse pileup does not occur, as it is often very difficult to model and correct completely. In focusing X-ray telescopes, regions in the detector plane affected by pileup are usually discarded, and an annulus ignoring the core of the point spread function is only considered for spectral analysis.

1.4 Calibrating X-ray Spectrometers on Ground

As all astrophysical X-ray spectrometers have to be flown to space to carry out observations, the response of the instrument needs to be determined first on the ground. We now discuss how experiments, modeling, and simulations can be carried out on the ground to address each of the factors in the spectral response of instruments discussed in the previous section.

1.4.1 Spectral redistribution

Spectral redistribution of an X-ray spectrometer can be determined as two components - gain parameters and the mono-energetic redistribution model, as discussed in Section 1.3.1. Gain parameters to convert the PHA spectrum to the PI spectrum (energy bins) can be determined by obtaining the spectra of mono-energetic lines at different energies, most often from radioactive sources. Fe-55 source, emitting lines at 5.89 keV and 6.49 keV, is widely used in the soft X-ray band, and Am-241, with the most prominent line at 59.54 keV, is used in hard X-rays. Other useful sources include Cd-109, Co-57, Eu-155, and Ba-133. Another option is to use fluorescence lines from various targets generated by illumination from X-ray tubes, but the quality of the spectral line would depend on how well the continuum is blocked. In many cases, there may be slight variations in the detector gain with operating conditions such as temperature, and thus, often, the gain parameters need to be determined for the expected range of various operating conditions. To ensure the linearity or to determine the non-linear effects, gain measurements shall ideally use spectral lines at energies spread over the energy band of the instrument.

For modeling X-ray spectral response, spectra acquired with radioactive sources can be used. However, spectra from radioactive sources often include multiple lines and may have contributions from other effects, such as backscattering from the source holder. Mono-energetic X-ray lines generated using Double Crystal Monochromators (DCMs) from a continuum X-ray beam, such as a Synchrotron beamline facility or an X-ray generator, provide a much cleaner incident spectrum for evaluating the redistribution model (see, e.g., Tiwari et al., 2013; Modi et al., 2019; Wang et al., 2023). More importantly, they offer the possibility to measure the mono-energetic response of the detector at different energies. Observed spectral redistribution of the detectors are then to be modeled with either fully physics-based models or physics-motivated empirical models with multiple components, such as the example shown in Figure 1.7 top panel for the SDD of *Chandrayaan-2* XSM (Mithun et al., 2021b). The model should be able to predict the spectral redistribution at other energies over the entire energy range of the instrument. Often, the spectral redistribution models would require analytical calculations or Monte-Carlo simulations of the detector geometry in tools like Geant4 (Agostinelli et al., 2003) to provide information such as the relative strength of the escape peak with respect to the photo peak. Finally, using the redistribution model and its parameters obtained from the measured mono-energetic response, one can generate the redistribution matrix that predicts the probability of detecting photons of any given energy (within the range of the instrument) in each of the pulse invariant channels (gain corrected energy

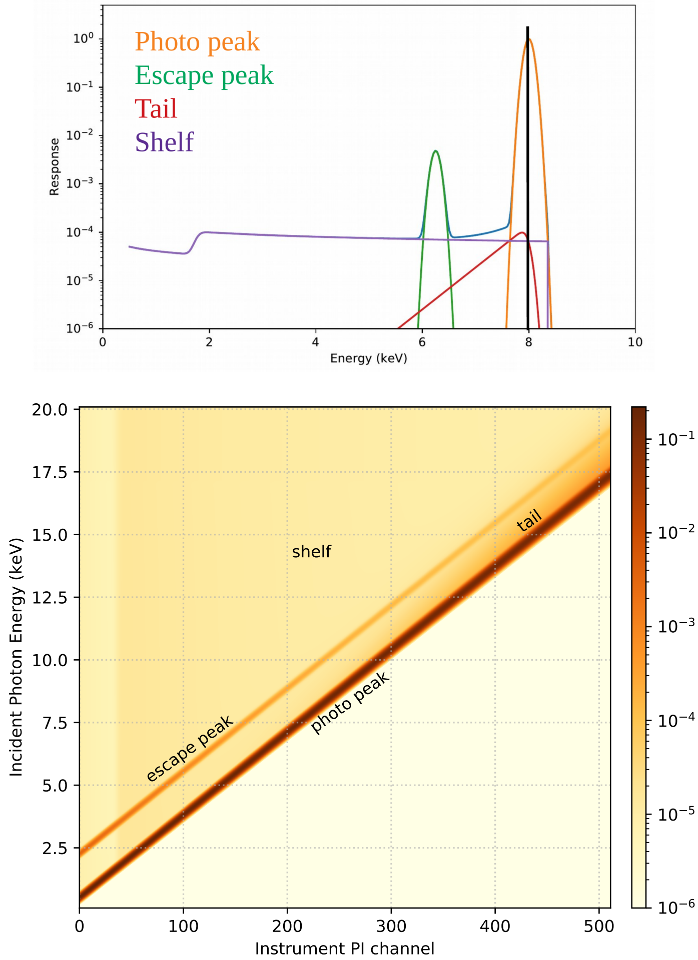

Figure 1.7: The top panel shows components of the redistribution matrix model for SDD used in *Chandrayaan-2* XSM for an incident mono-energetic photon of 8 keV, and the bottom panel shows the modeled redistribution matrix for the entire energy range of XSM showing the components. Details of the model are given in Mithun et al. (2021b).

bins) of the detector, similar to the one shown in the bottom panel of Figure 1.7. This redistribution matrix obtained from ground calibration may require further refinements and updates for use with in-flight observations.

1.4.2 Effective area

Measurement of the effective area as a function of the energy of the complete instrument on the ground has several limitations. This would require parallel continuum X-ray beams sufficient to cover the entrance area of the instrument. The energy spectrum of the beam should cover the entire energy range of the instrument, and the flux needs to be well-known. Due to these difficulties, various components contributing to the effective area are often measured separately, and by combining the measurements with models and simulations, the effective area for the instrument over the entire energy range is derived.

In the case of focusing X-ray telescopes, reflectivities of witness coating samples could be measured from each batch of mirror foils, and using the measured properties combined with ray-trace simulations (e.g. Carter et al., 2003) and reflectivity calculations (e.g. Mondal et al., 2021a), the effective area of the telescope is estimated. It is also often required to have provisions for estimating the effective area for the part of the Point Spread Function (PSF) that is selected for spectral extraction, including for off-axis observations. In the case of collimated detectors, the angular response can be measured for the range of off-axis angles expected and modeled to compute the effective area for any off-axis observations.

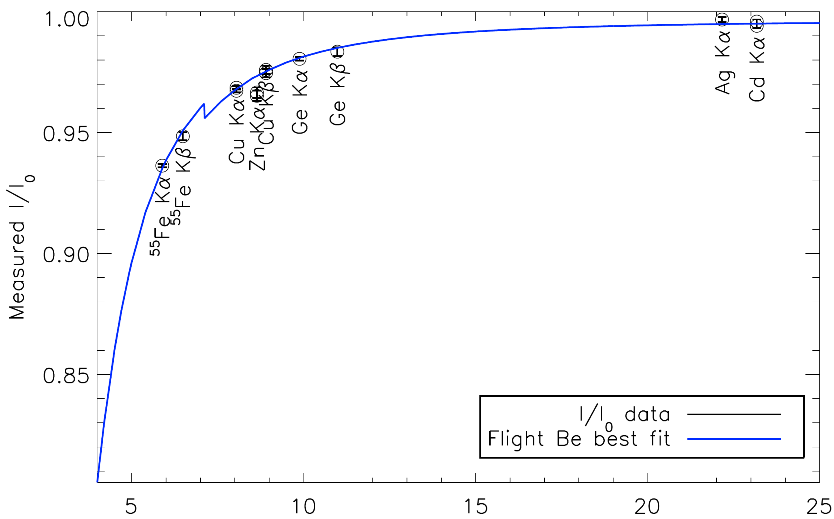

Figure 1.8: Measurement of transmission of Beryllium window of *NuSTAR* taken from Bhalerao (2012).

For the transmission of windows and filters, if they are available for experiments before integrating with the instrument, transmission can be measured at a few energies, which can be fitted with the model as shown in the example in Figure 1.8. Measurement of detector efficiency usually requires a calibrated detector with known efficiency used with a stable X-ray source or a well-calibrated X-ray source with known intensity. Theoretical estimates of efficiency can be obtained considering the nominal thickness and composition of the detector, which can be fine-tuned with the measurements.

The effective area of the entire instrument is then obtained by combining the contributions from different components. As discussed earlier, it is often difficult to experimentally validate it on the ground, and the effective area is one component of the instrument response that often requires further revisions during in-flight observations.

1.4.3 Background

Estimation of the background is the most essential aspect in the design and performance evaluation of any X-ray spectroscopic instrument, as it plays a major role in determining the sensitivity of the instrument. The first preference would be to reduce the background as much as possible with the design, and focusing X-ray telescopes provide this along with simultaneous measurement of background from the off-source locations in the detector plane. If the background events can be identified from the rest of the source photon events in the detector, it would be possible to selectively remove the background events, which in turn reduces the background. This is possible for particle-induced background events in some circumstances. One example of this is the selection of events based on *event-grade* in CCD-based spectrometers, where the morphology of multi-pixel events is used to identify and remove the particle events. Another example is the use of anti-coincidence shields or veto layers where simultaneous events in the main detector and the shield are deemed as background particle events or high-energy X-ray events and can be removed from the list of events considered for scientific analysis.

Estimation of background is usually carried out with Monte Carlo simulations by considering the different components of the background as discussed in

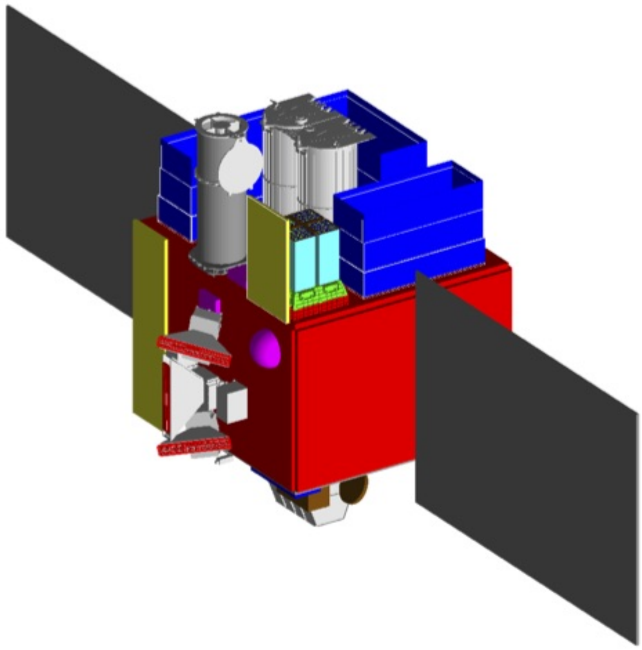

Figure 1.9: Rendering of *AstroSat* mass model in Geant4 taken from Mate et al. (2021).

Section 1.3.3. One of the most commonly used tools for this purpose is Geant4, which is for tracking high-energy particle and photon interactions with matter (Agostinelli et al., 2003). In Geant4, the 'mass model' of the instrument, along with the satellite structures, can be defined, like the example of Geant4 rendering of *AstroSat* mass model shown in Figure 1.9. Often, the detectors and important instrument structures are modeled with great accuracy using CAD models, and the other satellite structures are approximated with mass-simulating elements so that simulations are not extremely computationally intensive. Then, after defining the appropriate physics, simulations can be carried out in Geant4 with the mass model illuminating the spacecraft with various background components, such as the CXB spectrum, and the response of the detector can be recorded. It is also possible to include contributions from radioactive decay of short lived nuclei generated by the activation process (e.g., Odaka et al., 2018). Such simulations provide estimates of the background spectrum in orbit.

However, it is often difficult to use the models to predict the exact background for in-flight observations and use them for background subtraction, especially for background-dominated detectors with significant contributions from variable local charged-particle background. They are often used to have an understanding of the background, and an empirical model is used for background subtraction (e.g., Jahoda et al., 2006; Remillard et al., 2022). It is also possible to use physical models of background by fitting them with observations acquired over the years (e.g., Biltzinger et al., 2020).

1.4.4 Dead time

Dead time effects of the instruments can often be modeled using the two models discussed in Section 1.3.4. At least in some cases, the dead-time behavior of the instrument can be understood from its design itself. In some other cases, dead times are accounted for by the data acquisition systems. In either case, the dead time corrections can be verified on the ground with experiments illuminating the instrument at high count rates (e.g., Mithun et al., 2021b). This is only important in cases where observations are expected at high count rates where dead time effects will be important.

1.5 Necessity of In-flight Calibration

While the ground calibration provides the initial spectral response parameters, they often require further refinements during in-flight observations. Here, we discuss the necessity of in-flight calibration for various aspects in spite of detailed ground calibration activities. We also discuss the general approach to verification and updates to spectral response with in-flight observations.

1.5.1 Detector response variations

Detector response to mono-energetic X-rays, specifically the gain parameters and spectral resolution, may vary over time due to various factors. Semiconductor detectors often face an increase in leakage current and a reduction in charge collection efficiency owing to the generation of crystal defects caused by radiation damage. In gas-filled detectors, reduction in gas pressure and contamination of the gas can result in changes in detector gain and resolution with time. Thus, the spectral redistribution and gain parameters obtained during ground calibration may not remain applicable throughout the in-flight operation periods of the instruments and often require periodic updates.

One way to carry out the in-flight assessment of mono-energetic spectral response is by using radioactive sources carried with the instrument. The detector response to mono-energetic X-rays from the sources is used to track any changes in the gain and energy resolution with time to make periodic updates to the instrument calibration. *Chandra* and *XMM-Newton* instruments carry Fe-55 radioactive sources that can illuminate the full CCD while *Suzaku* XIS, *Swift* XRT, and *AstroSat* SXT have Fe-55 sources illuminating only small regions of the detector such as its corners. Hard X-ray spectrometers use sources with high energy lines, such as Am-241. For example, *RXTE* HEXTE used Am-241 source line to actively control the gain (Rothschild et al., 1998) and *AstroSat* CZTI uses alpha-tagged photons from Am-241 source for monitoring of gain while not adding to the background (see Chapter 2). While background spectral lines are a problem in getting background-subtracted source spectra, in some cases, they prove to be useful to keep track of the gain of spectrometers, particularly for hard X-ray spectrometers. In addition to the radioactive sources, a pulsed X-ray generator, producing X-ray continuum and line emission without interfering with source observations, has been used in *Hitomi* SXS (de Vries et al., 2012).

For imaging spectrometers using detectors like CCDs, the calibration sources are often insufficient to monitor the spectral response over the entire imaging plane. Thus, apart from the calibration source lines, observations of astrophysical sources are also used for this purpose. Supernova remnants such as Cas A that are extended sources having several well-known emission lines are ideal candidates for such calibration observations Guainazzi et al. (2015). The SNR 1E 0102.2-7219 is used for spectral response modeling of CCD-like spectrometers (Plucinsky et al., 2017).

In many cases, the gain and redistribution parameters may vary over time, and the variations are modeled empirically and are included in the CALDB so that appropriate gain parameters can be obtained for each epoch of observation. Continuous monitoring of the spectral response with various methods, as discussed above, is required over the mission lifetime for this purpose.

1.5.2 Background modeling

While pre-flight simulations can provide an estimate of expected background and their general characteristics, they will not suffice for subtracting the background from source observations, especially when there is a significant contribution from time-variable background components such as the trapped charged particles. In the case of focusing telescopes, there is a possibility of obtaining the background spectrum from parts of the detector plane that are not illuminated by the source, provided there are parts of the detector plane that are not covered by the source PSF and the background is uniform across the detector plane. For indirect imaging instruments, there is a possibility of subtracting the background by using the background observed by the closed pixels once the characteristics of the background are well understood. For collimated instruments, one has to rely on models of background that can predict the background spectra and light curves during source observations, which are then used to subtract out the background contribution.

To understand the background characteristics, special observations are usually carried out where the target areas are chosen to be 'blank sky' devoid of any sources that are detectable by the instrument. Such blank sky observations taken over time provide the data to be used for background models. Often, the models for the background are empirical, where correlations of the observed background with other parameters recorded by the instrument, such as the number of events above the high energy threshold and the number of events recorded by anti-coincidence detectors, as well as with other parameters such as the location of spacecraft, time since the crossing of SAA. For example, Figure 1.10 shows the *RXTE* PCA blank-sky light curve for several orbits plotted along with the VLE and L7 counter rates (see figure caption). The parameterized model for PCA background uses the correlation between L7 rates and background rates, along with a few other parameters, and the model has been successful in predicting the background (Jahoda et al., 2006). Similarly, the background modeling for *NICER* follows an empirical approach correlating the background spectra with three parameters related to the rate of high energy events within the focusing area, the rate of low energy events induced by particles at outer regions of the detector, and low energy excess due to sunlight (Remillard et al., 2022).

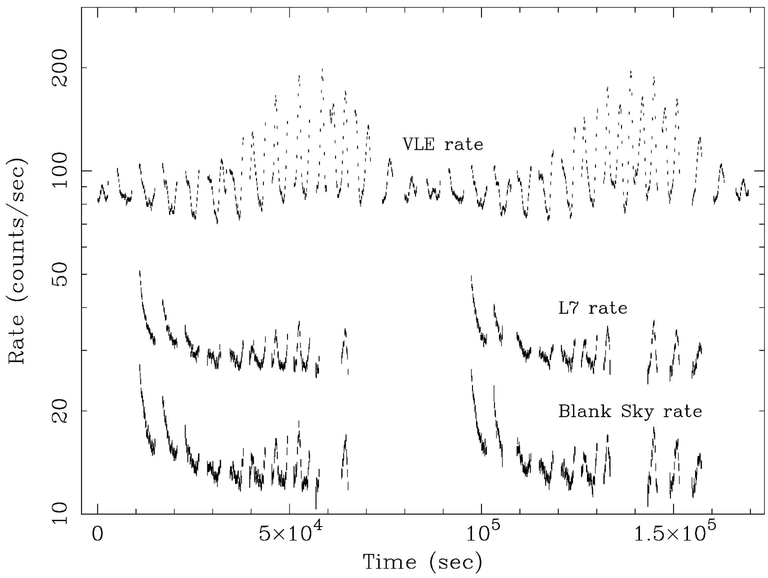

Figure 1.10: Background light curve from RXTE PCA obtained from long duration blank sky observations along with the VLE and L7 counter rates showing the correlation, figure taken from Jahoda et al. (2006). VLE (Very Large Events) correspond to the events having very high energy resulting in saturation of the detector. The L7 rate is the sum of all pairwise adjacent coincident rates. Background model using correlation f background rate with L7 rate provides the best results for RXTE PCA; see Jahoda et al. (2006) for further details.

As discussed in Section 1.3.3, some components of the background show a long-term variation, such as those due to activation and solar cycle modulation of cosmic ray flux while the components, such as that from trapped charged particles, show short-term variations. Thus, understanding the background characteristics and developing models would require blank sky observations over time to capture the variations completely. It is also often the case that with additional observations, background models can be improved to reduce the systematic errors in background subtraction (e.g., see *AstroSat* LAXPC models given in Antia et al., 2017 and Antia et al., 2022). Improvements in understanding and modeling are a continuous process over the mission lifetime and often years afterward, inching towards the eventual goal of statistically limited background subtraction.

1.5.3 Effective area and absolute flux calibration

Effective area calibration on the ground of the full instruments is often limited by the unavailability of parallel X-ray beams that can illuminate the full instrument and have known X-ray flux. Further, there are some factors of the effective area that vary over time. For example, molecular contamination on the entrance windows can cause additional absorption at low-energy X-rays, changing the effective area at those energies. It is also likely that some of the factors, like the alignments between various elements in the instrument and quantum efficiencies of the detector (especially near absorption/transmission edges), could not be very well estimated on the ground. Thus, in-flight calibration efforts to improve the effective area calibration are essential to reliably use X-ray spectrometers to measure the source spectral shape and absolute flux.

In the case of focusing X-ray telescopes, measurement of the point spread function (PSF) of the optics, as well as any PSF variations with energy, is important in getting the effective area. Observations of the point sources at on-axis and off-axis locations are usually used to model the PSF of telescopes. Observations of the same source at dithered locations are also used to derive the alignment details of the telescope. In the case of collimated instruments as well, the angular response of collimators can be refined with observations of a stable astrophysical point source placed at different angles with respect to the boresight of the instrument.

Often, even after incorporating corrections to these aspects as well as others, such as detector redistribution, as discussed earlier, the predicted spectrum obtained by the 'known' source photon model convolved with the instrument response (Equation 1.6) differs from the observed spectrum. The first issue here is that there is a need for sources with 'known' models that can be used as standard calibration sources. Sources that do not have much significant variability and have consistent models, as obtained from a few missions, are the best choices as standard candles. In case the sources are variable, simultaneous observations by multiple missions are required. In soft X-rays, these sources used for cross-calibration of effective areas include thermal SNR (1E 0102.2-7219), galaxy clusters, pulsar wind nebulae (G21.5-0.9), quasars (3C 273), and *BL Lac* objects (PKS 2155-304), which are observed simultaneously by various missions as part of campaigns coordinated by IACHEC (International Astronomical Consortium for High Energy Calibration[4], see Madsen et al., 2017a and references therein).

At higher energies, Crab is the defacto choice for calibration (Weisskopf et al., 2010b; Kirsch et al., 2005), though some other bright sources have also been used for cross-calibration, especially for the absolute flux calibration. For example, the unmodeled residuals of fitting the observed Crab spectrum to the canonical model are used to correct the effective area of *RXTE* PCA (Jahoda et al., 2006) and *NuSTAR* (Madsen et al., 2015b). Knowledge of the absolute flux of Crab is essential if it were to be also used to calibrate the absolute effective area of spectrometers. Recently, measurements of the Crab flux using stray light observations with *NuSTAR* (Madsen et al., 2017b) have been used in updates to the effective area for *NuSTAR* observations with the telescope (Madsen et al., 2022).

The in-flight calibration of spectrometers is a continuous process for multiple reasons. As discussed earlier, several factors are time-dependent, and keeping track of these variations and incorporating them in response is essential. Often, some aspects, such as background models, can be improved over time with the addition of more observations. For example, Figure 1.11 shows the fitted parameters of the Crab spectrum over the years obtained with the response from a previous version and an updated version, demonstrating the necessity of continuous monitoring and updates to calibration.

The eventual goal is to make spectral measurements limited only by the statistical uncertainties and have measurements consistent across observatories. Although reaching this statistical limit is possibly impractical, improvements

[4]https://iachec.org/

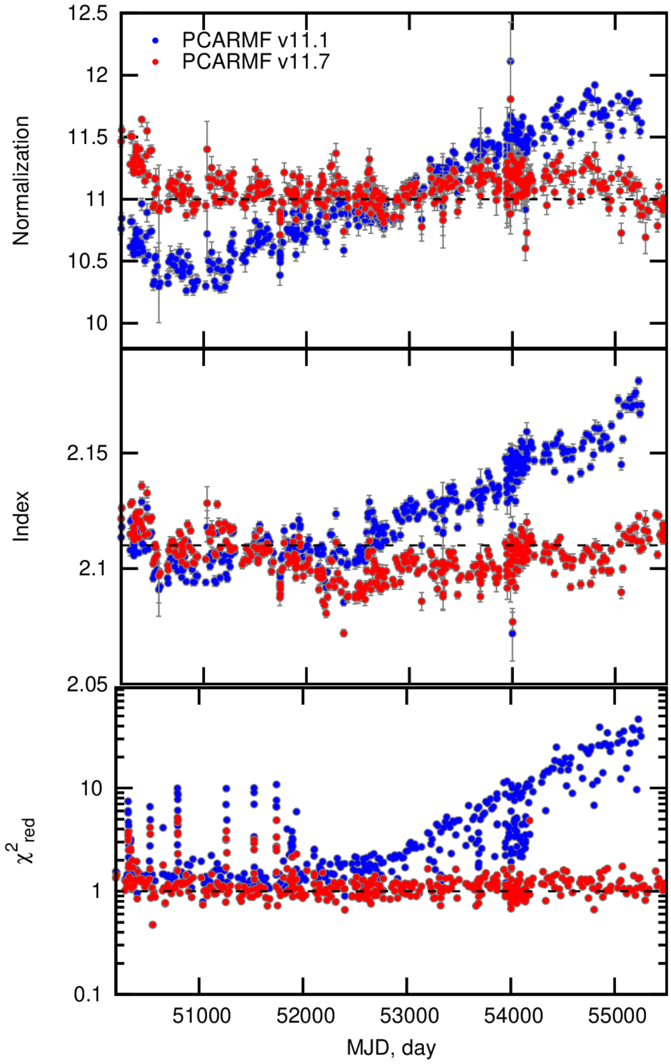

Figure 1.11: Fit parameters Crab spectra with RXTE PCA with an older version of response (blue) and an improved version of response (red), taken from Shaposhnikov et al. (2012).

in this direction is continued throughout the life of missions and even beyond that. With these improvements the inferences obtained from the observed spectra on the source photon spectra and the physics of emission mechanisms become increasingly reliable.

1.6 Thesis Objectives and Outline

X-ray spectroscopy provides the opportunity to probe the matter in extreme conditions and disentangle various physical processes. This is possible only when all aspects of the response of the X-ray spectrometers are well understood and modeled so that the incident source spectrum characteristics can be determined from the observed spectrum. Modeling the intricate details of spectral response begins with experiments, modeling, and simulations on the ground. However, it is often the case that the response requires further fine-tuning on various aspects, such as any response variations over time in space, background understanding and modeling, and updates to the effective area. These necessitate planning and execution of in-flight calibration, and it is a continuous process to keep updating the calibration until reaching the (often very difficult) goal of statistically limited measurements.

Cadmium Zinc Telluride Imager (CZTI; Bhalerao et al., 2017b) is a coded-mask imaging spectrometer on board *AstroSat* , the first Indian mission dedicated to astronomical observations, launched in September 2015. CZTI carries out observations in the hard X-ray energy band of 25–200 keV, and its primary targets are black hole/neutron star X-ray binaries. Solar X-ray Monitor (XSM; Shanmugam et al., 2020) is the soft X-ray spectrometer on board the *Chandrayaan-2* the second Indian lunar mission launched in July 2019. XSM observes the Sun as a star and provides spectral measurements in the energy range of 1–15 keV. Both CZTI and XSM have been calibrated on the ground to measure various aspects of spectral response (Vadawale et al., 2016; Mithun et al., 2021b), but as it became clear from the discussions in this chapter, further refinements based on in-flight observations will be essential. This thesis, in its first part, aims to investigate various aspects of the spectral response of CZTI and XSM instruments using in-flight observations and improve their capabilities to derive the characteristics of observed astrophysical sources from the observed spectra.

Further, in the latter part of the thesis, X-ray spectroscopic observations of the Sun, including that using the *Chandrayaan-2* XSM refined with the in-flight calibration, are used to investigate various aspects of solar flares of different scales from small microflares to larger flare events. Going beyond spectroscopy, the prospects of X-ray spectro-polarimetry of solar flares are explored in the context of a concept design of an instrument. This is extended further to a proposed concept for X-ray polarimetric studies of other astrophysical sources like black hole/neutron star X-ray binaries.

The rest of the chapters of this thesis are organized as follows:

- **Chapter 2:** ***Hard X-ray Spectroscopy with AstroSat CZT-Imager***

  This chapter presents the in-flight calibration of AstroSat CZT-Imager. Using observations acquired over six years of AstroSat operations, detector characteristics are assessed, and updated calibration is obtained. A new method for background subtraction is also developed. With the improvements, it is now possible to reach the statistical limit for spectroscopy with CZTI. The results presented in this chapter will be reported in Mithun et al. (in prep.).

- **Chapter 3:** ***Soft X-ray Spectroscopy with Chandrayaan-2 XSM***

  In this chapter, the in-flight performance assessment and calibration of the Chandrayaan-2 XSM instrument are presented. Various aspects of calibration, including the energy-dependent effective area at different angles has been updated, making use of the in-flight observations. With the updated calibration, XSM is established as a well-calibrated X-ray spectrometer having sensitivities down to sub-A class flares. Part of the results presented in this chapter are reported in Mithun et al. (2020).

- **Chapter 4:** ***Multi-Scale Solar Flares: An X-ray Perspective***

  This chapter presents an overview of the present status of our understanding of solar flares, specifically from the perspective of X-ray observations. It begins with a historical overview of the X-ray Sun and then discusses the observational aspects of solar flares and our present understanding of the flaring processes. Further, the role of small-scale solar flares in coronal heating is discussed. Specific areas where X-ray spectroscopic observations with latest generation instruments such as *Chandrayaan-2* XSM can provide further insights are identified and they are addressed in the subsequent three chapters.

– **Chapter 5:** ***Multi-Scale Solar Flares: Microflares and Coronal Heating***

This chapter is devoted to the investigation of X-ray microflares in the quiescent solar corona outside active regions during the solar minimum using observations with *Chandrayaan-2* XSM. We detected the largest sample of X-ray microflares outside active regions and obtained flare frequency distributions in the microflare energy regime to find that the frequencies are lower than the extrapolated distributions of EUV transients. Further, their implications on coronal heating are discussed. This work is reported in Vadawale, Mithun et al. (2021).

– **Chapter 6:** ***Multi-Scale Solar Flares: Heating of Multi-thermal Plasma in Flares***

This chapter presents the investigation of the multi-thermal nature of flaring plasma using X-ray spectroscopic observations with *Chandrayaan-2* XSM. We conclude that the X-ray spectra during the impulsive phase of intense flares suggest the presence of a bi-modal distribution of temperatures pointing towards two origins of plasma heating in flares. Results presented in this chapter are reported in Mithun et al. (2022).

– **Chapter 7:** ***Multi-Scale Solar Flares: Thermal and Non-thermal Energies of Flares***

In this chapter, the broadband spectroscopic study of a solar flare jointly observed by *Chandrayaan-2* XSM and *Solar Orbiter* STIX is presented. Using simultaneous modeling of X-ray spectra from soft to hard X-rays using both instruments, we obtain better constraints on the thermal and non-thermal energies associated with the event. The results of this chapter will be reported in Mithun et al. (to be submitted).

– **Chapter 8:** ***Beyond Spectroscopy: Prospects of X-ray Spectro-***

Polarimetry Continuing the discussions on the acceleration of particles in solar flares, we discuss the prospects of X-ray polarimetry of solar flares to discern between acceleration mechanisms that are not possible with spectroscopy alone. An instrument concept for Compton hard X-ray spectro-polarimetry of solar flares, its optimization, and expected performance are presented. Further, as an extension of the solar polarimeter, an instrument configuration for polarimetry of other astrophysical sources is provided along with the expected capabilities of the instrument.

– **Chapter 9:** ***Summary and Future Work***

  In this chapter, the results presented in the thesis are summarized, and conclusions are presented. The scope of future work on various aspects arising from the results in the thesis is also briefly discussed.

Chapter 2

Hard X-ray Spectroscopy with AstroSat CZT-Imager

2.1 *AstroSat* Mission

AstroSat is India's first dedicated satellite mission for observations of astrophysical sources (Singh et al., 2014; Agrawal, 2017; Navalgund et al., 2017). The mission carries a suite of instruments that observe the sky over a broad range of electromagnetic spectrum from ultraviolet to hard X-rays. The ultraviolet (UV) band is covered by the Ultraviolet Imaging Telescope (UVIT; Tandon et al., 2017), which includes two telescopes operating in Near UV and Far UV wavelengths. Additionally, UVIT also has a visible channel for deriving improved spacecraft attitude information required to analyze UVIT observations. The soft X-ray band is covered by yet another imaging telescope named Soft X-ray Telescope (SXT; Singh et al., 2017) that provides imaging and spectroscopy in the 0.1 – 10 keV energy range. SXT is a grazing incidence focusing telescope with an X-ray CCD at its focus. SXT is the first X-ray telescope to be designed and developed within India. At higher energies, Large Area Xenon Proportional Counter (LAXPC; Agrawal et al., 2017) provide timing and spectral observations in the 3 – 80 keV energy band. Three units of LAXPC provides an effective area of $\sim$ 6000 cm^2 (in 3-15 keV), the highest for any X-ray observatories. The high effective area coupled with the timing resolution of 10 μs make LAXPC well suited for timing studies apart from spectroscopy. Cadmium Zinc Telluride Imager (CZTI; Bhalerao et al., 2017b; Rao et al., 2017a) covers the energy range 20–200 keV, extending the spectroscopic capability beyond the LAXPC energy range. CZTI is a coded-mask imaging instrument that provides indirect imaging and spectroscopy in the hard X-ray band. These four instruments are co-aligned on the satellite to observe the same source whereas the fifth instrument Scanning Sky Monitor (SSM; Ramadevi et al., 2017) observes other parts of the sky searching for any transient events.

AstroSat was launched on 28 September 2015. The spacecraft is in a circular 650 km orbit with an inclination of 6°. The low inclination of 6° ensures that *AstroSat* passes only through the edges of the the South Atlantic Anomaly (SAA) region (Section 1.3.3). The Charged Particle Monitor (CPM; Rao et al., 2017b) on *AstroSat* alerts the other instruments of enhanced particle flux so that they can be brought to low voltage modes of operation (although only CZTI uses this CPM flag and other instruments use a more conservative preprogrammed SAA range). Considering the SAA duration and occultation by Earth, the typical observing efficiency, i.e., percentage effective exposure in the total observation duration, for CZTI and LAXPC is ∼50%. As SXT and UVIT have further observing constraints, their observing efficiencies are ∼25% and ∼15%, respectively.

After the initial performance verification phase, *AstroSat* has been operating as an observatory class mission, receiving proposals from observers. After eight years in space, CZTI and SXT instruments are operating nominally. One of the three LAXPC units has been powered off, another is being operated at a reduced voltage, and the third one (LAXPC2) is operating nominally. The NUV channel of UVIT is no longer available for observations, whereas the FUV channel is being used for observations.

This chapter addresses in-flight calibration aspects of the hard X-ray instrument on *AstroSat* , the Cadmium Zinc Telluride Imager. Section 2.2 describes the instrument, following which the details of in-flight calibration using CZTI observations over the years are discussed.

2.2 Cadmium Zinc Telluride Imager (CZTI)

Cadmium Zinc Telluride Imager (CZTI) is a hard X-ray coded aperture mask telescope of the *AstroSat* mission designed for imaging and spectroscopy in 20 – 200 keV energy range (Bhalerao et al., 2017b; Vadawale et al., 2016). CZTI employs an array of 64 pixellated CZT detector modules organized into four identical quadrants for measurement of incident photon energy. A coded aperture mask (CAM) with a pattern of open and closed squares of tantalum placed above the detector array allows indirect imaging and simultaneous background measurement. At energies above 100 keV, the coded mask and the collimators become increasingly transparent and CZTI acts like an all-sky detector. Figure 2.1 shows the CAD model of the CZTI instrument and photographs of the mask and the detectors as well as the placement of CZT detectors (designed with detector IDs) in the instrument. Bhalerao et al. (2017b) provides a detailed description of the CZTI instrument, and an overview is presented here.

As seen in Figure 2.1, the detectors in CZTI are organized as a 4x4 array in four quadrants. The quadrants are referred to with numbers as Quadrants 0, 1, 2, and 3 or with alphabets as Quadrants A, B, C, and D (both are interchangably used throught this chapter). The detector modules are manufactured by Orbotech Medical Solutions (now GE Healthcare). Each detector module in CZTI consists of a 39.06 mm (length) x 39.06 mm (breadth) x 5mm (thickness) CZT crystal and Application Specific Integrated Circuit (ASIC) based readout electronics. The detector has a continuous anode, whereas the cathode is segmented into a 16 x 16 pixel grid. Detector pixels have a size of 2.46 mm x 2.46 mm, except for the edge and corner pixels, whose size is 2.46 mm x 2.31 mm and 2.31 mm x 2.31 mm, respectively. Each of the 256 pixels is connected to independent readout chains in two ASICs that are part of the detector module, which provides digital PHA values corresponding to the incident X-ray photon energy. The detector module requires low voltage supplies for its functioning and a high voltage of 600 V for biasing the detectors. Specific pixels in the detector module can be turned off by command in case they become noisy.

CZTI uses the indirect imaging technique called coded mask imaging,

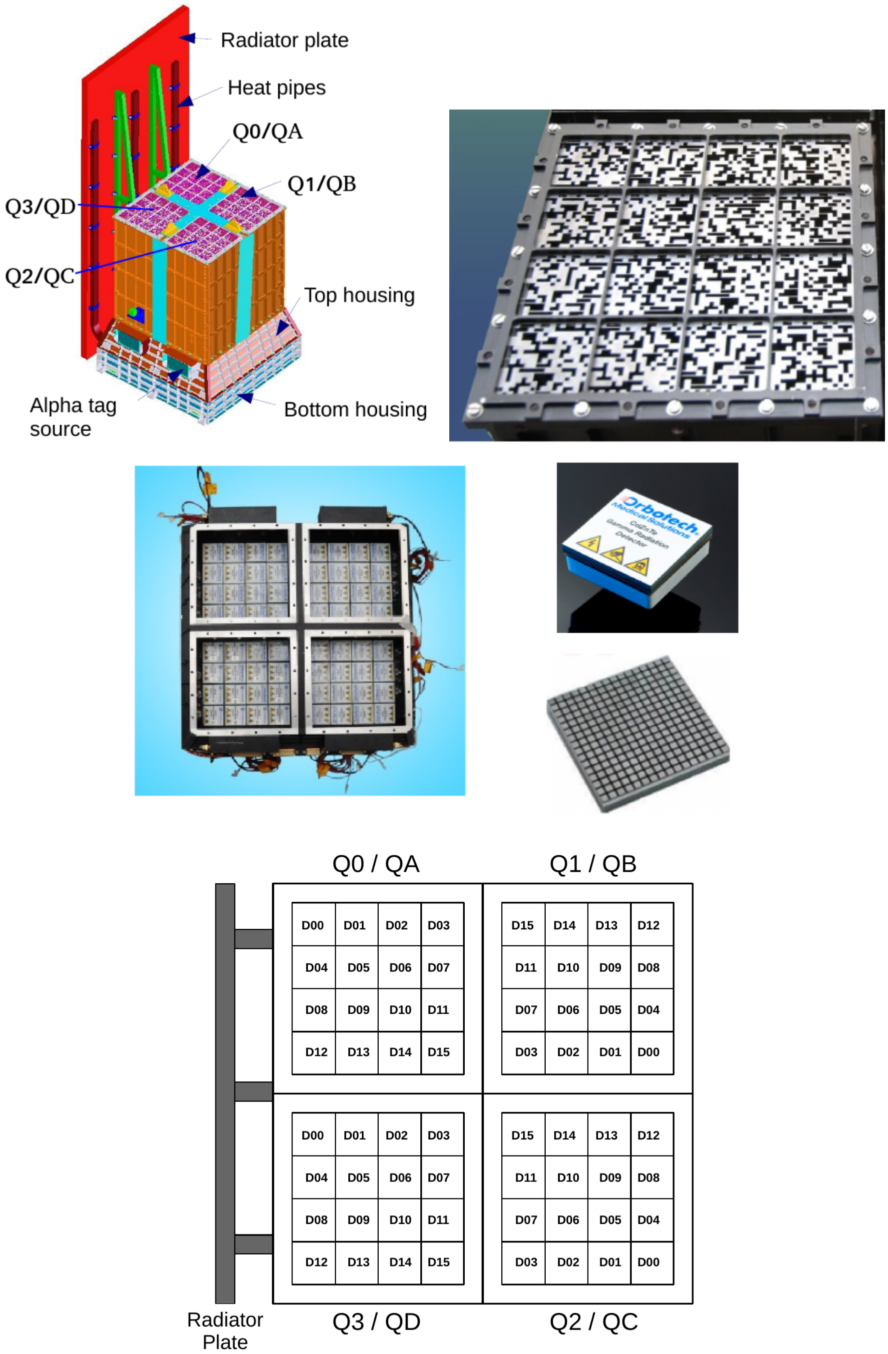

Figure 2.1: Top panel: CAD model of CZTI instrument (left). Photograph of coded aperture mask (right). Middle panel: Photograph of CZTI detector plane showing the array of CZT detectors (left) and zoomed-in view of one detector and pixelation of the detector (right). Bottom panel: Placement of detectors in each quadrant of CZTI. Image credit: *AstroSat* CZTI team.

where a random pattern of open and closed regions known as Coded Aperture Mask (CAM) is placed in front of the detector. This mask pattern casts unique shadow patterns on the detector plane for each source direction. The sky image can be reconstructed using the observed counts in each detector unit and the knowledge of the mask pattern. As the detectors with closed mask elements are observing the background, it also helps in obtaining simultaneous measurements of the background.

In CZTI, above the detector array in each quadrant, CAM made of 0.5mm thick Tantalum is placed at a height of 481 mm on top of collimators. CZTI adopts a 'box type' or 'simple' CAM where the mask consists of open and closed square pattern that matches the CZTI pixel pitch. Mask pattern casts unique shadow patterns on the detector plane for each source direction, and using this, the sky images can be reconstructed. The CZTI mask used seven among the possible sixteen 255-element pseudo-noise Hadamard set uniformly redundant array (URA, Fenimore & Cannon, 1978). These 16x16 patterns (255-element array added with a closed mask element) are randomly arranged to generate the mask pattern for quadrant A. Masks for the other three quadrants are obtained by rotating this pattern by 90°, 180°, and 270°. The coded mask in CZTI provides an imaging resolution of 8 arcmin (Vibhute et al., 2021). The collimators below the CAM have a height of 400 mm and are made of Aluminium alloy lined with Tantalum. The collimator assembly restricts the field of view (FOV) of the CZTI to 4.6° x 4.6°. As there is a gap between the lower edge of collimators and the detector plane, beyond this primary field of view, masks corresponding to one detector module would cast a shadow on the adjacent detector modules.

In between the detector plane and the collimator assembly, Am-241 radioactive sources are mounted at the edges of the detector plane (see Figure 2.1). The line at 59.6 keV from Am-241 is used for in-flight detector gain and resolution assessment. The radioactive nuclide is enclosed within a CsI scintillator crystal so that the alpha particle emitted along with 59.6 keV X-ray photon is absorbed within the scintillator while the X-rays pass through (Rao et al., 2010). Scintillation light produced by the alpha absorption is recorded with a photodiode, and triggers are generated corresponding to the detection of alpha particles. The on-board electronics checks for the coincidence of any X-ray photons detected in any CZT pixel of a CZTI quadrant with the triggers from the corresponding alpha detector to tag them as likely Am-241 events in the CZT detector. As discussed in later sections, these 'Alpha-tagged' events are used for generating the calibration source spectrum for each detector pixel.

Beneath the CZT detector plane in each quadrant, a 20 mm thick CsI(Tl) scintillator crystal with a size of 167 mm x 167 mm is placed. These scintillator detectors act as 'Veto' detectors that help to identify charged particle events or high energy photon events that contribute to background in the primary CZT detectors. X-ray within the 20 – 200 keV range incident on the CZT detectors has a very high probability of getting fully absorbed within the detector volume. However, higher energy photons or particles could deposit partial energy in the main CZT detectors and some energy in the veto detectors beneath. Any energy depositions in the veto detector would result in the generation of scintillation light, which is recorded by two Photo-Multiplier Tubes (PMTs) coupled to the scintillator crystal. PHA value corresponding to the energy deposited in the veto detector is obtained after pulse shaping and digitization electronics chain. Similar to the alpha detector, the on-board electronics checks for coincidence between X-ray events in the primary CZT detectors and any events in the veto detector of the respective quadrant. X-ray events with coincident veto events are tagged with the PHA value from the veto detector. Additionally, each second, the spectrum of events in the veto detectors is recorded.

When X-ray photons are incident on the CZT detectors, the charge deposited in the detector pixel is converted to digital Pulse Height Analysis (PHA) channel value by the ASIC within the detector module. For each event, the PHA value and pixel number within the detector are stored in a FIFO (First-In, First-Out) buffer within the detector module. The FPGA-based front-end electronics (FEB) of each CZTI quadrant continuously polls the detector modules for new events. If an event is stored in the detector buffer, it is read out, and a time stamp is given. As discussed earlier, it also looks for coincident alpha and veto events and assigns the alpha flag and veto flag (PHA value of veto event if present) for the X-ray event in CZT. Detectors are polled parallelly by the FEB in two groups of eight detectors each. As the maximum time required to read all eight detectors in each group if events are present in all detectors is 20 µs , the time resolution of the event time stamps is kept as 20 µs. For each event, the time stamp (20 µs counter within one second), PHA value, detector ID, pixel number, alpha flag, and veto PHA value, if present, are recorded in the RAM up to a maximum of 3072 events. At the end of each second, each quadrant FEB packetizes the event information with the housekeeping parameters and sends it to the central Processing Electronics (PE) package. The PE package collects data from all quadrants and sends the complete data packets to the Baseband Data Handling (BDH) system of the spacecraft for recording it in the onboard storage. Data recorded onboard are then downloaded to the ground during passes over the ground stations in Bangalore.

During the performance verification phase of the CZTI, it was observed that charged particle interactions result in successive events having time stamps that differ by zero or by the time resolution element of CZTI, which is 20 µs. We call these train of events with three or more such successive events as a 'bunch'. These events form about 90% of the recorded events but within less than 1-2% of the exposure time (Ratheesh et al., 2021). As these are essentially background events that are not useful for scientific analysis, removing them onboard would reduce the data rates significantly without losing much information. In February 2016, the onboard software in PE was updated to identify these 'bunch' events and include only some information about these events in the data stored onboard and sent to the ground.

Depending on the charged particle environment, storage space available onboard, and a few other factors, CZTI is operated in different modes. The default mode is the Normal Mode (Mode M0) when CZTI acquires event information from the detectors and sends the full information as discussed earlier, to the ground. In addition to the normal mode data at every second, secondary spectral mode (Mode SS) data with integrated CZT detector spectra, veto spectra, and CZT detector temperature are recorded every 100 seconds. To read the detector temperatures every 100 seconds, included in mode SS data, CZT FEB stops event acquisition for a while and resumes it after completion of the temperature reading. Due to this, events recorded by the detectors during the first ∼400 ms are read out later and assigned incorrect time stamps. Thus, events recorded within the first 400 ms of every 100-second tick of the CZT clock are to be ignored in the subsequent analysis.

During periods of SAA passage, the instrument is changed to SAA Mode (Mode M9). The CPM count rate or time-tagged commands trigger the changeover to SAA mode. After initial verification, this mode change has always been based on the CPM count rate. In the SAA mode, the high voltage to the CZT and veto detectors are switched off. Data packets are sent once every 100 seconds, including only the housekeeping parameters. While several other modes meant for contingency operations are available, they have never been used in the eight years, and only the three modes mentioned above are regularly used in CZTI operations.

As *AstroSat* is a proposal-driven observatory, observations are planned based on accepted proposals where the users have provided the source, required observation time, and instrument configurations if applicable. In the case of CZTI, there are no user-configurable instrument settings, and it operates in the default modes with the co-aligned instruments of the spacecraft pointed to the source of interest. While acquiring the observations of this target in its primary FOV, CZTI can also observe bright astrophysical transient sources outside the primary FOV at larger off-axis angles. The coded mask, collimators, and other supporting structures of CZTI become increasingly transparent to X-rays at energies beyond 100 keV. This makes CZTI act as an open detector beyond 100 keV sensitive to bright transient events such as Gamma Ray Bursts (GRB) occurring in other parts of the sky outside its FOV. A GRB was detected during the first day of observations with CZTI itself (Rao et al., 2016). So far, CZTI has detected over 500 GRBs [1]. As the X-rays from off-axis sources like GRBs pass through the satellite material and structures within the CZTI instrument before reaching the detectors, to infer the incident spectral characteristics, attenuation by the intervening materials need to be modeled. To obtain the off-axis response, simulations are done using Geant4 toolkit (Agostinelli et al., 2003) where the

[1] http://astrosat.iucaa.in/czti/?q=grb

AstroSat spacecraft with all instruments including CZTI are accurately modeled. This AstroSat mass model in Geant4 is used in the analysis of observations of off-axissources with CZTI (Mate et al., 2021). Off-axis CZTI observations have been used for spectroscopic analysis of GRBs (Chattopadhyay et al., 2021), discerning between the electromagnetic counterpart of gravitational wave event and a GRB (Bhalerao et al., 2017a), and in providing independent information on the location of the first EMGW event by virtue of non-detection (Kasliwal et al., 2017).

Another peculiarity with CZTI is its capability to measure hard X-ray polarization of bright astrophysical sources in the energy range of 100 – 400 keV (Chattopadhyay et al., 2014a; Vadawale et al., 2015). At energies above 100 keV, a fraction of the photons incident on the CZTI detector plane undergoes Compton scattering. Some of the scattered photons from one pixel can be absorbed by the neighboring pixels. If the incident X-rays are polarized, the azimuthal angle distribution of Compton scattered photons is modulated with an amplitude proportional to the degree of polarization and phase that differs by 90° from the angle of polarization. In CZTI, the histogram of azimuthal angles can be obtained by identifying the Compton scattered double pixel events, which is used to measure the X-ray polarization of astrophysical sources. As the instrument is not primarily designed as a polarimeter, polarimetric measurements are limited only to the brightest hard X-ray sources.

CZTI observations have been used to obtain the most precise measurement of hard X-ray polarization of Crab nebula and pulsar and show surprising variations of polarization properties in the off-pulse duration (Vadawale et al., 2018). Recently, CZTI observations of the high mass X-ray binary Cygnus X-1 has yielded measurements of high polarization in the intermediate hard state that suggests a jet component in the hard X-ray emission (Chattopadhyay et al., 2024). In addition to the polarimetric studies of these two bright persistent sources observed on-axis, CZTI has also been used to measure the polarization of GRBs incident off-axis to the detector plane. CZTI observations have resulted in the largest sample of X-ray polarization measurements of GRBs (Chattopadhyay et al., 2019, 2022). Aside from the sample studies, GRB polarization measurements with CZTI have also been used for investigations of peculiar cases (e.g., Chand et al., 2018; Sharma et al., 2019; Gupta et al., 2022).

While the observations with CZTI have been used extensively, exploiting its unique capabilities to measure X-ray polarization and investigations of all-sky transient events like GRBs, so far, there has been limited use of spectroscopic observation of the sources observed within its primary FOV. One reason is that there are a limited number of bright hard X-ray sources for which CZTI observations are possible, especially at energies beyond the LAXPC limit, providing complementary data. Another reason was the requirement for further refinement of spectroscopic techniques and calibration to use CZTI spectra for such analysis. While several improvements have been implemented in the CZTI analysis pipeline and calibration database over the few initial years of in-orbit operations, there are areas that required further improvements, such as the residuals in background subtraction and inconsistencies between quadrants. Understanding these aspects requires observations over longer time scales and thus could only be completed after having sufficient observations.

In this chapter, I present the systematic efforts undertaken to refine the spectroscopic calibration of CZTI primarily using the first six years of in-flight observations to improve its spectroscopic capabilities. In Section 2.3, a summary of the ground calibration is provided. Subsequent sections describe various aspects of in-flight calibration. Section 2.4 presents the in-flight characteristics of CZT detectors and updates to the gain parameters. Background characterization in CZTI is discussed in Section 2.5, and the improved methodology to extract background-subtracted source spectrum is presented in Section 2.6. A novel technique is used to measure the alignment of mask elements to the detectors, presented in Section 2.7. Section 2.8 presents updates to the effective area obtained by calibration against the canonical spectral model for Crab nebula and pulsar. Sensitivity of the CZTI and prospects of hard X-ray spectroscopy of various classes of sources are discussed in Section 2.9 and the specific case of phase-resolved spectroscopy of the Crab pulsar is presented in Section 2.10. Finally, a summary of the chapter is given in Section 2.11.

2.3 A Summary of Ground Calibration

As noted earlier, CZTI consists of 64 detector modules, each with 256 pixels, and thus essentially has 16384 independent detector elements. Each detector pixel has independent chains of readout electronics in the ASIC. Thus, it is likely that the characteristics of pixels would vary at least slightly. To use the collection of pixels as a single instrument for inferring the incident X-ray photon spectrum, it is required to calibrate each of them in terms of their gain parameters, lower and higher energy thresholds, and spectral redistribution matrices. Extensive exercise was carried out on the ground with the CZTI flight module to calibrate the instrument on these aspects, and the results of these form the initial calibration database for CZTI. A summary of the ground calibration of CZTI detectors is given here.

2.3.1 Gain calibration

To convert the PHA channel values for X-ray events to nominal energy, the gain parameters of the detector are needed, which, in the case of CZTI, could be different for each of the 16384 pixels. As the gain parameters are likely to vary with temperature, they need to be estimated at different temperatures within the operating temperature limits. For this purpose, experiments were carried out at Vikram Sarabhai Space Center (VSSC), ISRO, with the flight model of the CZTI instrument. Spectra were acquired from the detectors in each quadrant illuminated with X-rays from three radioactive sources: Cd-109 with lines at 22.0 and 88.0 keV, Am-241 with line at 59.54 keV, and Co-57 with lines at 122.0 and 136.0 keV. The experiment was done in a thermal chamber, keeping the ambient at five temperatures from 0°C to 20°C in steps of 5°C to obtain the detector characteristics at each of these temperatures.

During these ground tests, a fraction of pixels ($\sim$5%) were found to be noisy and were turned off, and calibration data from the remaining pixels were analyzed. By fitting Gaussians to the X-ray lines observed in each pixel, peak channels corresponding to the line energies were obtained. Linear fits to the energy-peak channel correlation provided gain and offset for each pixel at each

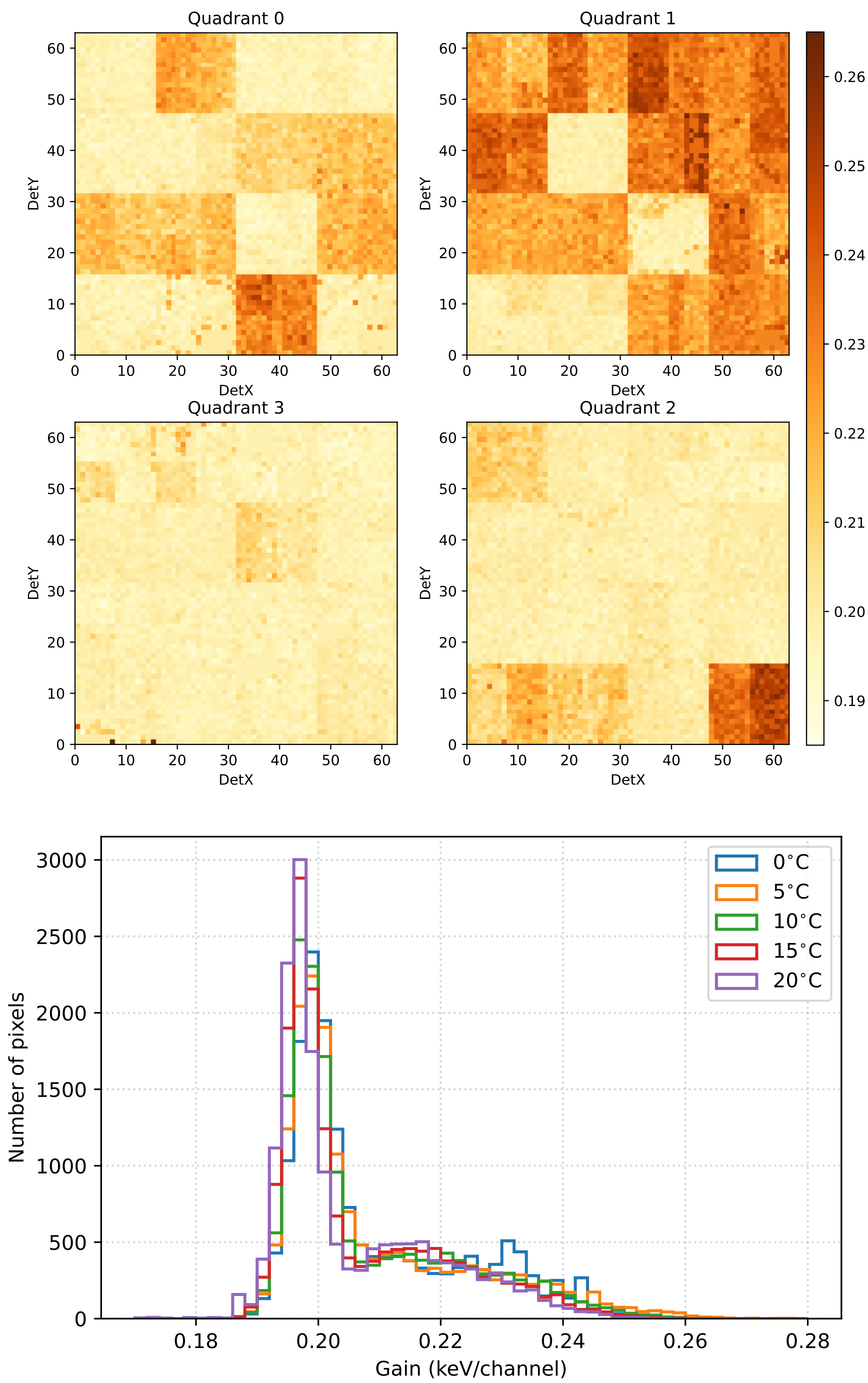

Figure 2.2: Gain values of pixels of all detectors of CZTI at nominal operating temperature of 10°C is shown in the top panel and histogram of pixel gains at different temperatures is given in the bottom panel.

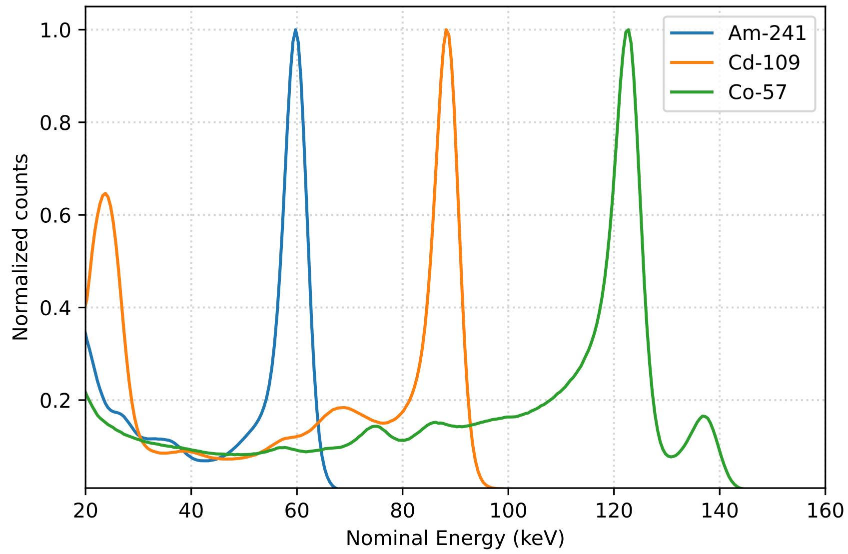

Figure 2.3: Calibration source spectra for three radioactive sources for quadrant A of CZTI at 10 deg C after correcting for individual pixel gains.

of the five temperatures. Spectra of a small fraction of pixels could not be fitted due to reasons such as bad quality or statistics, and for those pixels, average gain values of the other pixels in the same detector module were assigned. Figure 2.2 top panel shows the map of gain values of the pixels at the nominal operating temperature of 10°C, and the bottom panel shows the frequency distribution of gain values at different temperatures. Gain and offset values for all pixels at five temperatures are included in the CALDB for CZTI. Using the gain parameters of individual pixels, the raw spectra are converted to Pulse Invariant (PI) channels: 512 channels in 5–261 keV with 0.5 keV bin size. Figure 2.3 shows the gain corrected PI spectrum of the three sources for quadrant A of CZTI at 10°C. Ground calibration spectra are also used to determine each detector pixel's lower energy thresholds (LLD) by fitting an error function to the background spectra near the cutoff at low energies. These LLD values are also included as part of the CALDB for CZTI.

2.3.2 Spectral Redistribution and Effective Area

The gain corrected spectrum shown in Figure 2.3 shows the response of CZT detectors to mono-energetic X-rays. Apart from the Gaussian shape of the lines, low-energy tails are observed, which are more prominent at higher energies. This arises from the trapping of charge carriers, especially the holes, in the crystal defects and impurities, leading to incomplete charge collection. This is more pronounced in the case of CZT detectors, where the mobility-lifetime product of holes is rather low. This effect of spectral redistribution needs to be modeled accurately to infer the source spectrum from the observed spectrum.

Given the mobility and lifetime product of charge carriers, the mono-energetic line profiles observed by CZT crystals can be modeled by considering the fraction of charge collected using the Hecht equation (Hecht, 1932). Spectra of known mono-energetic lines can be fitted with this model to derive the mobility lifetime products, and the same can be used for generating the spectral redistribution matrix as done in the case of CZT detectors used in High Energy X-ray spectrometer (HEX) experiment on Chandrayaan-1 mission (Vadawale et al., 2012). In the case of CZT detectors used in CZTI, it was found that the tails observed at the lower energy line at 59.54 keV cannot be explained with charge trapping alone, and charge sharing between pixels also needs to be accounted for (Chattopadhyay et al., 2016a). CZT line profile model with charge trapping and charge sharing has been able to successfully describe the observed lines for the CZT detector from the same batch of detectors used in CZT-Imager, as shown by Chattopadhyay et al. (2016a).

This line profile model is used to model the calibration spectra of each of the pixels in CZTI to obtain the model parameters of each pixel: mobility lifetime product for electrons ($\mu\tau_{\rm e}$) and holes ($\mu\tau_{\rm h}$), Gaussian width (σ), and initial charge cloud radius (r_0). For each pixel, spectra of the three lines at 59.54 keV, 88.0 keV, and 122.0 keV are fitted simultaneously to obtain these parameters. As an example, spectra of the lines from one pixel with the best-fit models are shown in Figure 2.4. Similar fits are done for each pixel of CZTI at five different temperatures where the fitting was done parallelly using PRL Vikram-100 HPC cluster. Figure 2.5 top panel shows the map of $\mu\tau_{\rm e}$ and $\mu\tau_{\rm h}$ values for the detector pixels. With the model parameters of the line profile model, the redistribution matrix for each pixel can be obtained.

Storing the redistribution matrix of each pixel separately in the CALDB

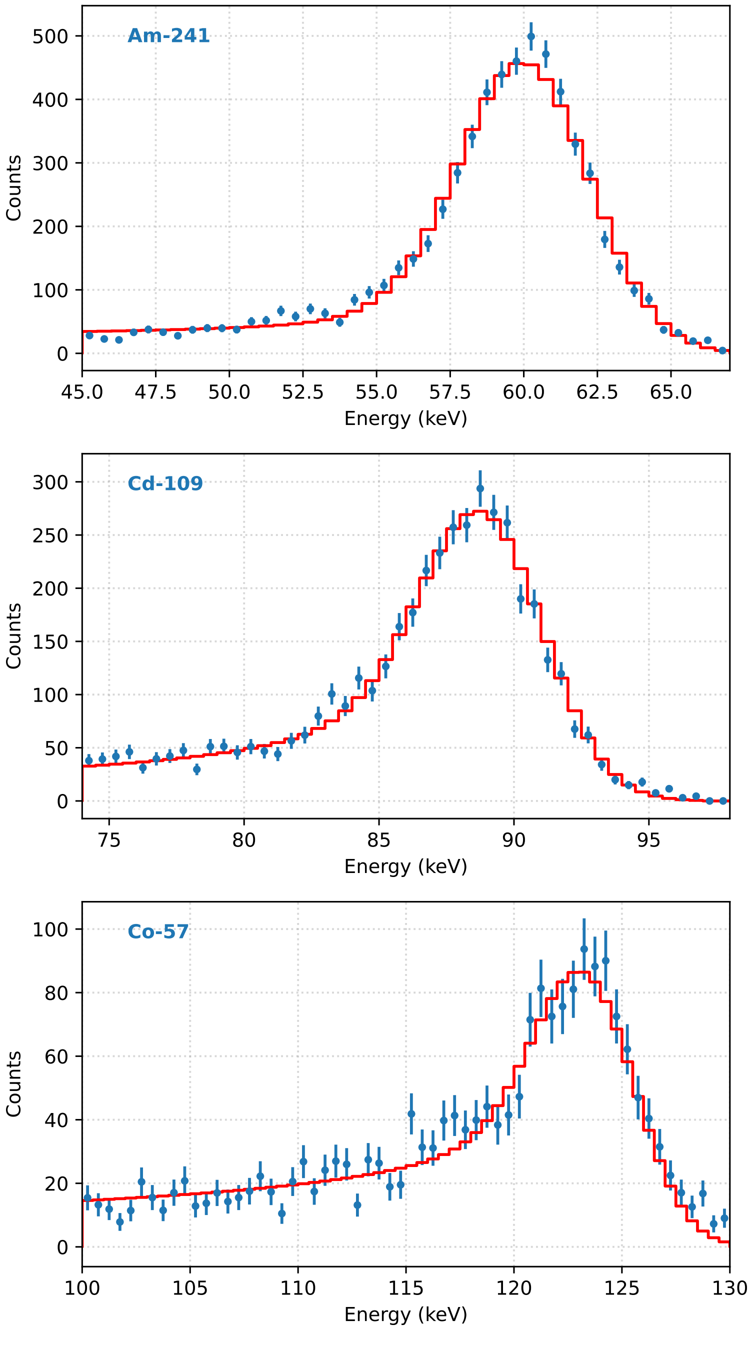

Figure 2.4: Mono-energetic line spectra from three radioactive sources obtained with one pixel of CZTI are shown. The best-fit line profile models that incorporate tailing due to charge trapping and charge sharing are overplotted in red.

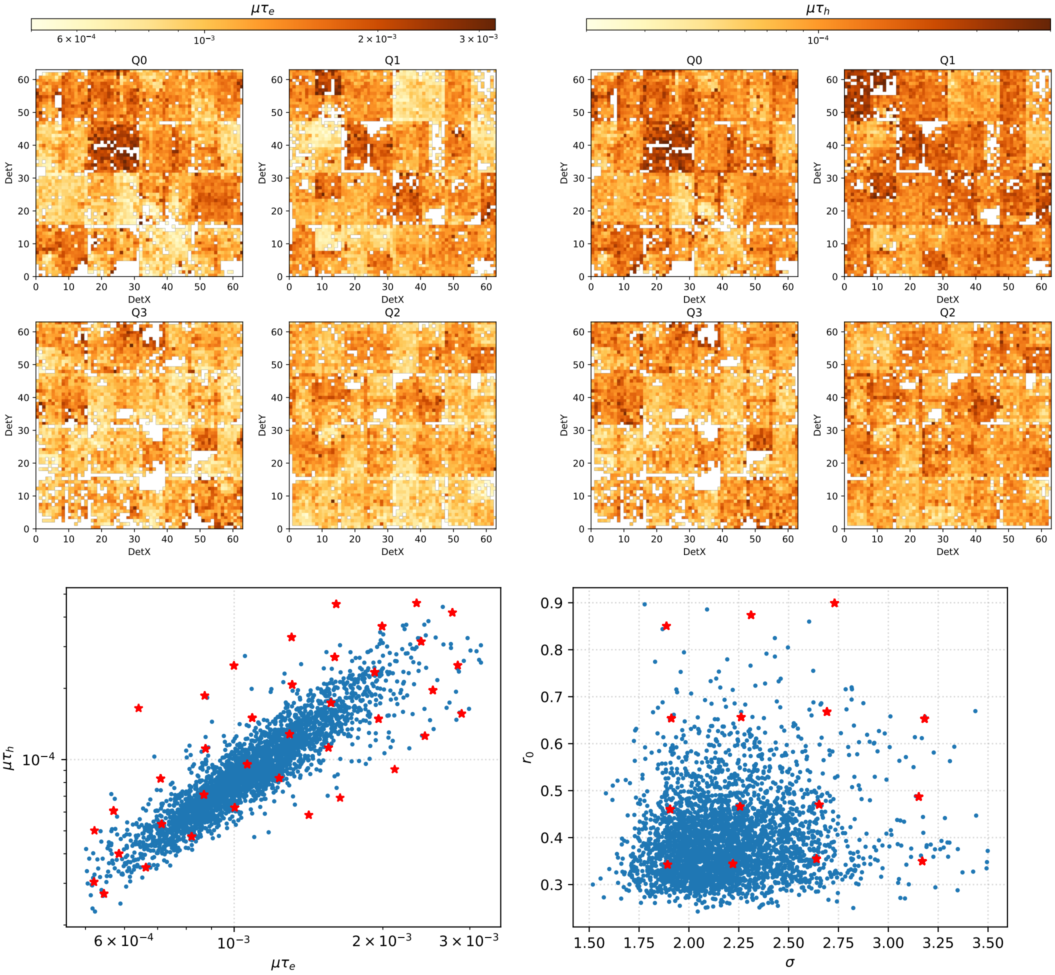

Figure 2.5: Top: Mobility lifetime products of electrons (left) and holes (right) obtained by fitting the spectral line profile of pixels. Bottom: Blue points show the redistribution model parameters, namely mobility lifetime product of electrons ($\mu\tau_e$) and holes ($\mu\tau_h$) (left) and Gaussian sigma (σ) and initial charge cloud radius (r_0) (right). The pixels are grouped based on similar parameters where the grouping of $\mu\tau_e$ and $\mu\tau_h$ parameters are along the principal component axes, and the other two parameters are grouped along each parameter value. Red stars show the parameters for each group of pixels that are used in generating the final redistribution matrix for each observation.

is impractical. Also, several pixels may have almost similar line profiles. Thus, we group the pixels with similar spectral redistribution model parameters. Figure 2.5 lower panel shows the correlation between $\mu\tau_{\mathrm{e}}$ and $\mu\tau_{\mathrm{h}}$ as well as that between σ and r_0 for all pixels. The $\mu\tau$ parameters correlate as one expects, and the other two do not show any apparent correlation. To group the pixels, we identify the principal components in the four-dimensional parameter space using Principal Component Analysis (PCA). Two principal components are found to be along the correlation of the $\mu\tau$ parameters and orthogonal to it, and the other two were close to the σ and r_0 axes. Thus, we divided the four-dimensional parameter space into bins along and across the correlation axes of $\mu\tau$ parameters and along σ and r_0 axes. For each bin, the average parameter values are obtained and shown by the red stars in Figure 2.5. After ignoring groups with no members, a total of 270 groups with distinct line profile model parameters are identified. Redistribution matrices for these 270 groups of pixels are pre-computed with the average parameter values and are recorded in the CALDB, along with the information on the membership of pixels in the groups. Redistribution matrices of each active pixel from the CALDB are averaged to generate the redistribution matrix of the instrument for a given observation.

The effective area of the CZTI instrument is estimated by considering the geometric area of the detector pixels, open fractions of the coded mask, transmission by the closed elements of the mask, transmission by mylar layer on CZT detectors, and CZT detector efficiency. For the coded mask, the design value of thickness is considered. For the detector parameters, we consider the manufacturer-provided values and absorption coefficients are taken from NIST database. While computing the effective area for an observation, open areas of active pixels are considered, and all efficiency factors are included.

As discussed in this section, various calibration parameters obtained from the ground calibration were part of the initial calibration database of CZTI. The CZTI data analysis pipeline uses the CALDB in the data analysis procedures. With systematic analysis of the in-flight observations, calibration parameters and analysis procedures have been refined, as discussed in the subsequent sections.

2.4 In-flight Detector Characteristics and Gain

2.4.1 Disabled and noisy pixels

During the initial commissioning phase in October 2015, quadrants of CZTI were powered on sequentially. By examining the counts in each pixel during observations over multiple days, a few pixels were found to be consistently noisy. These noisy pixels were identified and disabled through ground commands. Further, over the next several months, this exercise was continued, and the noisy pixels were disabled. Afterward, it was observed that not many pixels remain very noisy across observations, and only a handful of them have been disabled during subsequent years. Further, it was observed that Detector 00 in Quadrant D started misbehaving a few months after the launch, with half of the pixels showing zero counts and the other half having higher counts than usual, which can be seen in the detector plane histogram (DPH) shown in Figure 2.6. Initially, the detector recovered after a power cycling, but the issue reappeared and recurred even after power cycling. Thus, all pixels of this detector have been flagged as noisy and are ignored in the data analysis. Similarly, half of the pixels in Detector 14 in Quadrant C are also deemed noisy. Including the $\sim$5% of pixels disabled on the ground, at present, 7.83% of pixels have been disabled, and 2.14% of pixels are deemed noisy and ignored in the data analysis. Usually, a small fraction of additional pixels are found to be noisy during any given observation. As they do not remain noisy for long, instead of disabling them, the CZTI data analysis pipeline removes events from those pixels for further analysis.

2.4.2 Low-gain pixels

After ignoring the disabled and noisy pixels, the DPH showed some interesting features. Figure 2.6 top panel shows the DPH of all quadrants for a long observation. It can be seen that some patches of pixels show much lower counts than the rest of the pixels. As one patch in the quadrant A resembles the shape of a banana, we initially referred to these pixels as “banana pixels”. Subsequent investigation of the spectra from these pixels showed that they do not show the background Tantalum lines at ∼56.5 keV and ∼65.5 keV that are visible in other pixels. Spectra of alpha-tagged events from these pixels also did not show the presence of the Am-241 line at 59.54 keV. Further investigation concluded that these pixels have suffered from substantial gain shifts, making their low energy thresholds above 70 keV. Thus, the lines are not detected by these pixels. As these pixels will no longer be operating in the nominal energy range of CZTI and cannot be used for primary spectroscopic analysis, they need to be identified and flagged separately as spectroscopically bad "low gain pixels".

Earlier, using the observations from the first six months, the pixels were classified into low-gain pixels and spectroscopically good pixels. However, it was apparent that at least some pixels were misclassified due to insufficient statistics. Thus, as part of the efforts to improve the calibration of CZTI in the present work, we revise this by using all the data from October 2015 to May 2022 (80 months). Event files generated from the CZTI data analysis pipeline version 2.1 were used. Standard event selection procedures were followed, and event energies were obtained using the ground calibration estimates of gain. Alpha-tagged events were selected from the clean event list, and spectra of individual pixels were generated for each observation. They were added together to obtain monthly, yearly, and total spectra for each pixel. Similarly, we obtained the total spectrum, primarily dominated by background, for each pixel using the clean event list for each observation ID and were added together to get the monthly and yearly spectra.

Using the presence of the 59.54 keV line in the alpha-tagged event spectrum and that of the tantalum lines in the background spectrum, the pixels were classified as good pixels and low gain pixels. If present, the 59.54 keV line in the alpha-tagged event spectra for each pixel was fitted with a Gaussian to obtain the peak energy. After an initial classification based on the presence of lines, to confirm the classification status, we used the ratio of the total pixel spectrum to the module spectrum and the mean count rates. Further, it was checked whether the fit parameters of the alpha-tagged spectrum for each pixel (line energy and resolution) were outliers. From the yearly spectra, it was also confirmed that there is no change in the characteristics of good pixels and low-gain pixels over

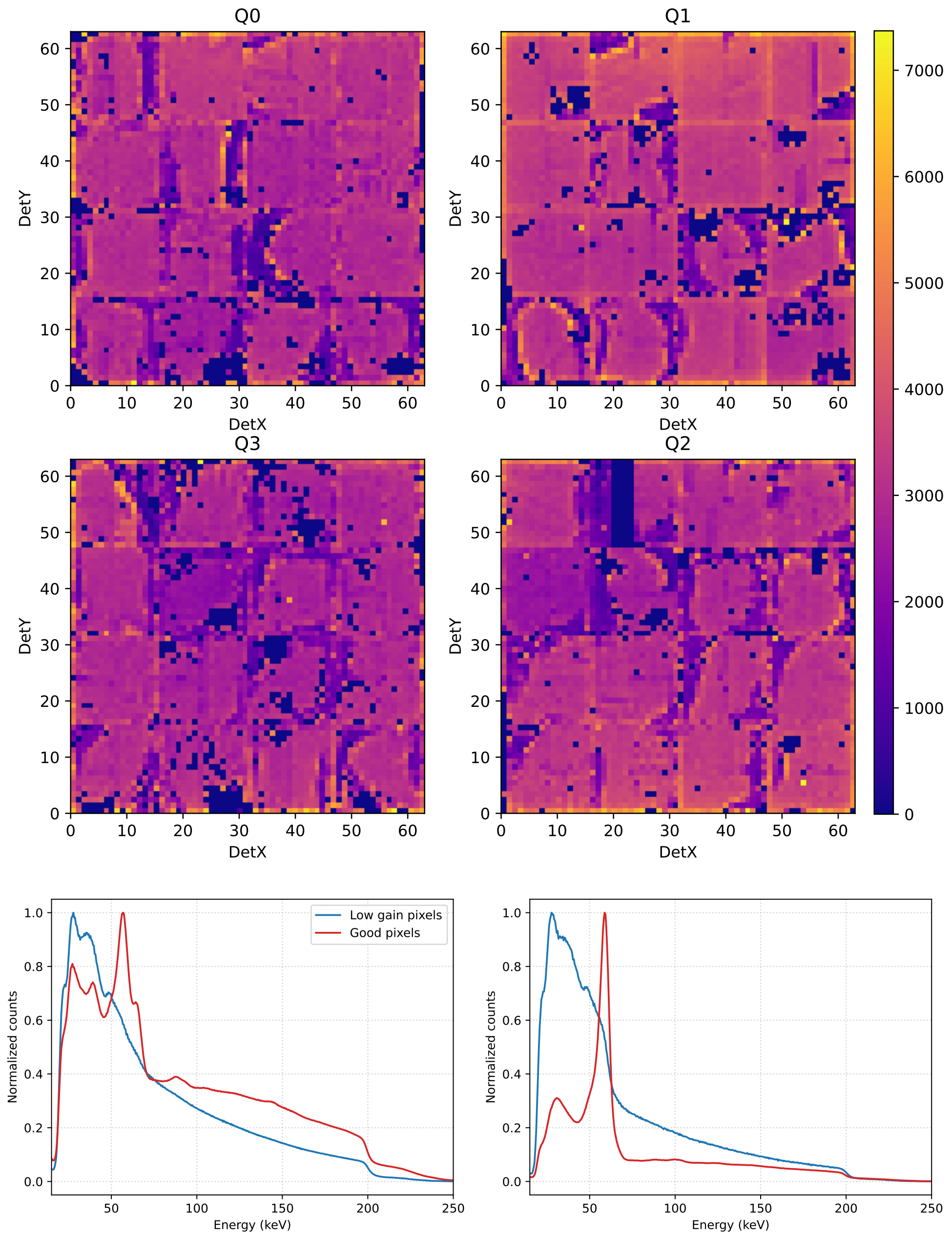

Figure 2.6: Top: Detector plane histogram showing counts detected in each pixel for one long observation of a blank sky field for about 200 ks. Bottom: Spectra of identified low gain pixels having low counts in the DPH above are shown in comparison to the rest of the good pixels. The spectrum of good pixels from the background observations shown on the left shows Ta lines that are missing in the case of low-gain pixels. The spectrum of alpha-tagged events on the right shows the Am-241 line for good pixels, which is not seen in low-gain pixels. The spectral slope is also significantly different for the low-gain pixels.

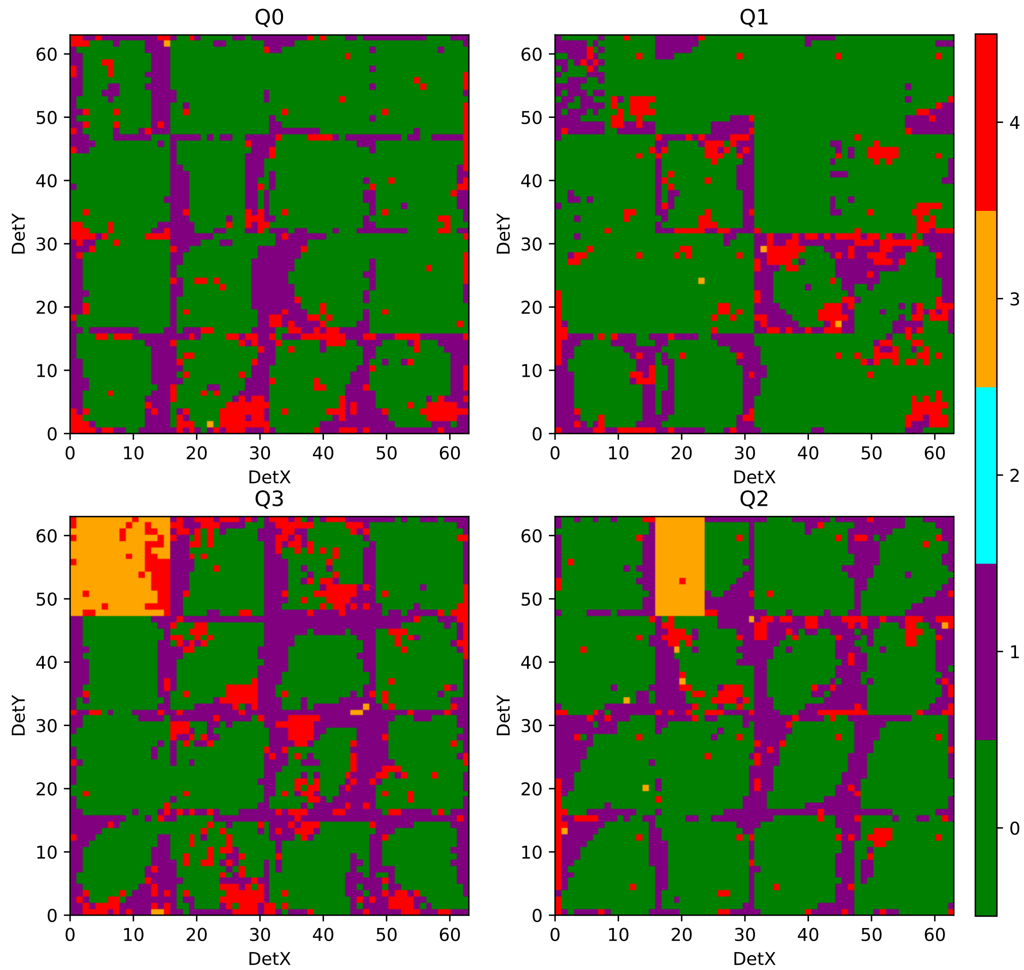

Figure 2.7: Map of the pixel quality flag in CZTI. Good pixels are flagged as 0, low gain pixels as 1, flickering pixels as 2 (not used), noisy pixels as 3, and disabled pixels are flagged as 4.

time. It is found that ∼68.6% of the total 16384 pixels are classified as good pixels that can be used in the spectroscopic analysis for CZTI. Figure 2.6 lower panel shows the co-added spectrum of alpha tagged events and background for the selected spectroscopically good pixels and low gain pixels separately. It can be seen from the figure that the low gain pixels do not show the spectral lines that are visible in the spectra of good pixels, and their continuum slope is considerably different from that of the good pixels. Figure 2.7 shows the map of good, low gain (spectroscopically bad), and disabled pixels in CZTI, and Table 2.1 provides the number of pixels in each category for each quadrant. Comparison of

Quadrant	Good	Low gain	Noisy	Disabled
A	2981	816	2	297
B	3103	650	3	340
C	2781	970	134	211
D	2375	1075	211	435
Total	11240	3511	350	1283
Total (%)	68.6	21.43	2.14	7.83

Table 2.1: Number of good, low-gain, noisy, and disabled pixels in each quadrant of CZTI as of October 2023.

the bad pixel map in Figure 2.7 with the DPH in Figure 2.6 shows the correspondence between low-gain pixels and those with low counts, as expected. Flagging of pixels into these categories is updated in the calibration database of CZTI for use by the data analysis pipeline.

2.4.3 Gain parameters of good pixels

For the good pixels, from the Gaussian fits to the alpha-tagged Am-241 photon spectrum, it was found that the line energy is not exactly where it is expected to be. This means that the gain parameters used in the data analysis require further corrections for the good pixels to obtain the correct energy spectrum. As any time dependence of gain parameters cannot be investigated from the pixel spectra due to poor statistics, we fitted the alpha-tagged spectrum for each month for each of the 64 detector modules, considering only the good pixels. A few detectors with no active pixels and low energy thresholds beyond 60 keV are not included in this analysis. Figure 2.8 shows the fit to background subtracted alpha-tagged event spectrum for one detector, as an example. The top panel of Figure 2.9 shows the peak energy for each detector module in each month since launch. It can be seen that the peak energy shows a significant spread, and the mean value is also different from the actual line energy at 59.54 keV. The difference in the mean value may be because the ground calibration gain

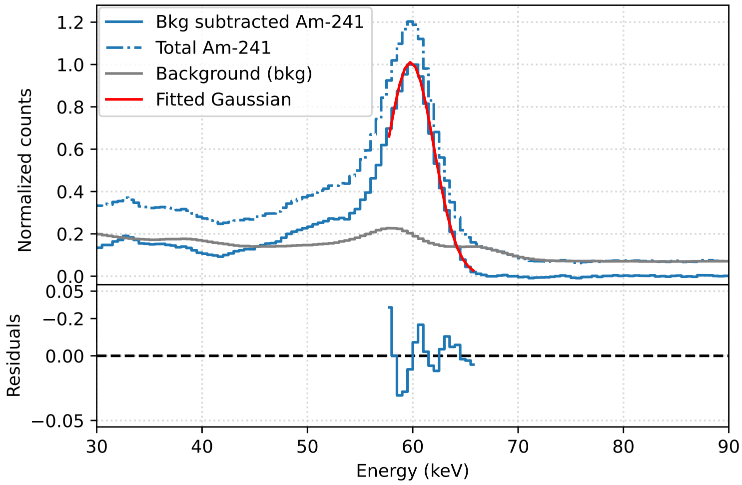

Figure 2.8: Spectrum from one detector of CZTI (sum from all pixels in the detector) of the alpha tagged events. The total spectrum, background spectrum, and background subtracted spectrum are shown. The Am-241 line in the background subtracted spectrum is fitted with Gaussian to obtain the peak energy and resolution.

estimates were carried out in atmospheric pressure conditions, and there may be a slight change in gain in vacuum conditions. However, it was confirmed that the ground calibration estimates had taken care of the temperature dependence of gain. This was validated by fitting the module-wise alpha-tagged event spectra generated by considering the gain only at 10°C, ignoring the detector temperature variations, which resulted in a much more significant spread in the line energies.

To correct the gain, we use the spectral fit to individual pixels and obtain additional correction factors to each pixel's gain parameters (from ground calibration). This additional multiplicative factor on gain for each pixel is incorporated into the analysis chain to obtain the corrected event energies. The second panel in Figure 2.9 shows the monthly module-wise spectral fit after considering the pixel-wise additional correction. It can be seen that the distribution of peak energies is now much narrower and is very close to the actual value. However, we notice a decaying trend in the peak energy, albeit very slowly. This decaying trend can be approximated as a linear change in gain over time. This additional time-dependent correction, common to all pixels, is also incorporated

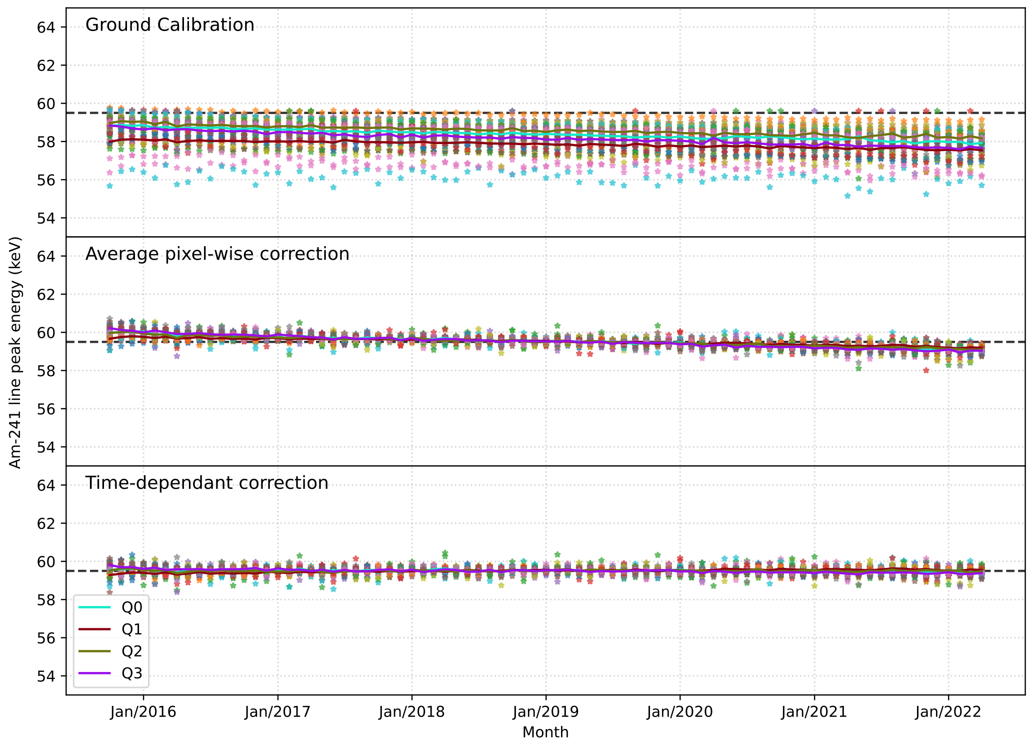

Figure 2.9: Peak energy of Am-241 line for each detector of CZTI over each month of CZTI observations as obtained by applying ground calibration gain (top), average pixel-wise correction to gain using in-flight data (middle), and an additional time-dependent correction (bottom). Dots of each color represent different detector modules. Average values for each quadrant are shown with solid lines in all panels and the dashed line correspond to the actual line energy. The scatter in the peak energies, as well as the reducing trend with time observed in the gain correction from ground calibration, are removed with the final additional corrections shown in the bottom panel.

into the data analysis procedures. The bottom panel of Figure 2.9 shows the peak energies after this final correction, which shows that the energy scales are now correct within one PI channel (0.5 keV) of CZTI. It may be noted that the low gain pixels also can be used in the spectral analysis if their gains are estimated, and this has been presented by Chattopadhyay et al. (2021) for spectral analysis of GRBs. However, as the energy range of these pixels is at higher energies, the methods employed to extract background subtracted spectra for on-axis

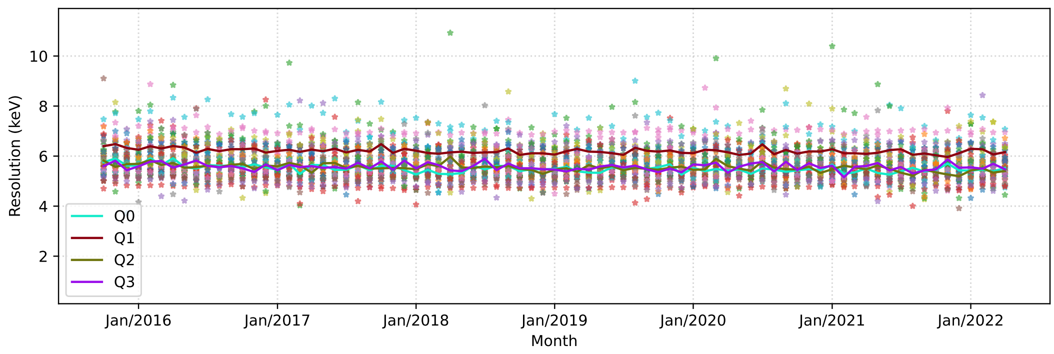

Figure 2.10: Spectral resolution measured as the full width at half maximum of the line at 59.6 keV for each detector of CZTI obtained from alpha-tagged event spectra of each month. The solid lines show average values for each quadrant. It can be seen that no degradation in resolution is observed over time.

sources (as presented in later sections) do not apply to these pixels. Thus, they are ignored in the analysis of on-axis sources, which is the focus of this chapter. Figure 2.10 shows the spectral resolution in terms of the Full Width at Half Maximum (FWHM) of the line at 59.54 keV for each detector obtained from the spectral fitting. This shows that the resolution of the detectors does not show any degradation with time, and the spectral redistribution model obtained from the ground calibration can be used for observations with CZTI.

2.4.4 Low energy and high energy thresholds

During the initial phase, detectors' Lower Level Discriminator (LLD) settings were also brought down (or up in some cases) to be sensitive to the lowest energies possible while not causing several pixels to be noisy. Even though the setting is common for one detector module, individual pixels have slightly different LLD values. Similarly, the higher energy limit of the pixels is determined by the Upper-Level Discriminator (ULD) which are also slightly different for each pixel. With the revised threshold settings and updates in gain, LLD, and ULD values (low and high energy thresholds) for each pixel needs to be estimated so that the total spectral response of the instrument can be computed correctly. LLD and ULD do not appear as a sharp cutoff in the spectrum but instead as slow decay

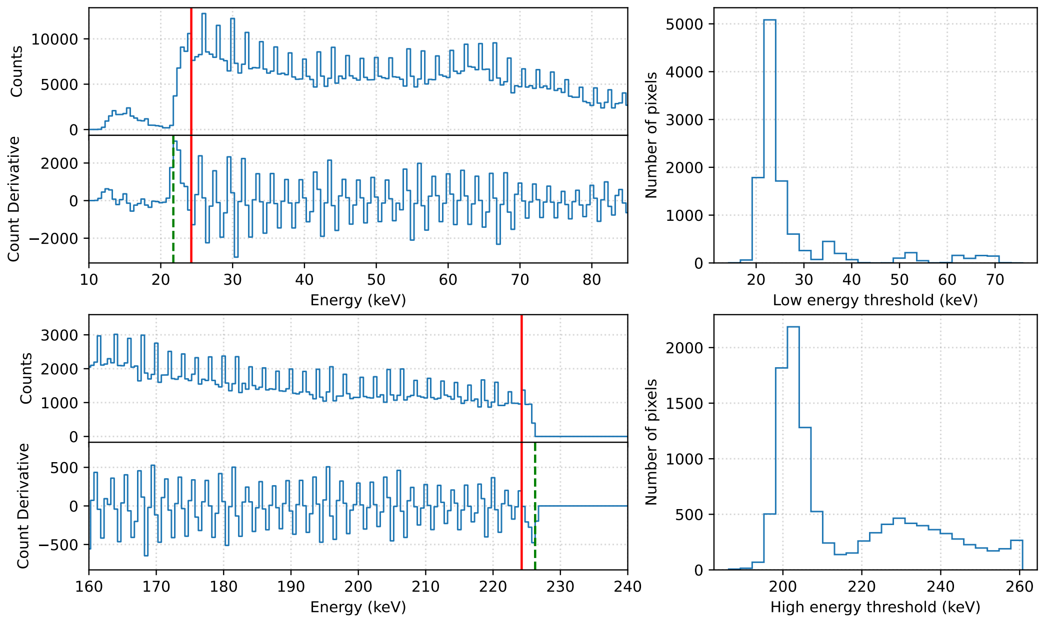

Figure 2.11: Left: The background spectrum observed by one detector pixel near the low energy end and near the high energy end are shown in the top and bottom panels. Beneath the spectra, derivatives of spectra are also shown from which the edge of spectral channels where the pixel records count is identified; the vertical dashed lines mark these. From these, low energy and high energy thresholds for the pixel are decided and marked by vertical red lines. Right: Histogram of pixel-wise low energy threshold (top) and high energy threshold (bottom) are shown.

to zero detection efficiency. Thus, one needs to identify the energy limits where the detection efficiency remains maximum. For this, we use each pixel's total background spectra and find the spectrum's derivative to identify the LLD and ULD. The peaks and dips in the spectrum derivative are used to estimate LLD and ULD as shown in Figure 2.11 top panels. In this manner, LLD and ULD for all active pixels were determined and the right panels of Figure 2.11 show the histogram of LLD and ULD of all pixels. It may be noted that the spread in the distribution of ULD of pixels are due to difference in pixel gains. LLD and ULD of pixels are incorporated into the calibration database of CZTI and events in a pixel having energy less than LLD and higher than ULD of the pixel are ignored by the data analysis pipeline for scientific analysis.

2.5 Background in CZTI

CZTI, much like any collimated hard X-ray detector, is dominated by background. Apart from a few photon events from the astrophysical source of interest, it records background events with different origins. While some of these events can be identified and removed from the list of events recorded, the rest are indistinguishable from source photons to be able to do so. Understanding the characteristics of this background is essential for robust techniques for extracting source spectrum and light curves from the background-dominated event lists. The first step in analyzing CZTI observations is performing the event selection process discussed below. Then, we proceed to investigate the characteristics of the background in CZTI.

As discussed in Section 2.2, it has been observed that some events caused by charged particle interactions occur 'bunched' in time and sometimes bunched near the same area in the detector plane. As genuine X-ray events from the source as well as background such as CXB are expected to occur random in time as well as across the detector plane, the distinct characteristics of these bunch events allow us to identify them and remove them from the event list without any significant loss of genuine events. Details of this event selection process to remove bunched events and associated post-bunch events are discussed in Ratheesh et al. (2021). Removal of these events results in loss of some exposure, which is tracked to correct for the same. Further, some of the CZTI pixels become noisy during the observations, and these noise events are also recorded. Pixels may be noisy for most of the duration of an observation, in which case it is easy to identify such pixels and remove any events from them for further analysis. It is also observed that some pixels flicker during the observations, with noise events generated only for some duration of the observation. In such cases, flickering pixels and detector modules are identified by examining the light curves of pixels and detector modules, and events from those pixels for the flickering periods are removed. Loss of exposure with time and the relative exposure of individual pixels are accounted for in later corrections. Additionally, events that are tagged with the alpha flag or veto flag (see Section 2.2) are also removed from the event list to finally generate the clean event file that includes events from the source of interest as well as background events.

Using the clean event files of CZTI observations from October 2015 to May 2022, we carried out an analysis of the background counts in CZTI to understand its characteristics. To extract the source spectrum and light curve, it is essential to characterize the variability of the total background rate, as well as the spectral shape over time, both short time scales of $\sim$ 100 minutes (orbital period) to a day and longer time scales of years, and over the detector plane. Analysis of the background concerning these aspects is presented here.

2.5.1 Short Term Variability and Data Selection

Figure 2.12 top panel shows the typical light curve from quadrant A of CZTI over more than a day of observations when no detectable sources are present in the FOV. From the figure, it can be seen that the background shows significant variability over this short period. Each segment in the plot corresponds to an orbit of *AstroSat* having period $\sim$ 98 minutes. There is significant background variability within each orbit, except for a few. Additionally, a quasi-diurnal variation can also be seen in the background rates. These variations result from the spacecraft passing through different latitude and longitude regions. In the lower panel of Figure 2.12, background rates at different latitude and longitude locations are shown in different colors. This figure is generated by including observations from several orbits. It can be seen that enhanced background is observed near the South Atlantic Anomaly (SAA) region and in the regions after exiting from SAA. As the spacecraft's orbit precesses, each successive orbit follows a different ground trace, resulting in different degrees of passage through SAA. The quasi-diurnal periodicity observed in the background results from this orbital precession, as also shown in the case of the LAXPC instrument on *AstroSat* by Antia et al. (2022).

Analysis of the spectra near the SAA regions with high background

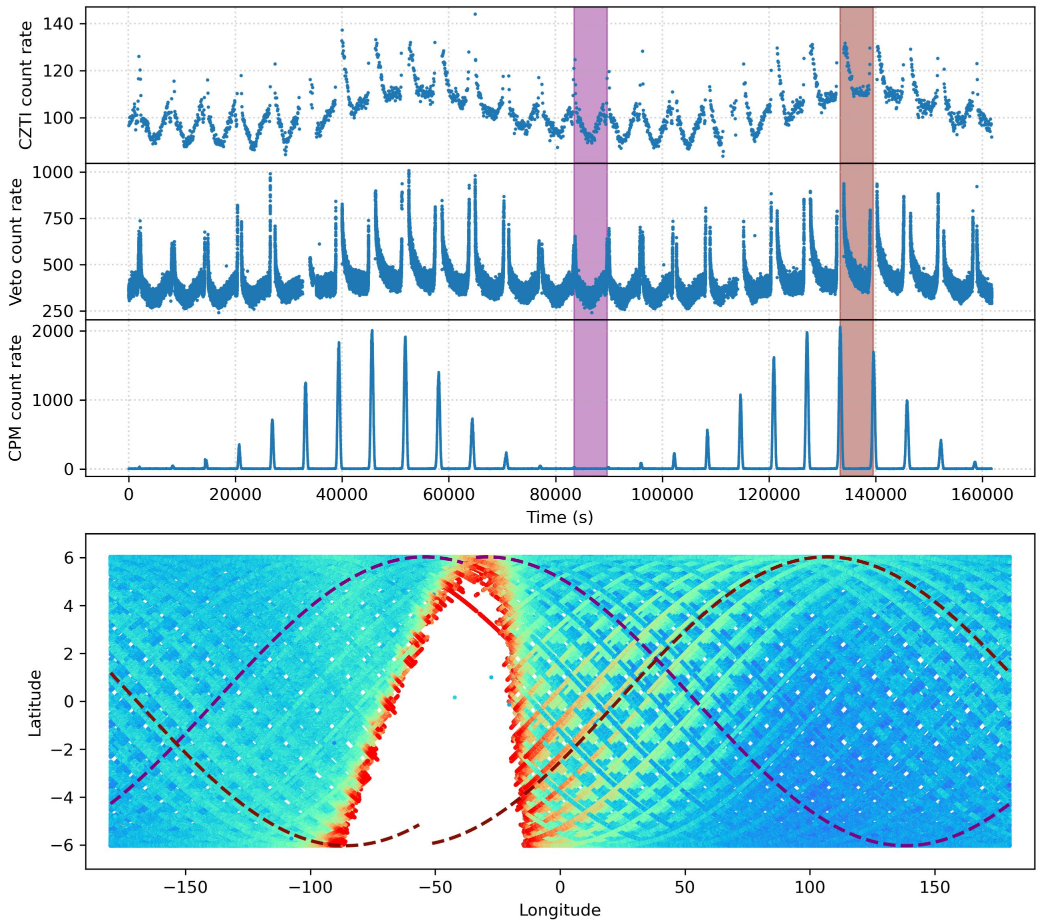

Figure 2.12: Count rates observed by one quadrant of CZTI, veto detector of one quadrant, and the Charged Particle Monitor (CPM) are plotted, showing variability within each orbit as well as quasi-diurnal variability. Background counts in CZTI are well correlated with the veto detector. In the bottom panel, count rates in the veto detector as a function of the satellite location are shown with different colors, where violet denotes the lowest counts, and red denotes the highest counts. Two representative orbits are shown by the purple and brown dashed lines corresponding to the shaded duration in the top panel with respective colors.

rates shows slightly different spectral signatures than the rest of the observations. Although it is desirable to use the data for as much time as possible, including data where the background characteristics are significantly different from the rest of the observation periods will deteriorate the overall efficacy of

Quadrant	Veto Threshold
A	450
B	500
C	500
D	480

Table 2.2: Threshold values of veto count rates for each quadrant to be considered in the selection of good time intervals for spectroscopic analysis with CZTI.

background subtraction. Thus, we need to balance the requirement for the highest useful exposures while ignoring times when the background is significantly higher. Based on Figure 2.12, one can avoid the high background in the near SAA regions by removing observations in certain ranges of latitudes and longitudes. However, this does not cover the excess background in some orbits for significant periods after passage through deeper SAA. Any attempts to include these will result in much more stringent limits that would reduce the exposures significantly. Moreover, it has also been observed that, sometimes, there are enhanced backgrounds in regions slightly away from the normal SAA region, somewhat similar to the 'SAA tentacles' [2] observed by NuSTAR (Grefenstette et al., 2022).

Thus, instead, we propose another criterion for the selection of the duration of data suitable for scientific analysis making use of the Veto detector count rates. In addition to flagging simultaneous events in CZT and Veto to discard events from the CZT detector, the total count rates in each Veto detector are also recorded in the CZTI data packets. It has been observed that the Veto count rates are a good indicator of background variability. As the CZT count rates can be affected by the presence of source events, veto count rates are a better proxy for background rates.

Using data from several long observations, we obtain histograms of veto count rates for each quadrant, shown in Figure 2.13. It can be seen that the distributions are slightly asymmetric, with a tail towards the higher count rate side

[2] https://iachec.org/wp-content/presentations/2016/NuSTAR.pdf

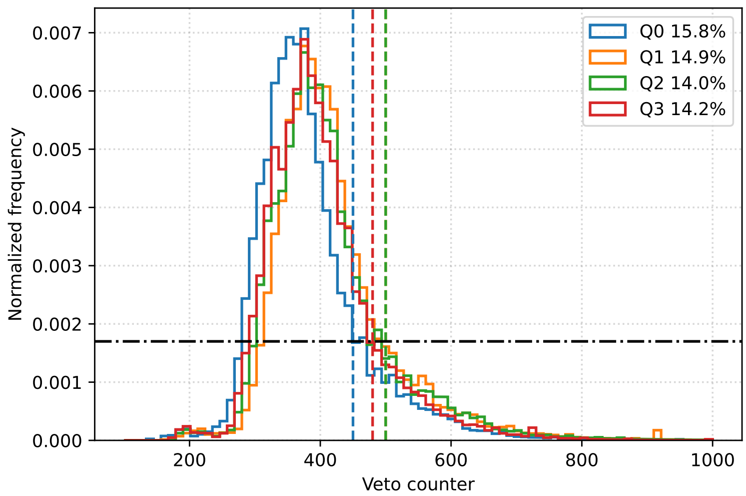

Figure 2.13: Normalized histograms of veto count rates for each quadrant of CZTI obtained from observations of approximately 2000 ks. The vertical lines denote the threshold for veto counter in different quadrants such that the similar duration of the data is ignored.

corresponding to the observations near SAA. Considering the mean count rates and standard deviations, we determine the upper threshold for veto counters of each quadrant such that good time interval selection based on them would result in the discarding of similar duration in all quadrants. The recommended thresholds for Veto count rates in each quadrant are shown by the vertical dashed lines in Figure 2.13 and listed in Table 2.2. The average fraction of times discarded by this selection for each quadrant is shown in Figure 2.13. Approximately 15% of the duration gets discarded, and the background rates in the selected periods show much less variability in the background. This provides observations with much lesser short-term variability (within each source observations that typically last more than a day) for further extraction of background subtracted source spectra and light curves.

2.5.2 Long Term Variability

We now examine the long-term variability of the background in CZTI. Figure 2.14 shows the monthly average background rate for all quadrants added together over the 80 months of observations from October 2015 to May 2022. Each point is the average rate computed from all observations within each month. It can be seen that the overall count rates show an increasing trend till late 2020/early 2021 and then start showing a decreasing trend. Overplotted in the figure in grey is the monthly average number of sunspots as a proxy for solar activity, and it can be seen that the observed background in CZTI shows an inverse correlation with solar activity. This is understood as the cosmic X-ray flux is known to show an inverse correlation with solar activity. During solar maxima, the solar wind magnetic field sweeps away the cosmic rays, reducing the flux, while during solar minima, this effect will be the least (e.g., Nandy et al., 2021). A similar trend is also observed in the background by LAXPC (see Figure 4 in Antia et al., 2022). Thus, any attempts to model the background with CZTI must also consider this long-term variability.

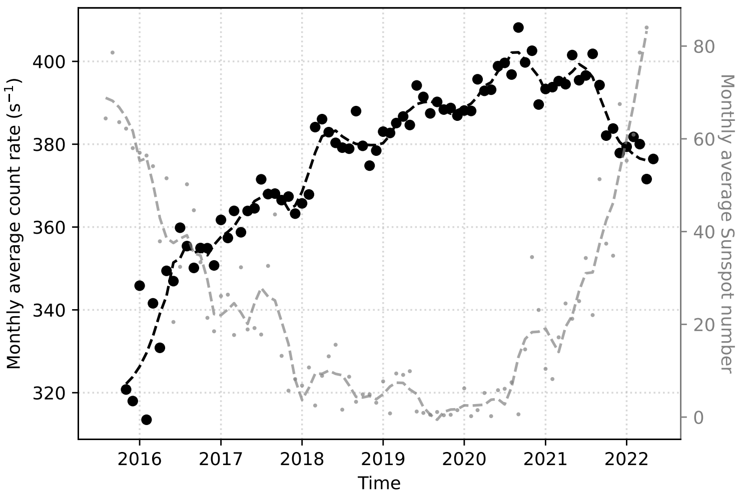

Figure 2.14: Monthly average count rates (all quadrants added) from CZTI are shown with filled black circles. Grey points show the monthly average sunspot number as a proxy of solar activity, showing an inverse correction with the observed background rate. Dashed lines show smoothed data points to show the trend clearly.

Further, we examine the background spectra over time. Figure 2.15 left panel shows the average spectrum for each month from October 2015 to May 2022. Only spectroscopically good pixels are considered to get the spectra, and

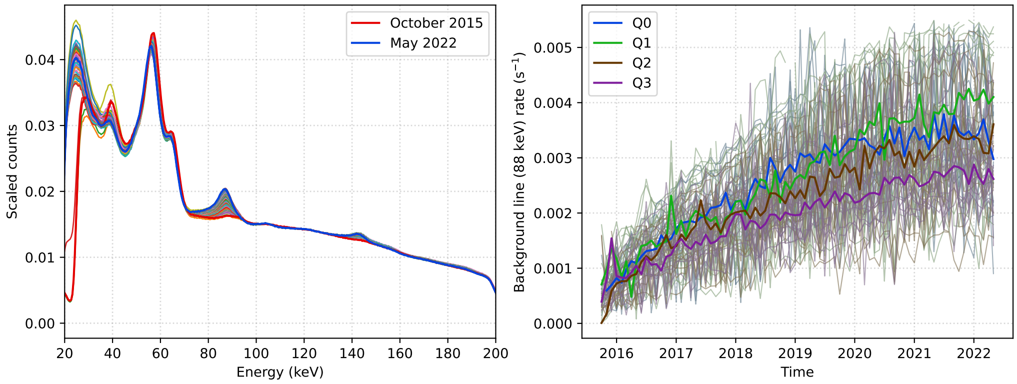

Figure 2.15: Left: Total background spectrum for each month of observation shown in different colors. Right: Intensity of line at 88 keV measured from the background spectrum for each module as a function of time, showing an increase with time and different levels across different detector modules.

they are scaled such that the continuum in the 100–130 keV energy band overlaps to demonstrate the variation in spectral shape alone. A striking feature is the appearance of new background lines at $\sim$ 88 keV and $\sim$ 145 keV. These lines are due to the activation of Cd and Te present in the detector, and similar lines have been observed in Hitomi HXI (Odaka et al., 2018) and NuSTAR (Grefenstette et al., 2022) that used similar detectors. As time progresses, intensities of these lines increase. This is shown in the right panel of Figure 2.15, which plots the count rate in the 88 keV line for each detector module of the CZTI as a function of time. Apart from the general increasing trend of count rates in spectral lines, it is also observed that the line fluxes are different across detector modules, suggesting that the background is not just variable over time but also across the detector plane.

2.5.3 Variability Across Detector Plane

To investigate the relative variation of background across the detector plane, we generated Detector Plane Histograms (DPH) in different energy bands using several long observations. The data were binned into ten keV bins in energy, and DPHs were generated for each observation and added together to obtain the total histograms. Figure 2.16 shows the DPHs in four of these energy bands. Analysis of the DPHs showed that apart from relative variations between background line intensities across detectors, the continuum also shows variations. Particularly, relative counts across pixels show significant variation in the lower energy bands compared to the higher energy bands. In other words, the background is much more uniform across the detectors at higher energies in comparison to lower energies. The difference in counts at lower energies over the detector plane is expected due to the different shielding levels faced by each pixel. As the collimators are designed to become increasingly transparent at higher energies, it is understandable that the background becomes uniform over the detector plane as we move to higher energies. Thus, the relative background across pixels is energy-dependent, which needs to be accounted for while developing methods for background subtraction.

Apart from the general trends of variation across the detector plane, another striking feature is the enhanced counts in the 55–65 keV energy band in some parts of the detector plane, which can be seen in Figure 2.16. As the locations where enhancement is seen are nearer to the mounting locations of alpha-tagged calibration sources in each quadrant, it was apparent that there could be some correlation with that. It may be noted that the background DPHs presented in Figure 2.16 are generated after removing alpha-tagged events from the event lists. The DPH of alpha-tagged events in CZTI detectors is shown in the left panel of Figure 2.17. It can be seen that there are enhanced counts near the locations of alpha sources in all quadrants. However, it is much more prominent in detector modules 13 and 14 in Quadrant 1 (QB), where the background DPHs in Figure 2.16 also show enhanced counts (refer to Figure 2.1 for quadrant and detector ID designations). To understand this further, we generate background spectra from these two detector modules of Quadrant 1 is plotted along with the representative background spectra from other detectors in Figure 2.17 bottom panel. The spectrum of alpha-tagged events of the same quadrant is also plotted for comparison. It is clear from the figure that the background counts in these two detectors of Quadrant 1 have a significant contribution from the Am-241 59.54 keV line in addition to the Tantalum lines and continuum. Thus, we conclude that some fraction of 59.54 keV photons from the Am-241 source incident on

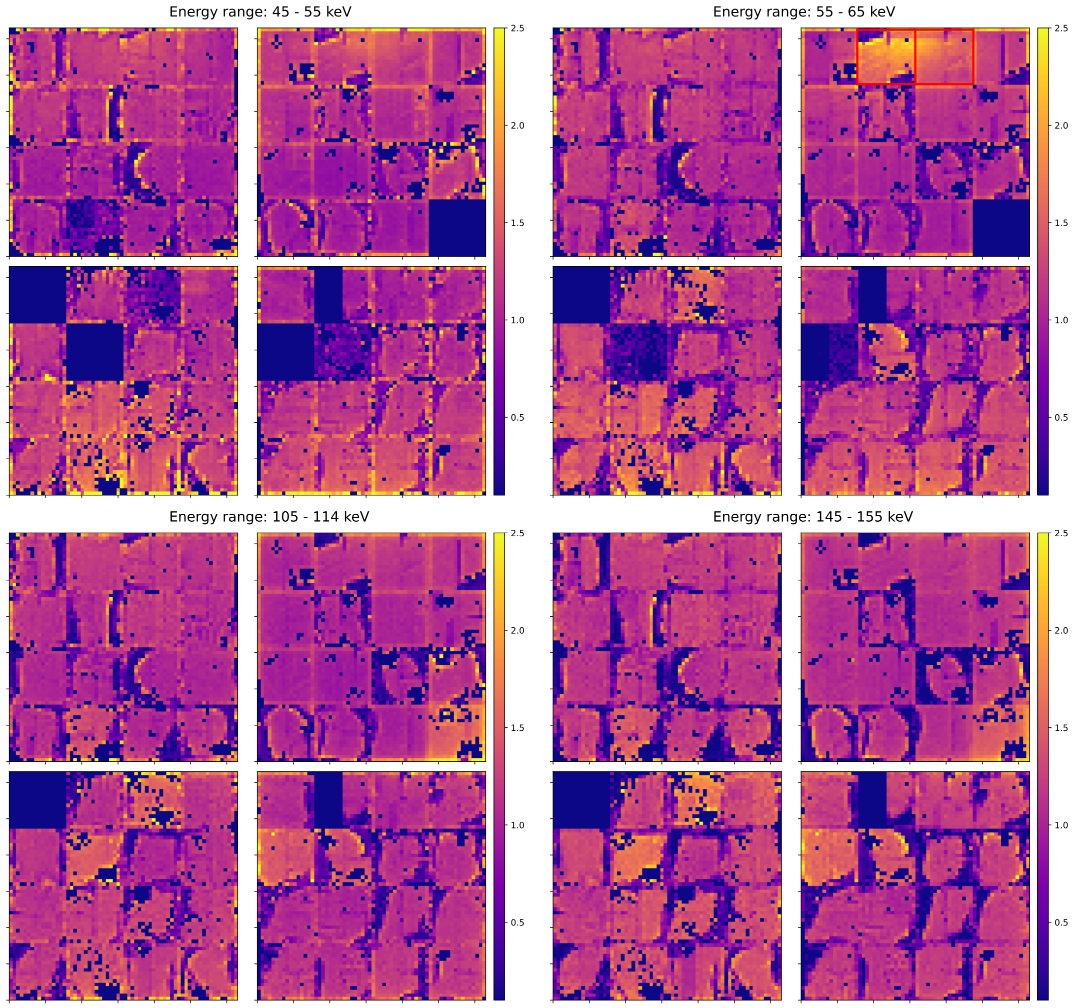

Figure 2.16: Detector plane histogram (DPH) of long background observations in four energy bands.

these CZT detectors are not associated with alpha detection and thus are not tagged and removed from the events used for scientific analysis. It is believed that this is due to slightly different threshold selection for alpha detection in Quadrant 1, which is substantiated by a lesser number of alpha tagged events recorded in Quadrant 1 compared to the other three quadrants. Thus, at least in some parts of the detector plane, the events selected for science analysis will also include calibration source events and the distribution of these events are highly non-uniform in the detector plane.

Analysis of the background in CZTI shows background variations in short time scales of the order of orbital period and a day and in the long term

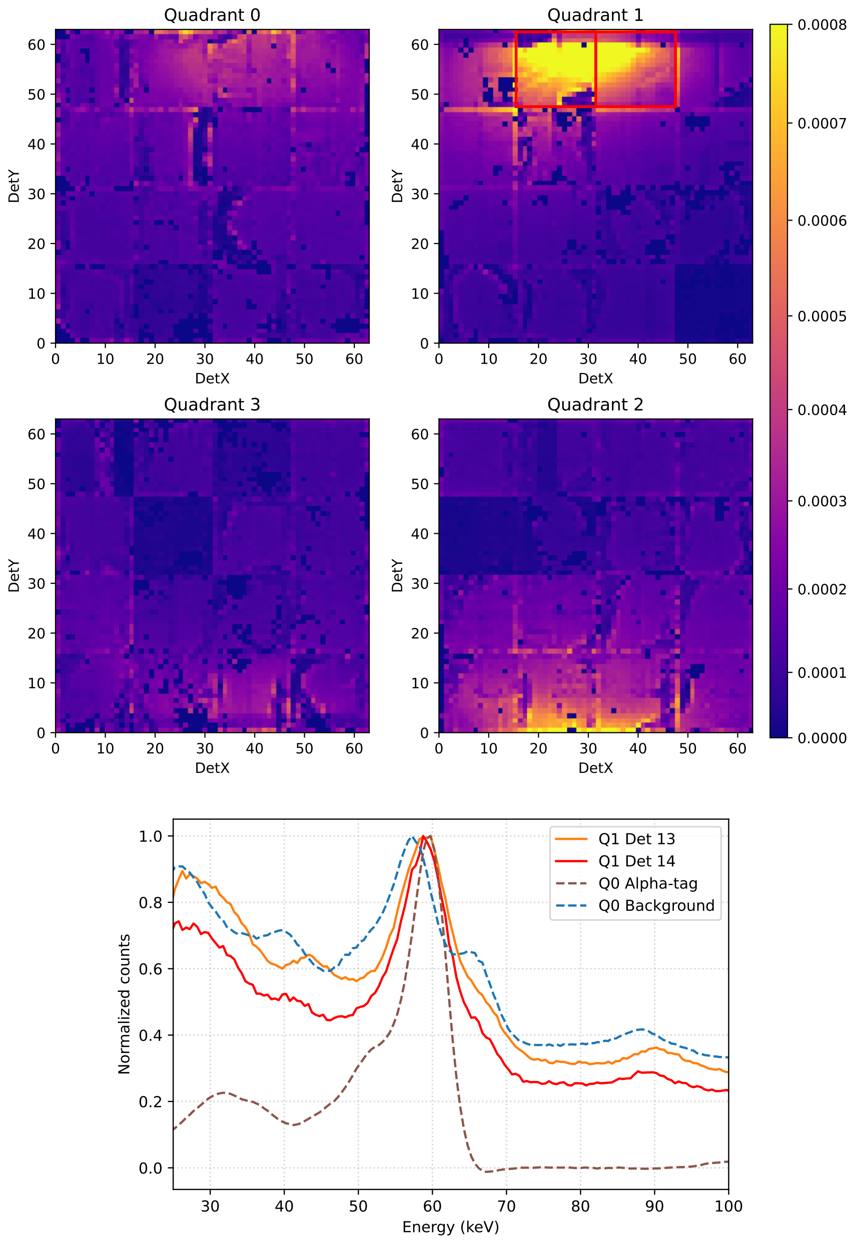

Figure 2.17: Top: Detector plane histogram of alpha-tagged events where some detectors show excess counts compared to the rest. Bottom: Background event spectrum (excluding alpha-tagged events) for two of the detectors of quadrant 1 marked in the top panel as well as in Figure 2.16 are shown in comparison to the average background and alpha-tagged event spectra in quadrant 0. It can be inferred that some Am-241 events not tagged with alpha are present in the background spectrum of these detectors.

over several months. Selection of good time intervals based on Veto counts can help reduce the short-term background variations in the data used for science analysis. Further, it is also shown that the background is not uniform across the detector plane, which is caused by the continuum variations and background spectral lines. Thus, any methodology employed to subtract background needs to take care of these aspects.

2.6 Spectral Extraction by Mask-Weighting

Generally, to obtain the background subtracted source spectra and light curves from observations with collimated X-ray instruments, one has to rely on background models (see Section 1.5.2). As CZTI employs a coded aperture mask, simultaneous measurement of the background is available from the masked pixels. When multiple sources are present in the field of view, coded mask instruments must rely on image reconstruction techniques in different energy bands to get the source spectra. However, when there is only one bright source in the FOV, a technique called 'mask-weighting' can be employed to obtain the background subtracted source spectra and light curves. This technique is used in the analysis of Swift BAT for bright single sources in the field of view such as GRBs [3].

Figure 2.18 top panel shows an ideal scenario where CAM elements mask half the number of pixels while the other half remains open. Pixels that are open measure counts from the source as well as the background, while the closed pixels measure only background counts. Thus, to obtain the source spectrum, one has to add up the spectra from open pixels and then subtract the total spectrum of the closed pixels. Mathematically, this can be achieved by assigning a weight of +1 to fully open pixels and -1 for fully closed pixels and doing a weighted addition of the counts from all pixels. To generalize this, consider that the pixel i has an open fraction f_i, which is the fraction of the area of the pixel illuminated by the parallel rays from the source of interest, given the coded mask and detector geometry. The open fraction f_i can be computed by ray tracing, given the instrument geometry, spacecraft pointing, and source coordinates.

[3] https://swift.gsfc.nasa.gov/analysis/bat_swguide_v6_3.pdf

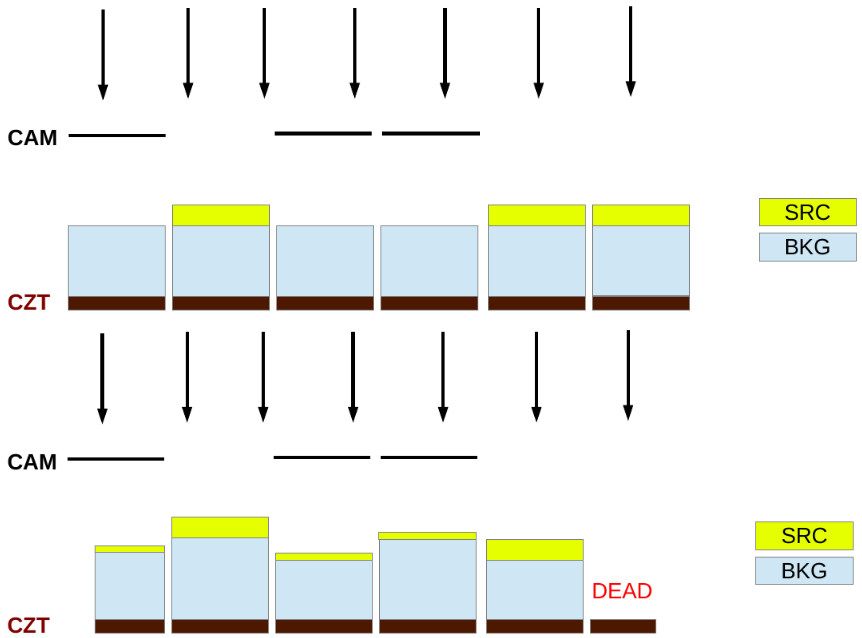

Figure 2.18: The ideal scenario (top) and realistic scenario (bottom) of the source and background counts in each detector element when coded mask blocks some of the detector elements.

Generalising the definition of +1 and -1 weights for fully open (f_i=1) and closed (f_i=0) pixels, respectively, to a pixel having open fraction f_i, we define a weight $w_i{}'$ for the counts in that pixel as:

$$w_i{}' = 2\ f_i - 1 \tag{2.1}$$

Now, in general, the total closed and open areas need not be equal. In such as case, even if we apply these weights to background observation with equal counts in all pixels, residual counts will be present. In order to ensure that the sum of weights is zero, we normalize these weights with a re-normalization factor D to obtain the final weights w_i for events in each pixel as

$$w_i = w_i{}' - D \tag{2.2}$$

$$D = \frac{\sum_{i=1}^{N} w_i{}'}{N} \tag{2.3}$$

Generating the histogram of energy of the detected events by assigning respective weights as computed above gives the background-subtracted source spectrum. Similarly, a histogram of time stamps with weights gives the background subtracted light curve.

However, this approach assumes that the background is uniform across the detector plane, which is not the case in CZTI, as discussed in the previous section. Figure 2.18 shows a realistic schematic of the background and source counts in the detector plane masked by a CAM, similar to the case in CZTI. The background counts in each pixel are not equal, and the relative variation of the background is energy-dependent as well. However, from the analysis of the background data, it is understood that the relative counts in pixels over each energy bin do not change significantly over time, whereas the overall spectral shape and counts change over time. While the fully masked pixels ideally should have zero counts from the source, as the mask is transparent at energies above 100 keV as well in the energy band just below the K-edge of Tantalum, these pixels also have non-zero source counts.

Considering these aspects, we devised the modified mask-weighting algorithm to obtain background-subtracted source spectra and light curves from CZTI observations. We define initial weight $w_i{}'$ for each pixel i with a mask open fraction f_i same as in Equation 2.1. Now, instead of a single re-normalization factor D, consider a vector $\mathbf{D}(I)$ having 512 elements corresponding to each PI channel/energy bin of CZTI. $\mathbf{D}(I)$ is defined as

$$\mathbf{D}(I) = \frac{\sum_i w_i{}' \, \mathbf{B_i}(I)}{\sum_i \mathbf{B_i}(I)} \tag{2.4}$$

where $\mathbf{B_i}(I)$ is the relative background spectrum for each pixel i, which defines non-uniformity of the background over the detector plane. Now, we compute the weights for each pixel at different energies, $\mathbf{w_i}(I)$, as:

$$\mathbf{w_i}(I) = w_i{}' - \mathbf{D} \tag{2.5}$$

Then, the background subtracted source spectrum $\mathbf{S}(I)$ is obtained from observed count spectrum $\mathbf{C_i}$(I) in each pixel as

$$\mathbf{S}(I) = \sum_i \mathbf{w_i}(I) * \mathbf{C_i}(I) \tag{2.6}$$

Statistical error associated with the spectrum $\sigma_{\mathbf{S}}(I)$ is computed as:

$$\sigma_{\mathbf{S}}(I) = \sqrt{\sum_i \mathbf{w_i}(I)^2 * \mathbf{C_i}(I)} \tag{2.7}$$

In a similar manner, the background subtracted light curve for a given energy range can also be obtained. If there is no source contribution, mask-weighted spectrum, and light curves should be consistent with zero.

It may be noted that there are a few other factors that need to be taken into account in the method described above. As discussed in the previous section, the variations in background spectra would be significant across the entire quadrant, such as in the case of Am-241 events in some detectors. Thus, instead of carrying out the re-normalization given by Equation 2.4 over the entire quadrant, it has been done for each detector module, which essentially provides the background-subtracted source spectrum of each detector. These are added together to get the total source spectrum. Further, the low and high energy thresholds of all pixels in a detector are not the same. So, not all pixels are active for a given energy bin closer to the lower or higher energy limit. Thus, while computing the re-normalization factor with Equation 2.4, weights of pixels are set to zero for energy bins below the low energy threshold and above the high energy threshold. If insufficient open and closed pixels exist for a given energy bin, the background subtraction will not be possible. So, only if a minimum of 100 pixels are available in each detector for a given energy bin spectrum is computed for that bin.

This procedure ensures that the mask-weighted spectrum obtained with Equation 2.6 is devoid of background counts, but at the same time provides a weighted source spectrum. Thus, in order to infer the true source spectrum parameters in spectral fitting, the same weighting needs to be applied to obtain the response matrix.

Let $\mathbf{r}_j(E, I)$ be the redistribution matrix (RMF) corresponding to group j of pixels obtained from ground calibration (see Section 2.3.2), $\mathbf{a}_i(E)$ be the effective area of pixel i as function of energy (E) including geometric area and detector efficiency factors, $f_i(t)$ be the mask open fraction of the pixel at time bin t (varies due to pointing jitter), $\tau(E)$ be the tranmission of the mask, ϵ_i be the fraction of total exposure time when pixel i data was used (see discussion on event selection in Section 2.5), and $\mathbf{w_i}(I)$ be the re-normalized mask weights given in Equation 2.5. Then, the response matrix $\mathbf{R}(E, I)$ for CZTI quadrant is computed as

$$\mathbf{R}(E, I) = \sum_i \mathbf{w_i}(I) * \mathbf{r}_{J(i)}(E, I) * a_i(E) * \mathbf{F}(t, E) * \epsilon_i \tag{2.8}$$

where

$$\mathbf{F}(t, E) = f_i(t) + (1 - f_i(t)) * \tau(E) \tag{2.9}$$

and $J(i)$ is the RMF group number corresponding to pixel i. As done in the case of spectrum, weights are set to zero for channels lower than the low-energy threshold and higher than the high-energy threshold while computing the response matrix as well.

2.6.1 Background Non-Uniformity Model

In order to implement this method, it is required to have a model of the relative background spectra $\mathbf{B_i}(I)$ in Equation 2.4. For this, we consider all long observations having > 100 ks exposure with CZTI over the first six years. Using the Swift-BAT catalog, we checked if these fields have any known hard X-ray sources to confirm if they can be used as background observations. Based on this analysis, we selected 11 observations having no sources with flux above 2 mCrab within the CZTI field of view for this analysis, having a total exposure of $\sim$ 2000 ks. Most of these observations are of UVIT targets with no significant X-ray counterparts. Details of these 11 observations are given in Table 2.3.

Data from these observations were reduced with the CZTI data analysis pipeline. As discussed in the previous section, recommended thresholds on Veto count rates were applied in generating GTIs. From the GTI-selected clean event files, spectra of each pixel were generated, ignoring the events beyond the respective pixel's low and high energy thresholds. It was verified that there is no significant variation in the ratio of spectra between pixels if we consider only part of these observations. Thus, pixel-wise background spectra obtained from these are directly used as $\mathbf{B_i}(I)$ values in Equation 2.4.

Sl No	Observation ID	Exp. (ks)	RA	DEC
1	20161103_G06_086T01_9000000774	163	299.999	65.148
2	20171211_A04_124T01_9000001766	174	176.316	79.681
3	20180703_T02_056T01_9000002210	187	203.654	37.912
4	20180923_T02_109T01_9000002386	150	57.604	17.246
5	20190213_A06_006T01_9000002720	254	53.123	-27.735
6	20191116_A07_007T04_9000003310	101	10.710	41.250
7	20210319_T03_286T01_9000004268	153	189.212	62.294
8	20170429_A03_102T01_9000001202	132	132.875	63.130
9	20180415_A04_199T01_9000002040	212	133.703	20.108
10	20190621_C04_001T01_9000002994	113	237.391	70.348
11	20200305_A07_165T01_9000003558	370	236.720	-78.214

Table 2.3: List of observations having no hard X-ray sources having flux above 2 mCrab within CZTI FOV, selected to obtain the relative background counts in each energy channel over the detector plane.

These pixel-wise background spectra are included in the updated calibration database of CZTI. The *cztbindata* task of the pipeline is modified to incorporate the mask-weighting algorithm described above by taking this input from the CALDB.

2.6.2 Efficacy of Background Subtraction

In order to validate the efficacy of the background subtraction method, we applied the method to other background observations. Another 12 observations with no bright hard X-ray sources ($>$ 2 mCrab) in the field were selected for this purpose. Mask-weighted light curves and spectra were generated for these observations using *cztbindata* considering the coordinates of the target of respective observations (which are UV sources having no detectable hard X-ray counterparts). As no sources are present in these fields, the mask-weighted light curves and spectra are expected to be consistent with zero within error bars over time and energy, respectively.

Figure 2.19 shows the total light curves and mask-weighted background-subtracted light curves with 100 s time bin for one of these long observations. It can be seen that the light curve is consistent with zero at all time bins even though the total light curve shows significant variations over time, establishing the efficacy of the background subtraction procedure. Figure 2.20 shows the total spectrum and the mask-weighted background subtracted spectrum for the same observation having an exposure of 190 ks. We also consider the ideal case where the total spectrum is the background spectrum and generate the background subtracted spectrum considering Poisson uncertainties, which is shown by the grey-shaded region in the figure. It can be seen that the mask-weighted spectrum is well within the statistical uncertainties of the 'ideal' background subtraction process, and hence there are no additional systematic uncertainties in the process for exposures similar to this.

However, to estimate the systematic uncertainties of the background subtracted spectrum, which would be relevant at longer exposures, we added the mask-weighted spectrum of all 12 observations (different from the ones used

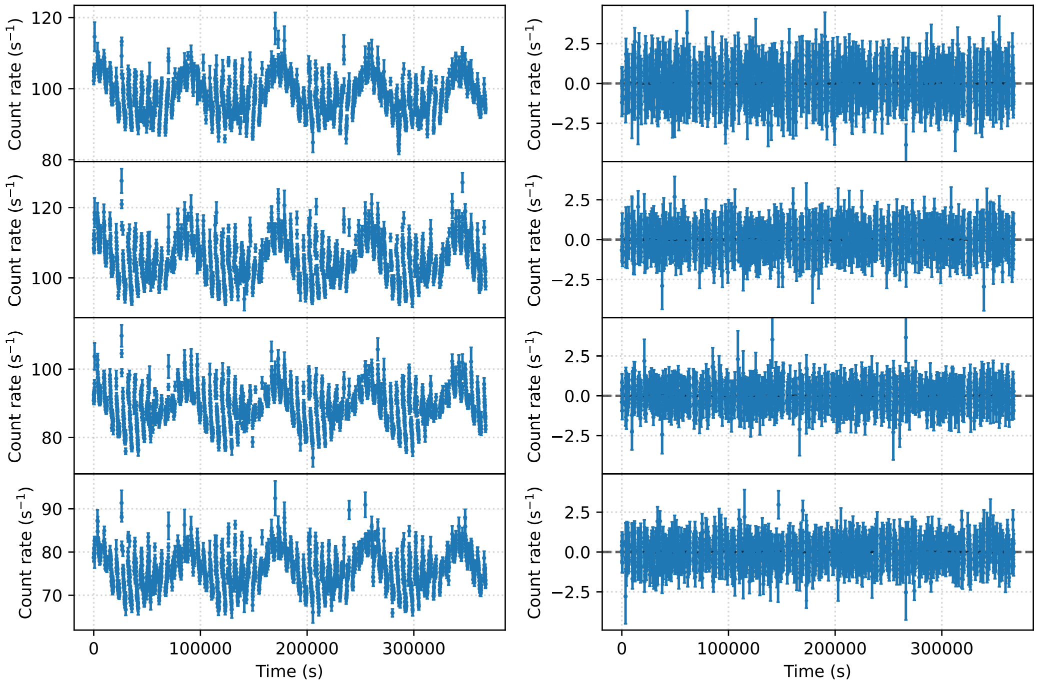

Figure 2.19: Total light curves (left) and mask-weighted background-subtracted light curves (right) of a long blank sky observation. The light curves are for 100 s time bins, and the four vertical panels correspond to quadrants A to D, respectively. While there are significant variations in the total light curve, the background-subtracted light curve is consistent with zero for the entire duration.

in the background non-uniformity model). Systematic uncertainty in the background subtraction is the absolute value of these residuals, ignoring statistical uncertainties as the total exposure is $\sim$ 2000 ks. Figure 2.21 shows the systematic error estimated this way in comparison to the statistical uncertainties of background at different exposures. It can be seen that the systematic uncertainties are comparable to the statistical uncertainties for exposures above 500 ks. Thus, for typical observations with CZTI having exposures in 50 ks - 200 ks, the background subtraction by mask-weighting provides results limited only by statistics.

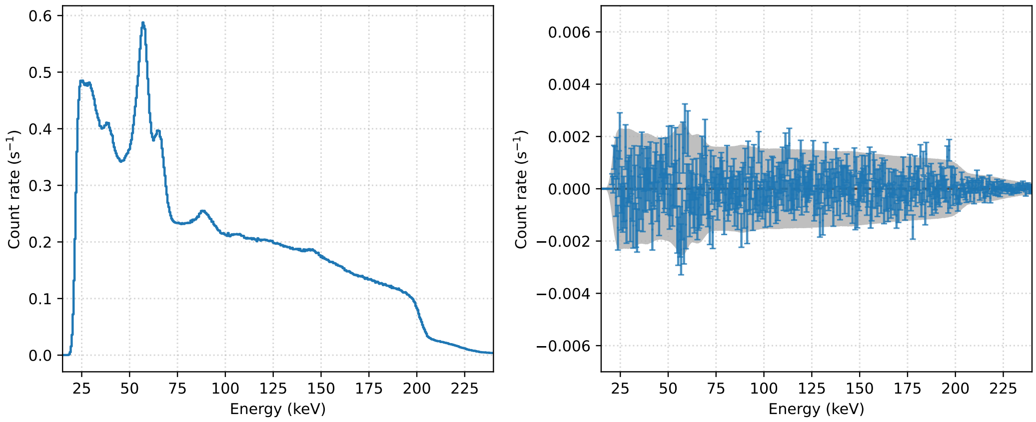

Figure 2.20: Total spectrum (left) and mask-weighted background subtracted spectrum (right) from Quadrant C for the observation shown in Figure 2.19, having total exposure of $\sim$ 190 ks. The grey-shaded region in the right panel corresponds to the Poisson limit of background subtraction.

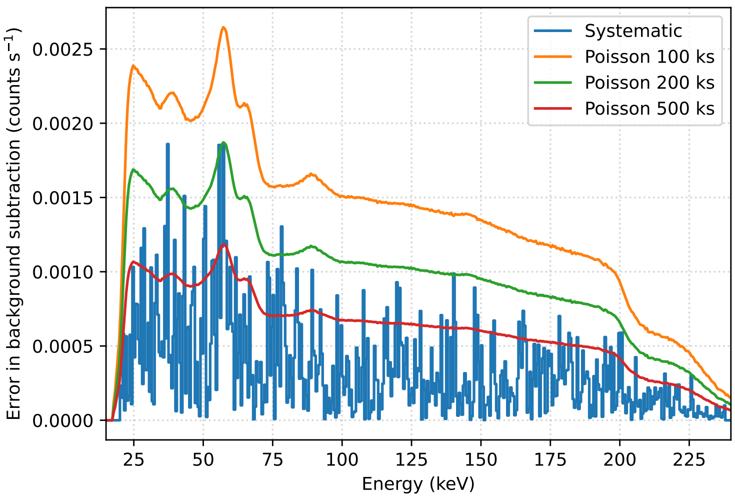

Figure 2.21: Systematic uncertainties in background subtraction obtained by co-adding background subtracted spectra of multiple observations of fields with no X-ray sources are shown in blue. Statistical limits of background subtraction, given the background count spectrum, are shown in different colors. The systematic uncertainties are comparable with statistical uncertainties for exposures of 500 ks.

2.7 Detector and Coded Mask Alignment

As described in the previous section, the mask-weighting algorithm to obtain the background subtracted source spectrum requires the open fractions of each pixel given the source location. Computing open fractions requires knowledge of the alignment of the CAM with detector pixels and of the CZTI instrument with the spacecraft axes. Mask-weights are very sensitive to slight misalignment and thus would result in the loss of the source flux when generating source spectra and light curves.

Imaging analysis of in-flight observation showed that there is a shift in the coded mask elements in at least three quadrants with respect to the detector pixels (Vibhute et al., 2021). By fitting the simulated mask shadow patterns with the observed shadow patterns during Crab observations, alignment shifts for each quadrant were estimated (Vibhute et al., 2021). There were also indications in the imaging analysis that additional detector-to-detector variations exist; however, no measurements were made. We generated the mask-weighted spectra for Crab observations for each individual detector considering the quadrant level shifts measured by imaging analysis. It was observed that the fluxes obtained for each detector were different further confirming the suspicions of slight misalignment between detector modules observed in imaging analysis.

As the mask-weighted fluxes are very sensitive to the alignment of the detectors with the mask, we employ the same in a novel way to measure the shifts for each detector. When there is no offset between the mask and the detector, for an on-axis source, if we consider the source to be at different angles (only along one axis for simplicity) and compute the mask-weighted flux, we get a profile as shown by blue points in Figure 2.22. However, this mask-weight profile is very different if there were shifts/offsets between the mask and detector, as shown by the other curves in Figure 2.22. Thus, computing the mask-weight profile for actual observations and comparing them with simulated mask-weight profiles for different source positions (corresponding to different angular shifts between the detector and CAM), we can obtain the angular shifts.

Two crab observations with exposures $\sim$100 ks were used for this anal-

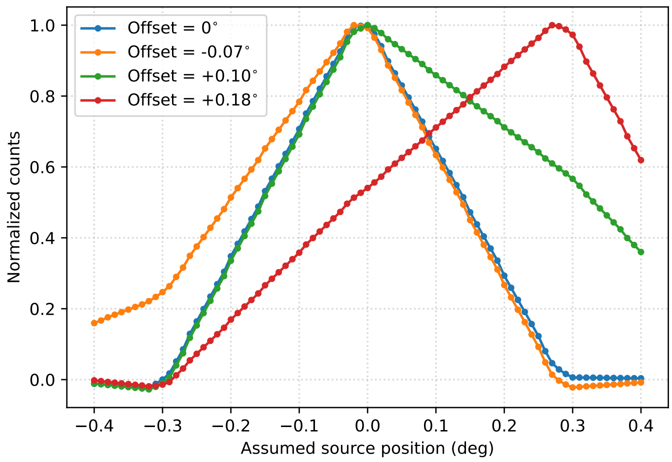

Figure 2.22: Mask-weighted flux profiles for different angular offsets between the mask and detector in CZTI are shown. These are obtained by considering the source position to be at different values and obtaining the mask-weighted flux, when the source is actually on-axis. It can be seen that the profiles have distinct shapes for different angular offsets between the mask and the detector.

ysis, and clean event files are generated as usual. For each detector, we compute the mask-weighted flux, assuming the source positions within 0.4 degrees on either side along the x and y directions separately. The mask-weighted profiles thus obtained from the observations are then compared with the simulated profiles, assuming different angular offsets between the detector and mask. Figure 2.23 left panels show examples of delta-chi between the observed profiles and simulated profiles at different angular offsets and the right panels show the observed profile with the best-fitted simulated profile having the least deviations from the observation.

In this way, we obtain the angular offsets of each detector along the x and y directions with respect to the CAM. Figure 2.24 shows the measured angular offsets in the x and y directions for all detectors of each quadrant. It is found that Quadrant A detectors have offsets close to zero, while others have non-zero offsets at least in one direction. Overplotted in the figure with stars are the quadrant-wise shifts measured by imaging analysis given in Vibhute et al. (2021). While the detectors of each quadrant have offsets clustered around the

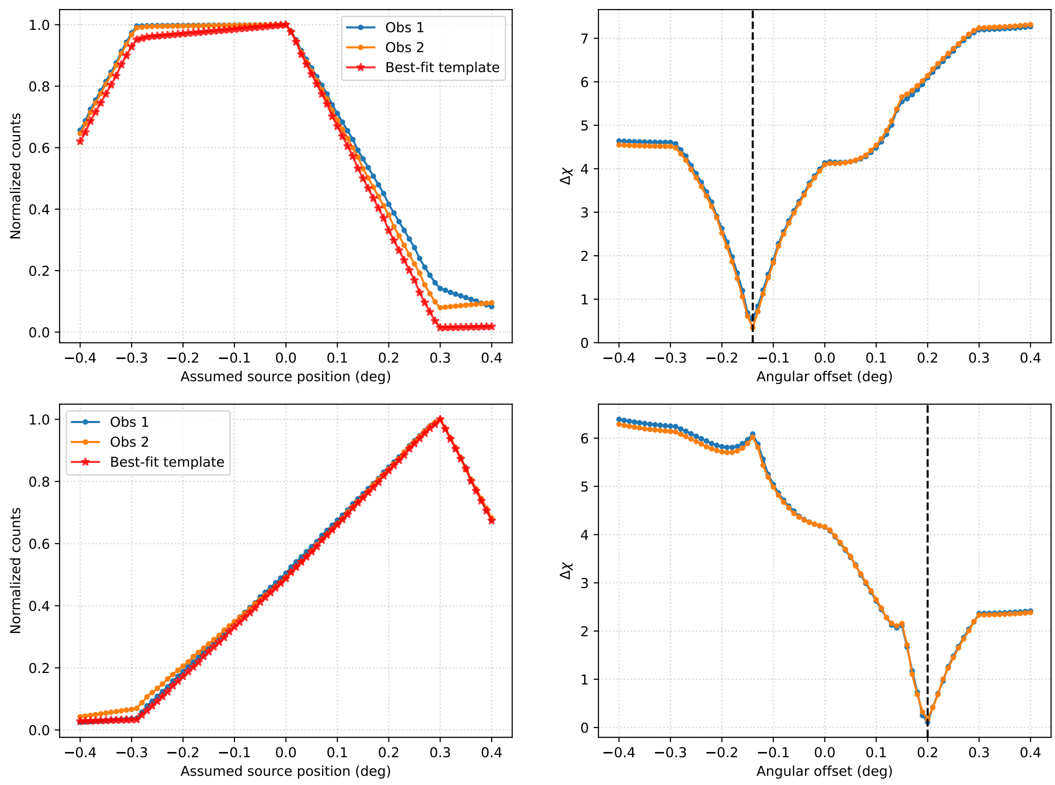

Figure 2.23: Measurement of angular offset by fitting the observed mask weighted flux profile: examples for Quadrant 1 DetID 06 x-axis and Quadrant 2 DetID 00 y-axis are shown in top and bottom panels, respectively. The left panels show the observed mask-weight flux profiles for two Crab observations, along with the best-fit simulated mask-weight profile. The right panels show the delta-chi between observed and simulated profiles for different offsets, and the vertical line corresponds to the offset measurement where it is minimum.

typical quadrant-wise offset measured from imaging analysis, there is clearly distribution of offsets for detectors within the quadrant. The scatter is the least within detectors of Quadrant A and is the highest among detectors of Quadrant D. We incorporate these detector-wise angular shifts while computing mask open fractions and mask-weights to obtain background-subtracted source spectra.

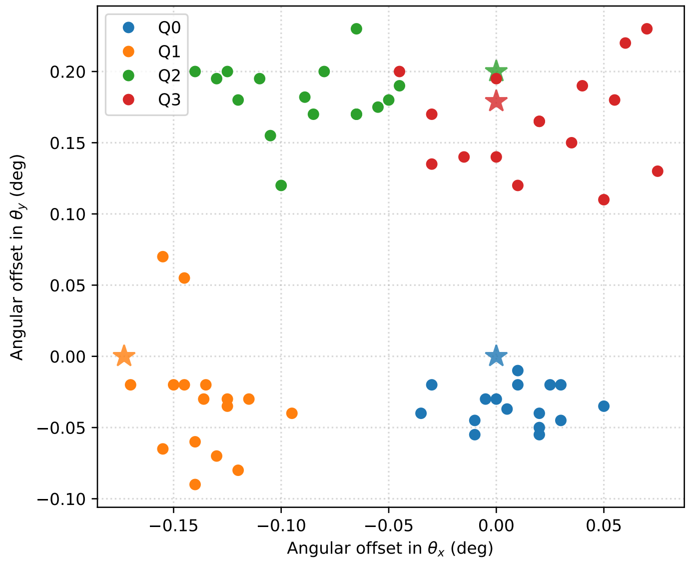

Figure 2.24: Angular offsets measured for each detector module are shown with the filled circles. Stars represent the offsets for each quadrant as measured from imaging analysis.

2.8 Effective Area Calibration

After incorporating the updates in detector characteristics, gain, background subtraction, and detector mask alignment, we now focus on the instrument's effective area. For this, we use several long observations of Crab, considered a standard source in hard X-rays (see Section 1.5.3). Table 2.4 lists the Crab observations considered in this analysis. We reduce the data for each observation using the CZTI data analysis pipeline that incorporates the algorithm and calibration updates discussed in the previous sections. Spectra and responses for each observation are obtained and co-added together to improve the statistics.

Figure 2.25 shows the co-added Crab spectra for all four quadrants of CZTI. If we consider the full energy range of CZTI, we find that the spectra are not well-fitted with the canonical power law model with an index of 2.1. Thus, instead, we fit the spectra in the energy range of 30 – 100 keV with a fixed index of 2.1 where the observed spectra are well fitted. The best-fit models are overplotted on the spectra in the figure, and the residuals for the entire energy range are shown in the respective lower panels. From Figure 2.25, it can be seen

Sl No	Observation ID	Exposure (ks)
1	20160822_G05_237T01_9000000620_level2	77.4
2	20161108_A02_090T01_9000000778_level2	53.5
3	20170114_G06_029T01_9000000964_level2	71.8
4	20170118_A02_090T01_9000000970_level2	105.0
5	20170927_A03_086T01_9000001568_level2	96.3
6	20180115_A04_174T01_9000001850_level2	137.4
7	20180129_A04_174T01_9000001876_level2	193.4
8	20180914_T02_091T01_9000002368_level2	41.7
9	20181029_T03_024T01_9000002472_level2	63.4
10	20190126_A05_159T01_9000002678_level2	101.5
11	20200829_A09_145T01_9000003848_level2	217.6
12	20200913_A09_145T01_9000003866_level2	47.2
13	20200923_A09_145T01_9000003900_level2	83.6
14	20200926_A09_120T02_9000003904_level2	106.8

Table 2.4: List of observations of Crab with CZTI used for effective area calibration.

that the spectra of all four quadrants show significant residuals at energies below 30 keV and at energies above 100 keV.

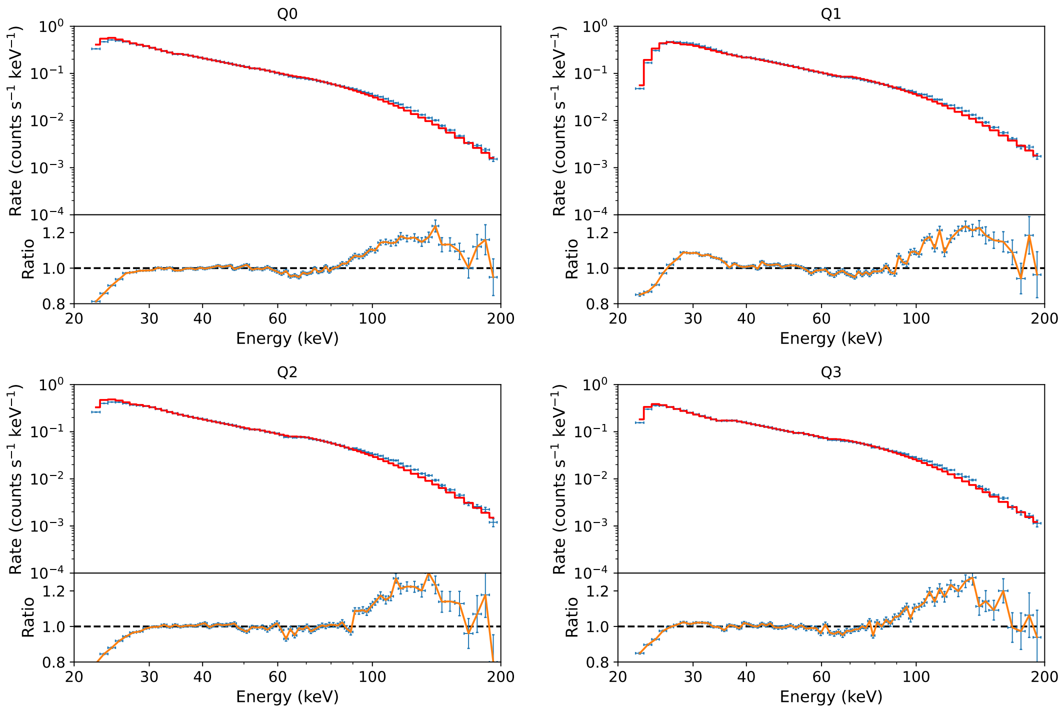

Figure 2.25: Co-added crab spectra of individual quadrants fitted with the canonical power-law model in 30-100 keV. Residuals of the fits are shown in the respective lower panels.

First, we turn our attention to the residuals at low energies. Residuals in three quadrants except quadrant B look identical at these energies. Unlike the other three quadrants, Quadrant B shows excess counts compared to the model at energies close to 30 keV. We generated spectra for each detector module to investigate this odd behavior in quadrant B. It was observed that the excess counts are present only in a few detectors of quadrant B, while the remaining detectors show residuals similar to those seen in other quadrants. As the exact reason for these excess counts in some detectors was not understood, low energy thresholds of these detectors were updated such that this part of the spectrum is ignored in spectral analysis.

After ignoring the low energy part of these anomalous detectors, the residuals for all quadrants in the energies below 30 keV show a similar trend. At lower energies, observed counts were progressively lesser than the model predictions. Near the low energy threshold of detectors, the detection probability is expected to reduce from unity to zero at lower energies gradually. This arises from the fact that pulse heights corresponding to a given energy vary within the instrument resolution and are compared against a fixed voltage level to decide if the event is considered as detected. Thus, the detection probability near the LLD channel would follow an error function profile. Although the LLDs of detector pixels are determined to correspond to unity probability as much as possible (Section 2.4), there would likely be some residual effects, especially as the LLDs are different for each pixel. Thus, we proceed to employ empirical corrections to the low energy response.

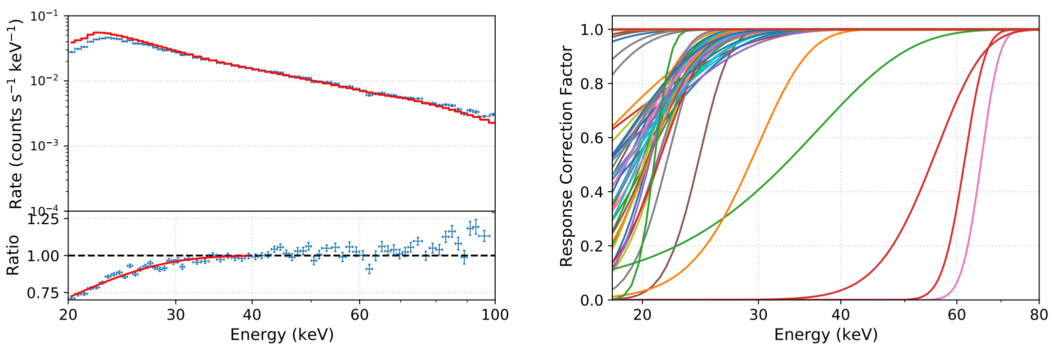

Figure 2.26: Left: Crab spectra with the low energy residuals fitted with an error function for one of the 64 CZT detectors. Right: Low energy response correction factors for all CZTI detectors obtained by fitting.

We fitted the residuals of the Crab spectrum in the low energy range for each detector using an error function model. Figure 2.26 left panel shows the fit to residuals of one of the detector modules. Best fit error function models obtained for each detector are shown in the right panel of Figure 2.26. These empirical functions are incorporated into the effective area calculations used to generate the response matrix for CZTI.

Now, we focus on the residuals at energies above 100 keV and slight residuals even at energies in the 60–100 keV energy range, as seen in Figure 2.25. In this case, all four quadrants show identical behavior, which suggests that the

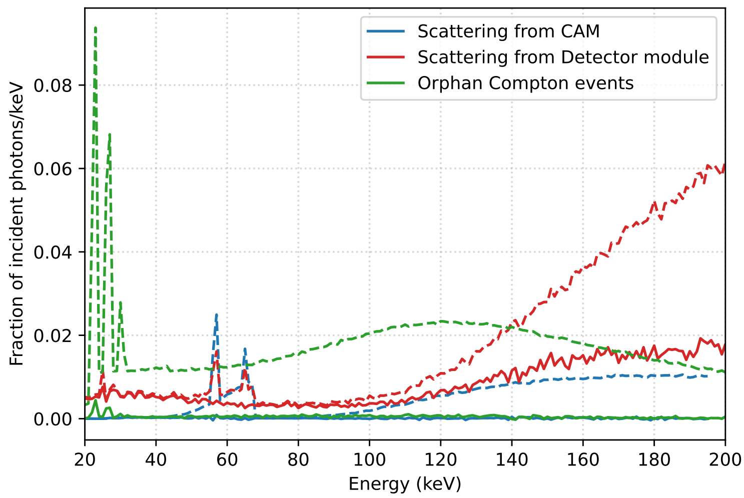

Figure 2.27: Simulation results showing the excess counts at higher energies due to various processes as marked in the figure. Dashed lines correspond to the total counts, whereas the solid lines show the counts that would remain after mask-weighting.

origin of this is something common for all quadrants. As discussed below, we explored various possibilities behind these excess counts at energies above 100 keV.

The coded aperture mask of CZTI made of Tantalum is efficient at stopping X-rays at lower energies. However, at higher energies, photons are likely to undergo elastic and inelastic scatterings in the mask and reach the detector plane. Source photons incident on a close mask element may get scattered and be detected in the corresponding or neighboring detector pixels. As these excess counts from scattered photons from the mask are not considered in the response matrix, we carry out Geant4 simulations to verify whether they can explain the observed excess in the spectrum. In Geant4, we import the CAD model of the mask and place detectors beneath at the same distance as in the CZTI instrument and carry out simulations by shining the mask with parallel X-rays with a flat spectrum in the 20-200 keV energy range. In Figure 2.27, the spectrum of photons detected in the CZT detectors after undergoing scattering interactions in the mask is shown as blue dashed line. As the source spectrum in CZTI is obtained by employing the mask-weighting technique discussed in Section 2.6, we apply the same to the simulation results. Using the spectrum in each pixel and the mask shadow pattern, we obtain the mask-weighted spectrum, shown as blue solid line in Figure 2.27. It can be seen that the spectrum is practically zero after incorporating the mask-weighting. Thus, even though there is a contribution from scattered events from the mask in the detector, it gets subtracted out in the mask-weighting and is not responsible for the residuals observed at higher energies.

Another possibility is the scattering from within the CZT detector module. The CZT detector module used in CZTI has a common cathode above the crystal, metallic anode pads below the crystal, a PCB with the ASIC, and a cold finger to remove the heat. Source photons incident on an open pixel may undergo scattering in these parts and finally get detected in a neighboring closed pixel. To check this possibility, we carried out Geant4 simulations incorporating the detailed modeling of various parts within the detector module and obtained the fraction of photons that undergo scattering within the detector module and get detected, shown by the red dashed line in Figure 2.27. As earlier, we apply mask-weighting, and the resultant spectrum is shown with solid red line. In this case, some residual effect is visible in the mask-weighted spectrum; however, the fraction of photons obtained from simulations is not sufficient to explain the residuals in the observed spectrum.

We also explored the possibility of 'orphan Compton events'. At energies above 100 keV, the incident photons can undergo Compton scattering within the detector, and a pair of adjacent pixels may record the energy deposition by scattering and energy deposition of the scattered photon (which are used for polarization measurement as discussed in Section 2.2). However, if the energy deposition in the scattering pixel is less than the low energy threshold of the pixel, that event will not be detected, but the scattered photon will be detected in the adjacent pixel. As the scattering event was not recorded, these 'orphan Compton events' will remain in the clean event file. Once again, we carry out Geant4 simulations to estimate the fraction of these events. Figure 2.27 shows the fractional spectrum of orphan Compton events as green dashed line and the mask-weighted spectrum as green solid line. Here also, we see that the mask-weighting process subtracts out the additional events caused by the orphan Compton events, and thus, they do not contribute to the residuals in the spectrum at higher energies.

As we ruled out various possible physical origins of the observed residuals, we resorted to calibrating the effective area against the crab spectrum at higher energies, similar to the method adopted for NuSTAR (Madsen et al., 2015b, 2022) and other hard X-ray instruments. Unlike in lower energies, where there is better consensus on the crab spectral model, at energies above 100 keV, there are several models that various authors have reported by analyzing data from different instruments. These models include canonical single power law (for e.g. Madsen et al., 2017b), a broken power law with break energy at 100 keV (Jourdain & Roques, 2009), and a band function (Jourdain & Roques, 2020). We fitted the observed CZTI spectra with all these different models, and the results are shown in Figure 2.28. From the residuals, it can be seen that there is not much difference between the different models within the energy range of CZTI up to 200 keV. This can be understood as the other models are obtained using the data up to much higher energies. Thus, we decided to obtain effective area correction based on the single power law model for Crab with an index of 2.1. It may be noted that, at this point, we do not fix the normalization of the Crab model.

In order to derive correction to the effective area, we consider that factors at discrete energy points define the correction term and use the linearly interpolated values at energies in between. Such a model with 12 parameters was implemented as a local model in pyxspec. The observed crab spectra of each quadrant were fitted with a power law model of a fixed index of 2.1 convolved with the effective area correction model to obtain the parameters of the correction model. The resultant best-fit correction models for all four quadrants are shown in Figure 2.29. It can be seen that the derived corrections terms are nearly identical for all four quadrants. These effective area correction terms are incorporated into the response matrix of CZTI.

We then re-analyze the crab observations with the updated pipeline incorporating the corrections. Crab spectra obtained after co-adding all observations for each quadrant are shown in Figure 2.30. They are well-fitted with

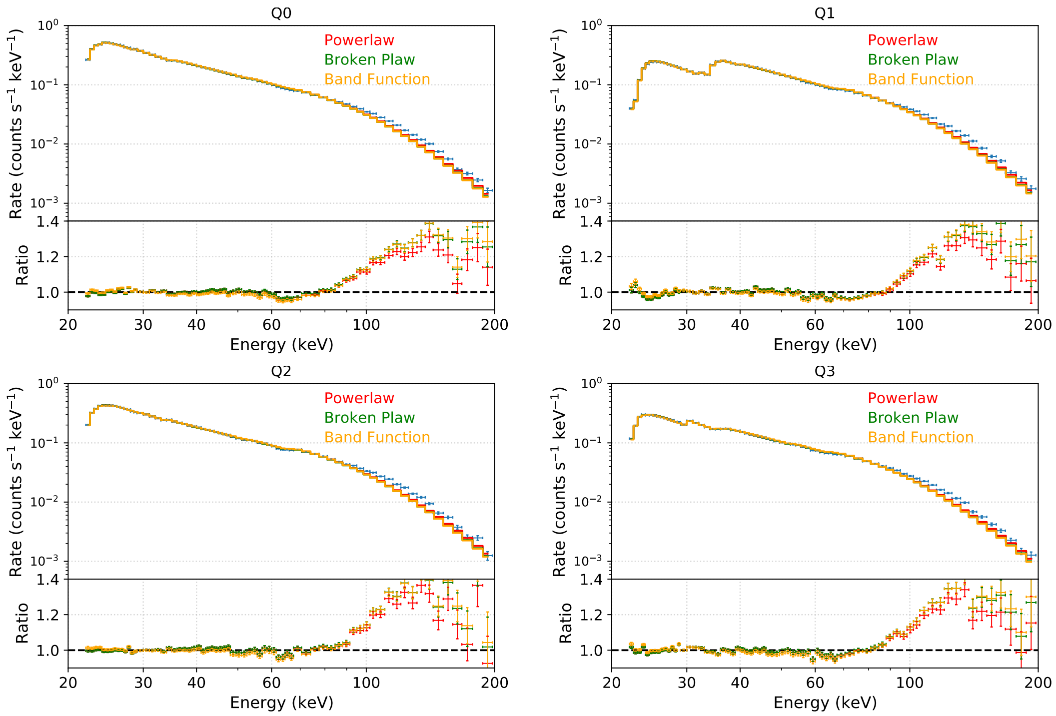

Figure 2.28: Crab spectra fitted with different models proposed by various observations: power law, broken power law, and band function. Residuals are shown in the lower panels, where it is clear that they are identical for all different models.

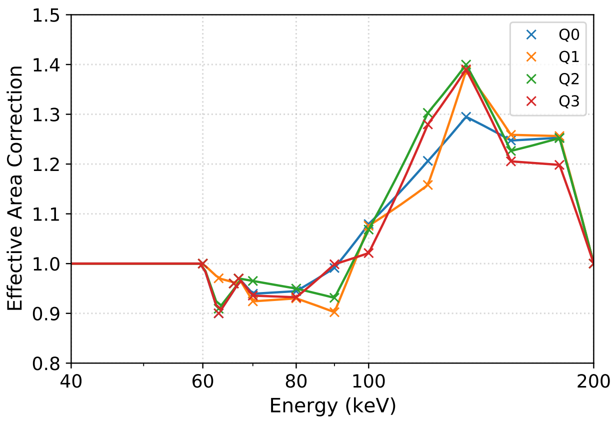

Figure 2.29: High energy response correction factor for each quadrant of CZTI obtained empirically by calibrating against the canonical crab spectral model.

a power-law with no significant residuals. Further, we fitted spectra of individual Crab observations of each quadrant to derive the power-law index and

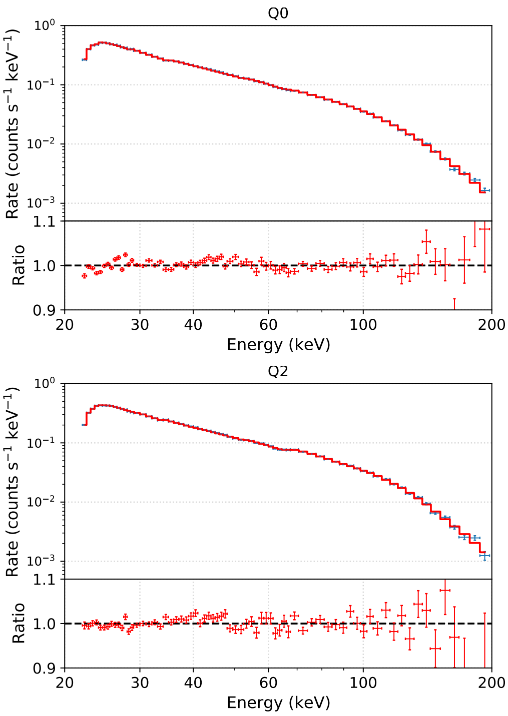

Figure 2.30: Crab spectra fitted with a canonical power-law model after incorporating the low energy and high energy effective area corrections in addition to the rest of the calibration updates.

normalization. Figure 2.31 shows the derived power law indices and norm values showing consistent results across observations and quadrants. We note that the overall norm factors between quadrants differ within ∼10%, and at this point, we do not make any corrections to the overall effective area to equalize these. It is recommended that relative normalization factors be used for each quadrant while simultaneously fitting the CZTI spectra of all quadrants.

2.9 Spectroscopic Sensitivity and Prospects

With the improved calibration of CZTI, we now estimate the realized spectroscopic sensitivity of the instrument for different exposures. For low exposure times, the sensitivity is expected to be limited by the statistical uncertainties of spectral measurements, whereas the systematic uncertainties in the background subtraction (Section 2.6.2) would limit the sensitivity at large exposures. To

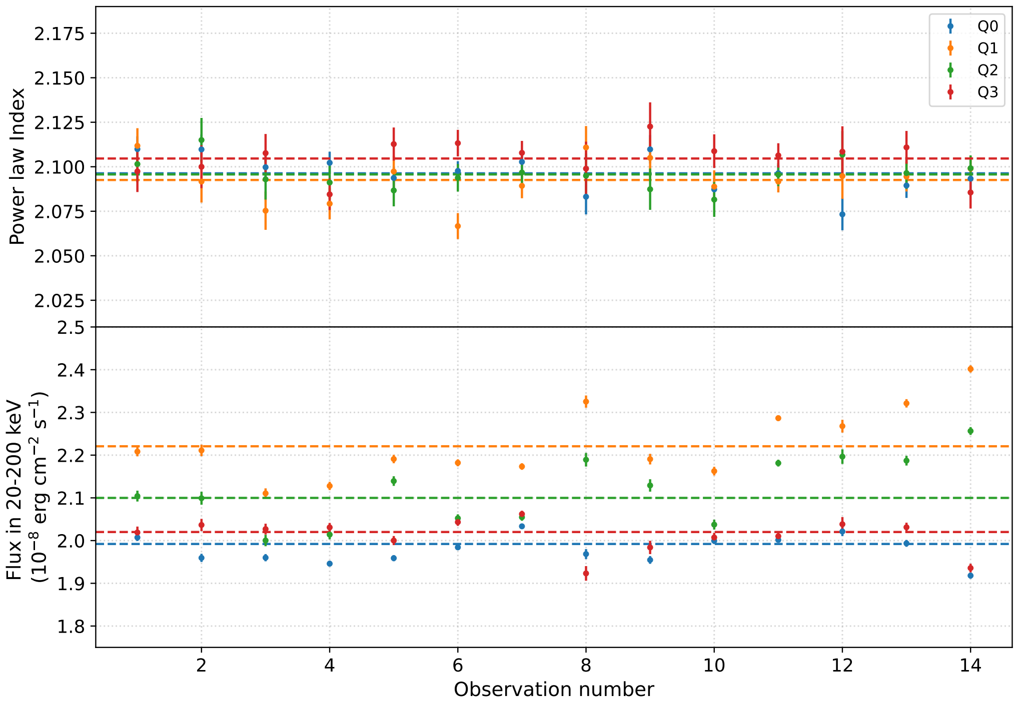

Figure 2.31: Spectral parameters of Crab obtained from all 14 observations. The top panel shows the power law index while the bottom panel shows the flux in 20-200 keV energy band. The dashed lines show mean values from each quadrant.

estimate the spectroscopic sensitivity, we consider a flat source spectrum and convolve it with the CZTI response matrix to obtain the detected count spectrum. By comparing the expected counts in each energy bin at different flux levels of this fiducial source with the total uncertainty of background subtraction for a given exposure time (including statistical and systematic uncertainties), we estimate the minimum source flux required for 3-sigma detection.

Figure 2.32 shows the resultant sensitivity as a function of energy for different exposure times. The dashed lines in the figure correspond to 1 Crab, 100 mCrab, and 10 mCrab. From this, we infer that exposures of 50 ks or higher provide a sensitivity of a few tens of mCrab in the lower energy band of CZTI. It can also be seen that the increasing exposures from 200ks to 500ks do not provide significant improvement in sensitivity, which is understandable as we have already shown that the systematic uncertainties in the background become

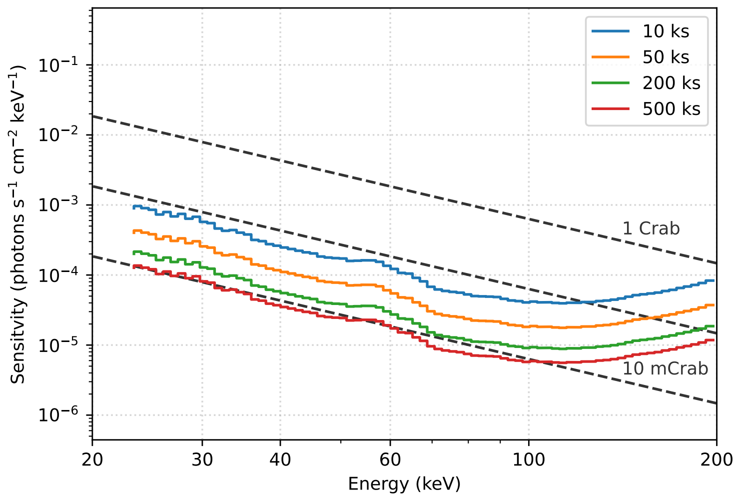

Figure 2.32: Spectroscopic sensitivity of CZTI at different exposure times considering logarithmic binning in energy. Dashed lines correspond to 1 Crab, 100 mCrab, and 10 mCrab. The sensitivity would not improve b significantly beyond 500 ks as systematic errors in background subtraction would become comparable to the statistical uncertainties.

comparable with statistical uncertainties at exposures of 500ks (Section 2.6.2).

With an estimate of the sensitivity of CZTI, we proceed to re-analyze all observations of CZTI from October 2015 to August 2022 that are available publicly. We analyze the data with version 3.0 of the CZTI data analysis pipeline [4] with the updated CALDB (version 20221209), including all the updates discussed in this chapter. Using the clean event files, we generate mask-weighted spectra and light curves from each quadrant of CZTI for all observations. We use the target coordinates provided by the proposers (present in FITS headers) for computing the mask weights. We co-added the spectra from four quadrants using *cztaddspec* module to obtain the total spectrum. Using the total counts in the mask-weighted spectra and the uncertainties, we compute the significance of the source detection in each observation. Appendix A provides the list of CZTI observations that resulted in nominal detection of sources at the 3-sigma level. Coordinates of these sources were matched against the Swift-BAT catalog, and counterpart details, when available, are also given in Table A.1. In most cases,

[4] http://astrosat-ssc.iucaa.in/cztiData

examining the spectrum in detail suggests proper detection of X-ray sources with CZTI. More importantly, the mask-weighted spectrum for the rest of the observations not listed here is consistent with zero, providing further confidence in the background subtraction technique. However, for a handful of cases, such as observation ID 20170423_G07_060T01_9000001200, we see that the mask-weighted counts are significantly above zero even though the source is expected not to be detected with CZTI. Examining the spectra in such cases (especially comparing spectra of individual quadrants) clearly show that the issue is due to the result of incorrect background subtraction due to specific peculiarities in the observation. Thus, we recommend to examine the individual quadrant spectra to confirm that the spectra are consistent before proceeding to spectral analysis.

With the improved spectroscopic capabilities of CZTI with the updates in spectral extraction and calibration, hard X-ray spectroscopy with CZTI has several interesting prospects. For example, hard X-ray spectrum from CZTI has been used along with spectra from other instruments to analyze faint objects such as the Compton thick AGN Circinus Galaxy (Kayal et al., 2023). Another area where CZTI spectra can complement the observations with AstroSat LAXPC and/or NuSTAR is for spectrum at energies beyond 80–100 keV. Table 2.5 lists the observations where the source is detected in the CZTI spectrum at energies beyond 100 keV, excluding the two bright sources, Crab and Cygnus X-1. These observations also provide a high-quality spectrum from 25 keV onwards with CZTI, which is very useful for analysis, such as the reflection spectroscopy of MAXI J1820+070 during its 2018 outburst (Banerjee et al., 2023, under review). As these sources have significant counts in CZTI at energies above 100 keV, they are also potential targets for X-ray polarization studies with CZTI. In such studies, in addition to polarization measurements, it is also important to have spectral context for interpretation, which can be provided by the mask-weighted CZTI spectra, like in the case of state-dependent polarization studies of Cygnus X-1 (Chattopadhyay et al., 2024). Preliminary spectroscopic investigations in this direction in the context of phase-resolved polarization measurements of the Crab pulsar and nebula are discussed in the next section.

Sl No	Obsid	Source	Exposure(ks)	Count Rate (100-200keV)	Flux(100-200 keV, mCrab)
1	20171026_T01_202T01_9000001640	Swift J0243.6+6124	36.838	0.76378	190.94
2	20190222_T03_083T01_9000002728	MAXI J1348-630	18.371	0.93832	234.58
3	20190228_T03_083T01_9000002742	MAXI J1348-630	18.578	0.83936	209.84
4	20190614_T03_120T01_9000002990	MAXI J1348-630	37.826	5.00610	1251.53
5	20170912_T01_191T01_9000001536	MAXI J1535-571	201.629	1.67876	419.69
6	20190922_A05_166T01_9000003192	GX339-4	28.285	0.71036	177.59
7	20210213_T03_275T01_9000004180	GX339-4	25.290	1.31016	327.54
8	20210302_T03_279T01_9000004218	GX339-4	78.892	1.37549	343.87
9	20170215_T01_156T01_9000001034	GRS 1716- 249	40.614	2.31427	578.57
10	20170406_T01_164T01_9000001140	GRS 1716- 249	10.807	1.45700	364.25
11	20180408_G08_070T01_9000002028	GRS 1758-58	73.776	0.42275	105.69
12	20180710_T02_060T01_9000002216	MAXI J1820+070	92.878	0.80103	200.26
13	20180330_T02_038T01_9000001994	MAXI J1820+070	36.818	14.14980	3537.45
14	20180508_G08_028T01_9000002080	GRS 1915+105	14.953	0.79876	199.69

Table 2.5: List of CZTI observations where the source is detected significantly at energies above 100 keV. This list excludes two bright sources Crab and Cygnus X-1.

2.10 Phase-resolved Spectroscopy of the Crab Pulsar and Nebula

One of the interesting results from AstroSat CZTI has been the measurement of hard X-ray polarization of Crab reported by Vadawale et al. (2018). A key observation made by them was that the polarization fraction and angle show some variations within the off-pulse region of the pulse profile as shown in Figure 2.33 taken from Vadawale et al. (2018), where it is expected that the properties remain constant as the emission is thought to be arising from the nebula alone with no contribution from the pulsar.

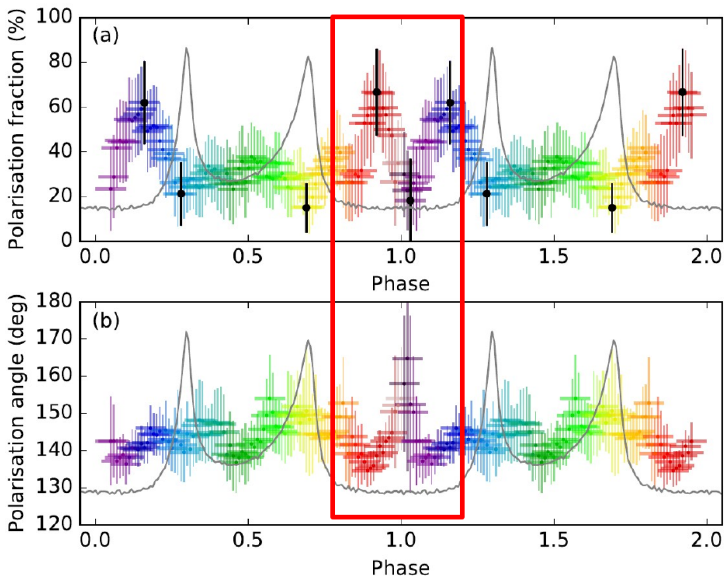

Figure 2.33: Phase-resolved polarization fraction of Crab obtained with CZTI, taken from Vadawale et al. (2018). The red box marks the variation in polarization fraction during off-pulse.

As the polarization signatures show variation within the off-pulse region, it would be interesting to examine if there are any spectral variations within the off-pulse region. As the usual assumption is that the off-pulse emission is constant and arising from the nebula, few studies have attempted to look into any spectral variations within the off-pulse duration. Thus, in this work, we carry out phase-resolved spectroscopy of Crab pulsar and nebular using AstroSat CZTI.

We chose all Crab observations over the first 7-year duration, which provided a total of ∼2000 ks of effective exposure. Event files were generated for each observation using the standard data reduction pipeline (version 3.0), and the barycentric correction was applied for all event time stamps. Using Jodrell bank ephemeris of the crab pulsar, pulse phases for each event were determined. We used cztbindata module of the analysis pipeline to compute the mask weights for each event.

Background subtracted pulse profiles were obtained by adding the mask weight of each event to the respective phase bin. Pulse profiles in different energy bands thus obtained are shown in Figure 2.34. The pulse profiles show the known behavior of increased interpulse peak to main peak ratio at higher energies.

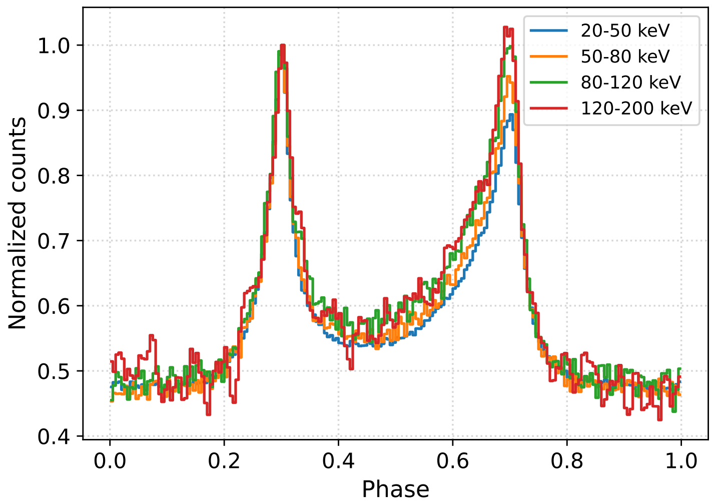

Figure 2.34: Crab pulse profiles in different energy ranges obtained from CZTI observations.

Then, we obtained spectra for different phase bins of the pulse profile. In order to get the spectral parameters of the pulse component alone, we generated the spectrum of the off-pulse region and used it as the background spectrum while fitting the spectra during the pulsed duration. Spectra were fitted with power-law models, and the resultant parameters are shown in Figure 2.35. We note that the variation of index across the pulse profile is very similar to that observed by other instruments reported by Tuo et al. (2019).

Now, we analyze the phase-resolved spectrum considering all phase bins,

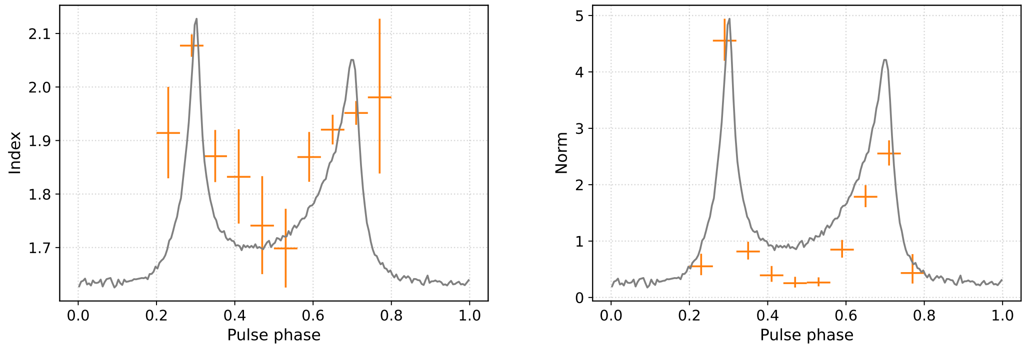

Figure 2.35: Spectral index (left) and normalization (right) of Crab pulsar obtained from CZTI spectra of the pulsed component alone in 22-200 keV.

including the off-pulse region. Spectra as different phase bins with different bin widths were obtained and fitted with power law to measure the index. The best-fit power law index is plotted as a function of phase in Figure 2.36. Different colors correspond to results from different phase bin widths, while the red color point shows the results from NuSTAR spectral analysis by Madsen et al. (2015a). It is noted that the results from broad phase bins obtained with CZTI match very well with the NuSTAR results. It is interesting to note that, with the finer phase bins, we see some slight variations in the spectral index during the off-pulse interval, which coincides with the observed swings in polarization fraction and angle.

We plan to take this preliminary investigation further by joint analysis of CZTI spectra with observations from other instruments, such as the NuSTAR, to obtain improved statistical significance of any spectral variations within the off-pulse interval. We also plan to carry out polarimetric analysis of the crab pulsar and nebula with refined techniques using all available observations so far and complement it with the spectroscopic studies to address the off-pulse variations and possible origin of the same.

2.11 Summary

CZTI has been operating in orbit for more than eight years at the time of writing. This chapter presented the improvements in various aspects of spectroscopy with

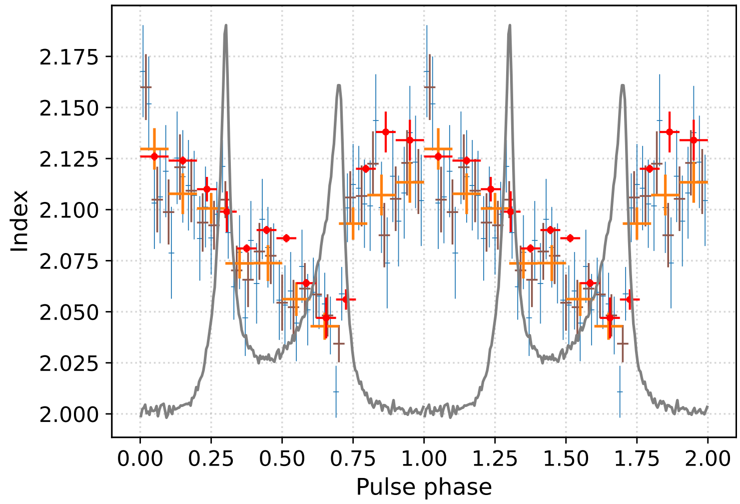

Figure 2.36: Phase-resolved spectral index obtained from CZTI spectra at different phase bin sizes. Overplotted in red are results from NuSTAR analysis taken from Madsen et al. (2015a).

CZTI, which has enhanced the usability of CZTI as a hard X-ray spectroscopic instrument in the energy range of 25 – 200 keV. With the use of in-flight calibration source observations as well as background spectra with Tantalum lines, detector pixel quality, gain, low energy threshold, and high energy threshold have been re-evaluated and included in the calibration database. These improvements established that the individual pixel responses are well understood. Further, by analyzing observations over the years, we learned the characteristics of background in CZTI in terms of short-term variability, long-term variability, and variability across the detector plane. With this improved understanding of the CZTI background, we provided a modified mask-weighting algorithm to obtain the background-subtracted source spectrum. It is shown that the background subtraction method is limited only by statistics for typical exposures with CZTI, which are of the order of 100 ks. Using a novel technique involving mask-weighted flux profiles, we measure the relative alignment of each CZTI detector with the coded mask, which removes inconsistencies in flux measurements across detectors. Finally, after incorporating these updates, we examine further departures in the effective area by using Crab observations. Empirical corrections to the effective area at energies below 30 keV and above ~100 keV are derived by calibrating against a power law model for Crab with an index of 2.1. With the updates in the effective area, we show that the analysis of Crab observations over time and across four quadrants provide consistent results, except for <10% variation in the flux levels across quadrants. We also estimate the spectroscopic sensitivity for CZTI to be a few tens of millicrab at low energies (< 100 keV), present the summary of a quick analysis of all observations with CZTI over the first seven years, and discuss prospects of the enhanced spectroscopic capability of CZTI. Specifically, we present the initial spectroscopic analysis results in the context of variations observed in hard X-ray polarization in off-pulse intervals for the Crab pulsar and nebula. Overall, the improvements in various aspects of spectral extraction techniques and calibration presented in this chapter has enhanced the capabilities of CZTI as a hard X-ray spectrometer.

Chapter 3

Soft X-ray Spectroscopy with Chandrayaan-2 XSM

3.1 Introduction

Chandrayaan-2 is the second Indian lunar mission with the objective of remote exploration of the Moon from an orbiter craft and in-situ exploration with a lander and a rover. It was launched from India's spaceport Shriharikotta on 22 July 2019 and reached lunar orbit in August of the same year. While the lander and rover could not meet their objectives in this mission (which is now accomplished by *Chandrayaan-3*), the orbiter has been operating successfully in its 100 km circular orbit around the Moon since then. The *Chandrayaan-2* orbiter carried a suite of eight scientific instruments: (i) Orbiter High Resolution Camera (OHRC; Chowdhury et al., 2019), (ii) Terrain Mapping Camera-2 (TMC-2; Chowdhury et al., 2020b), (iii) Imaging Infra-Red Spectrometer (IIRS; Chowdhury et al., 2020a), (iv) Dual Frequency Synthetic Aperture Radar (DFSAR; Putrevu et al., 2016, 2020), (v) Chandra's Atmospheric Compositional Explorer-2 (CHACE-2; Das et al., 2020), (vi) Dual Frequency Radio Science experiment (DFRS; Choudhary et al., 2020), (vii) Chandrayaan-2 Large Area Soft X-ray Spectrometer (CLASS; Radhakrishna et al., 2020), and (viii) Solar X-ray Monitor (XSM; Vadawale et al., 2014; Shanmugam et al., 2020).

The two X-ray spectrometers CLASS and XSM together carry out remote X-ray Fluorescence (XRF) spectroscopy experiment of the mission aimed at estimating elemental abundances on the lunar surface at a global scale. This involves the measurement of characteristic X-ray lines from the elements on the lunar surface emitted due to excitation by incident solar X-rays. From the line energies, elements present can be identified, and the strength of the lines indicates the abundance of elements. Quantitative estimates of abundances also require knowledge of the incident solar X-ray spectrum. As the solar X-ray flux and spectrum is highly dynamic, it is required to have a simultaneous measurement of solar soft X-ray spectrum. Thus, remote XRF spectroscopy experiments usually have one instrument that records the lunar X-ray fluorescence spectrum, while the other one records the incident solar X-ray spectrum. On the Chandrayaan-2 mission, the Chandrayaan-2 Large Area Soft X-ray Spectrometer (CLASS) measures the fluorescence spectrum from the Moon, while Solar X-ray Monitor (XSM) provides measurements of the solar X-ray spectrum in the 1–15 keV energy range with a resolution of $\sim$ 175 eV at a time cadence of one second.

Similar experiments have been flown on several past missions to various solar system objects such as the Moon (Apollo-15 and 16, Smart-1, Chandrayaan-1, Chang'e-2, Kaguya), Mercury (Messenger, BeppiColombo), and asteroids (NEAR, OSIRIS-REx). Dedicated instrument for spatially integrated solar X-ray spectral observations were part of these missions: X-ray Solar Monitors on board SMART-1 (Huovelin et al., 2002), Chandrayaan-1 (Alha et al., 2009), and Chang'e-2 (Dong et al., 2019); MESSENGER-SAX (Schlemm et al., 2007); Beppicolombo-SIXS (Huovelin et al., 2010); Solar X-ray Monitors on board NEAR-Shoemaker (Trombka et al., 2001) and OSIRIS-REx (Masterson et al., 2018). While these instruments are primarily meant to aid elemental abundance measurement of various solar system objects, observations with many of them have also been used for carrying out independent solar studies (Narendranath et al., 2014a; Dennis et al., 2015).

X-ray spectroscopic observations have contributed significantly to our present understanding of the physical parameters of the solar corona (Del Zanna & Mason, 2018). Such studies have usually used observations from solar X-ray instruments of two types: (i) X-ray imaging instruments capable of providing high spatial resolution images of the Sun over a broad energy range but without or with limited spectral information, such as Hinode XRT and (ii) crystal spectrometers that provide very high spectral resolution observations over a narrow energy band, often without spatial information (e.g., CORONAS-F RESIK). A major exception is the Reuven Ramaty High Energy Solar Spectroscopic Imager (RHESSI; Lin et al., 2002) that carried out imaging spectroscopic observations in the hard X-ray band above 6 keV. Broad-band spectral measurements with RHESSI have been used to model the X-ray spectrum over a wide range of energies to probe various aspects, including the contribution of the non-thermal processes in the corona to the X-ray emission. Of late, the NuSTAR mission (Harrison et al., 2013), which is meant primarily for observations of other astrophysical sources, have also been used for solar X-ray observations. More recently, Spectrometer/Telescope for Imaging X-rays (STIX, Krucker et al., 2020) has been added to the suite of X-ray imaging spectrometers. However, as the lower energy threshold of all these instruments is around 3 keV or higher, the capability to constrain the thermal component in the X-ray emission is limited. It may also be noted that RHESSI has completed its mission duration, and NuSTAR observations are possible only during quiet solar conditions.

Given that instruments that carry out imaging spectroscopy in broad energy ranges down to 1 keV are not available at present, instruments that provide spatially integrated measurements such as those on various planetary missions are of importance. Such measurements over a wide energy range in soft X-rays have been carried out sporadically over the past two decades by a few dedicated experiments: *Solar X-ray Spectrometer* (SOXS) on board GSAT-2 (Jain et al., 2005), *Solar Photometer in X-rays* (SphinX) on board CORONAS-Photon mission (Gburek et al., 2013), and the recent *Miniature X-ray Solar Spectrometer* (MinXSS) CubeSat missions (Moore et al., 2018a).

As there were no other dedicated solar instruments carrying out broadband X-ray spectroscopic measurements (during the initial years after Chandrayaan-2 launch), in addition to supporting the remote XRF experiment, observations with the Chandrayaan-2 XSM aptly complement the observations from wide-band X-ray imagers, narrow-band spectrometers, and hard X-ray spectrometers for investigations of the solar corona.

As discussed in Chapter 1, for utilizing any X-ray spectrometer to its full potential, rigorous analysis to validate and refine its calibration with in-flight observations is essential. In this chapter, I present the in-flight calibration of *Chandrayaan-2* XSM to establish its use as a solar X-ray spectrometer. A brief description of the instrument is given in Section 3.2 and Section 3.3 presents a summary of ground calibration of the instrument. In Section 3.4, various aspects of in-flight calibration of the XSM is presented, and Section 3.5 presents verification of the calibration's adequacy with spectroscopic analysis of XSM observations. A summary of the results is provided in Section 3.6.

Part of the in-flight calibration results of XSM presented in this chapter is published in Solar Physics *with the title 'Solar X-Ray Monitor on Board the Chandrayaan-2 Orbiter: In-Flight Performance and Science Prospects' (Mithun et al., 2020)*

3.2 *Chandrayaan-2* Solar X-ray Monitor (XSM)

The XSM is designed to carry out X-ray spectroscopy of the Sun in the soft X-ray energy range of 1 – 15 keV. It observes the Sun-as-a-star and provides disk-integrated spectra of the Sun at a time cadence of one second with a spectral resolution better than 180 eV at 5.89 keV. Specifications of the instrument are given in Table 3.1. A brief description of the instrument is given here and a detailed description can be seen in Shanmugam et al. (2020).

Figure 3.1 shows the XSM instrument, which is conceived as two packages: (i) a sensor package that accommodates the detector, front-end electronics, and a motorized filter wheel mechanism; (ii) a processing electronics package where the back-end readout electronics with FPGA-based data acquisition system, power electronics, and interfaces for data and commands with the spacecraft reside. The bottom panel of Figure 3.1 shows the Chandrayaan-2 spacecraft and the locations where the XSM instrument packages are accommodated. The sensor package is mounted on the -pitch panel of the spacecraft (see definition in Figure 3.1) such that no spacecraft structures block the instrument's field of view

Table 3.1: Specifications of the XSM.

Parameter	Specification
Energy Range	1 – 15 keV (up to ≈ M5 class)
	2 – 15 keV (above ≈ M5 class)
Energy Resolution	< 180 eV @ 5.9 keV
Time cadence	1 s
Effective area (on-axis)	0.135 mm^2 @ 1 keV
	0.367 mm^2 @ 5 keV
Field of view	±40 degree
Mass	1.35 kg
Power	6 W
Filter wheel mechanism properties	
Positions	3 (Open, Be-filter, Cal)
Filter wheel movement modes	Automated and Manual
Be-filter thickness	250 μm
Automated Be-filter movement threshold	80,000 counts s^{-1}
Calibration source	Fe-55 with Ti foil
Detector properties	
Type	Silicon Drift Detector (SDD)
Area	30 mm^2
Thickness	450 μm
Entrance Window	8 μm thick Be
Operating temperature	-35°C
Detector Readout Electronics parameters	
Pulse shaping time	1 μs
Dead time	5 μs
Number of channels in the spectrum	1024

(FOV).

A Silicon Drift Detector (SDD) is at the heart of the XSM instrument. The unique configuration of electrodes in SDD results in a low detector capacitance. Thus, they offer superior spectral resolution and count rate capabilities (see Vacchi, 2022 for more details). XSM uses Ketek VITUS H-30 SDD (30 mm^2 area and 450 μm thick) which is an encapsulated module containing the detector chip mounted on a thermo-electric cooler (TEC), a temperature diode, a FET that forms part of initial charge readout electronics, and an 8 μm thick beryllium entrance window.

When X-rays are incident on the detector, a charge cloud proportional to the energy of the photon is generated within the active volume of the detector. Electric fields within the detector cause the charge to drift towards the central anode and the charge is accumulated on a feedback capacitance. Subsequent analog readout electronics chain consisting of a reset type charge sensitive preamplifier (CSPA) and three pulse shaping amplifier stages (CR-RC-RC) converts the signal corresponding to the X-ray photon to a semi-Gaussian pulse. If this pulse has amplitude beyond the set minimum level (corresponding to a low energy threshold of $\sim$ 0.5 keV), an event is deemed to be detected. The back-end electronics identifies the peak height of the pulse and digitizes the same with a 12-bit analog-to-digital converter (ADC). A histogram of the significant 10-bit ADC value is generated on-board for each second duration. Counts in three pre-defined channel (energy) ranges are also recorded for each 100 ms. The full spectral data for one second, 100 ms light curves, and the instrument health parameters are packetized each second and sent to the spacecraft data handling system for storage. The recorded data is downloaded at designated passes over the Indian Deep Space Network (IDSN) ground stations.

As the detector's leakage current increases with its temperature and causes degradation in the spectral resolution, the SDD in XSM is maintained at a temperature of $\sim$ -35°C to achieve the required resolution of better than 180 eV. Since the ambient temperature of XSM is expected to vary over a wide range, the detector is actively cooled to -35°C using the in-built TEC. The hot end of the TEC is interfaced with a radiator plate that faces deep space to radiate the

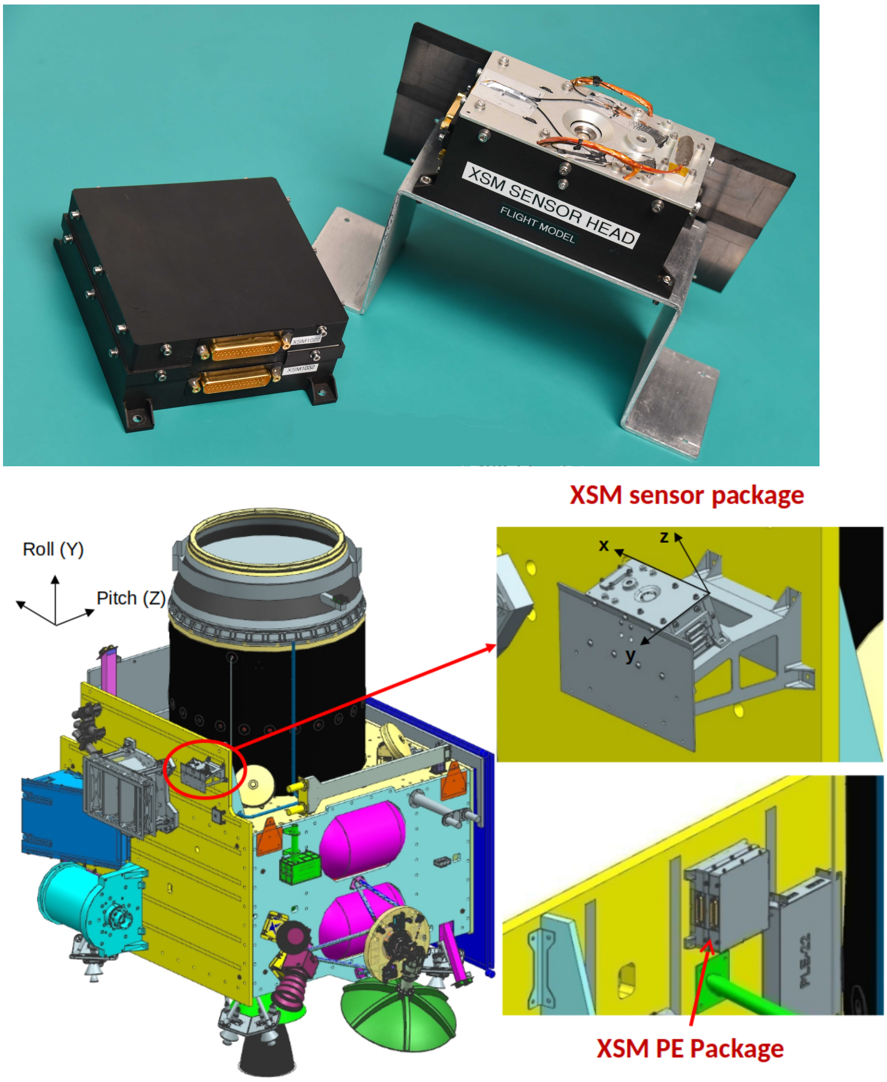

Figure 3.1: Top: A photograph of the Chandrayaan-2 XSM instrument packages: (i) sensor package that houses the detector, front-end electronics, and filter wheel mechanism (top right); (ii) processing electronics package that houses the FPGA-based data acquisition system, power electronics, and spacecraft interfaces (top left). Bottom: Schematic representation of the Chandrayaan-2 orbiter (bottom left) and the zoomed in view of the mounting location of the XSM sensor and processing electronics (PE) packages (bottom right). The spacecraft reference frame axes, Yaw(X), Roll(Y), and Pitch(Z), are marked in the figure. The sensor package is mounted on the -pitch panel of the spacecraft with a canted bracket (20° from the roll axis towards -pitch direction) to avoid any spacecraft structures obstructing its field of view. The PE package is mounted on the inner side of the -pitch panel (bottom right). Axis definitions for the XSM instrument reference frame are marked on the sensor package. The XSM reference frame is obtained by a rotation of $-110°$ about the X-axis of the spacecraft frame.

heat. The closed-loop temperature control in XSM ensures that the detector remains at this temperature as long as the ambient temperature is less than $\sim +30°$C.

Although the detector has an active area of 30 mm^2 with a 6 mm diameter, the collimator placed in front of the detector restricts the aperture to 0.684 mm diameter. An aluminium cap with a thickness of 0.5 mm coated with 50 μm thick silver on both sides with an aperture of 0.684 mm diameter placed in front of the detector acts as the collimator. The aperture has a tapered design so that the instrument has a wide field of view (FOV) of $\pm 40°$. This maximizes the duration of observation of the Sun with XSM even though it is fixed-mounted to the spacecraft causing the Sun angle to vary with time.

The aperture area of the collimator defines the geometric area of the instrument (maximum effective area) and ensures that the X-ray count rates from the Sun are within limits that can be handled for event mode readout. As the solar X-ray flux varies by more than 5 orders of magnitude (A-class activity to X-class activity; further details on solar activity are discussed in Chapter 4), it is often difficult to have a single spectroscopic detector having the dynamic range to cater to this. Thus, XSM employs a filter wheel mechanism with a 250 μm thick beryllium (Be) attenuator. When the count rate exceeds the set limit of 80,000 counts/s (adjustable through ground commands), the on-board logic triggers and brings the Be attenuator in front of the detector. This suppresses the X-rays below 2 keV from reaching the detector, reducing the count rates to within limits. When the count rate goes below a set threshold, the onboard logic decides the movement of the filter wheel mechanism back to the open position.

The filter wheel of the XSM also includes a 100μCi activity Fe-55 radioactive source covered with 3μm titanium foil. The Fe-55 source emits two mono-energetic X-ray lines at 5.89 keV and 6.49 keV and the fluorescence from the Ti foil provides two additional lines at 4.50 keV and 4.93 keV. The X-ray spectrum of this source is used to track the gain and spectral resolution of the instrument during in-flight operations. The XSM is continuously operating and is powered off only for orbital maneuvers and other mission-critical activities, about once in a month or two. During each power off of the instrument, calibration source spectra are acquired, which are used for tracking the instrument performance.

As the instruments of Chandrayaan-2 that are observing the Moon are mounted in the +yaw direction, nominally, the attitude of the spacecraft is maintained such that the +yaw direction always points toward the Moon. While the spacecraft attitude is not fixed in the inertial reference frame, the orbital plane is fixed, and thus, the angles between the orbital plane and the Sun vector changes over the year, as shown in Figure 3.2. This results in two observing seasons for Chandrayaan-2 and XSM: Dawn-Dusk (D-D) and Noon-Midnight (N-M). During the D-D season surrounding the day when the orbital plane is perpendicular to the Moon-Sun Vector, the spacecraft attitude is maintained such that the Sun is in the yaw-roll plane to optimize power generation. In this period, the Sun is within XSM FOV for a considerable duration; thus, almost continuous observations of the Sun are available. In the N-M season, the attitude follows the orbital reference frame around the day when the orbital plane is parallel to the Sun vector. During this time, the Sun remains completely out of the XSM FOV for a few days, and only short periods of solar observations are possible during other days. Figure 3.2 bottom panel shows the nominal fraction of each day when solar observations with XSM over the year. As noted before, in D-D seasons, there is good visibility of the Sun, and there are periods where continuous observations are possible. However, during the N-M season, XSM observations are rather sparse. Nominally, XSM is operated continuously, and data is being acquired. While carrying out the analysis, one needs to select times when the XSM was observing the Sun.

3.3 A Summary of Ground Calibration

As discussed in Chapter 1, to infer the parameters of incident photon spectrum from the spectrum obtained with an X-ray spectrometer like XSM, various aspects of instrument response needs to be accurately modeled. These include spectral redistribution matrix, the gain parameters, effective area, dead time and pile-up effects (Section 1.3).

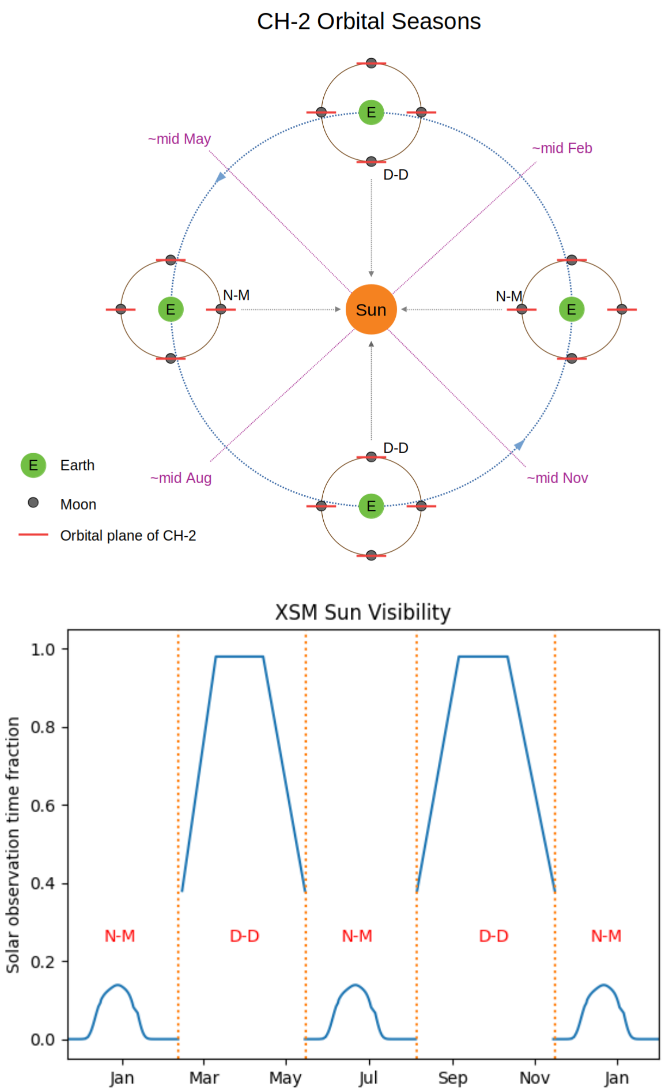

Figure 3.2: Top: Orbital geometry of Chandrayaan-2 spacecraft resulting in different seasons, Dawn-Dusk (D-D) and Noon-Midnight (N-M). Bottom: Approximate visibility fraction of the Sun with XSM with time showing distinct patterns for D-D and N-M seasons.

XSM records the number of counts in ADC or Pulse Height Analysis (PHA) channels. Conversion of this to nominal energies of photons requires gain parameters of the instrument, which may vary with observing conditions such as the temperature. The relation between the observed gain corrected energy spectrum and the incident photon spectrum is modeled as a matrix that considers the spectral redistribution effects and the effective area. The XSM effective area varies with time as the Sun angle changes, and this also needs to be considered in generating the response matrix. Further, as the count rates are expected to be higher for large solar flares, it is also required to validate the instrument performance for such conditions and understand the dead time and pile-up effects that would come into the picture. Specifically designed experiments were carried out on the ground to understand and model all these aspects of Chandrayaan-2 XSM. The results from this ground calibration form the initial calibration database and are used initially for analysis of in-flight observations. Mithun et al. (2021b) reported ground calibration results of XSM, and here I present a brief summary.

Gain: Channel to Energy conversion

The gain and spectral performance are first assessed using the Fe-55 calibration source that is part of the instrument. As this covers only a small range of energies compared to the entire XSM energy range, experiments were carried out at the Indus-2 synchrotron facility at Raja Ramanna Center for Advanced Technology (RRCAT) by shining the XSM instrument with mono-energetic X-rays having energies ranging from 1 keV to 15 keV. With this, it was established that the channel-to-gain relation remains linear throughout the energy range of XSM. The temperature dependence of gain parameters was obtained by acquiring the Fe-55 source spectrum over the entire range of expected temperatures in a thermo-vacuum facility. Further, the position of the interaction of X-rays in the detector was also identified as another factor that shifts the gain slightly. While this effect was very little, experiments were carried out by illuminating the detector at different distances from the center, and the variation of gain parameter with radial distance was also modeled. Thus, finally, for each one-second spectrum from XSM, the gain parameters for channel-to-energy conversion could be obtained for the given instrument temperature and Sun angle, which in turn determines the interaction position on the detector.

Spectral Redistribution

Photons of a given incident energy are generally recorded over a range of channels of any X-ray spectrometer (Section 1.3.1). In order to characterize the spectral redistribution of the XSM detector, spectra of mono-energetic beams of different energies were acquired with XSM at the Indus-2 facility of RRCAT. The obtained spectra were modeled with a physically motivated empirical model consisting of four components corresponding to the primary photo-peak, escape peak, an exponential tail due to incomplete charge collection, and a shelf component due to photo-electron escape from the active volume. Parameters of the model were obtained as a function of energy. Using this model, one can generate the redistribution matrix of XSM, which has the probability of a mono-energetic photon to be detected in each channel of the instrument.

Angular Response and Effective Area

The effective area of the XSM consists of various components: Geometric area determined by the collimator aperture, collimator angular response, detector beryllium window transmission, and detector efficiency. While the first two were obtained from measurements and experiments, the latter two had to be computed based on the details provided by the manufacturer of the detector. The geometric area of the aperture was determined using a projection facility. To obtain the angular response of the collimator, the XSM instrument was illuminated with continuum parallel X-ray beams from a temporary beam line at different angles. Using the experimental data and computed efficiencies, the effective area of XSM can be obtained as a function of incident angle.

Performance at high count rate, dead time, and pileup

Since the incident count rate of solar X-rays is expected to vary over a wide range, the stability of the performance of the spectrometer at high count rate needs to be examined. From experiments, it was found that the peak channel, as well as the spectral resolution of the instrument, remains stable up to an incident count rate of 10^5 counts/s. Dead time and pile-up must also be accounted for at high count rates. XSM implements a fixed dead time of 5 μs, and the expected relation between detected rates and trigger rates was validated against observations. A dead time correction methodology was also formulated using the trigger rate information. Pileup effects were also examined and were shown to be matching with the model expectations.

3.4 In-flight Performance and Calibration

After the launch of the *Chandrayaan-2*, the XSM was first powered on for a short duration in earth-bound orbit to verify its performance. Further short operations were performed after reaching the lunar orbit to investigate any effect on performance due to passage through the radiation belt. XSM began regular observations on 12 September 2019, with the instrument acquiring data continuously except for short periods of power-off.

In order to assess the validity of the calibration database obtained from ground calibration, various analyses were carried out with the in-flight observations of XSM. I use the XSM calibration source observations, solar observations, and background observations to assess the performance and sensitivity of the instrument. Further, various calibration aspects are refined using the in-flight observations to establish X-ray spectroscopy with XSM. In this section, I present these analyses of in-flight observations resulting in the updated calibration of XSM.

3.4.1 Energy Resolution and Gain

We use the on-board Fe-55 calibration source for monitoring the energy resolution and gain of the XSM instrument. Spectra of the calibration source were acquired a few times during the initial commissioning phase. Since then, calibration source spectra have been acquired each time before powering off XSM for activities such as orbital maneuvers, providing us with regular calibration data. The raw calibration source spectra were converted to pulse invariant (PI) channel spectra using the gain parameters obtained from ground calibration corresponding to the observing conditions. Figure 3.3 shows one of the calibration source spectra acquired by XSM at four instances. Spectral lines in the PI spectra were fitted with Gaussians to obtain the peak energy value and the resolution defined as the full width at half maximum (FWHM) of the line at 5.89 keV. The spectral resolution was measured to be ∼175 eV, which is the same as that observed on ground.

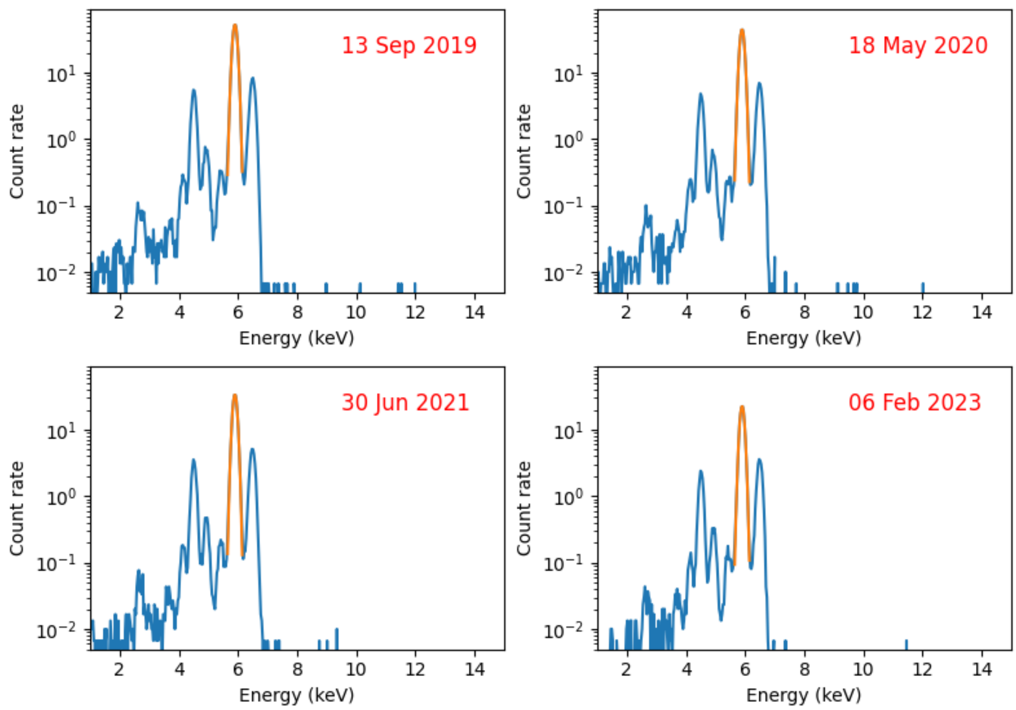

Figure 3.3: Calibration source Fe-55 spectra of XSM acquired at different dates. The line at 5.89 keV is fitted with a Gaussian (shown in orange) to obtain the peak energy and FWHM of the line.

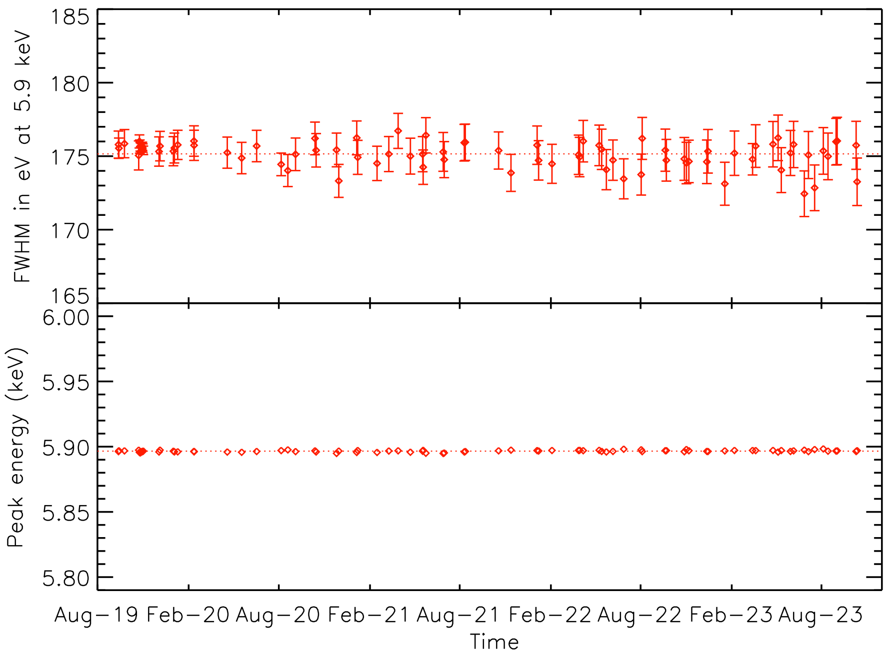

Figure 3.4: The energy resolution (FWHM) and estimated peak energy for the 5.9 keV line from the onboard calibration source for four years of in-flight operation of the XSM. The dotted lines show the mean values.

After about nine months of operations, the low energy threshold setting of the instrument was updated by ground commands. On analyzing the calibration source spectra after this modification in the instrument setting, it was observed that the line energies are slightly shifted. Based on the observed peak channels of calibration spectra in the new instrument setting, updates to gain parameters were computed and incorporated into the calibration database for observation since June 2020. For observations before this, no changes were made in the gain parameters. Figure 3.4 shows the energy resolution and peak channel energy for all calibration observations during the four years of XSM in-flight operations from September 2019 to September 2023. It can be seen the spectral resolution does not show any variation with time. The peak energy has also remained stable, showing that there has been no variation in the gain and no degradation has happened to the instrument's spectral performance over the four years.

Figure 3.5 shows the relative intensity of the 5.89 keV line obtained

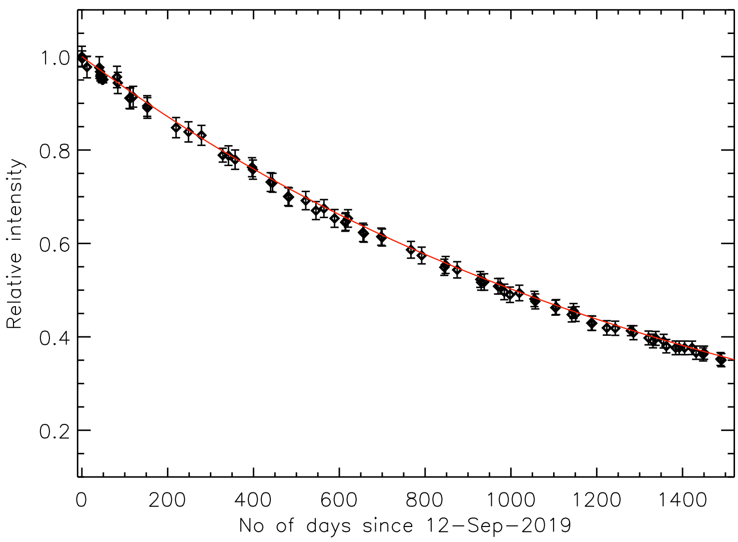

Figure 3.5: Relative intensity of the 5.89 keV line from the Fe-55 source is shown with the data points. The red line shows the expected trend of count rates computed from radioactive decay.

from the Gaussian fits as a function of time since the first in-flight operation. Overplotted in red is the trend expected from the radioactive decay of Fe-55 source, matching very well with the observed trend in count rates. This shows that the detector efficiency has not changed with time. It may be noted that the increase in errors on the FWHM shown in Figure 3.4 is due to the reduction in the count rates and the calibration observations are invariably done for a duration of five minutes.

3.4.2 Collimator Response and Effective Area

The effective area of the XSM is critically dependent on the collimator angular response and parameters such as the thickness of the window and detector thickness. As noted earlier, the angular response of the collimator was experimentally determined on the ground, whereas manufacturer-provided values were used for the parameters of the detector module (Mithun et al., 2021b). Here, the adequacy of the ground calibration estimate of the effective area as a function of observation angle is examined using in-flight observations.

Field of view

Using ground calibration observations, the field of view of the instrument has been estimated, and this shall be validated using in-flight observations. Count rates recorded by XSM are significantly higher than the background rate of $\approx$ 0.15 counts s^{-1} when the Sun is at least partially within its FOV. Thus, to identify the null points of XSM (the edge of the FOV), XSM count rate can be used.

All observations made during September 2019 to March 2020 were used for this purpose. We generated light curves for the entire period with a time bin size of 10 seconds. Durations when the Moon occults the Sun were ignored for this analysis. For each 10-second time bin, we computed the average polar(θ) and azimuthal (ϕ) Sun angles in the XSM instrument reference frame. Figure 3.6 shows the polar plot of the position of the Sun during each time bin. In the plot, the radial axis represents θ and the azimuthal axis represents ϕ. All time bins when the count rates are 5σ higher than the background rate are shown in blue, whereas the others are shown in black. The region of transition from blue points to black points represents the edge of the FOV of XSM. The loci of null points (edge of FOV) obtained from ground calibration are shown as a solid orange circle in the figure. It may be noted that all blue points are within the orange circle while the black ones are outside, showing that the in-flight observations are consistent with the FOV measured on the ground, which was symmetric. Further, it demonstrates that there are no unaccounted offsets between spacecraft and XSM instrument reference frames, as that would have resulted in an offset between the estimated FOV and ground calibration.

In Figure 3.6, it may also be noted that all observations have ϕ within a range of $-180°$ to $0°$(quadrants 3 and 4) and mostly have $\theta > 20°$. This arises from the specific attitude configuration of the spacecraft in different observing seasons and the mounting angles of XSM with respect to the spacecraft (Section 3.2). The asymmetry between points in quadrants 3 and 4 is caused as the intervals of occultation of the Sun, which happens only in quadrant 4 (as shown in Figure 3.6 where $\phi > -90°$), are not included in this figure.

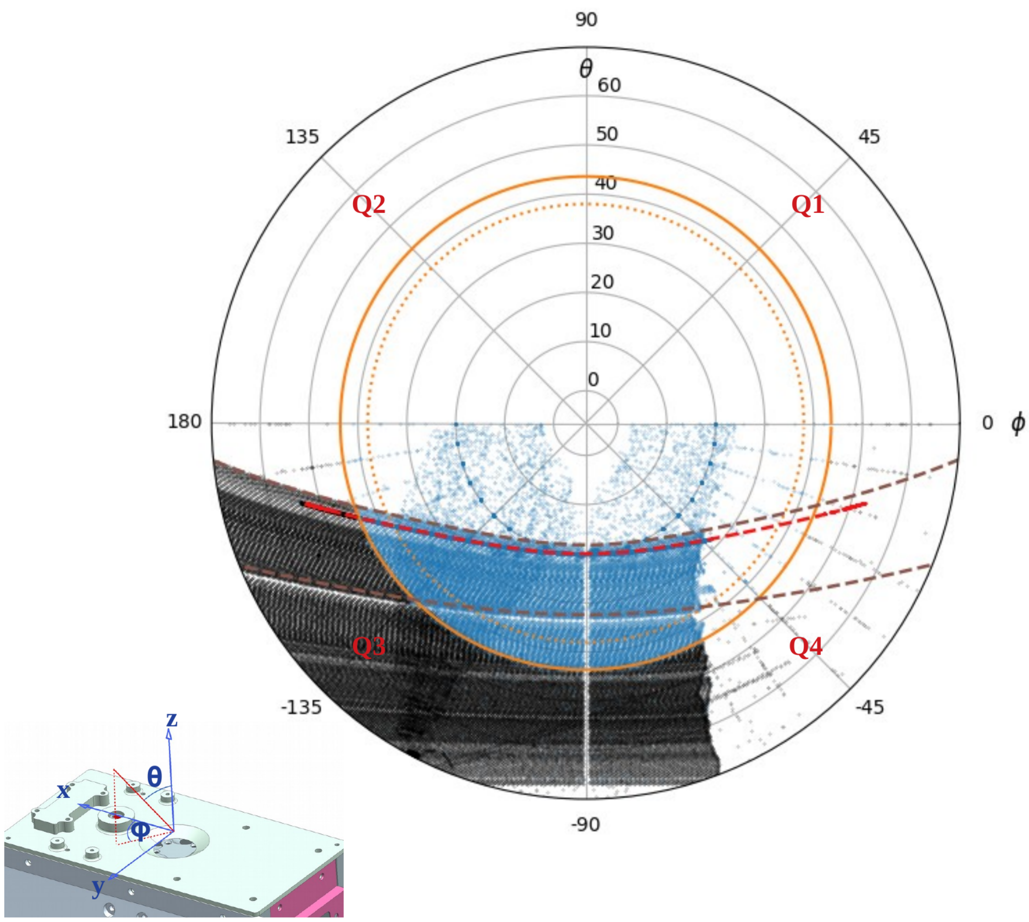

Figure 3.6: Position of the Sun with respect to XSM reference frame for 10s time bins are shown in this polar plot where the color of the points represents the count rate observed by XSM. Blue points denote time bins when the count rate is 5σ higher than the background rate, and other points consistent with the background are shown in black. At the center of the polar plot, polar angle θ is zero and corresponds to XSM boresight. The radial axis represents θ values up to 70° whereas the azimuthal angle (ϕ) is defined in the range from $-180°$ to $+180°$. The solid orange circle represents the null points of the XSM FOV as obtained from ground calibration, and the in-flight observations are found to be consistent with the same. The full FOV of XSM is shown as an orange dotted circle. The dashed lines correspond to the track of the Sun in XSM FOV at different times; see text for details. The Schematic at the bottom left corner shows the definition of the XSM reference frame.

During D-D seasons, the Sun follows a single track in XSM FOV shown by the red dashed line in Figure 3.6 while the spacecraft is in the nominal attitude configuration. Exceptions to this are during observations with the DFSAR instrument when the spacecraft is rotated, and these result in the sparse points seen in the figure with $\theta < 20°$. During the N-M seasons, the Sun follows tracks parallel to that in the D-D season while within the FOV of XSM. In Figure 3.6, the brown dashed lines show parts of the track made by the Sun during two representative days in the N-M season. As the observing geometry is different during the D-D and N-M seasons, the effective area needs to be validated for each of these cases.

Effective area calibration: Dawn-dusk observations

X-ray spectrometers generally rely on observations of the standard candle source Crab nebula and pulsar for in-flight validation and calibration of effective area (Section 1.5.3). However, given the small aperture area of XSM and wide FOV, the count rates from Crab for XSM are less than the background count rates. Thus, we have to make use of solar observations for this purpose. We use quiescent Sun observations when the inherent variability of solar X-ray intensity is minimal. Although the absolute effective area calibration is not feasible with this, as the XSM Sun angle varies within each orbit during nominal observations, it is possible to characterize the relative effective area as a function of angle.

The raw light curves obtained with XSM are expected to show variations even when the incident solar flux is constant due to the changes in the solar angle. However, after incorporating the corrections in the effective area with the angle obtained from ground calibration, it is expected that these modulations will disappear. The gray line in the top panel of Figure 3.7 shows raw light curves for the observation on 17 September 2019 during quiet solar conditions with minimal X-ray variability. Polar (θ) and azimuthal (ϕ) Sun angles during the observation are shown in the lower two panels of the figure. The raw light curve shows modulations with the Sun angle. Light curve corrected for the effective area as obtained from ground calibration is shown in blue in the figure, which still shows some modulation during periods when $\phi < -90°$.

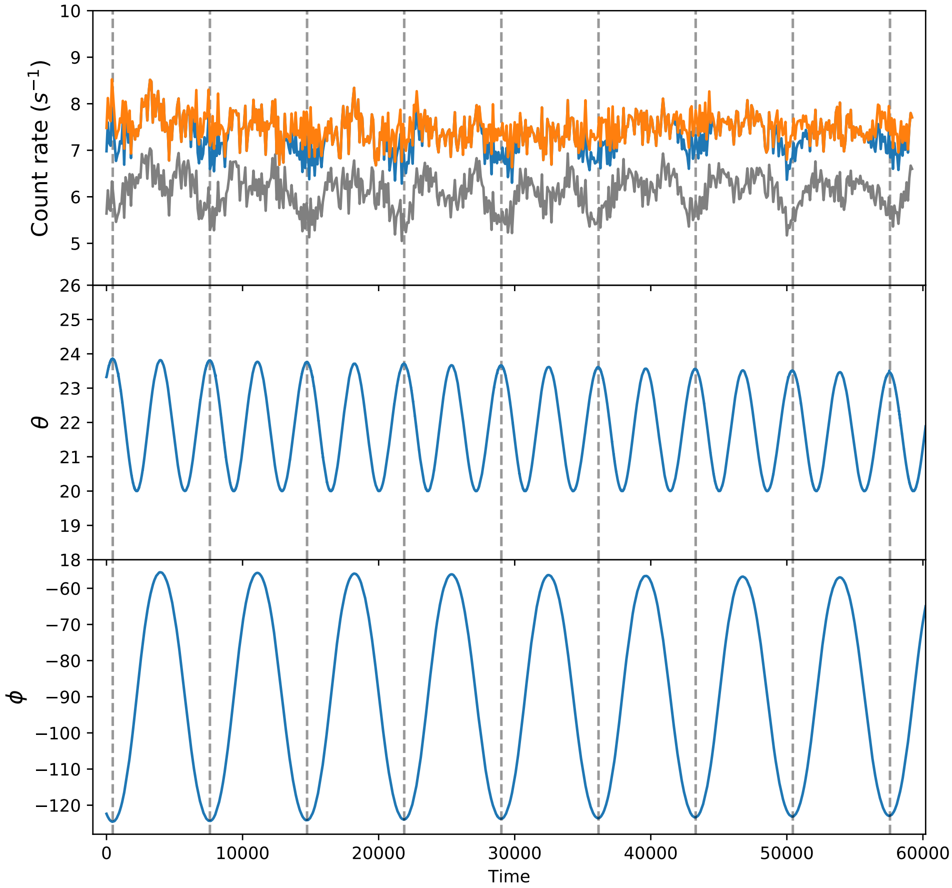

Figure 3.7: Light curves obtained with the XSM on 17 September 2019 when the Sun was quiet without much inherent variability in the X-ray flux are shown in the top panel. The raw light curve (gray), the light curve corrected with ground calibration effective area (blue), and that was corrected with the updated effective area (orange) is shown. Note that the mean value of the effective area corrected light curves is higher than the raw light curve as they are scaled to provide count rates corresponding to on-axis observations with the XSM. The polar(θ) and azimuthal(ϕ) Sun angles are shown in the middle and bottom panels. The raw light curve shows significant modulation during the minima of the azimuthal angles marked by the vertical dashed lines in the figure, which has not been corrected by the effective area from ground calibration. With refined effective area correction, the modulations in the light curve have been removed to within 1% (see text for details).

Various hypotheses were considered for the observed residual variations in the effective area. One possibility we looked at was any change in background count rates, possibly due to emission from other astrophysical sources entering the field of view of the instrument. However, based on the analysis of background observations as presented in Section 3.4.4, it was confirmed that the variability in background is an order of magnitude lower and uncorrelated with the variation observed here. Another possibility considered was the asymmetry in the mounting of the XSM instrument with respect to the spacecraft. This was ruled out based on the analysis presented earlier in the FOV section. Thus, we conclude that the uncorrected modulation in the light curve observed over half of the orbital phase shows that the effective area has an azimuthal angle dependence. As the collimator response measured on the ground did not show any such azimuthal variation, it possibly arose from the efficiency factors that assumed uniform thickness of the detector beryllium window and dead layer. This suggests that the effective area obtained from ground calibration needs further refinement. As discussed earlier, the angle variations in D-D and N-M seasons have distinct profiles and thus, this analysis is carried out first for the D-D season.

We considered all available observations in D-D seasons up to March 2020 and identified periods when there was minimal variability in the solar X-ray flux. The light curves were manually examined, and the duration when any transient events, such as small flares or any other kind of variability within the time scales of one day were ignored, and observations over 42 days were finally considered for the analysis. For all these observations in the D-D season, the Sun follows the same track in XSM FOV as shown by the red dashed line in Figure 3.6.

For observations of each day, we obtained effective area corrected light curves in the 1–15 keV energy with a time bin size of 10 s. The mean polar (θ) and azimuthal (ϕ) Sun angles were also computed for each time bin. We estimated the mean count rates from the light curves as a function of θ for two azimuthal angle ranges where an asymmetry is observed. Count rates as a function of polar angle were obtained for $\phi < -90°$ (in quadrant 3 of the XSM reference frame, hereafter Q3) and $\phi > -90°$ (in quadrant 4 of the XSM reference frame, hereafter

Q4) separately. The count rates were scaled to the value at $\theta = 20°$ for each day to remove any effect of variations between incident flux between days. The top panel of Figure 3.8 shows normalized count rates as a function of θ for Q3 (blue stars) and Q4 (blue open squares). It can be noted from the figure that the normalized count rate corrected with the effective area from ground calibration remains constant in the case of Q4. However, for Q3, there is a clear reduction with increasing angle. Thus, it is concluded that the angular dependence of effective area from ground calibration is correct in the case Q4, whereas, for Q3, it needs to be steeper than the original estimate.

This additional reduction in effective area for observation in Q3 could either be due to differences in collimator response, which is independent of energy or due to efficiency which would be energy-dependent. We used light curves in two energy ranges, 1.0–1.2 keV and 1.2–1.5 keV, to probe the energy dependence of the variation in count rate with angle. From these daily light curves, the ratio of count rates in lower energy and higher energy bands were computed for each θ bin. As earlier, the values are normalized to those at $\theta = 20°$ and averaged and shown in the middle panel of Figure 3.8. It can be seen that this count rate ratio does not remain constant with the angle for observations in Q3. This suggests that the difference in the effective area from that estimated from ground calibration depends on energy. As the ratio decreases with an increase in angle, the XSM effective area in Q3 seem to require an additional angle-dependent absorption factor.

We used the spectral data to quantify this apparent additional absorption factor in the effective area. Spectra were generated for each one-degree bin of θ for observations in both quadrants of the quiet period of solar observations selected earlier. The ratio of the solar spectrum for each θ bin when the Sun is in Q3 to that when the Sun is in Q4 were computed for all days of observations. The average ratio obtained from these day-wise spectral ratios is computed, and a few are shown in the lower panel of Figure 3.8. It may be noted that this exercise could be done up to θ of 28° as the observations in Q4 are limited to that angle (beyond θ=28°, the Sun is occulted by the Moon). The figure shows that observations in Q3 record fewer counts at lower energies compared to the

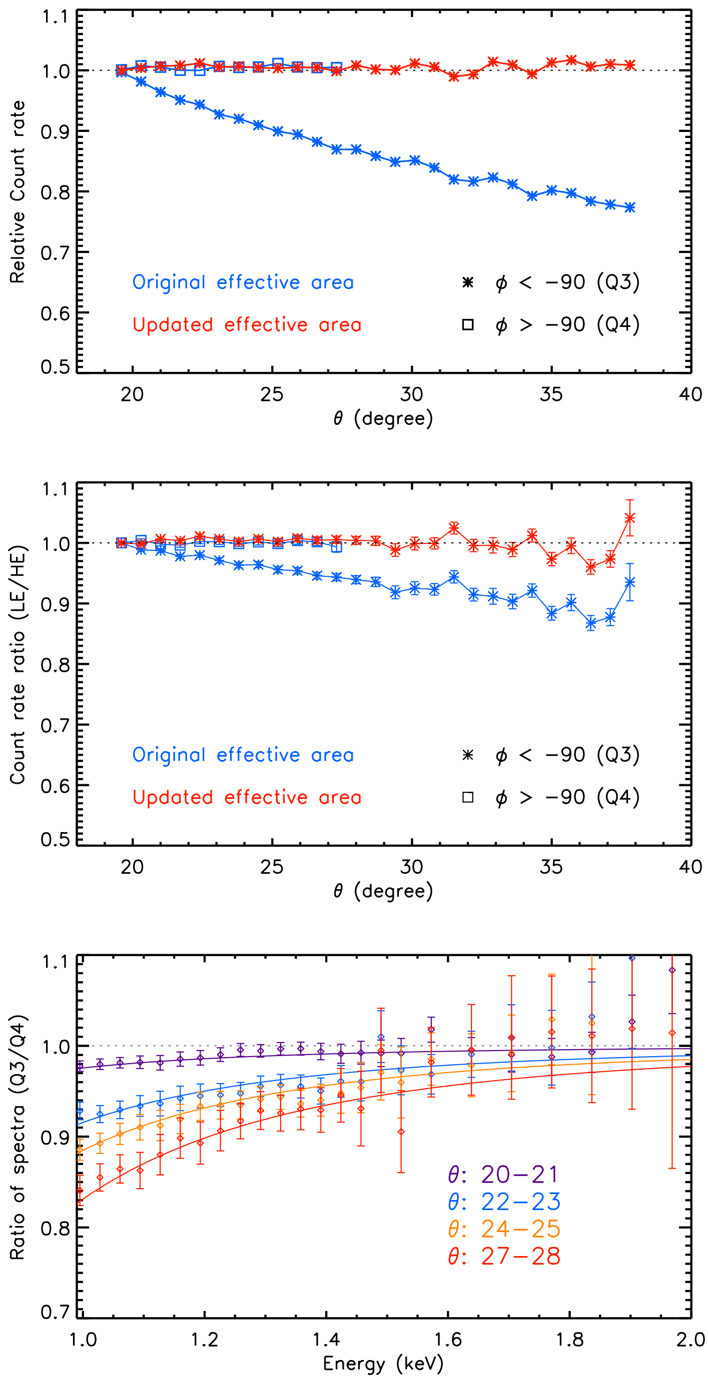

Figure 3.8: Top panel: Mean XSM count rates during quiet Sun observations normalized to that at $\theta = 20°$ as a function of polar angle (θ) for Q3 (star) and Q4 (open square). Middle panel: Normalized ratio of count rates in the energy ranges 1–1.2 keV (Low energy or LE) to 1.2–1.5 keV (High energy or HE) as a function of θ. Bottom panel: Ratio of spectra for observations in Q3 to that in Q4 for different bins of θ. Solid lines show the additional absorption required for observations in Q3 to explain the observed deviation of spectral ratio from unity at lower energies.

observations in Q4. It can also be seen that this deviation increases with angle, confirming the presence of additional absorption in this quadrant, which increases with angle.

While it is difficult to conclude on the origin of this additional absorption factor in only one region of the FOV, the most probable scenario is variation in the entrance window thickness across the detector. Thus, we model this additional absorption factor for Q3 empirically from the observed spectral ratios by considering absorption by the additional thickness of beryllium. The best-fitted models of additional beryllium absorption are shown by the solid lines overplotted on the measured spectral ratios in the lower panel of Figure 3.8. These correspond to absorption by extra thickness of beryllium ranging from $\approx 0.2\mu$m to $\approx 1.6\mu$m for different angles. The figure shows that the derived effective area correction factors match the observed spectral ratios very well. Although the spectral ratios are available only up to 28°, the correction terms for higher angles were obtained by extrapolating the model.

These additional effective area terms are incorporated into the calibration database and we generated the light curves taking into account the updated effective area. Effective area corrected count rates and count ratio in two energy bands are again computed as a function of θ and are shown in red in the top and middle panels of Figure 3.8. We note that the count rates and ratio now remain constant with the angle, showing the efficacy of the corrections incorporated. Further, the light curve for 17 September 2019 generated with the updated effective area is shown in Figure 3.7 top panel. It can be seen that the residual modulations that were present in the light curve disappeared, confirming that the updated effective area is indeed correct.

Aside from the beryllium window thickness, another possibility that we could have considered as the reason for the change in the effective area at lower energies is the thickness of the silicon dead layer in front of the active volume of the detector chip. Any changes in dead layer thickness would have the most effect at energies just below the Si K edge around 1.84 keV. However, from Figure 3.8 (lower panel), it can be seen that the spectral ratios do not show any significant deviation from unity at these energies. Based on this, the variation of dead layer thickness across the detector was ruled out, and thus, the change in beryllium window thickness was deemed the most probable reason. Although the relative variations in dead layer thickness are ruled out, there is a possibility that the absolute values of the thickness provided by the manufacturer of the detector (100 μm Si and 80 μm SiO_2) maybe slightly uncertain. Any uncertainty in the effective area near the Si K-edge could possibly result in uncertainties of measurements of abundances of Si from the solar X-ray spectrum having Si line complex near the same energy. To estimate this effect, we simulated spectra assuming different dead layer thicknesses ranging from zero to double the quoted value. While fitting these spectra to obtain the incident spectral parameters, including the abundance of Si, we used the response matrix that considers the dead layer thicknesses as provided by the manufacturer. It was found that the measured Si abundances are within $\pm 0.5\%$ of the actual value, even with this assumption of an extreme range of dead layer thicknesses. These uncertainties are well within the statistical uncertainties and thus can be ignored. Any other line complexes and continuum solar spectrum will be less affected than the Si line complex, and hence, we conclude that uncertainties in dead layer thickness have no significant impact on spectroscopic analysis with XSM.

We used the area corrected count rates in different angle bins shown in Figure 3.8 top panel to estimate the overall uncertainties in the angle-dependent effective area. We find that the standard deviation of the count rates is $\approx 0.8\%$, and hence, we quote a conservative limit of 1% uncertainty in the relative effective area with angle.

Effective area calibration: Noon-midnight observations

The analysis presented in the previous section was for the observing geometry corresponding to D-D seasons, where the Sun moves along a single track in the FOV. However, during N-M seasons, the Sun moves along different tracks across the XSM FOV, as discussed earlier. Although the additional beryllium window thickness obtained for one range of θ and ϕ corresponding to D-D season observations would serve as a starting point; it is not necessary that the same applies to other ranges as the X-rays would pass through other parts of the beryllium window where the thicknesses may be different.

Thus, we carry out a similar analysis for N-M seasons, but this time considering the count rates, ratios, and spectra for each θ and ϕ bin in Q3 and Q4, where XSM observations are made. This can be mapped to different locations on the XSM detector where the X-rays are incident for ease of representation. The analysis showed that in Q3, other parts also require an additional absorption factor in terms of extra thickness in the beryllium window. However, the additional window thickness also shows variation across the entire quadrant, not just along the polar angle direction. With the updated effective area, modulations in the light curve disappear, like the case for D-D season observations.

Low energy effective area

After incorporating the corrections for the effective area as described in the previous section, the analysis of solar spectra has shown that there is some uncertainty in the effective area in the lower energies up to 1.30 keV. It is seen that predicted counts from the best-fit model that describes the higher energy spectrum are higher than the actual observed counts. One possibility that was considered to be responsible was the low energy threshold setting.

The threshold pulse height setting in the readout electronics determines the low energy threshold below which XSM does not detect X-rays. Initially, the low energy threshold was set to the default value that corresponds to $\sim$ 900 eV. The observed spectrum is not expected to have a sharp cutoff at this energy. Instead, the detection probability starts to increase from zero for energies less than 900 eV and then increases to unity at higher energies. This detection probability can generally be described with an error function (e.g., Prigozhin et al., 2016). Considering this possibility, later on, the low energy threshold setting for the XSM was reduced further. However, on analysis of the data after this change, a lower effective area than expected is observed at energies below 1.3 keV. As there are uncertainties in the effective area of XSM at energies less than 1.3 keV, it is recommended that this part of the spectrum is ignored in spectral analysis.

Any corrections to the effective area in the 1 – 1.3 keV energy range would require independent simultaneous measurement of solar X-ray spectrum from a well-calibrated X-ray spectrometer. Dual-Zone Aperture X-ray Solar Spectrometer (DAXSS; Schwab et al., 2020; Woods et al., 2023) instruments flown on recent rocket flights and on the Inspiresat-1 satellite provide this opportunity. In the future, it is planned to use observations with DAXSS and XSM to derive effective area corrections for the 1–1.3 keV energy range to make that part of the spectrum also useful in spectral analysis.

3.4.3 Deadtime Correction

Based on the validation of the dead time model using ground calibration experiments, a method was devised to correct the dead time effects in the observed spectrum (Mithun et al., 2021b). This is done by modifying the exposure time (T_{exp}) of the observed spectrum by:

$$T_{\mathrm{live}} = T_{\mathrm{exp}} * \frac{n_{\mathrm{d}}}{n_{\mathrm{t}}} * (1 \; - \; n_{\mathrm{t}} \; \tau_1) \tag{3.1}$$

where n_{t} and n_{d} are the trigger and detected rates, respectively and τ_1 is the deadtime corresponding to pulse shaping time of 0.96 µs. It can be noted that, for low count rates, the correction term is negligible, whereas at higher rates, this becomes important.

However, on analysis of in-flight observations with XSM, it was observed that the trigger rates were typically 20-50 counts higher than the detected count rate, even when the average count rate was as low as 0.15 counts/s during background observations (excluding ULD events of $\sim$ 1 counts/s). Figure 3.9 shows the detected counts in each second for one day of background observations and the trigger rates for the same duration. The lower panel shows the difference between the two, which should have been ideally close to zero but instead shows a difference of about 20-50 counts.

In Figure 3.10, detected event rates are plotted against event trigger rates from the data acquired by XSM in four years. The blue points show the detected and trigger counts each second when at least one ULD (Upper-Level Discriminator) event is recorded. ULD events deposit energy greater than the

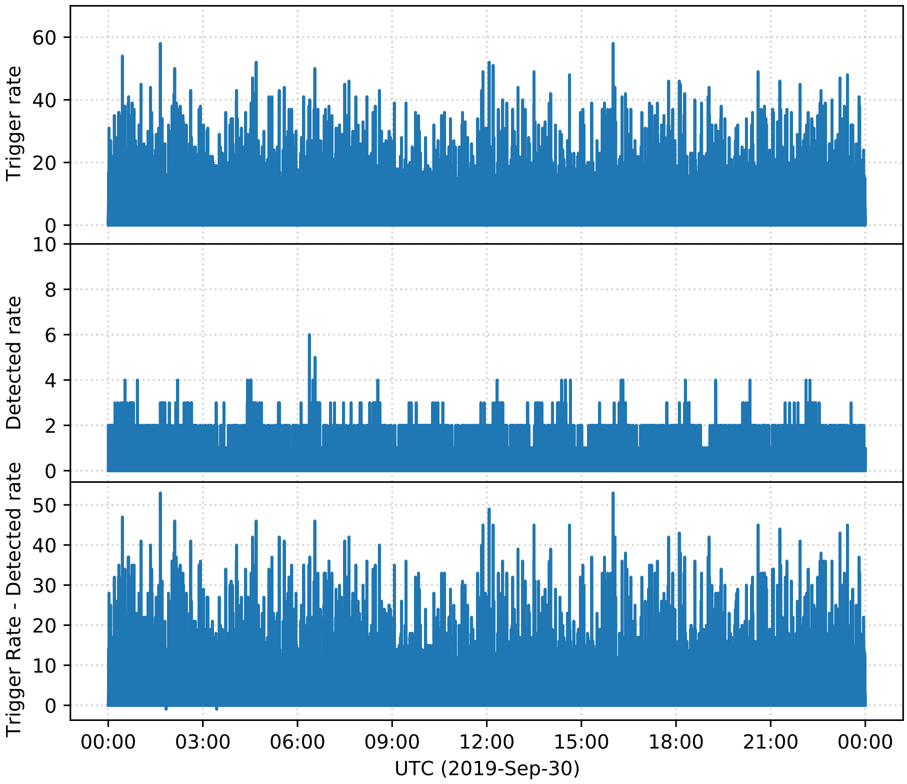

Figure 3.9: Trigger rates and detected rates excluding ULD events for a background observation are shown in the top two panels. Differences between trigger and detected rates are shown in the last panel.

high energy threshold of the XSM and are recorded in the last channel of the instrument. Orange points in the figure show the detected and trigger rates when no ULD events are recorded. The relation between trigger rates and detected rates, as expected from the dead time model obtained from ground calibration, is overplotted with a dark green dashed line. The figure shows that the trigger rates show expected behavior when no ULD events are recorded in the corresponding second. However, when ULD events are present, in many cases, additional spurious events are recorded as event triggers. Based on this, we infer that these additional trigger events are possibly the result of ringing effect of the pulse after a particle-induced event, which usually gets recorded as a ULD event.

In any case, as there are spurious events present in the trigger count, it would not be possible to use trigger rates to correct for dead time effects using Equation 3.3. While the excess in trigger counts is generally less significant

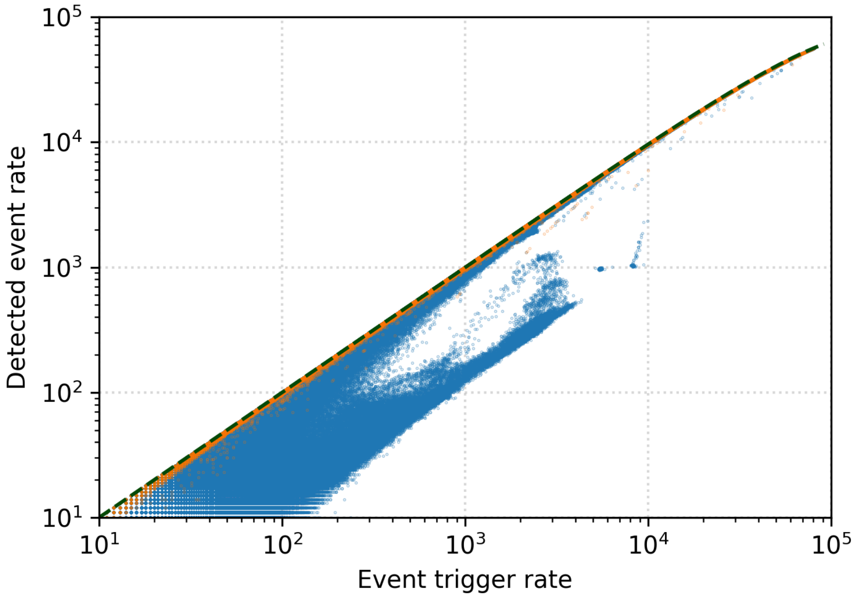

Figure 3.10: Detected event rate and trigger rate for one-second duration when at least one ULD event is recorded are shown by the blue points, whereas the same when no ULD event is recorded are shown by orange points. The dark green dashed line shows the model prediction.

at high count rates ($> 10^4$counts/s), as seen from Figure 3.10, they are very significant at low count rates. If we were to apply the corrections using trigger rates, it would result in incorrect updates to exposure times at low count rates. Instead, it is required to derive the correction term only based on the detected rate ignoring the trigger rate.

The relation between detected rate (n_d) and actual incident rate (n_a) is:

$$n_\mathrm{d} = n_\mathrm{a} \exp(-n_\mathrm{a}\tau_2) \tag{3.2}$$

where τ_2 is the paralyzable dead time of 5 µs implemented in XSM, which is also used in getting the model relation shown in Figure 3.10. However, this cannot be inverted to compute the actual incident rate from the detected rate. Instead, we generate a lookup table between n_d and n_a based on this relation and use that to get the incident rate corresponding to the detected rate. The only drawback is that this will not result in unique solutions if count rates are higher than 2×10^5

counts/s. But this will only be happen for very strong X-class flares such as X5-class flares, and thus is expected to be very rare. From the estimated incident rate based on the lookup table and the detected rate, the exposure times are modified as:

$$T_{\mathrm{live}} = T_{\mathrm{exp}} * \frac{n_{\mathrm{d}}}{n_{\mathrm{a}}} \tag{3.3}$$

where the symbols have the same meaning as earlier. Dead time corrections following this method is now implemented in the analysis of XSM observations.

3.4.4 Background and Sensitivity

The non-solar background rate in the XSM detector will dictate the sensitivity limit for measurements of the lowest solar X-ray flux levels. Since XSM had wide FOV and small aperture, the diffuse Cosmic X-ray Background (CXB) has the dominant contribution to the background. Using the CXB spectral model given by Türler et al. (2010) and XSM instrument details, we estimate the expected CXB background spectrum. The total count rate due to CXB in XSM is estimated to be 0.1 counts s^{-1}. Additional contribution from charged particles is expected to be less than this.

Measurements of non-solar background in XSM are available when the Sun is either out of the FOV or is occulted by the Moon. Figure 3.11 shows the XSM light curve of the Sun obtained during the commissioning phase with intervening durations of the background due to occultation. The mean background rate from this observation is ~ 0.15 counts s^{-1}, which is not significantly higher than the estimated CXB rate. Excess counts are expected to arise from charged particles. This is also substantiated by the observed $\sim 1 - 2$ counts s^{-1} ULD events that deposit energy beyond the higher energy threshold and are recorded in the last spectral channel. It may be noted from the figure that the background rate is about 35 times lower than the count rate from the Sun when the solar flux levels were well below A1 level based on GOES XRS measurements of the same time. However, exact flux levels were not available from GOES XRS at this time as the solar X-ray flux levels were below the sensitivity limit of the GOES XRS.

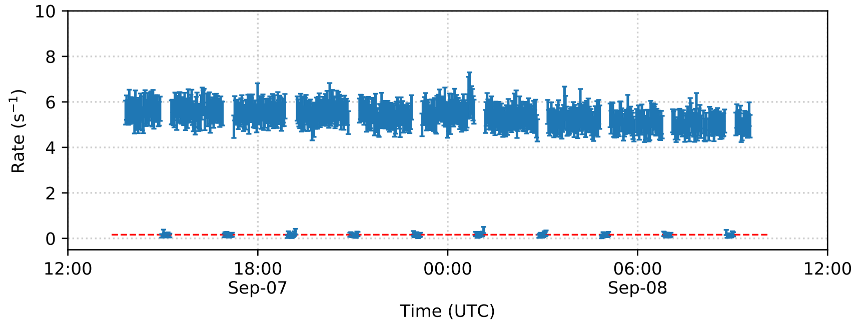

Figure 3.11: XSM light curve with 100 s bin size during 07-08 September 2019 with periods of solar observations and occultation by the Moon. The red dashed line shows the mean background count rate during the periods when the Sun was occulted by the Moon, which is ≈ 0.15 counts s^{-1}. During this period of very low solar activity, counts from the Sun are detected by the XSM well above background.

First B class flares after XSM started observations occurred on September 30 and October 1 of 2019, which were also detected by the GOES XRS instrument. Figure 3.12 top panel shows the XSM 1–15 keV light curve in 100-second time bins during this period. Flux in the 1-8 wavelength range (GOES XRS long channel) obtained by integrating the XSM observed spectrum is shown in the middle panel, and the dynamic spectrum is shown in the lower panel. For comparison with solar X-ray rates, the typical non-solar background rate is shown with a dashed line in the top panel of Figure 3.12. Evidently, the solar X-ray count rates are significantly higher than the background, even when the solar activity was an order of magnitude lower than the A1 class. This shows that the low background in XSM allows it to detect the quietest X-ray flux levels from the Sun and can observe transient events with peak fluxes lower than A1 flares.

Background variability

While any slight variations in the background rates will not affect the feasibility of detecting X-rays from the Sun, the variations would have implications on using the spectrum at higher energies where the solar X-ray flux will become comparable with the background. CXB, the dominant component of the XSM

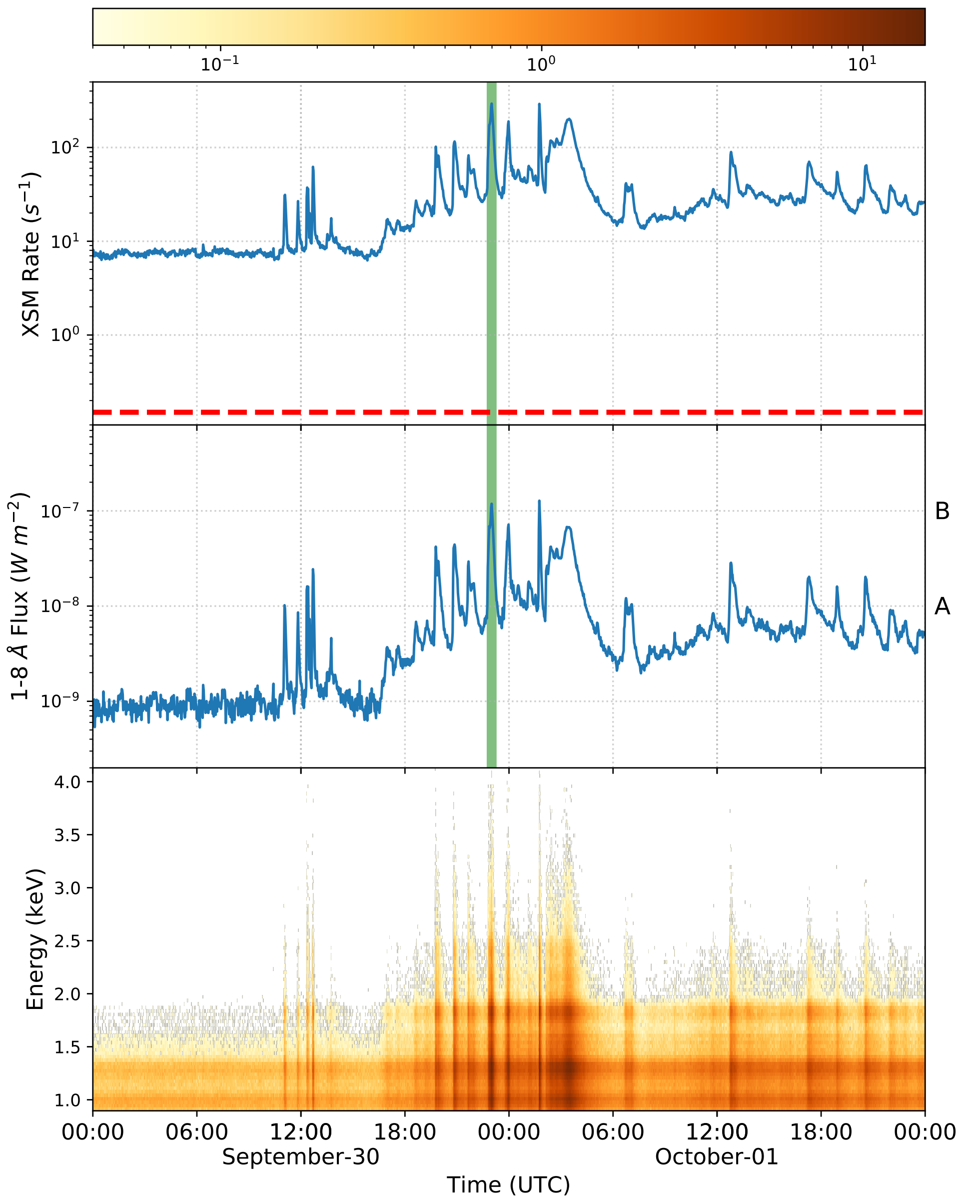

Figure 3.12: Solar light curve (top), X-ray flux in the 1-8 Å(1.55-12.4 keV) range estimated from the XSM data (middle), and the dynamic spectrum (bottom) with a time bin of 100s. In the top panel, the red dashed line corresponds to the background count rate. The duration includes periods of very low activity, showing a few A-class and sub-A-class flares and two B-class flares. The dynamic spectrum shows the spectral variability during the flares.

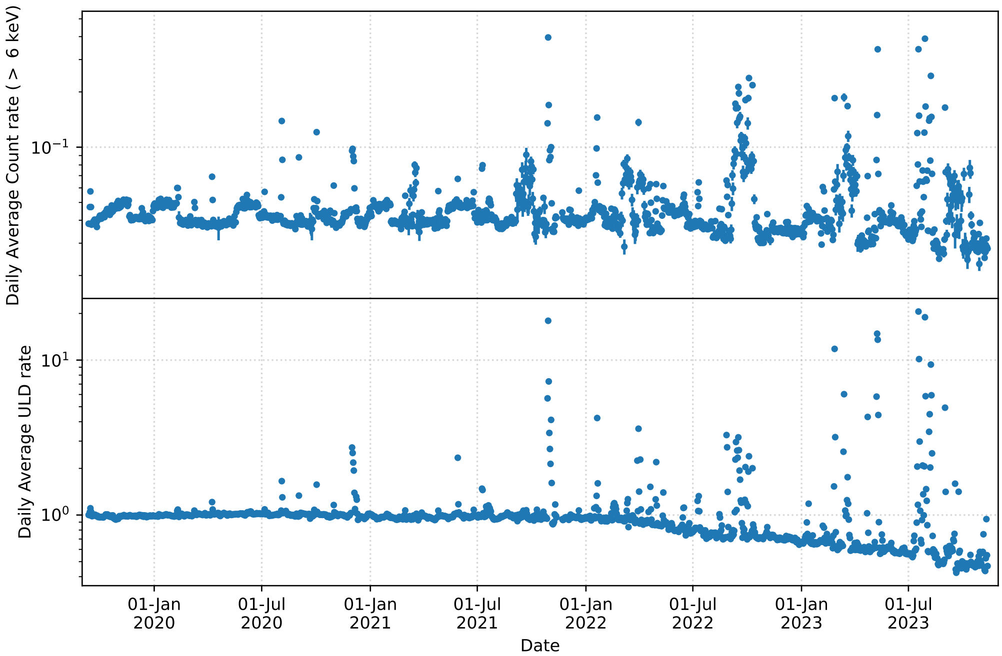

Figure 3.13: Top: Daily average XSM count rate above 6 keV plotted as a function of time. Bottom: Corresponding daily average ULD rates. Calculation of these averages excludes periods when the total XSM count rate exceeds 100 counts/s to remove the contribution from solar emission.

background, is not expected to vary with time. However, particle-induced background and background from any other sources can be variable.

To investigate the variability of background in XSM, we examine the light curve in the 6-15 keV energy range. We exclude times when the total count rate is greater than 100 counts/s to avoid periods of higher solar activity so that the contribution from the Sun is negligible in the 6-15 keV band and can be considered as a proxy for the background. The XSM light curve in this energy range for the four-year duration is shown in the top panel of Figure 3.13, where the points correspond to the mean value for each day. The bottom panel shows the daily average of ULD events arising primarily from charged particles.

From the light curve, it can be seen that there is a small yet clear variability in the background. There are multiple short periods when the background increases. These coincide with the enhancements in the daily average ULD event rates and thus are related to enhanced particle background. To examine this fur-

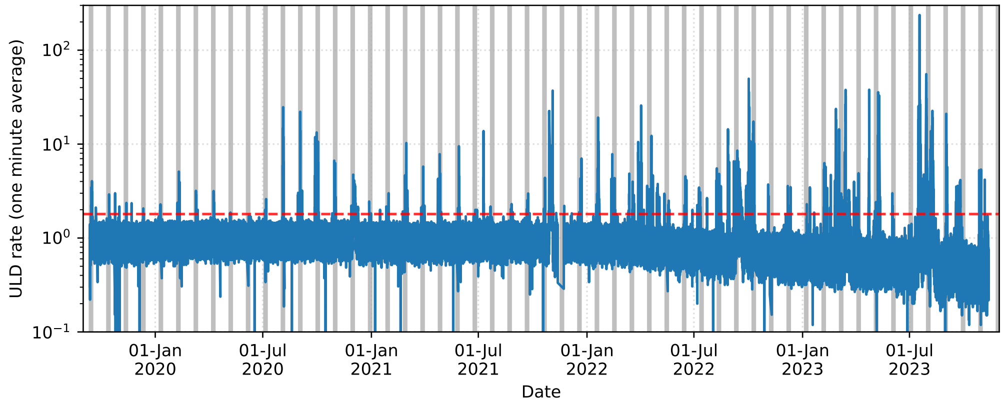

Figure 3.14: ULD count rates at a cadence of one minute are shown. Grey-shaded periods correspond to the passage of the spacecraft through the Earth's magnetospheric tail. The red dashed line corresponds to 1.8 counts/s, which is the upper limit of typical variability seen in the ULD rates, except for specific events such as magnetospheric pass and SEPs.

ther, Figure 3.14 plots the ULD count rates at a cadence of one minute for the entire observation period of four years. ULD rates shown in this figure display four kinds of variability, as discussed below.

- ULD rates show periodic enhancements in several instances, and these coincide with the passage of the spacecraft through the magnetospheric tail of the Earth, marked by the gray-shaded regions in the figure. Earlier geo-tail observations have shown enhanced particle densities (Narendranath et al., 2014b), which explains the observed enhancement in the ULD rates.

- There are still higher enhancements in the ULD rates not associated with passage through the magnetospheric tail, and many of them are associated with solar energetic particle (SEP) events resulting from eruptive flares.

- In addition to the short-term variations, there is also a distinct gradual trend of reduction in ULD rates seen in Figure 3.14 and Figure 3.13 as well as in the background rate. This is due to the reduction in cosmic ray flux over time with increasing solar activity.

- The dips in the ULD rates are associated with observations of the calibration source where the source and aluminium material of the mechanism

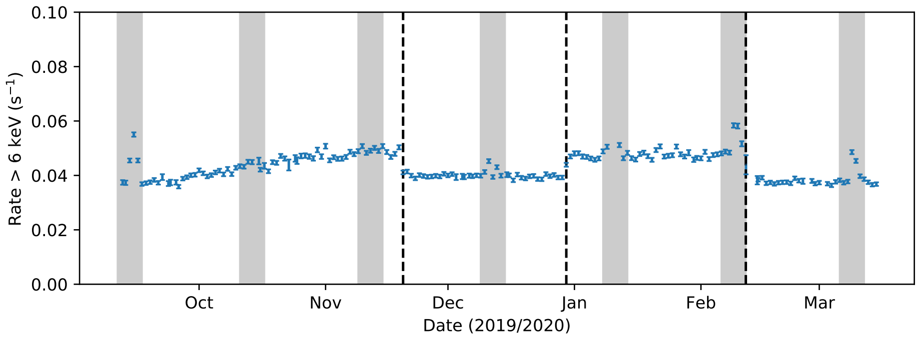

Figure 3.15: Zoomed in view of daily average background rates above 6 keV shown in Figure 3.13. Grey-shaded durations correspond to magnetospheric passes, and the vertical dashed lines correspond to times when the attitude configuration of the spacecraft was changed.

covers the entrance aperture of the detector, resulting in a reduction of particle flux on the detector. These are not important to consider for the purpose of understanding background variability during solar observations.

Thus, the particle background variability due to magnetospheric tail, SEPs, and cosmic ray flux modulation by solar activity explains the short-term enhancements as well as the decaying trend in the background rates shown in Figure 3.13.

In addition to the short periods of enhanced background and the decaying trend towards the latter part, some systematic variations are also seen in the background rate shown in Figure 3.13. If we look at the early part of the background light curve, it can be seen that it increases systematically for some duration, and then sudden changes are seen, which is better visible in Figure 3.15. These changes coincide with the times when changes are made in the attitude configuration of the spacecraft during the changeover from D-D to N-M season and in the middle of the N-M season. Thus, it can be inferred that the slight systematic variations in the background are correlated with the attitude configuration of the spacecraft.

We investigated various possible reasons for the variations in the background. Finally, we concluded that the variations are the result of emission from the astrophysical source Sco X-1. Sco X-1 is the first extrasolar astrophysical

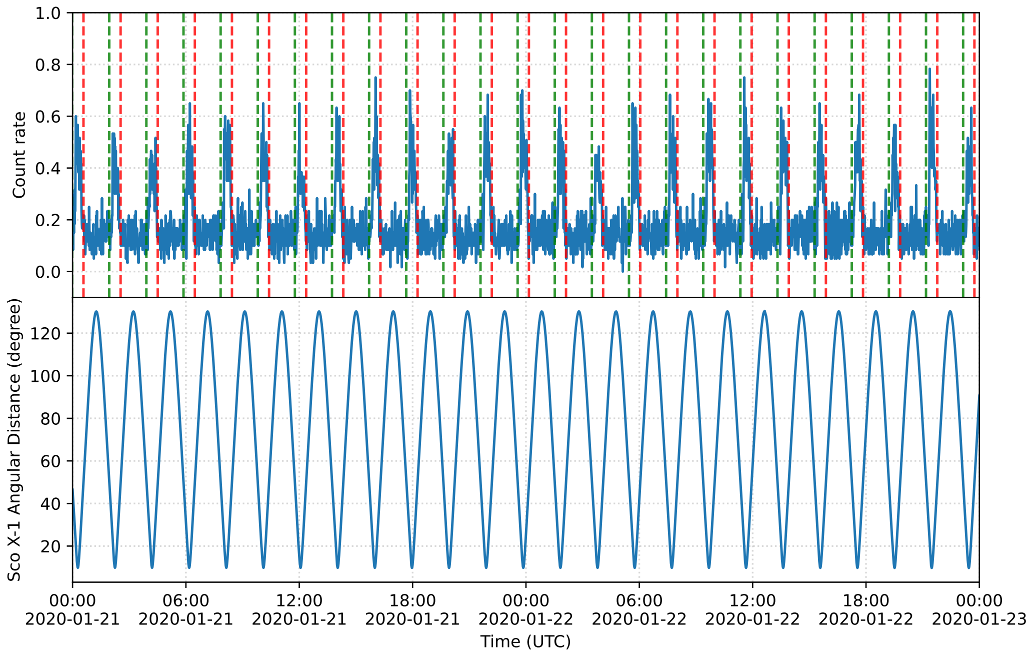

Figure 3.16: Background light curve for full energy range (1 – 15 keV) during times when the Sun was always out of XSM FOV, showing periodic enhancements (top). The angle between the XSM axis and the Sco X-1 location is plotted in the bottom panel. Vertical green dashed lines correspond to the times Sco X-1 enters the XSM FOV, and the red dashed lines mark the exit times.

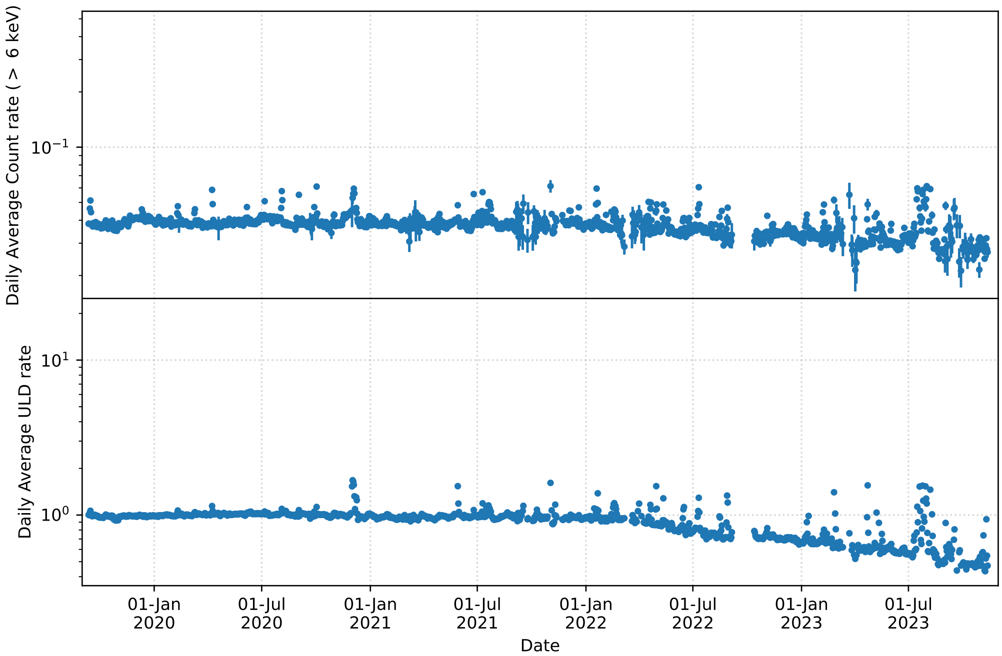

Figure 3.17: Daily average count rates in 6–15 keV (top) and ULD rate (bottom), similar to Figure 3.13, but excluding periods when Sco X-1 is in the XSM FOV and ULD count rates for one minute intervals are higher than 1.8 counts/s.

source detected to emit X-rays (Giacconi et al., 1962), and it is the brightest persistent source in soft X-rays, having a very steep energy spectrum. Figure 3.16 shows the XSM light curve spanning two days when the Sun is always out of its FOV. The angle between XSM boresight and Sco X-1 is also shown in the figure. It can be seen that the count rates show a systematic increase when Sco X-1 is within the field of view of XSM, confirming that the excess counts are coming from Sco X-1.

Further, we generate light curves in 6-15 keV band as earlier but selecting only times when Sco X-1 was not within FOV of XSM and when ULD count rates for each minute is less than 1.8 counts/s (red dashed line in Figure 3.14). Daily count rates obtained this way are plotted in Figure 3.17. It can be seen that the background rates show much less variability after excluding periods when Sco X-1 was in FOV and when ULD rates were high, confirming the origin of the observed variability. There are still some enhancements in the background that correspond to a slight increase in the ULD rates. Additional very small

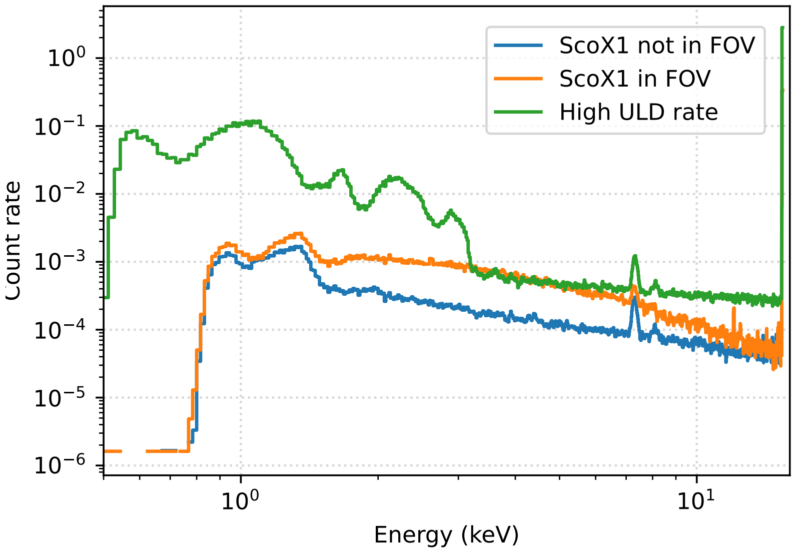

Figure 3.18: Background spectra acquired when the Sun is out of XSM FOV, with different observing conditions as marked in the figure.

variations may be due to other effects, such as the change in the fraction of the FOV occulted by the Moon that decides the CXB contribution.

Figure 3.18 shows the average background spectrum when Sco X-1 is not present within FOV, and Sco X-1 is present in the FOV. Also shown is the background spectrum in an extreme case when there is an enhanced background due to a SEP event. The presence of Sco X-1 in the FOV also causes changes in the background spectral shape. However, it may be noted that, in general, the overall average background over a day will have only a small contribution from the times when Sco X-1 is within the FOV. Also, the change in total background rate is not very significant in comparison to the X-ray fluxes from the Sun. Thus, the background variability has no impact on the sensitivity of XSM to measure solar activity in the soft X-ray band at flux levels of at least two orders of magnitude lower than A1 class events. As the variations are not very high, XSM can detect flare events below the A1 class and provide spectral measurements. However, the energy ranges used in spectral analysis shall be limited based on the solar and background spectrum as there could be enhanced background at higher energies.

From the spectrum shown in Figure 3.18, it can be seen that enhanced

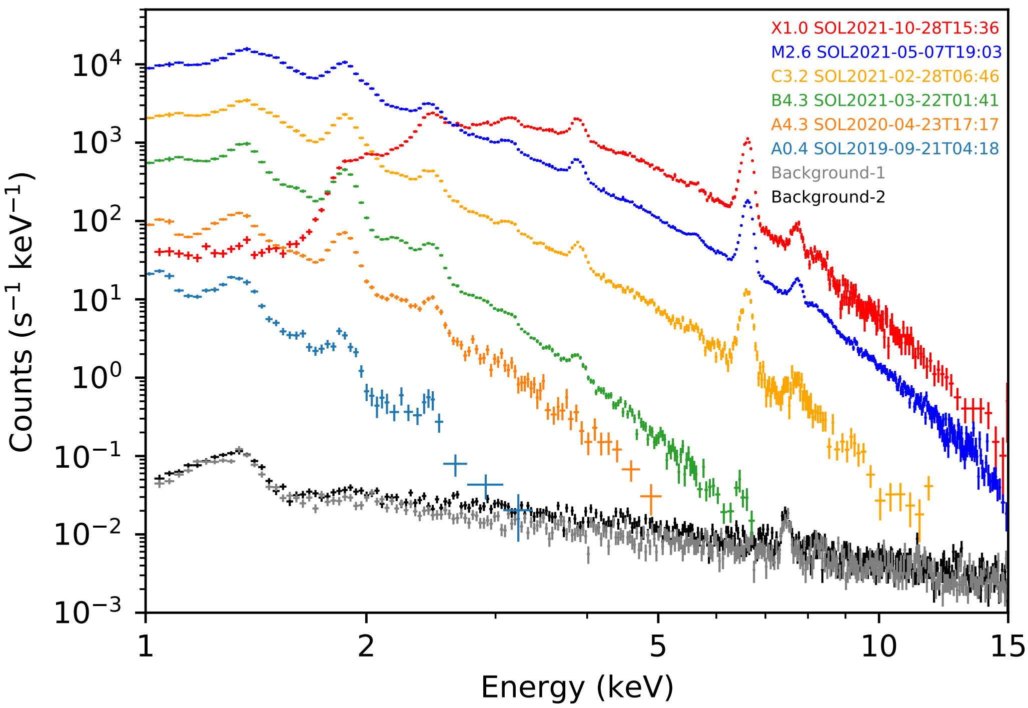

Figure 3.19: XSM spectra of flares of different intensity levels are shown. These correspond to one-minute intervals around the peak of each flare. Day average background spectra when Sco X-1 is present in the FOV for some time and when it is not in the FOV for the entire day are also shown.

particle rates can result in significant changes in the background spectrum. Often, these are associated with SEP events occurring at high solar activity levels, and in those instances, generally, the X-ray flux from the Sun is much higher than this background level. However, it is advisable to examine the ULD rates during an observation to assess the possible contribution of background, especially at higher energies.

Flare spectra and background

In Figure 3.19, XSM observed solar flare spectra are shown for X-class flare to sub-A class flare (Chapter 4). The spectra are obtained for one-minute integration around the peak of representative solar flares from each class. Also shown are the background spectra, as discussed earlier. It can be seen that for the smallest event, the solar flare spectrum is above the background up to 3 keV and the energy range is extended to higher energies for larger flares. As there is slight variability in the background, it is recommended to limit the energy range to where the solar spectrum is comparable with the background, as background subtraction may not be perfect beyond that energy. In case of a requirement to use spectra beyond that, which is possible only after integrating for longer periods, the background spectrum shall be selected with care by considering the Sco X-1 presence and any enhanced background due to particle events.

3.5 X-ray Spectral Analysis with XSM

The previous section presented refinements to ground calibration of the XSM based on solar observations . The updated calibration has been incorporated into the calibration database (CALDB) that is used by the XSM Data Analysis Software (XSMDAS). XSMDAS consists of software tools that generate calibrated level-2 XSM data products from the raw data, considering calibration and other corrections. A detailed description of XSMDAS is reported by Mithun et al. (2021a).

In order to demonstrate the adequacy of the updated calibration of XSM, we analyzed the spectrum of one B-class flare. The duration around the peak of the B class flare shown by the shaded time interval in Figure 3.12 is considered for this analysis. Spectrum was generated for this duration using *xsmgenspec* task. Ancillary Response File (ARF) with the effective area was also generated by the same tool, and the spectrum file header had information of the Redistribution Matrix File (RMF) to be used in spectral analysis.

The spectrum and response files were used in the X-ray spectral fitting tool XSPEC (Arnaud, 1996) to carry out modeling of the X-ray spectrum. The XSPEC model named `vapec`, which computes thermal plasma emission based on AtomDB atomic database, is used for this purpose. As noted earlier, the spectrum below 1.3 keV is ignored in the analysis. Similarly, as the solar spectrum becomes comparable to the background at 5.0 keV, the spectrum up to 5.0 keV is considered for spectral fitting. The spectrum, along with the best-fit model and residuals, are shown in Figure 3.20, where the best-fit model corresponds

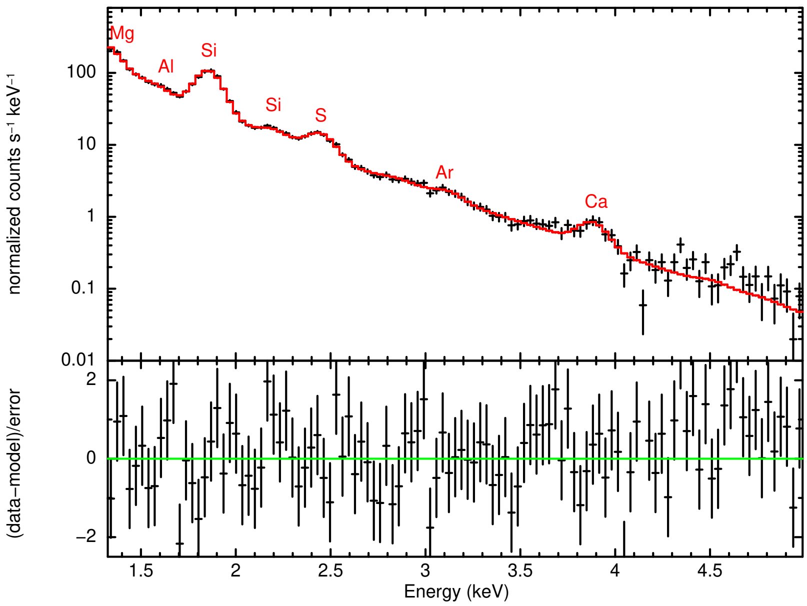

Figure 3.20: XSM spectrum of the B1 flare on 30 September 2019 shown in the shaded time interval in Figure 3.12 along with the best-fit model. The best-fit model for a temperature of 6.45 MK is shown in red, and the residuals are shown in the lower panel. Line complexes of different elements are also marked in the figure.

to a temperature of 6.45 MK. It can be seen that the convolved model fits the observed spectrum very well. This demonstrates the capability of XSM observations in X-ray spectroscopic investigations of the Sun.

3.6 Summary and Prospects with XSM

The XSM has been in lunar orbit and operational for more than four years at the time of writing. The spectral performance of the instrument has remained constant during this time and matches that on the ground. The updated instrument gain corrections that take into account the dependence on instrument temperature and X-ray interaction position in the detector is able to provide energy measurement with an accuracy of 10 eV. The effective area at different observation angles as obtained from ground calibration has been refined using quiet Sun observations for all observing seasons of XSM. The resultant effective area is shown to have relative uncertainties less than 1%. Based on the in-flight observations, a new method that does not involve trigger counts has been proposed for dead time corrections to XSM observations. Non-solar background counts seen by XSM are well within expectation, and hence, XSM is sensitive to detect transient solar X-ray events at the sub-A class level of solar activity. Slight variability in the background is also observed, and the reason for the same is understood. Recommendations for considering energy range for spectral analysis based on background are also provided. We also demonstrated the adequacy of calibration of XSM by showing spectral fitting for a flare.

XSM has been the only soft X-ray spectrometer available for observations of the Sun during its initial years of observation, including the solar minimum period. With its unique characteristics, XSM observations provide the opportunity to address various open questions in solar physics. XSM observations have been used in various studies, such as investigation of the elemental abundances in X-ray bright points and active regions (Vadawale et al., 2021; Mondal et al., 2023a; Del Zanna et al., 2022), evolution of abundances during solar flares (Mondal et al., 2021b; Nama et al., 2023), and role of nanoflares in coronal heating (Mondal et al., 2023b; Upendran et al., 2022).

In this thesis, I use XSM observations to investigate multi-scale solar transients from microflares to larger solar flares. In the next chapter, an X-ray perspective of multi-scale solar flares is given, and some areas where XSM observations can provide further insights are identified. Investigations in these areas, primarily using XSM observations, are presented in the subsequent three chapters.

Chapter 4

Multi-Scale Solar Flares: An X-ray Perspective

The Sun was the first astrophysical source from which X-ray emission was detected and is the brightest celestial X-ray source. The visible surface of the Sun, the photosphere, has temperatures of $\sim$ 6000 K and does not emit any significant flux in X-rays. However, the temperature increases significantly at higher altitudes in the solar atmosphere, reaching a million Kelvin in the outer atmosphere, named the corona, which emits X-rays. The reason for this increase of temperature by orders of magnitudes in the solar atmosphere is one of the unresolved problems in solar physics. In addition to quiescent X-ray emission from the solar corona, sudden brightenings that result in flux enhancements by orders of magnitudes called solar flares are also observed. Solar flares also result in emission at other wavelengths over the entire electromagnetic spectrum, from radio to gamma rays. Often, they also result in the ejection of energetic particles into the interplanetary medium, impacting the space weather. Observations in X-ray wavelengths offer the possibility of the most direct diagnostics of the flaring process and have contributed significantly to our understanding of solar flares.

This chapter provides an overview of the X-ray properties of solar flares with energies ranging over several orders of magnitude. Section 4.1 provides an overview of the X-ray Sun, including a brief history. Observational aspects of solar flares and our current understanding are summarised in Section 4.2. The occurrence of small-scale flare events and their contribution to the heating of the solar corona is discussed in Section 4.3. Section 4.4 presents aspects of X-ray spectroscopic investigations of flares with current generation X-ray spectrometers and provides some of the areas where these investigations can provide further clues.

4.1 The X-ray Sun

4.1.1 A Historical Overview

In order to explain the observed E-layer of the Earth's ionosphere, it was theorized that X-rays, ultraviolet, or other forms of ionizing radiation should be arriving at the Earth from astrophysical sources (Hulburt, 1938). However, at that time, no such sources were known. The brightest and nearest object was the Sun, which would be the ideal source of X-ray emission to support this. However, the visible surface of the Sun, the photosphere, having a temperature of $\sim$ 5800 K, is incapable of emitting any significant flux in the X-ray wavelengths.

It was well known by then that the Sun has an outer atmosphere, which was named the corona, that was visible during total solar eclipse. Some unusual emission lines were observed from the solar corona that did not match with the known transitions, and they were initially (19^{th} century) attributed to a potential new element, 'coronium'. However, in the early 1940s, it was identified that these emission lines observed from the corona correspond to forbidden transitions of highly ionized atoms of heavy elements (by Edlén, see Swings, 1943). For the highly ionized species to exist, the temperatures of the corona had to be in the order of a million kelvin, which meant that the solar corona would be a potential source of X-ray emission. Early attempts to observe X-rays from the Sun were carried out at the U.S. Naval Research Laboratory (NRL) with the V-2 rockets, and in 1948, evidence of X-rays from the Sun was first detected on a photographic plate covered with Be window (Burnight, 1949). Further observations also showed that X-rays from the Sun are getting absorbed over a narrow region of altitudes that are consistent with the E-layer (Friedman et al., 1951). These initial observations were followed by several experiments on rocket flights, which showed that the X-ray flux from the Sun varies over time, matching the sunspot cycle (Friedman, 1963a).

Early attempts to identify locations of the X-ray emission from the Sun used an ingenious technique where multiple rocket flights with X-ray detectors were flown during a total solar eclipse in 1958. One part of the limb was covered with 'active regions' as identified by plages from optical observations, while the other limb had almost no such features. X-ray observations of the crescent with active regions showed much higher flux than the other, which showed that the X-ray emission from the corona is localized with higher flux from the regions associated with plages (Friedman, 1963a). Pinhole camera images of the X-ray Sun then conclusively showed the association of bright X-ray emission with active regions (Blake et al., 1963). Further imaging observations with grazing incidence telescopes have resulted in the identification of various coronal X-ray features such as the active regions, bright points, and coronal holes (Vaiana et al., 1973).

Rocket flights with X-ray detectors also lead to the detection of enhanced X-ray emission associated with flares observed in optical wavelengths. Events of different intensity levels were observed, and some of them were associated with eruptive processes such as prominence eruptions (Mandel'Štam, 1965). Observations of energy spectra with proportional counter detectors during the solar flares showed considerable evolution of the spectral shape with a rapid increase in flux at shorter wavelengths compared to the quiet period, showing an increased temperature. The launch of satellites such as the Orbiting Solar Observatories (OSO) series and the Ariel series, as well as space stations like Skylab, allowed more detailed studies of X-ray observations of flares by providing continuous and longer observations. High-resolution soft X-ray spectral observations using crystal spectrograph instruments flown on rockets and satellites lead to the detection of lines from highly ionized species along with continuum (Doschek, 1972). They offer the diagnostics of plasma properties like temperature and density of the thermal electrons. Hard X-ray emissions at energies above 10 keV were also detected for some of the flares, which showed impulsive behavior and power-law spectra. Thermal interpretation of the hard X-ray emission requires extremely high temperatures that are unphysical. In addition to the hard X-ray emission, direct detection of particles, radio emission, and nuclear gamma rays showed that non-thermal processes are also involved (Culhane & Acton, 1974). Bremsstrahlung emission due to non-thermal electrons was deduced to be the reason for the observed hard X-rays (Brown, 1971).

Reviews of early X-ray observations of the Sun and solar flares are provided by Friedman (1963b); Mandel'Štam (1965); Culhane & Acton (1974); Doschek (1972). An account of the evolution of early EUV/X-ray spectroscopic observations at NRL is given in the memoirs by George Doschek (Doschek, 2021). Since the 1980s, sophisticated X-ray spectroscopic and imaging instruments on satellite missions such as Solar Maximum Mission (Bohlin et al., 1980), Yohkoh (Acton et al., 1992), Hinode (Kosugi et al., 2007), and RHESSI (Lin et al., 2002) and EUV instruments such as Atmospheric Imaging Assembly (AIA, Lemen et al., 2012) on Solar Dynamics Observatory (SDO, Pesnell et al., 2012) have contributed significantly to our current understanding of the solar corona and solar flares.

4.1.2 Coronal X-ray Features

Figure 4.1 shows EUV and X-ray images of the Sun showing the typical coronal features. Regions of bright emission in X-rays and EUV with bright loops of plasma associated with sunspots are the 'active regions'. These active regions are associated with the high magnetic field locations in the photosphere, as can be seen from the corresponding photospheric magnetogram images shown in Figure 4.1 right panel. Coronal loops connecting the positive and negative magnetic polarity regions filled with relatively hotter plasma having temperatures of $\sim$ 3 MK in the active regions are responsible for the intense emission in these regions (Reale, 2014). Intense solar flares originate from the active regions, and they usually have complex structures (Toriumi & Wang, 2019). Apart from the bright active regions, smaller bright regions are present in the X-ray/EUV images of the solar corona (Figure 4.1), and these are called 'coronal bright points'

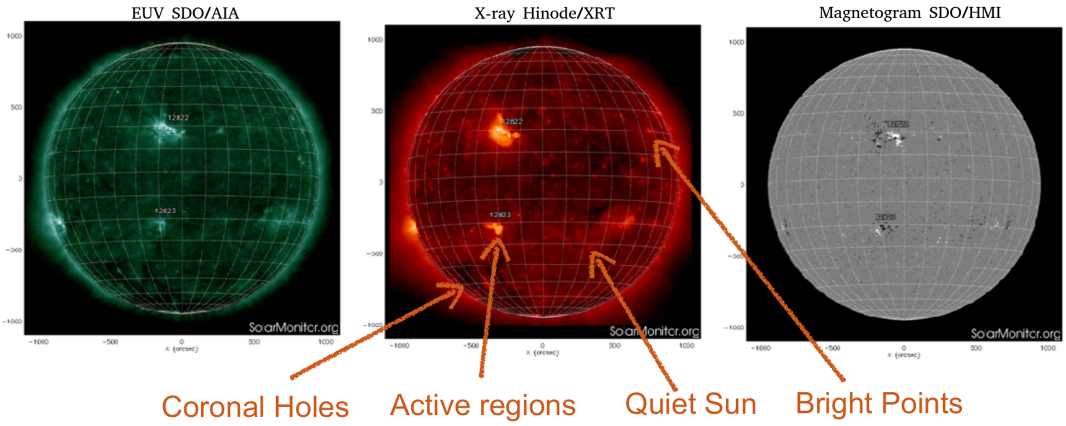

Figure 4.1: EUV image from SDO AIA 94 Å(left) X-ray image from Hinode XRT Be-thin window (middle), and photospheric magnetogram from SDO HMI (right) are shown. Different coronal X-ray/EUV features, active regions, bright points, quiet Sun, and coronal holes are marked in the images.

(CBP) or 'X-ray bright points' (XBP). XBPs are associated with magnetic bipolar regions having lesser magnetic field strengths than the active regions (Madjarska, 2019). There are also regions having no significant X-ray/EUV emission as marked in the figure and they are termed as 'coronal holes'. Unlike in active regions and XBPs, where magnetic field lines are closed, in coronal holes, the magnetic field lines are open and extend to the interplanetary medium. The fast component of solar wind originates from these coronal holes (Cranmer, 2009). The remaining region with weak X-ray emission outside the active regions, bright points, and coronal holes is often termed as 'quiet Sun'. Here, the plasma temperatures are lower than that in the other brighter features.

The overall X-ray emission from the corona and the presence of coronal features follow a cycle with a period of approximately eleven years. This corresponds to the eleven-year Solar Cycle when the polarity of the solar magnetic field reverses (Hathaway, 2015). During the solar maximum, a larger number of sunspots are present and, hence, more active regions. This results in higher levels of overall X-ray flux from the Sun. During the minima of the Solar Cycle, fewer numbers of sunspots are present, and at times no sunspots are present on the solar disk. When no active regions are present during solar minima, the XBPs dominate the X-ray emission from the Sun. Figure 4.2 shows the representative

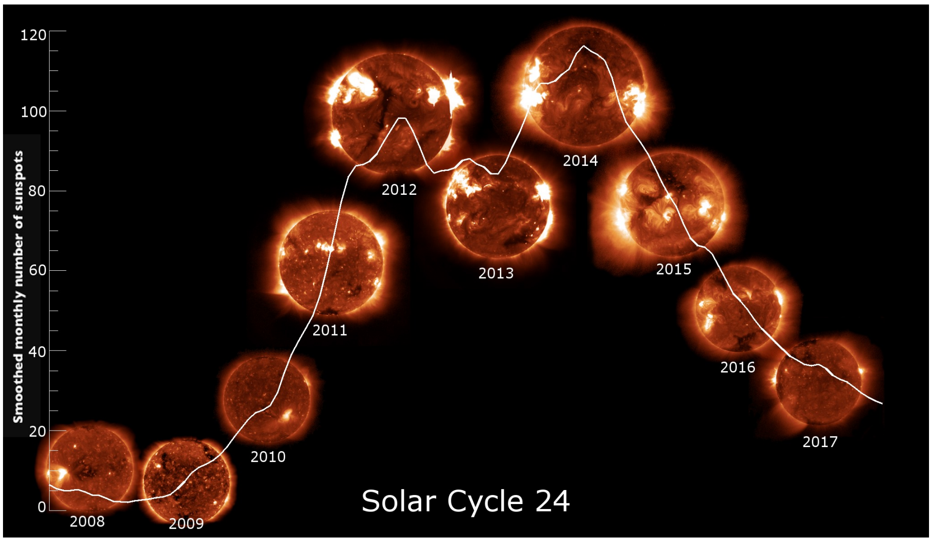

Figure 4.2: X-ray images of the Sun obtained with *Hinode* XRT over Solar Cycle 24 showing the X-ray flux variation along with the sunspot number. Figure courtesy: XRT picture of the week

X-ray images from *Hinode* XRT over one Solar Cycle, showing this behavior.

4.1.3 Solar flares

Solar flares are sudden intense emissions often observed across the electromagnetic spectrum from a relatively small region on the solar disk. They are sometimes accompanied by the ejection of energetic particles into the interplanetary medium. Solar flares are the result of impulsive releases of energy in the solar atmosphere triggered by the reconnection of magnetic fields. The first observations of solar flares were in optical wavelengths by Carrington and Hodgson in 1859 (Carrington, 1859; Hodgson, 1859). Later, it was understood that there is intense emission in the H-α band during such events. Earlier classification schemes of solar flares relied on the area and intensity of the emission in the H-α band during the peak intensity of the emission. Depending on the fractional area of the emission, classes of S,1,2,3, and 4 were assigned to the flare, and a qualitative assignment of letters f, n, and b was given that corresponds to faint, normal, and brilliant.

After the detection of intense X-ray emission from solar flares, X-ray flux has become the basis for the modern classification of solar flares. Since the

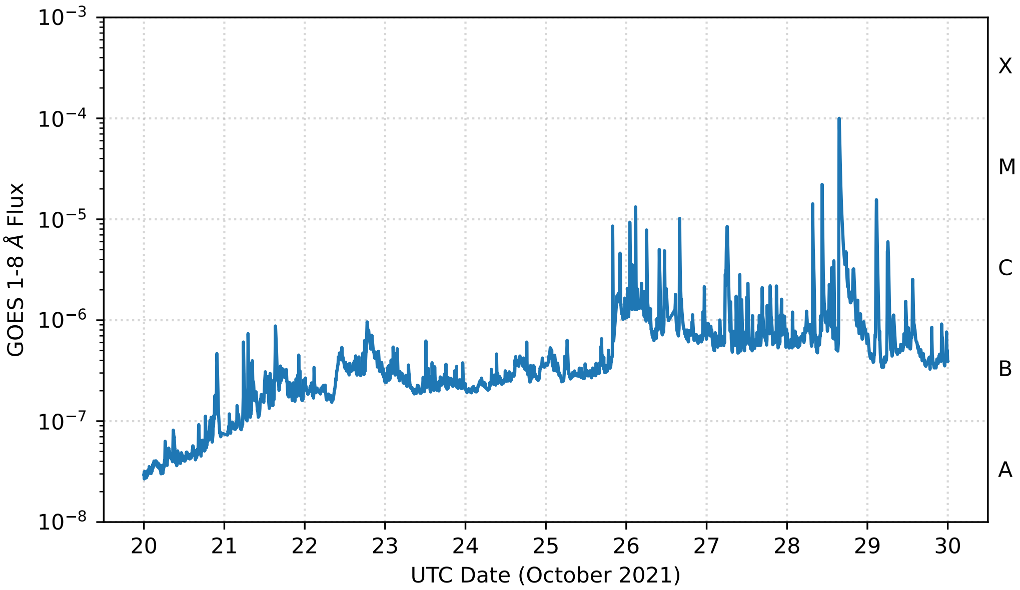

Figure 4.3: X-ray light curve obtained with GOES XRS showing several flares. Flares are classified based on the peak X-ray flux in the GOES long wavelength band of 1–8 Åin Wm^{-2}.

1970's GOES series of satellites have carried instruments that provided broadband X-ray flux measurements in two wavelength bands in X-rays. The peak flux measured by GOES X-ray sensor (XRS) instruments in the 1–8 Å band is used to classify the flares into different classes named A, B, C, M, and X. A-class flares are the weakest, having peak flux of 10^{-8} Wm^{-2} and subsequent flares classes have fluxes an order of magnitude higher than the previous. X-class flares have peak fluxes higher than 10^{-4} Wm^{-2}. Figure 4.3 shows the X-ray flux light curve from GOES showing a few flares of different classes. Within each class of flare, an integer suffix is used to denote the factor of its peak flux. For example, an M2 class flare has a peak flux of twice the M1 flare.

Much like the quiescent X-ray emission, the number of solar flares also follows the 11-year Solar Cycle. During solar minima, intense flares like X-class flares do not occur, and weaker A and B-class events are present. Overall, the number of flares is also lower during those periods. During the maxima, generally, intense flares occur more frequently.

4.2 Flare Observations and Standard Flare Model

X-ray and EUV observations provide the most direct diagnostics of the high-temperature plasma and non-thermal particle populations generated by solar flares. The standard flare model, also known as CSHKP model (Carmichael, 1964; Sturrock, 1966; Hirayama, 1974; Kopp & Pneuman, 1976), has been successful in explaining several observed features of solar flares. In this scenario, the reconnection of magnetic fields is considered to be the origin of energy release in solar flares. Recent reviews of solar flare observations and current understanding are provided by Fletcher et al. (2011) and Benz (2017). Magnetohydrodynamic processes associated with flares are reviewed by Shibata & Magara (2011), and different particle acceleration processes subsequent to reconnection are discussed in Zharkova et al. (2011). Spectral diagnostics in soft X-rays (and EUV) of the thermal plasma is presented by Del Zanna & Mason (2018), while a review of the hard X-ray emission and the techniques of inferring non-thermal electron properties is given by Krucker et al. (2008) and Kontar et al. (2011). A brief account of major observational features of solar flares and the standard flare model scenario to explain these observations are discussed here. We also discuss various aspects of the standard flare scenario where the details are yet to be understood.

Figure 4.4 shows different phases of a typical solar flare and the X-ray light curves. In the pre-flare phase, sometimes enhanced X-ray and EUV emission is observed due to the heating of the plasma before the flare in regions closer to the location of the flare, but not necessarily the exact location of subsequent emission (McTiernan et al., 1993; Battaglia et al., 2009, 2023). Hard X-ray emission is observed during the impulsive phase of the flare, which is considered to be the primary energy release phase. Hard X-ray emission is observed mostly at the chromospheric footpoints of coronal loops. There are also observations where hard X-rays are observed from coronal loop tops (e.g., Masuda et al., 1994). Beyond the impulsive phase, the emission in soft X-rays and EUV increases and reaches the maximum. The soft X-ray and EUV emissions arise from the coronal loops that get filled with hot plasma. The increase in soft X-ray emission begins during the impulsive phase and matches the start of hard X-ray emission.

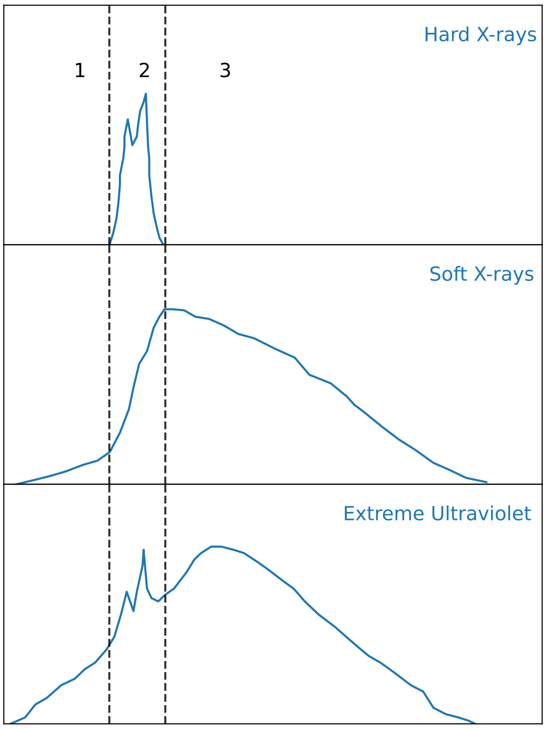

Figure 4.4: Schematic of hard X-ray, soft X-ray, and EUV light curves of a solar flare showing the typical behavior. The vertical dashed lines separate the pre-flare phase (1), impulsive phase (2), and gradual/decay phase (3). This figure is based on Fig. 2 from Benz (2017).

Empirically, it is found in many flares that the soft X-ray emission closely follows the integral of hard X-ray emission, which is termed as Neupert effect. In the subsequent decay phase, EUV and soft X-ray fluxes return to their pre-flare levels as the plasma cools down.

As noted earlier, there is considerable evidence that the energy release in solar flares is from the reconnection of magnetic fields. Figure 4.5 shows a schematic representation of the standard flare model scenario that relies on magnetic reconnection in the corona.

As the flares are impulsive in nature, magnetic stress must be built up over time and then released suddenly. Larger flares (except small-scale events, as discussed in the next Section) usually occur in active regions associated with strong photospheric magnetic fields and in the vicinity of the polarity inversion

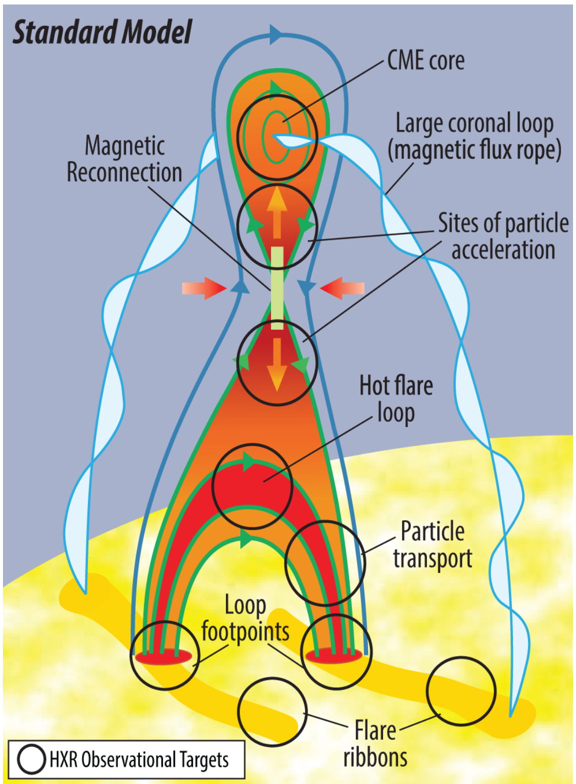

Figure 4.5: A schematic representation of the standard flare model scenario from Christe et al. (2017).

line that divides the regions of upward and downward magnetic fields. Observations suggest that many larger flares occur in regions where significant magnetic shear exists that stores free magnetic energy, and a possible trigger happens due to magnetic flux emergence (Benz, 2017 and references therein). While there is still debate on the reconnection site, evidence such as the presence of coronal loop top sources (e.g., Masuda et al., 1994) and reconnection features observed in images (e.g., Su et al., 2013) points to a reconnection happening in the corona as marked by the acceleration site in Figure 4.5. In this scenario, the anti-parallel fields along the legs of large coronal loops that are fixed at the foot points reconnect, and the top of the loop is ejected into the interplanetary medium. This is supported by imaging observations showing an apparent 'X' point of reconnection and above that coronal mass ejection (see Fig 16 of Benz, 2017). Aside from this single-loop scenario, reconnection of two loops is another possibility, which can also result in non-eruptive events without any ejection of plasma.

The magnetic reconnection results in the acceleration of electrons (and ions) that originally had thermal energies corresponding to pre-flare coronal plasma in the vicinity. The mechanism of conversion of the magnetic energy to the bulk kinetic energy of particles is an open question. Given the typical energies of the accelerated particles, the process has to be extremely efficient. As the acceleration process has to occur faster than the time scales of collisions, which would result in energy loss, the acceleration has to be within one second (Benz, 2017). Multiple processes are proposed to explain the efficient acceleration process in flares, including stochastic acceleration, acceleration in electric fields, and shock acceleration. There is a possibility that more than one of these processes is involved in the flare particle acceleration.

The accelerated electrons precipitate along the coronal loops to the chromospheric footpoints, where they lose their energy, which results in the hard X-ray emission from the footpoints by the thick target bremsstrahlung process. This explains the footpoint hard X-ray sources observed in flares. The observed foot point sources also spatially coincide with the H-α ribbons, matching with this picture (Figure 4.5). Loss of energy by accelerated electrons by Coulomb collisions in the chromospheric footpoints results in an increase in temperature. This causes the pressure to exceed the ambient pressure, and the heated plasma expands along the magnetic field lines. This process that fills up the flare loops with hot plasma is termed 'chromospheric evaporation'. Observations of blue-shifted lines originating from plasma of high temperatures provide evidence of chromospheric evaporation. The evaporated hot plasma in post-flare loops is responsible for most of the observed soft X-ray emission. This scenario predicts a correlation between the integrated energy deposited by the non-thermal electrons and the energy of the thermal plasma, which is consistent with the observed Neupert effect of similar correlations between observed non-thermal X-ray flux and thermal X-ray flux seen in many of the flares.

However, observations of thermal X-ray sources in the corona that appear before the hard X-ray emission (e.g., Krucker et al., 2008) are incomprehensible in this standard scenario. One possible explanation for this is the direct heating of particles in the corona due to the reconnection. Particles that get energized in the corona undergo frequent collisions such that they still remain in thermal distribution. A fraction of particles are also accelerated to non-thermal energies, which results in chromospheric evaporation of hot plasma. Observations of superhot components in large solar flares, in addition to a hot component that is hypothesized to be arising from direct heating and evaporated plasma, provide evidence for such a scenario (Caspi & Lin, 2010; Warmuth & Mann, 2016a,b). On the other hand, the densities required to explain the observed thermal X-ray emission from coronal sources are higher than the typical coronal densities pointing to the possible origin of the material from chromosphere, but not necessarily from the loop footpoints (Benz, 2017). Partition of the energy into various components, such as the non-thermal electrons, ions, thermal plasma, ejected particles, etc, can provide further clues about the involvement of various processes.

To summarize, while there is consensus on the overall picture of the flare model, several aspects, such as the particle acceleration site, acceleration process, involvement of any direct heating in addition to acceleration, etc, are still not fully understood. To enhance our understanding of energy release, acceleration, and heating in flares, comprehensive knowledge of the physical parameters of the accelerated electrons and thermal plasma is essential. Thus, deriving these parameters and thus the energy associated with each component, making use of newly available observational facilities, is of prime importance.

4.3 Coronal Heating: Nanoflares and Microflares

Observation of temperatures exceeding a million Kelvin in the solar corona compared to the photospheric temperature of $\sim$6000 K remains one of the long-standing puzzles in solar physics. While there is consensus that magnetic fields play a significant role in heating the corona, there is no conclusive evidence yet that points to the mechanism involved. Two of the widely considered options involve Magneto-Hydrodynamic (MHD) waves and magnetic reconnection events. While it is possible that both these processes occur in the corona, the question of interest is which one is more dominant over the other and can provide the required energy to heat the corona (Klimchuk, 2006).

Large-scale solar flares resulting from magnetic reconnection, as discussed in the previous section, release energies in the range of 10^{30} to 10^{33} erg; however, previous studies have shown that they account for only ∼20% of the energy required for maintaining the coronal temperatures (Sakurai, 2017). Early observations of smaller flares, termed microflares (e.g., Lin et al., 1984), prompted Parker (1988) to propose that the even smaller reconnection events called nanoflares having the energy of the order of $\sim 10^{24}$ erg occurring everywhere on the Sun may be sufficient to explain the coronal heating problem. However, these small-scale events cannot be resolved with the current observational capabilities, and other approaches, such as investigating high-temperature thermal emission in quiescent phases (e.g., Tripathi et al., 2011; Del Zanna et al., 2015), non-thermal emission from the non-flaring corona (e.g., Hannah et al., 2010; Buitrago-Casas et al., 2022) and investigating intensity fluctuations in Fourier domain such as by wavelet analysis (e.g., Pauluhn & Solanki, 2007; Upendran et al., 2022) are followed to identify their signatures (Hinode Review Team et al., 2019). Another approach is to infer the frequencies of nanoflares by extrapolating the frequency distribution of the smallest observable microflare events to lower energies, where the distribution usually follows a power law (Hannah et al., 2011). For the small-scale events to be dominant over the large flares and potentially have sufficient energy to heat the corona, the power law index of the distribution has to be greater than two (Hudson, 1991). Thus, determining the frequency distribution of the smallest observable flares is important in testing the nanoflare hypothesis.

This has prompted several studies to obtain the microflare frequency distribution using observations in different wavelength ranges. The first statistical study of X-ray microflares was done by observing an active region over five days with the *Yohkoh Soft X-ray Telescope* (SXT). Temperatures and emission measures of the microflares were obtained using filter ratio, and their energies were found to be distributed in the range of 10^{26} to 10^{28} erg (Shimizu, 1995). The most comprehensive statistical study of microflares has been done with X-ray

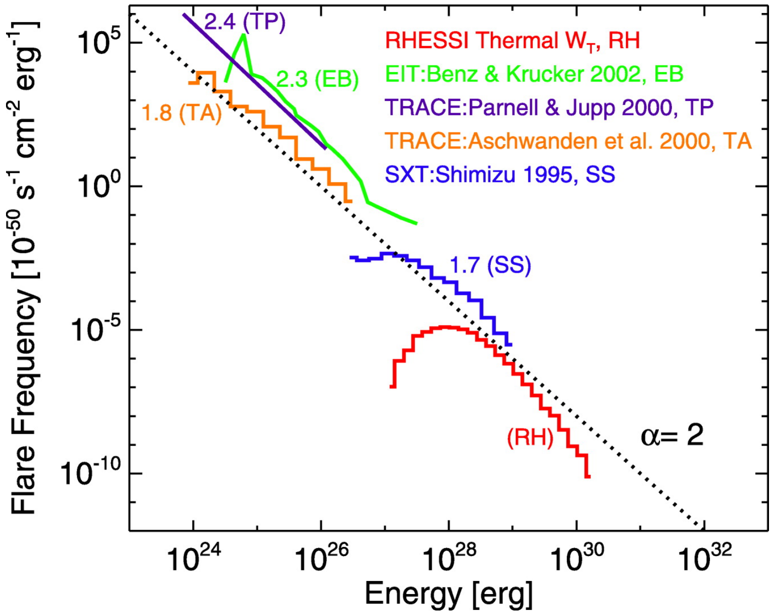

Figure 4.6: Frequency distribution of thermal energies of solar flares obtained with RHESSI along with other measurements of flare energy distributions taken from Hannah et al. (2008).

observations using the *Reuven Ramaty High Energy Solar Spectroscopic Imager* (RHESSI) observatory. Using observations spanning over five years, more than 25000 flares were detected. including several microflares with energies of the order of 10^{27}erg or higher (Christe et al., 2008). X-ray spectra were used to determine the plasma parameters and energetics, including the non-thermal energies for this sample of flares(Hannah et al., 2008), and the imaging confirmed that these events always occur in the active regions. Figure 4.6 shows the frequency distribution of flare thermal energies as obtained by RHESSI along with the measurements from *Yohkoh* SXT.

It can be seen that the RHESSI events have energies higher than the 10^{27} erg, and the SXT events go down to slightly lower energies. However, it may be noted that the energy measurements with *Yohkoh* SXT were using filter ratios rather than any spectroscopic measurements. Also, as noted earlier, both these samples of events are confined to active regions. If the nanoflares were ubiquitous, they should also be present in regions outside the active regions in the quiet Sun, but these detected X-ray microflares are confined to active regions.

Detection of burst-like events in the quiet Sun in EUV wavelengths have been reported using observations with SOHO EIT (Krucker & Benz, 1998; Benz & Krucker, 2002) and TRACE (Aschwanden et al., 2000b; Parnell & Jupp, 2000). These events have thermal energies in the range of $10^{24} - 10^{26}$erg and follow the expected power law distribution as shown in Figure 4.6. While the energies of these events are in the range of nanoflares, it is not clear whether these are resulting from reconnection events or other EUV brightenings.

More sensitive observations in X-ray energies would make it possible to search for even fainter events than those observed by RHESSI and in regions outside active regions. With X-ray spectroscopic observations, it would be possible to get better measurements of temperature and emission measure and, hence, more accurate estimates of thermal energy. There have been a few reports of the detection of microflares in the quiet Sun, such as with *NuSTAR* (Kuhar et al., 2018). However, as only a limited number of such events are observed, statistical properties of such microflares in quiet Sun were not feasible. Thus, the quest still continues for observations of X-ray microflares, orders of magnitude fainter than the large-scale flare events, in the quiet Sun with the objective of finding if those events are ubiquitous and whether their frequency distribution extrapolated to nanoflare energies support the coronal heating requirement.

4.4 X-ray Spectral Investigations of Solar Flares

The energy released in large-scale flare events (Section 4.2) and small-scale reconnection events (Section 4.3) would result in the acceleration of particles and heating of the plasma. These populations of thermal and non-thermal particles are not directly observable. The accelerated non-thermal electrons emit hard X-rays by non-thermal bremsstrahlung while the hot plasma produces line and continuum emission in soft X-ray and Extreme Ultraviolet bands (Del Zanna & Mason, 2018). Thus, observations in X-rays, specifically spectroscopic observations, provide the most direct diagnostics of the hot thermal and non-thermal plasma in solar flares of all scales (Fletcher et al., 2011). A brief discussion of spectroscopic diagnostics of thermal and non-thermal X-rays and current X-ray observatories that enable such investigations in this thesis is provided below.

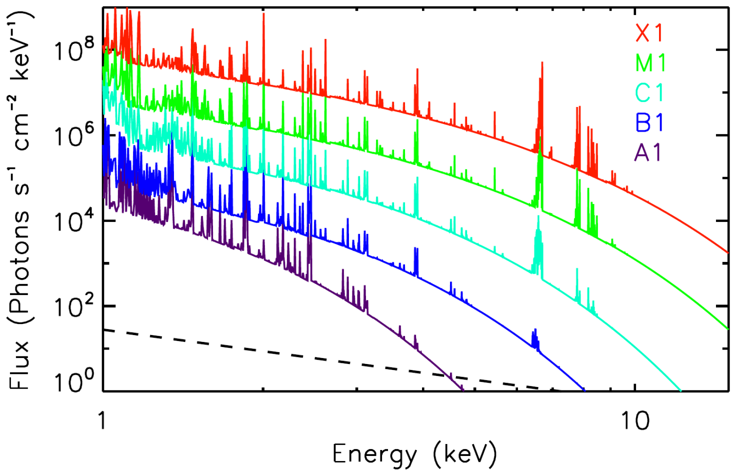

Figure 4.7: Typical soft X-ray spectra of solar flares of different classes arising from thermal plasma. These model spectra include continuum and line emission from isothermal plasma.

4.4.1 Thermal emission

The thermal plasma in the solar corona in different features like quiet Sun, X-ray bright points, and active regions, as well as that in solar flares emit profusely in soft X-rays and extreme ultraviolet. This thermal emission includes continuum as well as line emissions. The continuum component includes free-free emission (thermal bremsstrahlung), free-bound emission, and the two-photon process (see Section 1.1.2). The line emission arises from bound-bound transitions of various ionized species that are collisionally excited (see Section 1.1.2).

In order to compute the X-ray continuum and line emission spectrum from collisionally excited plasma such as that in the solar corona, various atomic data are required. These include the line energies of various species, their transition probabilities, collisional excitation rates, recombination rates, and equilibrium ionization fractions. Atomic data for these calculations are available in databases such as AtomDB (Foster et al., 2012) and CHIANTI (Del Zanna et al., 2021b). AtomDB is mostly used in the analysis of astrophysical plasmas, and the CHIANTI database is widely used in the analysis and interpretation of the X-ray and EUV spectra of the Sun.

X-ray spectrum from isothermal plasma depends on the temperature of the plasma, the amount of plasma present, which is usually defined in terms of volume emission measure as $\int {N_\mathrm{e}}^2 dV$, and the abundances of various elemental species. Figure 4.7 shows synthetic X-ray spectra computed from the CHIANTI database for isothermal plasma at different temperatures and emission measures corresponding to typical values for different classes of solar flares. It can be seen that the spectra include a continuum component as well as lines from various species at different energies.

As the soft X-ray spectrum is sensitive to the plasma temperature, emission measure, and abundances, modeling the observed spectrum with synthetic spectra can provide measurements of these parameters. In the generalized case where the plasma is multi-thermal, the temperature distribution of the plasma is defined by differential emission measure (DEM):

$$DEM(T) = \frac{d({N_\mathrm{e}}^2 V)}{dT} (\mathrm{cm}^{-3}\mathrm{K}^{-1}) \tag{4.1}$$

where V is the volume and N_e is the electron density. By modeling the X-ray spectrum, DEM can also be obtained, but it is usually difficult to obtain unique solutions.

4.4.2 Non-thermal emission

Accelerated electrons by the flare reconnection travel down to the chromospheric footpoints, where they encounter material of higher density and emit hard X-rays by bremsstrahlung while suddenly decelerating. The emission by electrons would be the sum of the instantaneous emissivity of the electron until it is thermalized, and it is termed the 'thick-target' process (Brown, 1971). If the densities of the target medium where the electrons are propagating are low such that the energy loss by the electrons can be neglected, it is called the 'thin-target' process. This is applicable for hard X-ray emission from coronal loop top sources.

Using the bremsstrahlung cross-section obtained with Bethe-Heitler formalism, by integrating over the electron energy distribution, the photon spectrum for thick-target [1] and thin-target [2] bremsstrahlung can be obtained. The energy

[1] https://hesperia.gsfc.nasa.gov/ssw/packages/xray/doc/brm_thick_doc.pdf
[2] https://hesperia.gsfc.nasa.gov/ssw/packages/xray/doc/brm_thin_doc.pdf

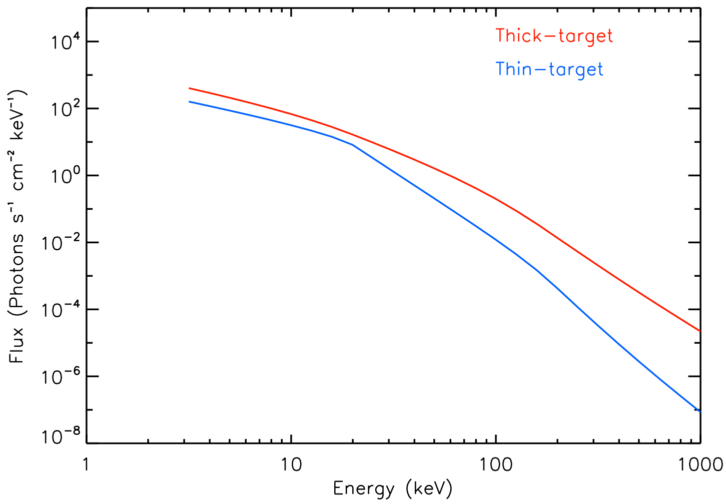

Figure 4.8: Typical hard X-ray spectrum in solar flares arising from non-thermal bremsstrahlung. Two spectra corresponding to thick-target and thin-target bremsstrahlung are shown.

distribution of accelerated electrons is considered to be a power law with a low-energy cut-off and a high-energy cutoff. The low-energy cut-off is essential so that the total energy content does not diverge. Figure 4.8 shows the photon spectra from thick-target and thin-target models for an electron distribution with low energy cut-off at 20 keV. The low-energy cutoff manifests in a flattening of the X-ray spectrum at energies below the low-energy cutoff, as seen from the figure. It can also be seen that the thick-target spectrum is harder than the thin-target emission, as the former includes emission from the decelerating electrons.

By modeling the observed hard X-ray spectrum, it is possible to deduce the properties of non-thermal electrons, such as the power law index, low-energy cutoff, and the total electron flux. However, it may be noted that at the lower energy end, the observed emission includes the thermal emission as well as the non-thermal emission. Thus, the flattening below the low-energy cutoff is often buried within the much brighter thermal emission, making the measurement of the low-energy cutoff particularly challenging. Measurement of the total energy content in non-thermal electrons critically depends on the low-energy cutoff, so this results in difficulties in estimating the flare energetics.

It is also worth noting that the hard X-ray emission by non-thermal bremsstrahlung is not necessarily isotropic. Depending on whether the accelerated electrons are beamed or isotropic, the resultant X-ray emission can be direction-dependent (e.g., Kontar et al., 2011). The hard X-ray emission is also modified by the scattering from the photosphere, called photospheric albedo, which depends on the observing direction as well as the location of the flare on the solar disk. The non-thermal X-ray emission can also be polarized, which can provide diagnostics of the electron anisotropy (see Chapter 8).

4.4.3 Solar observatories

In order to probe the thermal and non-thermal emission in X-rays and EUV, spectroscopic and imaging observations from different solar observatories are used in this thesis. A brief overview of the solar observatories used is given here.

Chandrayaan-2 XSM

Solar X-ray Monitor (XSM) on board the *Chandrayaan-2* mission is a soft X-ray spectrometer observing in the energy range of 1–15 keV. XSM observes the Sun-as-a-star and provides the disk-integrated spectrum at a cadence of 1 second. In Chapter 3, details of the XSM instrument and its in-flight calibration were presented. It was also shown that the XSM is sensitive to detect X-rays from the Sun at flux levels below GOES A1 class.

Solar Orbiter STIX

The Spectrometer Telescope for Imaging X-rays (STIX) is a hard X-ray imaging spectrometer on board the *Solar Orbiter* mission (Krucker et al., 2020). It provides the measurement of the X-ray spectrum in the energy range of 4–150 keV and also imaging in the same energy range using indirect imaging techniques.

STIX detector system consists of 32 coarsely pixelated CdTe detectors. In front of the detector, two X-ray opaque grids made of tungsten are placed at a distance of 55 cm between the grids. The grid consists of 32 sub-areas that correspond to each of the 32 detectors having parallel slits at equal distances. The two grids corresponding to one detector have slightly different pitch or orientation of slits such that a Moire pattern is formed on the detector parallel to its edges. By measuring the observed pattern, each set of grids and detectors provides a specific Fourier component of the source angular distribution. STIX can provide imaging within a field of view of 2x2 degrees with the finest angular resolution of 7 arcsec.

STIX data are recorded onboard over 32 adjustable energy channels in the 4 – 150 keV at varying time cadences. In the early days of nominal operation, the energy bins in the lower energy end have widths of 1 keV, and the bin width increases at higher energies. There have also been observations in later times with finer bin sizes at lower energies (private communication). The low latency telemetry data that is available for all STIX observations provides spatially integrated light curves in five energy bands. For events of interest, the full spectrogram data stored onboard are downloaded from which spectra and images can be obtained.

Hinode **XRT**

X-ray Telescope (XRT) on *Hinode* (Kosugi et al., 2007) carries out imaging observations in the soft X-ray below $\sim$2-3 keV with an angular resolution of 2 arcsec (Golub et al., 2007). It consists of a grazing incidence X-ray telescope with an X-ray CCD at its focus. Imaging in nine X-ray filter bands such as Be-thin, Be-med, Al-mesh, etc are available that allow X-rays in different energy bands and hence sensitive to plasma at different temperatures. While XRT observations do not provide significant spectroscopic information like XSM, they offer complementary information on the location of X-ray emission with the imaging capabilities of the instrument.

Solar Dynamics Observatory **AIA**

The Atmospheric Imaging Assembly (AIA) onboard Solar Dynamics Observatory (SDO, Pesnell et al., 2012) is an extreme ultraviolet imager providing imaging with an angular resolution of 1.5 arcsec typically at a cadence of 12 seconds (Lemen et al., 2012). The AIA instrument employs four telescopes to provide images in seven narrow bands in the EUV wavelengths. The bands are chosen to be centered around prominent lines from various ionized species of Fe and He that are formed at different temperatures. There are also two additional filters that provide observations in the ultraviolet band. The AIA images in different bands are sensitive to plasma at temperatures in the range from 60,000 K to 20 MK. The AIA bands at 94 Å and 131Å are sensitive to higher temperatures and thus provide a closer approximation to the locations of soft X-ray emission.

4.4.4 Solar X-ray spectral analysis

The analysis of continuum X-ray spectra of solar flares follows a forward folding approach as discussed in Section 1.3. Model spectra from thermal and non-thermal emission processes are convolved with the instrument response and fitted with the observed spectra to obtain the parameters. OSPEX package in *Solar-Soft*, which implements this approach, is widely used in the analysis of solar X-ray spectra such as those obtained with RHESSI. OSPEX includes models of thermal emission computed based on the CHIANTI database as well as models of non-thermal emission by thick-target and thin-target processes. OSPEX has certain limitations, such as the lack of the option to model spectra from multiple instruments simultaneously. Thus, in this thesis, the XSPEC spectral fitting package (Arnaud, 1996) is used for analysis. By default, XSPEC does not include models for thermal X-ray emission from the Sun with the CHIANTI database and non-thermal bremsstrahlung models. Thus, we use models of these emission processes included locally in XSPEC for analysis.

For the thermal component, the spectral model `chisoth`[3] is implemented as a local model in XSPEC is used. It uses tabulated spectra computed using CHIANTI for each elemental species (up to Zn) over a grid of temperatures to obtain model spectra for any temperature, emission measure, and abundances, as described in Mondal et al. (2021b). This can also be extended to incorporate emission models from multi-thermal models as discussed in Chapter 6.

For the non-thermal emission, we make use of the available Python

[3] https://github.com/xastprl/chspec

implementation of the thick target emission model in the `sunxspex` package[4]. By using the base implementation of the process, a local pyxspec (Python interface of XSPEC) model for thick-target bremsstrahlung[5] is implemented which is used in the spectral analysis.

The discussions in this chapter have brought out our current understanding and unresolved questions on solar flares, from the small-scale events that might be contributing to coronal heating to large-scale solar flares where particles are accelerated and plasma is heated to high temperatures. The following specific questions on various aspects of multi-scale solar flares are identified to be addressed in this thesis.

- Are there ubiquitous small-scale flares present all over the Sun? What are their frequency distributions? Will those be enough to heat the corona?
- What is the temperature distribution of the X-ray emitting plasma during solar flares? What does it say about the heating mechanisms?
- Is the energy associated with non-thermal electrons sufficient to heat the plasma? How do we obtain better constraints on the energetics?

X-ray observations, specifically spectroscopic observations, provide useful diagnostics to probe the heated plasma and accelerated particles in solar flares and to address these questions. The subsequent three chapters investigate these questions, primarily using X-ray spectroscopic observations with *Chandrayaan-2* XSM.

[4] https://github.com/sunpy/sunxspex

[5] https://github.com/elastufka/sunxspex/blob/xspec_functions/sunxspex/xspec_models.py

Chapter 5

Multi-Scale Solar Flares: Microflares and Coronal Heating

Impulsive release of energy by magnetic reconnection results in solar flares having energies spanning several orders of magnitude. Small-scale unresolved ubiquitous events dubbed as nanoflares with energies nine orders of magnitude smaller than the largest solar flares are considered a potential energy source to maintain the solar corona at multi-million Kelvin temperatures, and thus, observations of any small flares are of great interest. Microflares, the smallest observed X-ray flares, have been confined to the active regions except for a handful. In this work, we present the first comprehensive analysis of observations of the largest sample of X-ray microflares occurring in the quiet Sun, using observations with Chandrayaan-2 Solar X-ray Monitor (XSM). Observations spanning 76 days during the 2019-20 solar minimum resulted in the detection of 98 microflares having peak flux below GOES A-class flares. Using X-ray spectra of the events, we obtained the temperature and emission measure of the flaring plasma, and the volume is estimated using the counterpart images in EUV from Solar Dynamics Observatory/Atmospheric Imaging Assembly (SDO-AIA). Thermal energies associated with the events are estimated to be in the range of 3×10^{26} to 6×10^{27} erg and we present the flare frequency distribution with energy for these events compared to previous observations in EUV. We discuss the implications of the observed small-scale events outside active regions on coronal heating.

A version of this chapter is published in ApJL *with the title 'Observations of the Quiet Sun during the Deepest Solar Minimum of the Past Century with Chandrayaan-2 XSM: Sub-A-class Microflares outside Active Regions' (Vadawale, Mithun et al., 2021)*

5.1 Introduction

Nanoflares, small-scale reconnection events having nine orders of magnitude lower energy than the larger solar flares that are hypothesized to be responsible for coronal heating, are not directly observable. One approach to infer their presence is to observe slightly larger microflares and extend their frequency distributions to lower energies (Section 4.3). Earlier comprehensive statistical study of the smallest observable X-ray flares with RHESSI concluded that the events are occurring in active regions. However, the proposed nanoflares are expected to be ubiquitous, even in the quiet solar corona outside the active regions. Detection of burst-like events in the quiet Sun in EUV wavelengths have been reported using observations with SOHO EIT (Krucker & Benz, 1998; Benz & Krucker, 2002) and TRACE (Aschwanden et al., 2000b; Parnell & Jupp, 2000). These events have thermal energies in the range of $10^{24} - 10^{26}$erg and follow the expected power law distribution. However, it is not clear whether these events are impulsive heating events reaching coronal temperatures or other EUV brightenings (Aschwanden et al., 2000a,b). Such an ambiguity does not arise for X-ray microflare events as the X-ray emission arises from higher temperature plasma, but few observations of quiet Sun X-ray microflares are available. Only a handful of X-ray microflares are observed in the quiet Sun with *Yokoh* SXT (Krucker et al., 1997), *SphinX* (Sylwester et al., 2019), and *NuSTAR* (Kuhar et al., 2018). Thus, the statistical study of X-ray microflares in quiet Sun has not been possible so far.

In this work, we use observations with Chandrayaan-2 *Solar X-ray Monitor* (XSM) (Vadawale et al., 2014; Shanmugam et al., 2020) to investigate microflares in the quiet Sun. It has been shown that the XSM has the sensitivity to measure X-ray flux at levels two orders of magnitudes less than the GOES

A-class flux level (Section 3.4.4). XSM carried out observations during the 2019-20 solar minimum at the end of Solar Cycle 24, which was the deepest in the past 100 years (Janardhan et al., 2011, 2015). During this time, there were several extended periods when no visible active regions were present on the solar disk, thus providing a unique opportunity to look for microflares in the quiet Sun with disk-integrated observations of XSM. Here, we present the detection of the largest sample of X-ray microflares observed outside active regions, their flare frequency distribution, and implications on coronal heating. Section 5.2 describes the observations and analysis. Results are presented and discussed in Section 5.3 followed by a summary in Section 5.4.

5.2 Microflare Observations and Analysis

We use the soft X-ray spectroscopic observations of the Sun in the 1 – 15 keV energy range by XSM. The visibility of the Sun with XSM varies with observing seasons, and continuous visibility is available in the 'Dawn-dusk' (DD) seasons alone (see Section 3.2). The present work uses the XSM observation during the first two DD seasons from September 12 to November 20, 2019 (DD1) and February 14 to May 19, 2020 (DD2). From the raw data of XSM of the selected days, we generate effective area-corrected time-resolved X-ray spectra at a time cadence of 2 minutes using the XSM Data Analysis Software (XSMDAS; Mithun et al., 2021a). We then generate the flux light curve $L(t)$ in the energy range of 1 – 15 keV by integrating the spectra from $E_1 = 1$ keV to $E_2 = 15$ keV from the spectra $S(E, t)$ using the equation:

$$L(t) = \sum_{E=E_1}^{E_2} \frac{S(E,t)\ E}{A(E)} \tag{5.1}$$

where $A(E)$ is the on-axis effective area of the XSM. In this calculation, we ignore the actual spectral redistribution matrix and assume a diagonal redistribution matrix, but it is sufficient to get fluxes in the broad energy ranges as done here.

Figure 5.1 top panel shows the 1–15 keV XSM light curve for the first DD season. As seen in the figure, there are periods when the baseline X-ray

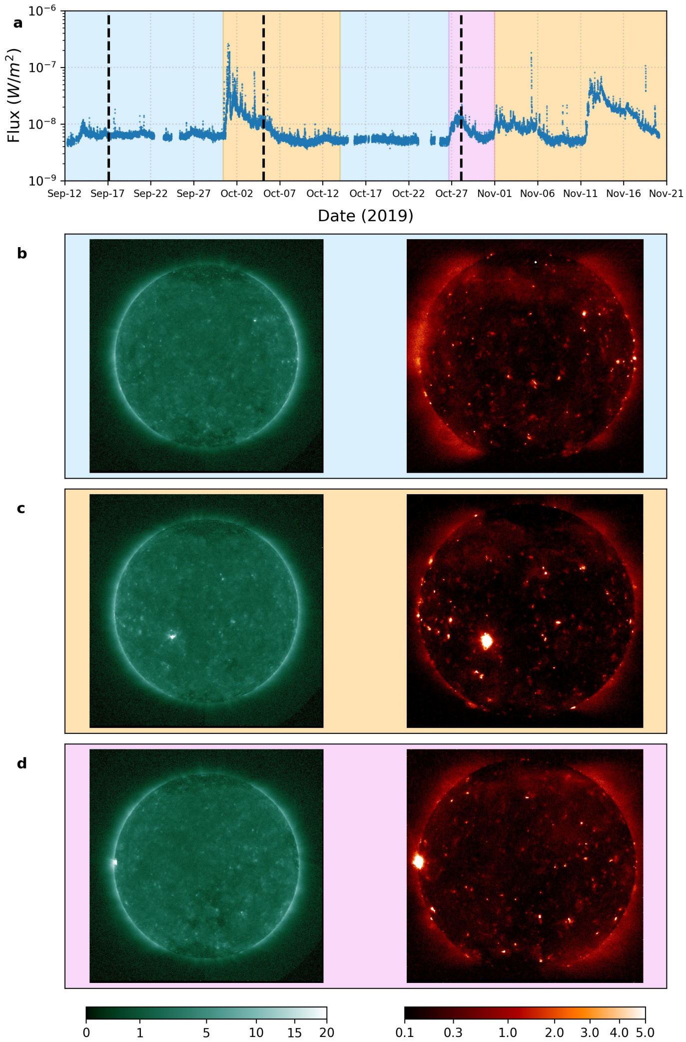

Figure 5.1: Panel **a** shows the light curve of solar X-ray flux measured by the XSM during DD1 season. Background shades in the light curve represent intervals with different solar activity, with *orange* representing periods when NOAA active regions are present; *pink* representing periods of enhanced activity visible in both the XSM light curve as well as EUV/X-ray images but not classified as AR; and *blue* representing periods selected for the present study when no major activity was observed on the Sun. Panels **b-d** show representative EUV (left) and X-ray (right) images for each of the three periods, indicated by the background color of the panels. The EUV images are from SDO AIA in 94 Å band, and the X-ray images are from Hinode XRT with the Be-thin filter. All AIA and XRT images follow the respective color scales shown. The vertical dashed lines in panel **a** correspond to when these images are taken.

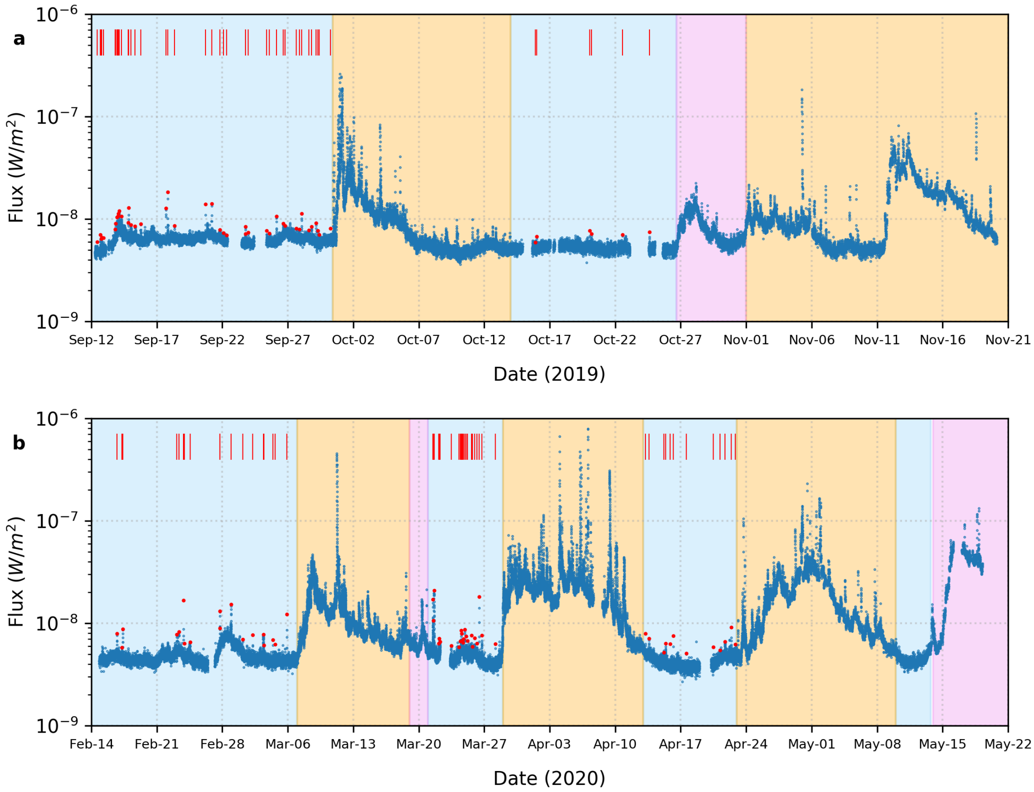

Figure 5.2: Panels **a** and **b** show the X-ray flux in the $1-15$ keV energy range with a time cadence of 120 s, as measured by the XSM during two observing seasons DD1 and DD2, respectively. Background shades represent different levels of solar activity, the same as Figure 5.1. The 98 microflares detected during the quiet periods (blue background) are marked with red points, representing their peaks, and red vertical bars, representing their time.

emission levels are enhanced and periods of quiet X-ray activity. Intervals, when NOAA active regions were present on the solar disk, are marked with an orange background in the figure, where an enhanced baseline X-ray emission is observed. Representative EUV and X-ray images from Solar Dynamics Observatory Atmospheric Imaging Assembly (SDO AIA; Lemen et al., 2012) and Hinode X-ray Telescope (XRT; Golub et al., 2007), on the left and right, respectively, during this period are shown in the lower panels of Figure 5.1. The pink background denotes intervals when NOAA has not assigned the presence of any active regions, but the X-ray flux levels show enhancements. It can be seen from the corresponding AIA and XRT images that some bright regions are present. Since the objective of the present work is to examine quiet periods of the Sun to look for small-scale flares, we consider only the intervals marked by the blue background in the figure when no active region-like feature is present on the solar disk, as also can be seen from the representative images given in the figure. These intervals considered in the present work are: September 12-30, 2019; October 14-26, 2019; February 14-March 7, 2020; March 21-29, 2020; April 13-23, 2020; and May 10-13, 2020. These span a period of a total of 76 days and are marked with a blue background in the XSM light curves for both DD seasons shown in Figure 5.2.

For these days, we generated XSM count light curves with a two-minute cadence in the energy range of 1–5 keV, as we observed that no appreciable solar flux was detected at energies beyond 5 keV in this low activity period. As the flares are expected to have higher temperatures and hence a harder spectrum, we also generated light curves in the 1.5–5 keV energy range where it would be easier to detect flaring events above the quiescent solar emission. We identified candidate flare events using a semi-automated technique to identify the flare peaks, followed by a manual verification. For each of these candidate events, the start and end times of the flare were obtained from the light curve. Events with total counts at 5σ above the average pre-flare count rate were only selected as flares. We identified 98 microflares during the quiet Sun periods, marked by the red points in Figure 5.2, and the vertical bars in the figure represent their peak times.

5.2.1 EUV Counter Parts of Microflares

As the disk-integrated observations with XSM do not provide the spatial location of the microflare on the solar disk, we use observations in other wavelengths for that purpose. For each of the XSM microflares, we examined the EUV images from SDO AIA during the flare periods to identify the EUV counterparts. As the 94 Å band of AIA has the response to higher temperatures ($\sim$ 6-10 MK) that would correspond to the X-ray emission, we used images in this band. For the interval around each microflare, Level-1.5 Synoptic AIA images at a cadence of two minutes were obtained from the Joint Science Operations Center (JSOC).

Images corresponding to each flare were looked for any brightening coinciding with the microflare observed in XSM. Any brightening was confirmed to be the counterpart to the X-ray event if the EUV light curve obtained around the identified location showed a similar trend as the X-ray light curve. Among the 98 microflares, EUV counterparts could be identified for 74.

For the flares with identified EUV counterparts, to obtain an estimate of the volume of the flaring region, we generated maps of Fe XVIII emission around the flaring region that trace the plasma having temperatures in the range of 3-6 MK following the method given by Del Zanna (2013). We use the AIA images in 94 Å 211 Å and 171 Å bands at the peak of the microflare to obtain Fe XVIII contribution using the equation from Del Zanna (2013):

$$I(FeXVIII) = I(94) - \mathrm{I(211)/120} - \mathrm{I(171)/450} \tag{5.2}$$

Fe XVIII images were generated in this manner for a region of 5' × 5' surrounding the microflare location, and the pixel with the highest intensity was identified. All pixels having Fe XVIII intensity at least 10% of the peak intensity are considered part of the flaring event, and the corresponding area is estimated from the number of pixels. From the estimated area (A), the volume (V) of the flaring plasma is computed as $V = A^{3/2}$.

5.2.2 X-Ray Images and Photospheric Magnetograms

We used X-ray images from the *Hinode X-ray Telescope* (XRT) (Golub et al., 2007) and magnetograms from the SDO *Helioseismic and Magnetic Imager* (HMI) (Scherrer et al., 2012) to examine the X-ray activity before and after the microflare and the structure of the photospheric magnetic field associated with the flare location. For the events with identified EUV counterparts, we selected X-ray images and photospheric magnetograms before and after the flare from the available Hinode XRT full disk images and hourly synoptic SDO HMI magnetograms. As the low energy efficiency of the Be-thin filter for XRT is comparable to that of XSM, Be-thin images are expected to trace the spatial distribution of X-ray emission observable in the XSM at lower energies. Thus, we use Be-thin filter images for XRT. We generated cutouts of XRT images and

HMI magnetograms around the location of each flare (with the EUV counterpart identified) after considering the solar rotation. As the Hinode XRT full-disk images are not always available at regular intervals, at least in some cases, the XRT image times differ from the flare times by a day or more. We also note that magnetograms may not be very reliable for the events near the limb.

5.2.3 X-Ray Spectroscopy of Microflares

Soft X-ray spectra of the microflares observed with XSM are used for determining the temperature and emission measure of the flaring plasma. For each microflare, we select the interval around the peak that covers 50% of the flare duration, as shown in the example in Figure 5.3. For each event, the integrated spectrum for this interval (similar to the red-shaded regions in Figure 5.3) is obtained using XSMDAS modules. We also generated the integrated spectrum for the quiet Sun periods of each day by selecting periods excluding the flare duration with sufficient margin as shown by the green shaded region in Figure 5.3. Analysis of this quiescent solar X-ray spectra to determine the temperature, emission measure, and abundances of the quiet Sun is presented in Vadawale et al. (2021).

XSM spectra of the microflares are fitted using the X-ray spectral fitting package XSPEC (Arnaud, 1996). We consider the spectrum above 1.3 keV to ∼3–4 keV, where the solar spectrum dominates over the non-solar background. To model the X-ray spectrum, we use the 'chisoth' isothermal plasma emission model (Mondal et al., 2021b) based on the CHIANTI atomic database. The X-ray spectrum of the microflare includes the emission from the flare and the quiescent solar emission that was present even before the flare. One approach to remove the pre-flare contribution is subtracting the pre-flare spectrum from the flare spectrum and proceeding to the modeling. However, in the case of XSM, this is not recommended. This is because the effective area of the instrument varies with time as the Sun angle changes; thus, a simple subtraction will not take care of the effective area differences between flare and pre-flare observations. Instead, we fit the quiescent Sun spectrum obtained for each day of the observation and determine the spectral model for the quiet periods. As no significant variations

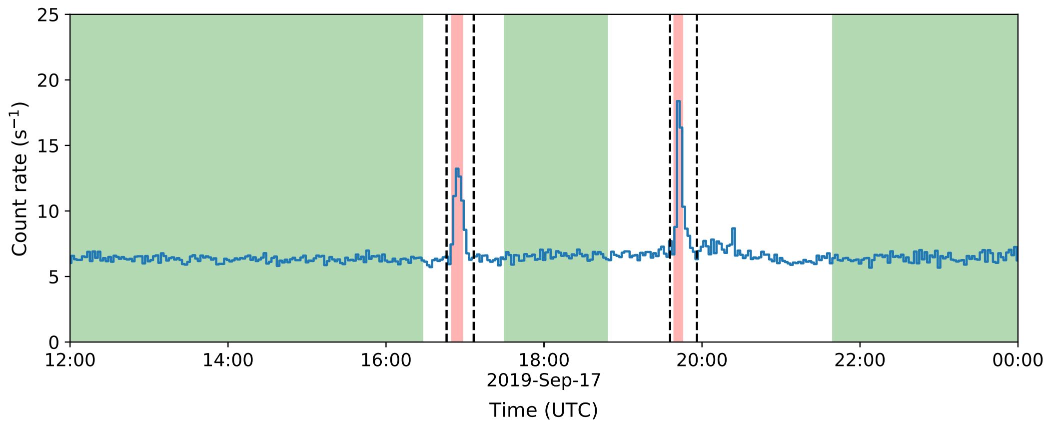

Figure 5.3: An example of the identification of flares and duration for flare and quiet Sun spectroscopy is shown. Vertical dashed lines show the start and end times of the two microflares. The red-shaded region corresponds to the flare peak period identified for spectroscopy of the microflares. Duration shown in green shades, which excludes flare duration with additional margin before and after the flare, is used to obtain the spectral model for the background quiet Sun.

are observed in the quiet Sun spectrum over a day (and even longer), this quiet Sun spectral model can be used to fit the microflare spectrum. In spectral fitting of the microflare, we then use a two-component model where both are isothermal plasma emission models, and one corresponds to the quiet Sun while the other corresponds to the flare emission. The parameters of the quiescent component are frozen to the spectral model of the daily average quiet Sun spectrum. For the flare component, the temperature and emission measure are free parameters of the fit. At the same time, the abundances of elements are frozen to the values obtained for the quiet Sun periods as there are insufficient counts in the microflare spectra of short duration to constrain the abundances. We also note that the uncertainties on the parameters of the quiet Sun spectral model are much smaller than those of the microflares. Thus, they have no significant effect on the microflare parameters and error obtained from the fitting where the quiet Sun component is frozen to its best-fit parameters.

5.3 Results and Discussion

As shown in Figure 5.2, 98 microflares have been identified during the 76 days of observations when no active regions were present on the solar disk. Although the observations spanned 76 days, the effective exposure of XSM during this period is 53.3 days, and thus the average microflare rate observed in the quiet Sun is ~ 1.84 day^{-1}. If we consider the individual epochs of the quiet Sun observations (each interval shaded in blue in Figure 5.2), the mean flare rates vary from ~ 0.75 day^{-1} to ~ 3.4 day^{-1}. We designate each event with IDs corresponding to their peak times, following the standard convention (Leibacher et al., 2010). The list of microflares and their parameters are listed in the Appendix of Vadawale, Mithun et al. (2021).

Although there have been a few previous reports of X-ray microflares occurring outside ARs earlier with Yokoh (4 microflares, Krucker et al., 1997), SphinX (16 microflares, Sylwester et al., 2019), as well as recently with NuSTAR (3 microflares, Kuhar et al., 2018), the present work is the first observation of the largest sample of quiet Sun X-ray microflares within a span of a few months This observation suggests the flaring events are not confined only to the active regions and thus provides support to the hypothesized presence of ubiquitous small-scale impulsive events everywhere in the solar corona.

Figure 5.4 shows the X-ray light curves for a representative set of the observed microflares. In most cases, the light curves display fast rise and slow decay, suggesting energy release impulsively. There are, however, few events that do not follow this behavior. This is likely due to the blending of multiple energy release processes, or they may have intrinsically different origins.

5.3.1 Microflare location

The flaring location on the solar disk was identified for 74 of the XSM microflares using the AIA 94 Å images. By comparing the EUV light curves with the X-ray light curves, we confirm the association of the X-ray event with the EUV event. An example of the counterpart identification is shown in Figure 5.5. XSM light curve for the event is shown in Figure 5.5a and Figure 5.5d shows

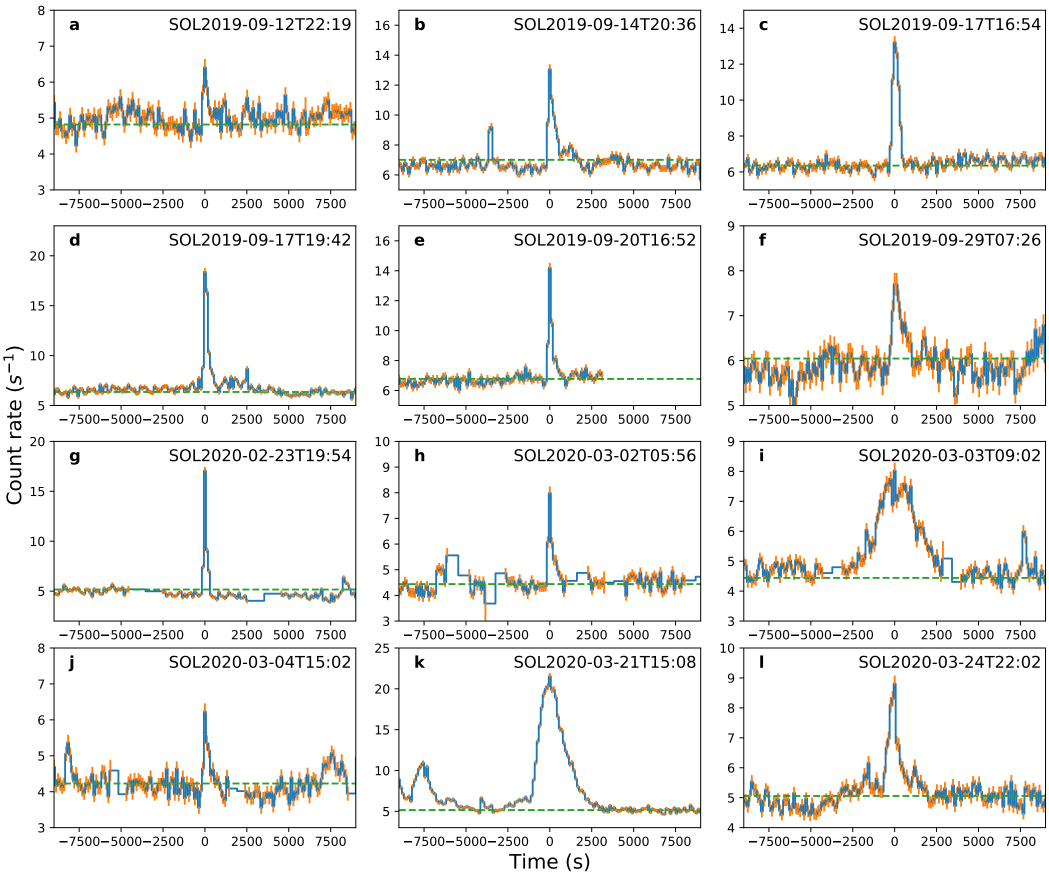

Figure 5.4: X-ray light curves in 1–5 keV of a representative set of microflares observed by the XSM. Flare IDs are shown in the respective panels. Error bars correspond to one sigma uncertainties. Green dashed lines show the mean count rate for the duration considered for non-flaring quiescent emission.

the corresponding AIA light curve integrated over the identified flare location (marked in Figure 5.5b and c). We use the FeXVIII images generated from AIA images in three bands to identify the flaring region corresponding to the high-temperature emission. We find that the region is often very small and limited to only a few pixels; thus, it is difficult to infer the shape of any loops. Thus, for uniformity, we estimate the emission volume for all events based on the number of pixels with significant FeXVIII emission as discussed in Section 5.2.1. Figure 5.5e shows the FeXVIII image of the flaring region, and the pixels considered to be part of the flare emission volume are shown in Figure 5.5f.

Further, for events with identified EUV counterpart locations, we ex-

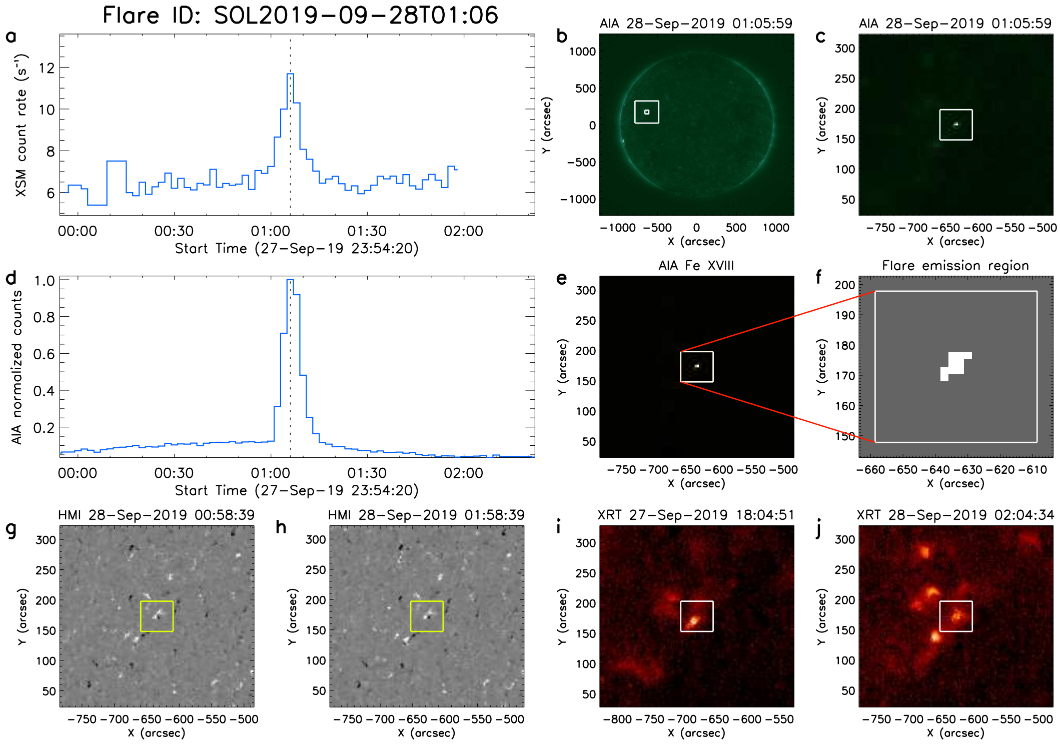

Figure 5.5: Identification of the location of one of the XSM microflares with the 1–5 keV light curve shown in panel **a**. The flare location is marked on the SDO AIA 94 full disk image in **b** and a 5' × 5' cutout is shown in **c**. Panel **d** shows AIA 94 light curve for the flaring pixels as shown in panel **f**. FeXVIII image of the flare location is shown in panel **e**, and the map of pixels of the flaring plasma based on FeXVIII emission is given in **f**. Available synoptic HMI magnetograms and XRT Be-thin images nearest to the flare peak time are shown in panels **g**-**j**. Similar figures for all 98 microflares are available as an online figure set of Vadawale, Mithun et al. (2021).

amined the photospheric magnetic fields and X-ray emission before and after the microflare, as shown for an event in Figure 5.5g- 5.5j. It is observed that in cases where reliable magnetograms are available (not too close to the limb), the microflare locations are associated with magnetic bipolar regions. However, photospheric magnetic field strengths at these sites are much weaker than the active regions. The association of the microflares with bipolar regions indicates that they are the result of reconnection in the coronal loops as suggested by the standard flare model, but at much smaller scales of energy release.

It is also observed that most of the microflares occur in X-ray Bright points (XBPs, Golub et al., 1974) seen in the XRT images. There are a few cases where we observe XBPs in X-ray images before the event but not after (e.g., flare id SOL2019-09-17T16:54) and vice-versa (e.g., flare id SOL2019-09-13T23:06). These interesting observations can provide insights into the formation and evolution of XBPs(Priest et al., 1994; Madjarska, 2019). More interestingly, there are a few flares that do not seem to be associated with any XBP (e.g., flare id SOL2020-04-20T12:11). But, given the significant gaps between successive X-ray images, it is difficult to draw any firm conclusions.

5.3.2 Temperature and Emission Measure

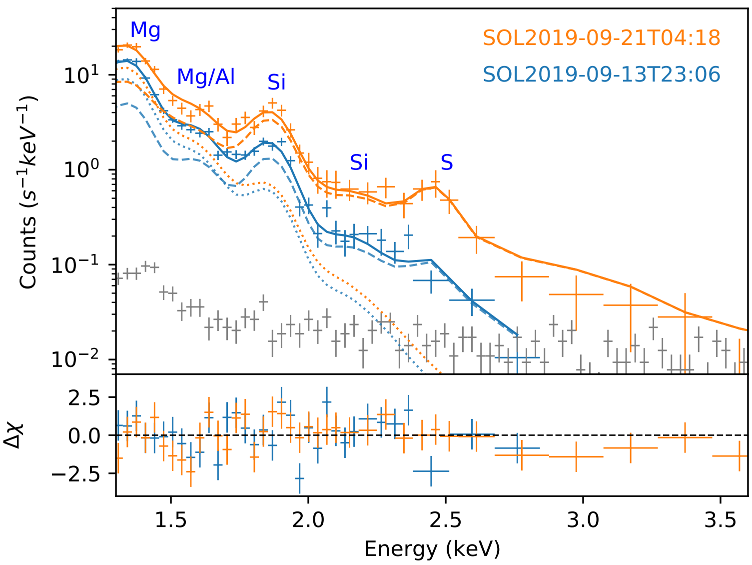

Figure 5.6: XSM spectra for two representative microflares (data points with errors) are shown with the respective best-fit models. The best-fit models for microflares, shown with solid lines, consist of two components: one corresponds to the background quiet Sun emission (dotted lines), and the other corresponds to the flaring plasma emission (dashed lines). The gray color points represent the non-solar X-ray background spectrum. Residuals are shown in the bottom panel.

XSM spectra of the microflare are fitted to obtain the temperature and emission measure (EM). Observed spectra and respective best-fit models are shown for two microflares in Figure 5.6. Two temperature models with one component frozen to the quiet Sun parameters fit the observed spectra very well as can be seen in the figure. Robust measurements of temperature and EM with uncertainties could be obtained for 86 of the 98 microflares. For the rest, the counts in the spectrum were too low; thus, we do not report parameters for those events.

Figure 5.7 presents the plot of temperature and EM of the XSM microflares along with the reported parameters from other microflare observations. The dashed lines in the figure represent isoflux curves corresponding to 1–8 Å flux. It can be seen from the figure that XSM has detected events with peak flux from $\sim 10^{-10}$ Wm^{-2}. The orange shaded region in the figure shows the temperature and EM range (lower end) of the AR microflares observed by RHESSI (Hannah et al., 2008), and it can be seen that the XSM microflares have much lower temperature, EM, and thus flux compared to those events. On the other hand, the parameters of XSM microflares are very similar to the NuSTAR events, including the four events observed in active regions. This again suggests that microflares observed in the quiet Sun with XSM arises from the same physical processes as that of the flares in AR.

It may be noted from Figure 5.7 that two of the NuSTAR quiet Sun microflares (Kuhar et al., 2018) are weaker than all the XSM events, which is not surprising given the sensitivity of NuSTAR. We also note that the temperature and EM of the 16 microflares from SphinX show systematic differences from that of XSM and NuSTAR events. One possibility is that the parameters for SphinX are obtained by fitting a single temperature model without subtracting or accounting for separate quiet Sun component (Sylwester et al., 2019). Although the temperature and EM differ for the SphinX events, they fall along the same isoflux lines and are thus similar.

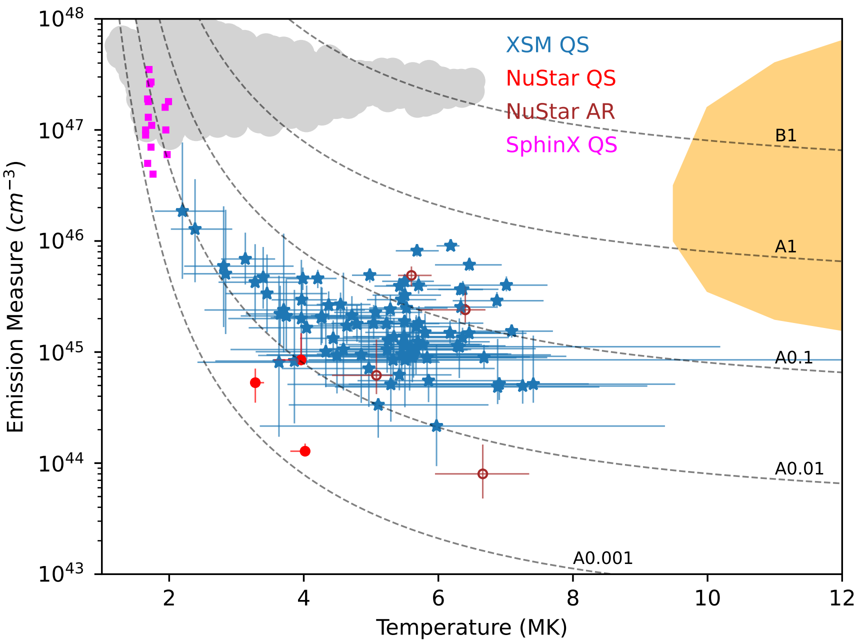

Figure 5.7: Temperature and EM for 86 of the 98 quiet Sun (QS) microflares observed by the XSM are shown with blue star symbols. The error bars represent 1σ uncertainties. Magneta squares and red filled circles correspond to QS microflares observed by SphinX (Sylwester et al., 2019) and NuSTAR (Kuhar et al., 2018), respectively. Parameter space of active region (AR) events observed by RHESSI (Hannah et al., 2008) and SphinX (Gryciuk et al., 2017) are shown with orange and gray shades, respectively. The brown open circles represent the four AR microflares reported by NuSTAR (Wright et al., 2017; Glesener et al., 2017; Hannah et al., 2019; Cooper et al., 2020). Dashed lines represent the isoflux curves corresponding to GOES/XRS $1-8$ X-ray flux levels from A0.001 (10^{-11} Wm^{-2}) to B1 (10^{-7} Wm^{-2}).

5.3.3 Flare Thermal Energy Distribution

To estimate the thermal energy associated with the microflares, we use the temperature (T) and emission measure (EM) obtained from X-ray spectral analysis and the volume (V) estimates from the area calculated using AIA images. Thermal energy (E_{th}) is computed using the following equation (Hannah et al., 2008):

$$E_{th} \sim 3\ k_{\rm B}T\ \sqrt{EM \times V} \tag{5.3}$$

where $k_{\rm B}$ is the Boltzmann constant. In this calculation, an upper limit of the filling factor of one is assumed. It may also be noted that the volume is estimated from EUV images that may represent plasma at even lower temperatures than the X-ray emission region. Thus, the volume may also be considered as an upper limit. So, the energy estimated is an upper limit to the thermal energy associated with the events. Among the 98 microflares, temperature, EM, and volume are available for 63 events, and thermal energy could only be estimated for these events. Uncertainties (only statistical) associated with thermal energy were computed by propagating the uncertainties on measured temperature and EM.

The estimated thermal energies of the events range from 3×10^{26} to 7×10^{27}erg. Figure 5.8a shows the histogram of thermal energies of the microflares, normalized with exposure time and the Sun disk area. Errors on the histogram are computed from counting statistics. It can be seen from the figure that the distribution agrees reasonably with a power law, but there is a departure from the power law at the lowest energy bins. This is expected as it is less likely to detect fainter events against the quiet Sun background emission. Similar trends are seen in the distribution of flares from previous studies as well (Hannah et al., 2011).

We then fitted the observed frequency distribution ($N(E)$) with energy (E), ignoring the first two bins, with a power law model as

$$N(E) = N_0 \left(\frac{E}{10^{25}}\right)^{-\alpha} \tag{5.4}$$

We find that the best fit power law index $\alpha = 1.92$ and normalization $log(N_0) =$

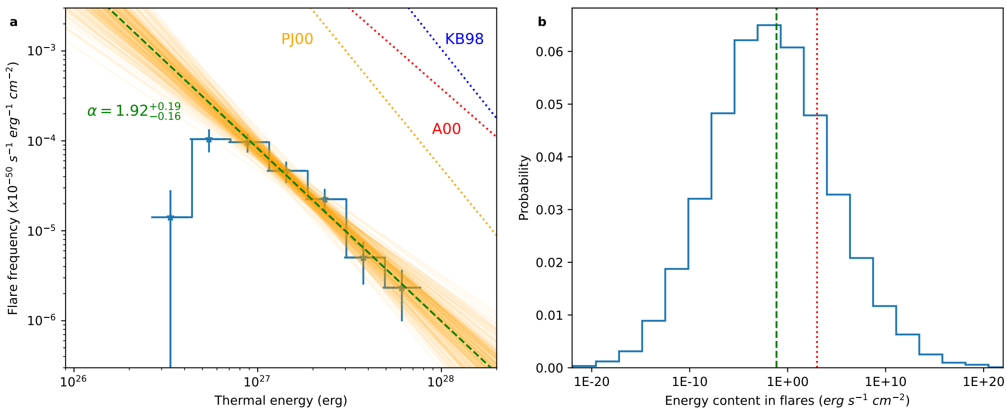

Figure 5.8: Panel **a** shows the frequency distribution of thermal energies of microflares. The green dashed line corresponds to the best-fit power law, and the yellow lines correspond to representative power law parameters from the posterior distribution shown in Figure 5.9. The dotted lines correspond to power laws reported from quiet Sun EUV observations by Krucker & Benz (1998)[KB98], Aschwanden et al. (2000b) [A00], and Parnell & Jupp (2000) [PJ00] as shown in Figure 10 of Aschwanden et al. (2000b). Panel **b** shows the posterior distribution of total energy content of the power law integrated over the range of $10^{24}-10^{28}$erg. The green dashed line represents the most probable value corresponding to the best-fit power law. The red dotted line shows the typical heating requirement of the quiet corona during solar minima.

−0.24. Integrating this power law distribution from the typical nanoflare energies (10^{24} erg) to microflare energies (10^{28} erg), we find that the total thermal energy released by such small-scale reconnection events is ~ 0.08 erg cm^{-2} s^{-1}, which is significantly lower than the heating requirement of the quiet corona ($\sim 10^3$ erg cm^{-2} s^{-1}) during solar minimum (Aschwanden, 2001).

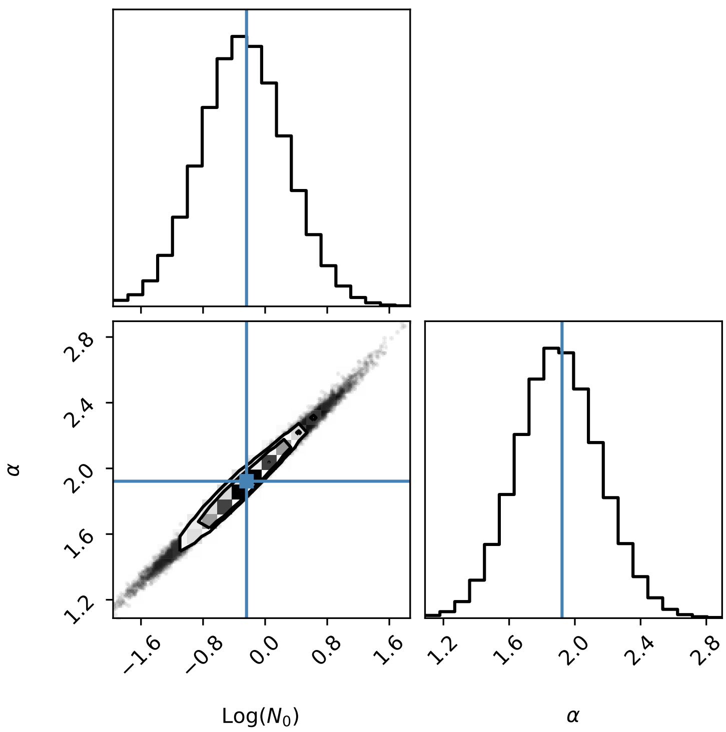

Figure 5.9: Posterior distributions of power law model parameters obtained from Monte Carlo simulations as discussed in text. Blue lines mark the best fit parameters.

To estimate the realistic uncertainties on the power law parameters, we resort to Monte Carlo methods following a Bayesian approach. A large number (10^7) of parameter values were randomly sampled from a uniform distribution over the range of 1–3 for α and -2 to +2 for $log(N_0)$. Posterior probabilities were determined in each case by evaluating the Poissonian likelihood for the observed frequency distribution given the randomly sampled parameters, and they were accepted/rejected by comparing the probability against a uniform random variable. The final posterior density of the two parameters of the model obtained is shown in Figure 5.9. Marginalized distributions for both parameters are also shown in the same figure. For each of the accepted sets of random parameters, the total energy content is obtained by integrating the power law, and the probability density of the estimated energy content is shown in Figure 5.8b. Power law models for a set of 200 parameters randomly drawn from the posterior distribution are overplotted as yellow lines along with the observed frequency distribution in Figure 5.8a.

Thus, considering the uncertainties in the power law index, a much wider range of energy release rates is possible. This is evident from the estimated posterior distribution of the total energy release rate depicted in Figure 5.8b. Although the uncertainties of the power law index prevent us from conclusively determining whether the nanoflares alone are sufficient to heat the quiet solar corona; our measurements are undoubtedly incompatible with a much flatter power law, which would have ruled out the possibility with a high significance (Hudson, 1991).

Even though the present observations provide the largest sample of microflares in the quiet Sun, the total number is insufficient to make conclusive statements about the power law index and energy input to coronal heating. However, the observed histogram is certainly significantly different from the power law derived from previous quiet Sun nanoflare observations in EUV (Krucker & Benz, 1998; Aschwanden et al., 2000b; Parnell & Jupp, 2000) extrapolated to higher energies (see Figure 5.8a). Two of the flare frequency histograms in EUV were obtained during the solar minimum in 1998-99; thus, the difference may not be entirely attributed to the solar activity. One possibility is a significant change in the flare frequency distribution between typical nanoflare and microflare energies. The other possibility is that the EUV events have a different origin than the X-ray events. In either case, the present observations of the largest sample of X-ray microflares in the quiet Sun provide insights for further studies on understanding the role of small-scale reconnection events in coronal heating.

Another point to note is that we considered only the thermal energy associated with the flare, like many previous studies. The energy released in impulsive events may manifest in other forms, such as non-thermal particles and waves. It is important to consider the energy partition in various forms to fully understand the energy budget (Benz, 2017). Even for the thermal energy, we considered an isothermal plasma, which is not strictly correct. Recent studies have shown that the thermal energies of microflares are slightly underestimated when considering isothermal approximation as opposed to a more detailed DEM analysis considering multi-wavelength observations, including X-ray and EUV (Athiray et al., 2020). However, X-ray observations alone are generally considered consistent with isothermal plasma. In Chapter 6, we analyze the X-ray spectra of larger flares and show the presence of multi-thermal plasma as a step towards better estimates of thermal energies from X-ray observations alone.

With recent X-ray spectroscopic observations with NuSTAR, it has been possible to segregate thermal and non-thermal components in an A-class microflare, providing the possibility of estimating thermal and non-thermal energies (Glesener et al., 2020). Broad-band X-ray observations of small-scale events using the soft X-ray observations from XSM along with the hard X-ray instruments such as Solar Orbiter STIX (Krucker et al., 2020) and NuSTAR will provide better constraints on the thermal and non-thermal energies. Towards this, in Chapter 7, we present the joint spectral analysis of a C-class flare with XSM and STIX to obtain estimates of thermal and non-thermal energies.

5.4 Summary

In this chapter, we presented observations and analysis of the largest sample of sub-A-class microflares occurring in the quiet Sun using Sun-as-a-star observations with Chandrayaan-2 XSM. During the extended periods when no active regions were present on the solar disk, XSM detected 98 microflares, most of which followed an impulsive profile. Wherever the locations of the microflares could be identified using the EUV images from AIA, it is observed that they are associated with magnetic bipolar regions in the photosphere. From the analysis of X-ray spectra and EUV images, the temperature, emission measure, and volume were estimated for the microflares. Using these parameters, the thermal energies are estimated to range from $\sim 3 \times 10^{26} - 6 \times 10^{27}$ erg, and the flare frequency distribution with thermal energy follows a power law. With the observations in this chapter, we obtain stringent limits on the average rates of microflares in the quiet Sun during solar minimum having flux above $\sim 10^{-10}$ Wm^{-2} (thermal energies above $\sim 4 - 7 \times 10^{26}$erg) to be ~ 1.84 day^{-1}. Even though this was the largest sample of quiet Sun microflares, the statistics were insufficient to draw firm conclusions on the power law index of the flare frequency distribution and the contribution of small-scale events in coronal heating, observations of microflare events outside active regions do support the hypothesis of the presence of small-scale impulsive heating events in the solar corona.

Chapter 6

Multi-Scale Solar Flares: Heating of Multi-thermal Plasma in Flares

X-ray spectroscopic observations provide excellent diagnostics of the temperature distribution in solar flare plasma. In this work, we analyze the X-ray spectra of three representative GOES C-class flares from Chandrayaan-2 XSM to investigate the evolution of flaring plasma during the flare. The soft X-ray spectra in the energy range of 1–15 keV are modeled with the continuum and line complexes of elements like Mg, Si, and Fe, considering isothermal and multi-thermal X-ray emitting plasma. We show that spectra during the impulsive phase of large solar flares are inconsistent with an isothermal model and are best described with bimodal DEM distributions. The hotter component in the doubly peaked DEM distribution rises faster than the cooler component. We interpret the two distinct temperature components as arising from the direct heating of the plasma in the corona and the evaporation of plasma from the chromospheric footpoints. We also show that the Mg, Si, and Fe abundances reduce from nearly coronal to nearly photospheric values during the rising phase and recover during the decay phase of the flare, which is consistent with the chromospheric evaporation scenario.

A version of this chapter is published in ApJ *with the title 'Soft X-Ray Spectral Diagnostics of Multithermal Plasma in Solar Flares with Chandrayaan-2 XSM' (Mithun et al., 2022)*

6.1 Introduction

Understanding the plasma heating in solar flares requires knowledge of the temperature distribution of flaring plasma, which is best inferred from the X-ray and EUV observations (Benz, 2017; Krucker et al., 2008; Benz, 2017). Emission across different wavelengths suggests that the flaring plasma is multi-thermal. The differential emission measure (DEM) quantifies the amount of thermal plasma at different temperatures along the line of sight. As spectral lines from different species are formed at different temperatures, spatially resolved spectroscopic observations would be best suited for inferring the DEM of flaring plasma. There have been concept designs of instruments that would provide such measurements (Laming et al., 2010; Matthews et al., 2021; Del Zanna et al., 2021a), but there are currently no such instruments available.

Spatially resolved DEMs can be obtained by using imaging observation in different wavelength bands, such as in EUV with SDO AIA (Cheung et al., 2015; Su et al., 2018) or in X-rays with Hinode XRT (Goryaev et al., 2010), although they provide limited spectral information. Even though the wavelength bands are relatively narrow for AIA, multiple spectral lines formed at different temperatures fall within. In the case of XRT, there is a significant contribution from the continuum, which is strongly dependent on temperature monotonously. Due to these reasons, the temperature responses of different wavelengths are relatively broader, making it difficult to get unique DEM solutions.

Another possibility is using spatially integrated high-resolution X-ray or EUV spectra where individual lines formed at different temperatures are well resolved. Early observations using X-ray crystal spectrometers such as SMM/BCS and Yokoh/BCS provided evidence of multi-thermal plasma distributions (Doschek, 1990; Feldman, 1996). In recent times, DEMs have been measured in this manner using observations with SDO EVE (Warren et al., 2013) and RESIK (Sylwester et al., 2014; Kepa et al., 2018). As X-rays are more sensitive to hotter plasma ($\sim>$ 10 MK) than EUV, joint analysis of X-ray and EUV observations is useful. For example, joint analyses of EUV spectra from SDO EVE and hard X-ray spectra ($>$ 3 keV) with RHESSI have been used by

Caspi et al. (2014) and McTiernan et al. (2019) to obtain better constraints on DEM. More recently, similar studies have been done with the FOXSI hard X-ray imaging telescope (Athiray et al., 2020). As RHESSI observations start above 3 keV, observations in low energy X-rays down to 1 keV would complement the observations with RHESSI and the EUV observations. In this context, there have been attempts to use soft X-ray broadband flux measurements from GOES XRS along with EUV spectra to constrain the DEM (Warren, 2014). As the broadband counts from GOES are dominated by the continuum (Del Zanna & Woods, 2013), it provides limited temperature diagnostics compared to having spectral information.

Spatially integrated and spectrally resolved observations in soft X-rays would provide better diagnostic potential and complement EUV and hard X-ray observations. In the past, there have been a few such instruments like SOXS, SphinX, and MinXSS, which provided such observations. Often, spectra from these instruments are modeled with isothermal approximation; however, some studies have used X-ray spectra to infer the DEM (Awasthi et al., 2016). Soft X-ray spectra with sufficient energy resolution to resolve line complexes of individual elements can also measure the elemental abundances alongside the DEM, providing insights into the flaring process.

In this chapter, we investigate the evolution of DEM and elemental abundances during solar flares using observations with Chandrayaan-2 XSM. In Chapter 5, it was shown that the soft X-ray spectra of sub-A class microflares observed with XSM are consistent with emission from isothermal plasma. Another study of B-class flares with XSM observations found that isothermal models describe the X-ray spectra throughout the flare duration (Mondal et al., 2021b) and no inferences on multi-thermality of plasma could be derived from X-ray spectra alone in such cases. Here, we examine the X-ray spectra of larger, more complex C-class events and check their consistency with isothermal approximation. Further, we provide a scheme for DEM analysis of X-ray spectra, such as from XSM, considering simple functional forms for the DEM, and they are used to obtain the DEM evolution during the flares.

Details of flare observations and data reduction are given in Section 6.2.

Section 6.3 presents the analysis of spectra considering an isothermal approximation, and the analysis results considering a more generalized multi-thermal plasma are given in Section 6.4. Discussion of the results and conclusions are presented in Section 6.5.

6.2 Flare Observations

In this work, we selected three representative GOES C-class flares having 1-8 Å peak fluxes ranging from 1.5×10^{-5} Wm^{-2} to 8.5×10^{-5} Wm^{-2}, for which Chandrayaan-2 XSM observations are available for the entire flare duration. The flares considered are SOL-2020-10-16T12:57 (C1.57), SOL-2021-10-07T02:46 (C5.70), and SOL-2021-09-08T17:32 (C8.40). For each flare, X-ray light curves for different energy bands for 1-minute time bins are generated from the XSM raw data using `xsmgenlc` task from the XSM Data Analysis Software (Mithun et al., 2021a). It may be noted that these are corrected for effective area variations with time due to changes in Sun angle. XSM light curves in different energy ranges for all three flares are shown in Figure 7.2. Grey lines in the figure show the 1–8 Å flux measured by the GOES-16 XRS instrument.

The figure shows that all three flares follow an impulsive rise and gradual decay phase. As expected, the light curve in the higher energy bands peaks earlier than progressively lower energy bands. The derivative of the soft X-ray (1 – 15 keV) XSM light curve is computed and is also shown in the figure. This derivative light curve is expected to resemble the impulsive hard X-ray emission, following the Neupert effect (Neupert, 1968). We denote the peak of the flux derivative as the impulsive phase peak, which is marked by a vertical dashed black line in the figure. The figure also shows the peak times of 1 – 15 keV light curves with vertical blue dotted lines.

Further, for spectral modeling, we generate time-resolved spectra for the flare duration at an interval of one minute using `xsmgenspec` module of the XSMDAS. We also examined spectra at lower time bins, but a bin size of 1 minute was chosen to ensure sufficient statistics in the spectra to perform the fitting. Response files in standard formats compatible with XSPEC (Arnaud, 1996) were

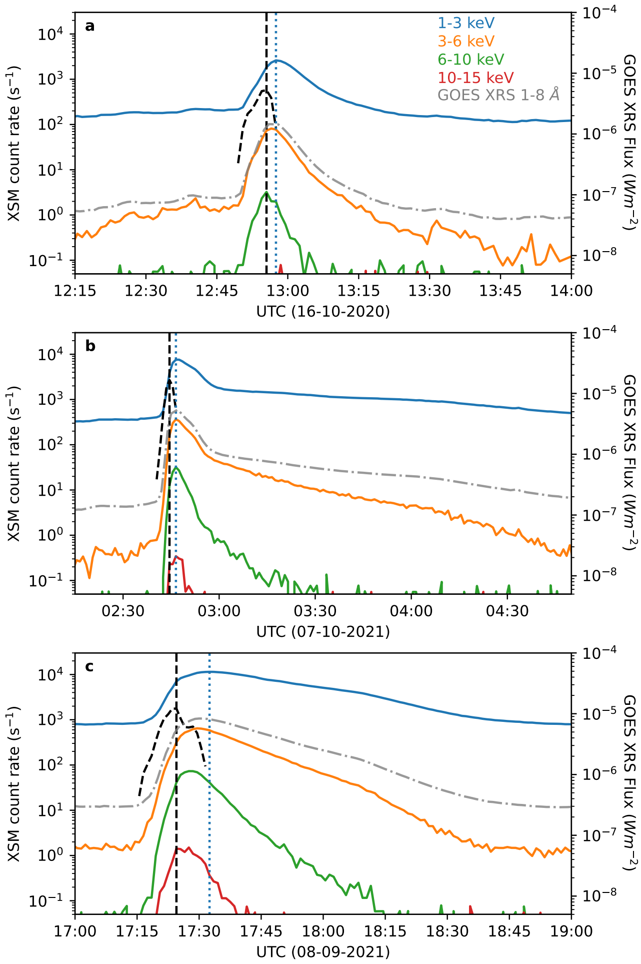

Figure 6.1: XSM light curves in different energy bands at 1 minute cadence for the three C-class flares on 16-Oct-2020 (**a**), 07-Oct-2021 (**b**), and 08-Sep-2021 (**c**). The grey dot-dashed line shows GOES XRS 1-8 Å band flux. The y range of the figures is restricted so that the counts shown are detected at least at two sigma significance. The black dashed line corresponds to the derivative of the XSM 1–15 keV count rate, and the vertical black dashed line denotes the peak of the impulsive phase where the derivative is maximum. The blue vertical dotted line corresponds to the peak of the 1–15 keV light curve.

also generated along with the spectra. By default, spectra are generated for an energy bin size of 33 eV. However, at higher energies, counts in individual channels of 33 eV bins are too low; so, counts in such channels were grouped using the `grppha` in FTOOLS [1]. As discussed in Section 3.4.2, the effective area of

[1] https://heasarc.gsfc.nasa.gov/lheasoft/ftools/fhelp/grppha.txt

XSM is not well modeled by the response below 1.3 keV. Thus, only the spectrum above 1.3 keV is considered in the spectral fitting. Using observations when the Sun was out of the XSM FOV, the non-solar background spectrum was obtained, and this background spectrum is considered while fitting the flare spectra. The solar spectra have much higher counts at lower energies than the background, which is not the case at higher energies. So, we identify the energy where the solar spectrum becomes comparable to the background and limit spectral fitting till that energy for that spectrum. For this reason, the energy range considered in fitting will slightly differ for each spectrum.

6.3 Isothermal Approximation

The soft X-ray spectra of solar flares are often modeled with an isothermal approximation with the model parameters as temperature, volume emission measure, and abundances of various elemental species. The previous chapter (Chapter 5) shows that the soft X-ray spectra of small sub-A class flares are consistent with isothermal approximation. Further, in an investigation of B-class flares observed by XSM during the first two observing seasons by Mondal et al. (2021b), it has been shown the spectra in different intervals during the flares are also consistent with isothermal models. Previous studies of C-class flares using Chandrayaan-1 XSM by Narendranath et al. (2014a) have shown that the spectrum above 1.8 keV are reasonably consistent with isothermal models. As isothermal models are the simplest, we first analyze the spectra of the three C-class flares selected for this work using them.

We use the time-resolved spectra generated, as discussed in the previous section, in PyXSPEC[2], the Python interface for XSPEC for spectral fitting. We use the model `chisoth`[3], the same as that used in the analysis of sub-A class flares in the previous chapter for spectral fitting. As an initial value, the abundances of elements are set to the coronal abundances from Feldman (1992) while fitting. For each spectrum, elements with major line complexes within the energy range

[2] https://heasarc.gsfc.nasa.gov/xanadu/xspec/python/html/index.html
[3] https://github.com/xastprl/chspec

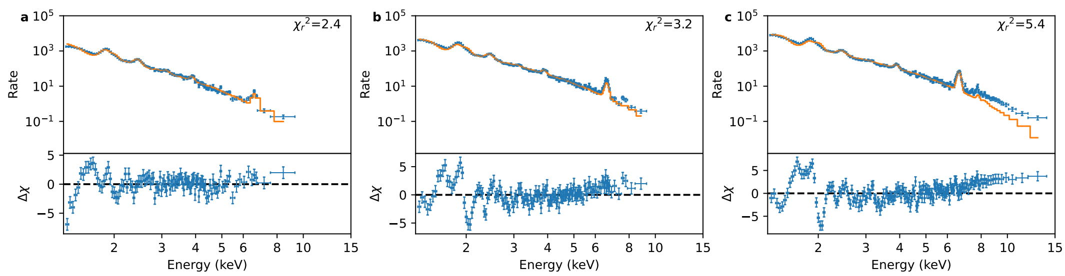

Figure 6.2: XSM spectra of the three flares (panel **a**: C1.57, panel **b**: C5.70, panel **c**: C8.40) at their impulsive phase peak (marked by vertical dashed lines in Figure 7.2) fitted with an isothermal model. Orange lines show the best-fit models and residuals are shown in the lower panels.

considered for fitting are identified. Abundances of these elements are left as free parameters in the fitting, while the rest are frozen to the initial coronal values. For example, if a given spectrum extends to energies beyond the Fe line complex at $\sim$ 6.5 keV, the abundance of Fe is a free parameter in fitting along with the abundances of other elements with line complexes in the 1.3 – 6.5 keV energy range. Mg and Si lines are prominently present in all spectra, and their abundances are varied to fit all spectra. Abundances of other elements with major lines, i.e., S, Ar, Ca, and Fe, are allowed as free parameters for spectra in some intervals depending on the presence of the corresponding line complex in the spectrum. In the analysis of sub-A class flares in the previous chapter, a separate component for pre-flare emission was considered in the fitting as the quiescent and flare emissions were comparable. In the case of C-class flares considered in this chapter, the quiescent emission is negligible compared to the flare emission. It has been observed that, even for B-class flares, the pre-flare emission has no significant impact on the inferred parameters of the flare emission (Mondal et al., 2021b). Thus, we do not include a separate pre-flare quiescent emission component in the spectral analysis.

XSM spectra for one-minute intervals at the peak of the impulsive phase of all three flares are shown in Figure 6.2 along with the respective best-fit isothermal models and residuals. The figure shows that the isothermal model can explain the spectrum successfully for the weakest event in the sample (2020-10-16).

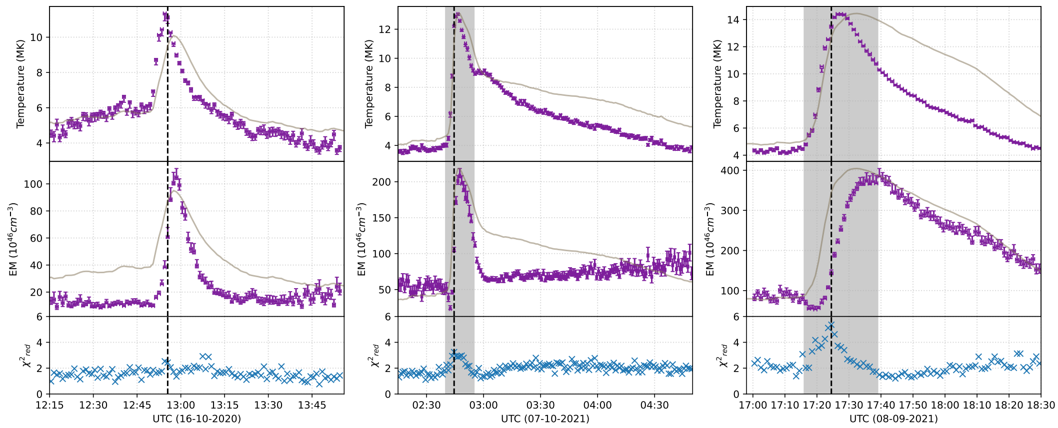

Figure 6.3: Results of an isothermal fit to the time-resolved spectra of the three flares. The top and middle panels show best-fit temperature and emission measure with one-sigma uncertainties. Lower panels show the reduced chi-squared of the spectral fits. The vertical dashed lines mark impulsive phase peak times. For the two brighter events, the reduced chi-squared is higher than the acceptable range around the impulsive peak, marked by the grey-shaded region.

However, this is not the case for the other two events. From the residuals and goodness of fit given by chi-squared, we can conclude that the isothermal model is insufficient for those two events at these time bins. For all three flares, the results of spectral fits to each one-minute interval during the flare are shown in Figure 6.3, where the three vertical panels correspond to temperature, emission measure, and reduced chi-square. In all cases, the reduced chi-square values are within acceptable range during the early and late decay phases of flares, suggesting that the spectra are consistent with emission from an isothermal plasma. For the weakest event on 16 October 2020, the isothermal model reasonably fits the spectra for the entire flare duration. For the other two events, the isothermal approximation is not valid during the impulsive phase of the flares marked by the grey-shaded region in Figure 6.3, as apparent from the increased reduced chi-square values. The peak of the impulsive phase determined from the soft X-ray light curve derivative in Figure 7.2 is shown with the vertical dashed line in Figure 6.3. It can be seen that the departure from the isothermal model (maximum value of reduced chi-square) coincides with the impulsive phase peak.

6.3.1 Effect of temporal averaging

It may be noted that the temperature and emission measure increases rapidly during the interval when there is a significant departure from the isothermal model. As the spectra are averaged over one-minute intervals, one possibility is that this temporal averaging is the reason for the observed inconsistency with single-temperature models. To investigate this, we carried out the following analysis.

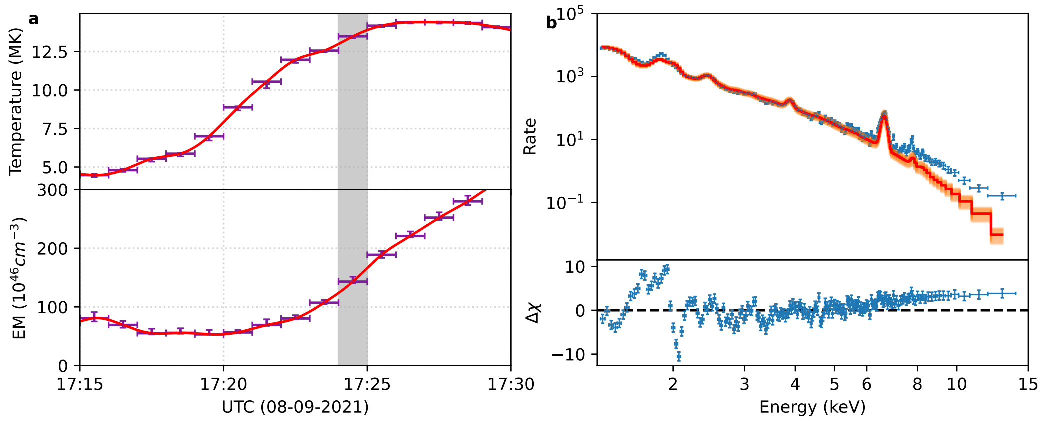

Figure 6.4: Panel **a** shows temperature and emission measure of the 08-Sep-2021 flare. The red line is interpolated values from the measurements at one minute. The spectrum for the grey-shaded interval (17:24-17:25) is shown in panel **b** with blue data points. Isothermal models corresponding to the interpolated temperature and EM for each second within the interval are shown with light orange lines. The solid orange line shows the average model considering the variation of temperature and EM. Residuals of the observed spectrum with this average model (solid orange line in upper panel) are shown in the lower panel.

Temperature and emission measure obtained from modeling one-minute cadence spectra show smooth variations with time (see Figure 6.3). Thus, we can interpolate the fitted parameters at each minute to obtain the parameters at each second, as shown in Figure 6.4a for the event on 08 September 2021. Then, we compute the model spectrum for each one-minute interval by summing the isothermal spectra at each second with the interpolated temperature and emission measure values. It may be noted that the abundances were not interpolated as they do not have any significant impact. In Figure 6.4b, a comparison of this model taking into account the temporal averaging with the observed spectrum is shown. It can be seen that the model is not consistent with the observations, and there is only marginal improvement with respect to isothermal model fits. We also generated spectra for shorter intervals than a minute near the impulsive peak and found that they are inconsistent with isothermal approximations, even with higher statistical uncertainties. Based on this analysis, we conclude that temporal averaging of spectra when the temperature and emission measure evolves at a fast rate does not explain the deviations from the isothermal models; thus, the soft X-ray spectra during the impulsive phase of flares show the presence of multi-thermal plasma.

6.3.2 Range of temperatures in multi-thermal plasma

As it is clear that the plasma is multithermal, we analyzed the spectrum differently to get the range of temperatures involved. The low energy part of the spectrum, which is expected to be sensitive to lower temperatures, and the high energy part of the spectrum, which is sensitive to higher temperatures, are fitted separately. As shown in Figure 6.5, spectrum in the 1.3 – 4 keV range and 4 – 15 keV range are fitted separately with isothermal models, with abundances frozen to the best fit isothermal fit results. A model with the log of temperature (logT) of 7.03 (shown in blue in the figure) fits the spectrum below 4 keV well while severely under-predicting the emission at higher energies. On the other hand, the isothermal model corresponding to logT of 7.26 fits the high energy part of the spectrum, including the Fe line complex, but deviates from the observations at lower energies. Specifically, the model predicts very different line shapes for Mg, Si, and S line complexes. Although the abundances were frozen initially, we checked if any reasonable variations in abundances (between photospheric and coronal values) could explain the deviations and found that abundances do not impact the inferences. Thus, we conclude that at the peak of the impulse phase, plasma having temperatures closer to these two values is required to explain the observed spectrum. In the next section, we model the spectra with multi-thermal distributions to obtain the actual temperature distributions.

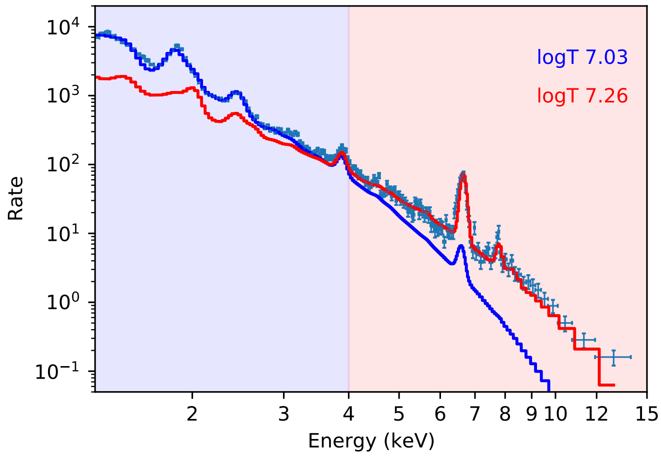

Figure 6.5: Spectrum during the impulsive phase of the 08-Sep-2021 flare (17:24-17:25 UTC) fitted with two different isothermal models considering only part of the spectrum. The spectrum below 4 keV (blue-shaded interval) is fitted to obtain the best-fit model shown in blue and a fit to the spectrum above 4 keV (red shaded interval) gives the best-fit model shown in red.

6.4 Multithermal Plasma: Differential Emission Measure Analysis

The Differential Emission Measure (DEM) describes the distribution of multi-thermal plasma, which provides the amount of plasma along the line of sight having temperature between T and T+dT (Del Zanna & Mason, 2018). Using non-imaging observations, as the spatial distribution of the plasma cannot be measured, we obtain the differential on the volume emission measure (cm^{-3}) over temperature (T) defined as:

$$DEM(T) = \frac{d({N_e}^2 V)}{dT} (\mathrm{cm^{-3} K^{-1}}) \tag{6.1}$$

where V is the volume and N_e is the electron density. In other words, the volume emission measure is the integral of DEM over temperature:

$$EM = \int DEM(T)\, dT \tag{6.2}$$

Several techniques have been developed to measure the DEM from the observations over different wavelengths. The most common approaches are direct inversion and forward fitting by χ^2 minimization (see Del Zanna & Mason (2018) for a review of methods for DEM estimation). For inferring the DEM from XSM spectra, we follow the χ^2 minimization approach. In DEM analysis with other instruments, such as the EUV imagers, flux in a few energy bands is the available measurement, not the entire spectrum. Thus, even for X-ray observations, counts over broader energy bins are often used as input to the DEM analysis. As the full energy spectrum is available with XSM observations, we first investigate the sensitivity of different XSM channels to different temperatures to decide the better inputs for DEM analysis.

6.4.1 XSM temperature response and temperature sensitivity of line profiles

To investigate the sensitivity of XSM spectra to distinguish different temperatures, we compute the temperature responses of XSM energy channels. Isothermal model spectra are computed using the `chisoth` model for different temperatures and then convolved with the XSM response matrix to obtain the simulated count spectrum at different isothermal temperatures. In Figure 6.6a temperature responses of XSM for each 1 keV energy band from 1 keV to 15 keV are shown. It can be seen that the shape of temperature responses in all energy channels except two are similar with increasing response to higher temperatures. This can be understood as the continuum dominates the emission in all these energy bands. In contrast, the 1 – 2 keV and 6 – 7 keV bands include strong line contributions from Mg/Si and Fe, respectively. Temperature response of 1 – 2 keV band shows a local maximum around logT of 7.1. Normalized temperature response for finer energy bins around the Si line complex is shown in Figure 6.6b. Different energy channels are most sensitive to different temperatures in the range of log T from $\sim$6.9 to $\sim$7.3, which explains the local maximum seen in the temperature response of the 1 – 2 keV band. Lines from different ionization states of Si are formed at different temperatures, and although these lines are blended, the energy resolution of XSM allows to disentangle emission at different temperatures. Another way to look at this is as in Figure 6.6c, where normalized spectra near the Si line complex are shown for different temperatures, demonstrating the change in line shapes with temperature. Similar changes in line profiles are observed for the Fe line complex, albeit to a much lesser extent, as shown in Figure 6.6d.

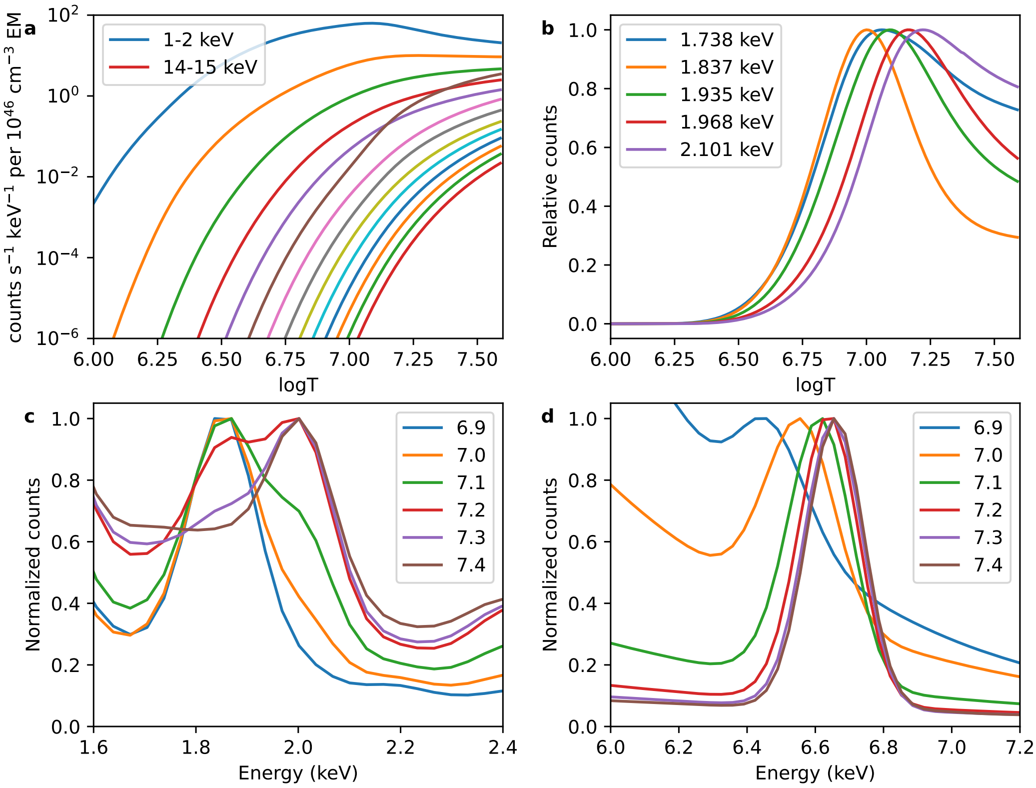

Figure 6.6: Panel a shows the temperature response of the XSM in 1 keV energy bins from 1 to 15 keV in sequence, while panel b has normalized temperature responses of selected energy channels near the Si line complex. Simulated XSM spectra near the Si and Fe line complexes at different temperatures are shown in panels c and d, respectively.

From this analysis, we infer that the XSM spectra, especially near the Si and Fe line complexes, show distinctly different responses at different temperatures, making it possible to determine contributions from different temperatures in the range of logT 6.9-7.3. As the line shapes are crucial features allowing to distinguish between different temperatures, we conclude that it is best to use the full spectrum in DEM analysis instead of considering counts in broader energy bands.

6.4.2 Emission measure loci

The emission measure loci method allows us to assess plasma distribution at different temperatures without any fitting (Del Zanna & Mason, 2018). In this, we plot the ratio of observed counts in each energy bin to the expected counts in that energy bin arising from isothermal plasma at different temperatures obtained from simulations. The loci of these curves form the upper limit to the emission measure distribution. In the case of emission from isothermal plasma, the curves of all energy bins would intersect at the same point.

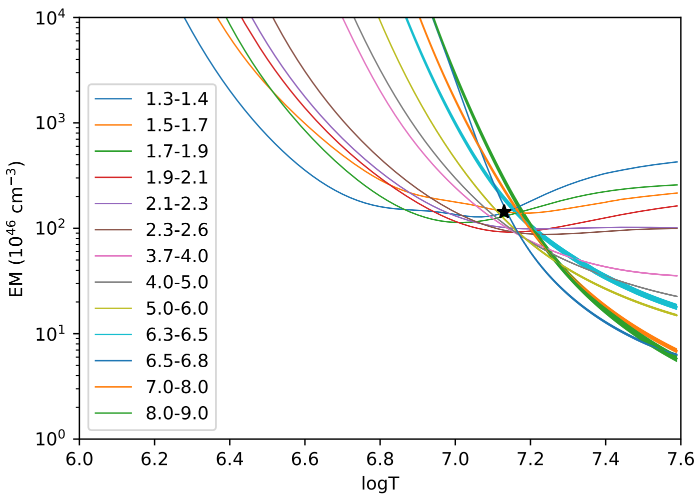

Figure 6.7: EM loci curves obtained from XSM spectrum during the impulsive peak of the 08-Sep-2021 flare. Each line corresponds to the ratio of the observed counts in the given energy range to the counts predicted by the model for an isothermal plasma with the EM of 1 cm^{-3} at different temperatures. The width of the lines takes into account the one-sigma uncertainties of the observed counts. The black star shows the best fit isothermal temperature and emission measure.

Figure 6.7 shows the EM loci curves for the XSM spectrum at the peak of the impulsive phase of the flare on 08 September 2021. Ideally, we can plot one curve for each spectral channel of XSM. However, to avoid overcrowding in the figure, we choose only specific energy bins near various line complexes and some corresponding to the continuum at different energies. As the curves do not intersect at the same point, it is again confirmed that an isothermal approximation is invalid. Some intersect at a point that matches the temperature and EM from the isothermal fits. Still, there are other curves that do not pass through this point, which is not surprising given the residuals seen for the isothermal model.

6.4.3 Multi-thermal model fitting

EM loci curves in the previous section provide an upper limit to the true DEM. It is possible the DEM distribution may take any shape below this upper limit. However, to obtain an estimate of the DEM, we need to make some assumptions for functional forms of the DEM shape. As discussed earlier, to use the full information available, we use the XSM spectra in all channels as the input to the DEM analysis. So, we use the standard forward folding approach for DEM analysis, similar to the isothermal analysis. For a given DEM distribution defined by a set of parameters, the model spectrum is computed, convolved with the instrument response, and then fitted with the observed spectrum using PyXSPEC. The parameters defining the DEM are obtained from the spectral fitting. In this work, we consider three DEM models: two-temperature model, Gaussian DEM, and double Gaussian DEM.

The most straightforward extension of an isothermal model is the sum of two isothermal models with independent temperatures and emission measures, given that the analysis in Section 6.3.2 suggested that spectra may be fitted with two temperatures. This can also be considered as a DEM with two delta functions at two temperatures. Such models have been used in studies of flares earlier (e.g., Caspi & Lin, 2010). Analysis with this model is straightforward in PyXSPEC (or XSPEC) as the model with two `chisoth` model components added together with independent parameters.

For a broader temperature distribution, a natural choice is a Gaussian distribution(Aschwanden et al., 2015a) defined by the temperature T_p at the peak EM, the peak emission measure (EM_p), and the width of the Gaussian (σ) as:

$$DEM(T) = EM_p exp\left(- \frac{(log(T) - log(T_p))^2}{2\sigma^2} \right) \tag{6.3}$$

Such a model has been implemented within XSPEC named `chgausdem`[4], which provides a model spectrum for a Gaussian DEM with peak temperature, width, and peak emission measure as input parameters. This is an extension of the `chisoth` model where isothermal spectra over a grid of temperatures are added together, weighted with the emission measure at each temperature as defined by the Gaussian DEM function. In addition to Gaussian parameters, abundances of elements are also parameters of this model.

Although the Gaussian function provides a broad temperature distribution, there is a constraint that only one maximum exists. The actual DEM may likely have multiple peaks, and one way to accommodate this is by considering the summation of multiple Gaussians (Caspi et al., 2014). However, such a model would have many free parameters leading to several degenerate results. Thus, instead, we consider a DEM function with only two Gaussians where the parameters of Gaussians are independent. One can consider that this is a more generalized and realistic version of the two-temperature model as it allows finite width to the EM distributions at two temperatures instead of delta functions.

Temperature and EM distribution

We fitted the spectra during the flares with the three multi-thermal models, leaving the DEM parameters and abundances of elements with prominent lines (similar to isothermal analysis) as free model parameters. As an example, Figure 6.8 shows the fit results for the spectrum at the impulsive peak for the event on 08 September. The observed spectrum overplotted with best-fit models is shown in Figure 6.8a, and the residuals are also shown for each case. Respective best-fit DEM distributions are shown in Figure 6.8b, where one-temperature and two-temperature models are shown with delta functions.

[4] https://github.com/xastprl/chspec

Comparing the residuals, it is clear that all multi-thermal models better fit the observed spectrum than the isothermal model. There is a significant reduction in residuals near the Si line complex (below 2 keV) and at higher energies, which is also reflected in the reduced chi-square values. It is important to note that all three multi-thermal models fit the observations equally well, and it is difficult to favor one among these models based on goodness of fit alone as they are all equally acceptable.

As seen in Figure 6.8b, the two-temperature model has one component at temperatures below 10 MK and another at higher temperatures, with a lower emission measure for the high-temperature component. The isothermal temperature and emission measure falls in between these two. Gaussian DEM fitted to the spectrum is a very broad distribution peaking at logT of 6.8, having emission measures distributed over lower and higher temperatures. The double Gaussian models have peaks closer to the temperatures obtained from the two-temperature model fit, and the distributions are much narrower compared to the single Gaussian DEM.

Further, we did a Markov Chain Monte Carlo (MCMC) analysis to estimate the best-fit DEM models' uncertainties. This was done using the `chain` command within PyXPEC, and the selected MC parameters were written out. Thin lines in Figure 6.8b show the DEMs computed from the few randomly selected parameter values from the MCMC result, and the spread of these DEMs around the best fit DEM (thicker line) represents the uncertainties. It can be seen from the figure that the lower temperature component of the two-temperature model is less constrained as compared to the higher temperature component. In the case of the Gaussian DEM, we also notice that the DEM at lower temperatures has larger uncertainties. Given that the XSM spectra are less sensitive to lower temperatures in the presence of high-temperature plasma, this is consistent with the expectations.

To obtain the temporal evolution of the DEM, we fitted the spectra of each one-minute interval with the three DEM models. As the faintest of the three flares (event on 16 October 2020) was consistent with the isothermal model for the entire flare duration, we do not consider that event for multi-thermal analysis.

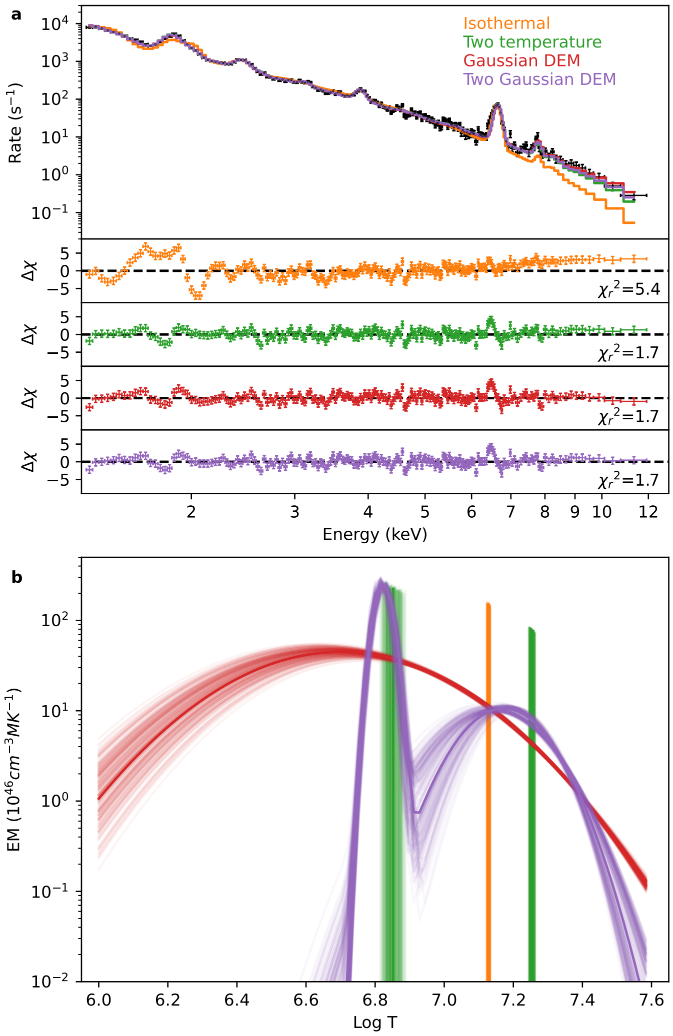

Figure 6.8: **(a)** XSM spectrum of the impulsive peak of the 08-Sep-2021 flare fitted with the three multi-thermal models and isothermal model. The best fit with each model is shown in different colors, and the residuals are shown in the lower panels. **(b)** The best fit DEM models from the spectral fit in the panel **a** are shown with the respective colors as thick lines. Lighter color lines correspond to DEMs from 100 random samples from the MCMC analysis, showing the uncertainty of the derived DEM models.

Figure 6.9 shows the evolution of DEM obtained from the spectral fitting for the 08-Sep-2021 flare (panel a) and the 07-Oct-2021 flare (panel b). The top three panels show the temporal evolution of the DEM considering the two-temperature model, the Gaussian model, and the double Gaussian model. The color denotes

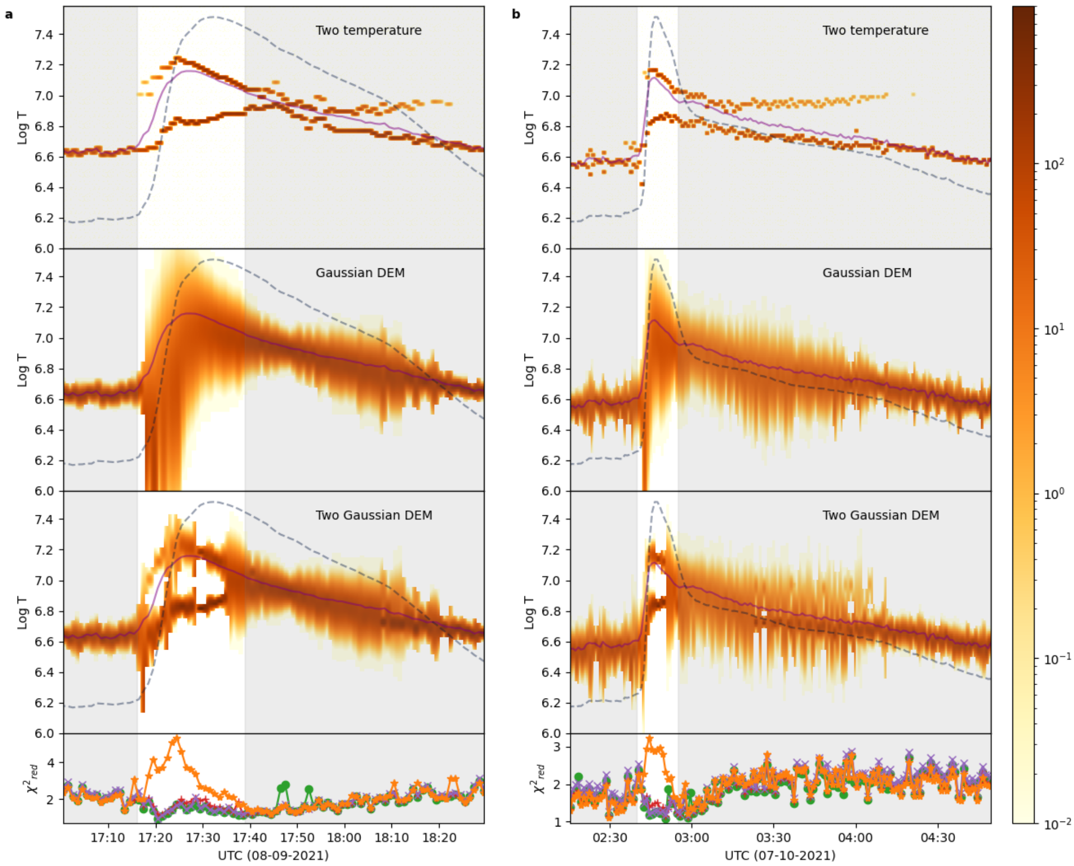

Figure 6.9: Evolution of DEM for the 08-Sep-2021 flare (a) and the 07-Oct-2021 flare (b) obtained from spectral fitting. The top three panels show DEM with two-temperature, Gaussian, and double Gaussian models, respectively. Color represents the EM in units of $10^{46} cm^{-3} MK^{-1}$. The isothermal temperature measurements (purple solid line) and 1–15 keV X-ray light curves (dashed line) are also shown for reference. The reduced chi-squared of the fit with the two-temperature (green), Gaussian (red), and double Gaussian (purple) models are shown in the lowermost panels. The reduced chi-squared for the isothermal fit is shown in orange for comparison. Intervals when the isothermal and multi-thermal models fit similarly to the spectra are greyed out. During the remaining period in the impulsive phase, the DEM models better fit the spectra than the isothermal model.

the emission measure at each temperature for a given time bin. The X-ray light curve and the isothermal temperatures are overplotted for reference. The reduced chi-square of the fit with all three DEM models is shown in the lowermost panels along with that of the isothermal fit.

During the early and decay phases of both events (grey shaded region in Figure 6.9), all three models converge to a narrow distribution around the isothermal temperatures. Both temperature parameters in two-temperature and double Gaussian models are almost equal during these periods. This is consistent with the fact that isothermal models could fit the spectra for these periods, as found in the previous section, and the reduced chi-square for all three DEM models and the isothermal model are almost the same. However, as the reduced chi-square values show, the multi-thermal models better fit the spectra during the impulsive phase. We also note that, similar to the example in Figure 6.8, all three DEM models are equally acceptable for all the time bins.

In the temporal evolution of DEM shown in Figure 6.9, it can be seen that the two-temperature model and double Gaussian model results in two distinct temperature components in the impulsive phase, where the Gaussian distributions are narrow and around the temperatures obtained in two-temperature model fits. On the other hand, the single Gaussian model results in a very broad distribution extending to lower temperature with significant EM. However, soft X-ray spectra are not very sensitive to these lower temperature and the MCMC analysis also showed that there are higher uncertainties in the DEM at these temperatures. Thus, broad Gaussian DEM is less likely to be the actual DEM. While the two-temperature model with two delta functions as DEM is an over-simplification, the double Gaussian DEM could be likely closest to the true DEM during the impulsive phase of the flares.

Elemental abundances

The time-resolved spectral analysis of the flares also provide an interesting result on the variation of elemental abundances as they are also left as free parameters in spectral fitting. The best-fit abundances of the low-FIP elements Mg, Si, and Fe during the 08 September 2021 flare is shown in Figure 6.10. Abundances obtained from DEM fitting with different models are shown in different colors. In the figure, coronal abundances from Feldman (1992) is shown by pink dashed line, active region coronal abundances from Del Zanna (2013) is shown by the grey dashed line, and photospheric abundances from Asplund et al. (2009) is shown by the yellow dashed line.

It can be seen that abundances obtained assuming the three DEM models are very close to each other, except for some differences in the values obtained with the Gaussian DEM model in the impulsive phase. Anyways, the abundance variation follows the same trend in all cases. The Mg and Si abundances started close to coronal values before the flare and were reduced to the photospheric values during the rising phase. They return to the coronal value during the decay phase of the flare. As the Fe line is not observed in the spectrum during early or later intervals of the flare, it is impossible to capture the Fe abundance variation for the entire duration. However, Fe abundances also show a similar trend with some changes in the available measurements. It may be noted that a similar trend of variation of abundances was reported by Mondal et al. (2021b) for smaller B-class events observed by the XSM. The results show that the same applies to large flares, especially for Fe abundances, as it was not measurable for smaller flares.

6.5 Discussion and Conclusions

This chapter presented the analysis results of time-resolved soft X-ray spectra of three representative GOES C-class flares using observations with Chandrayaan-2 XSM. It has been shown that while the early and late phases of the flare spectra are consistent with isothermal plasma, the spectra during the impulsive phase of the two higher-intensity flares (C5.7 and C8.4 events) are not. Analysis of the spectra with three different multi-thermal DEM models composed of simple parameterized functions showed that the DEM models are favored over the isothermal assumption; however, all three different DEM models, i.e., two-temperature, Gaussian, and double Gaussian, provide equally acceptable fits to the spectra. During the impulsive phase, the derived DEMs are either a very

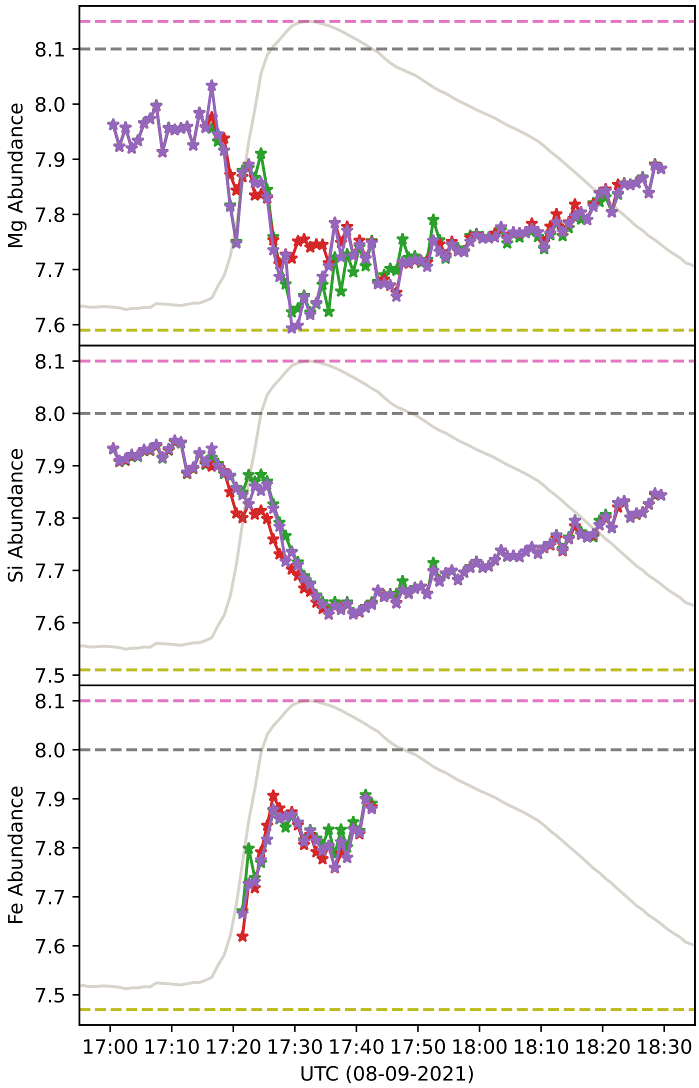

Figure 6.10: Measured abundances of Mg, Si, and Fe during the 08-Sep-2021 flare obtained from spectral fitting considering three different multi-thermal models: two-temperature (green), Gaussian (red), and double Gaussian (purple), are shown. Coronal abundances from Feldman (1992) and Del Zanna (2013) as well as photospheric abundances from Asplund et al. (2009) are shown with purple, grey, and yellow dashed lines, respectively. The X-ray light curve is shown in grey for reference.

broad distribution or a double-peaked distribution with two distinct temperature components. Given that the XSM spectra in the soft X-ray band are not sensitive to very low temperatures (logT $<\sim 6.3$), the broad Gaussian DEM is not well constrained at lower temperatures. The lower temperature part likely had to exist because the DEM shape is constrained to be a Gaussian. However, this is not the case with the doubly peaked Gaussian distribution, and it is more likely to be closer to the actual DEM.

The observed evolution of the DEM of flares with a broad DEM in the impulsive phase and a narrow DEM during the decay phase is similar to some of the previous reports (Warren et al., 2013; Caspi et al., 2014). DEMs with two peaks, as found in this work, have also been observed for flares with the REISK X-ray spectrometer (Sylwester et al., 2006; Kepa et al., 2008). The two temperature components likely have different origins if the DEM has a bimodal distribution during the impulsive phase, as inferred from the XSM spectra. One component corresponds to the evaporated chromospheric plasma filling the post-flare loops, while the other may be the plasma from direct heating in the loop/loop-top. Imaging observations of several flares in hard X-rays have shown the presence of coronal loop top sources in addition to the foot point sources (Krucker et al., 2008). In RHESSI observations of an X-class flare, Caspi & Lin (2010) reported the presence of a super-hot ($>$ 30 MK) component located higher in the corona and another hot component from the chromospheric footpoints. As the C-class flares in the current study are much weaker than the X-class flares, it is not surprising that the higher temperature components in the DEMs are not as high as this super-hot component. If we look at the rate of increase of the two temperature components, it can be seen that the higher temperature component rises much faster than the lower temperature. This further supports the idea that the former may be associated with the direct heating near the reconnection region.

The variation of abundances of low-FIP elements observed for the C-class flares in this chapter is similar to that observed by Mondal et al. (2021b) for B-class flares. Abundances going down from coronal to photospheric values during the rising phase of the flare are consistent with chromospheric evaporation. As suggested by Mondal et al. (2021b), the quick recovery back to coronal abundances is puzzling, and one possibility is the involvement of flare-induced Alfvén waves causing fractionation. Another interesting observation is that the

Fe abundances do not decrease to reach the photospheric values at the peak, unlike the trend in Mg and Si. This may be the result of the difference in abundance of the two temperature components while they are tied together in the fitting process, resulting in an intermediate value. Suppose the hypothesis that the hotter component plasma in corona is heated in situ is true; in that case, it will have coronal abundances with fractionated low-FIP elements, while the evaporated plasma from the chromosphere at lower temperatures would have photospheric abundances. Fe line is much more prominent at higher temperatures than lower temperatures, unlike Mg and Si lines (see Figure 6.5). Thus, abundance measurement considering the same values to both temperature components would have higher chances of getting an intermediate value for Fe than the other elements. The analysis with different Fe abundances for the two temperatures did not yield proper results, so this could not be confirmed. However, previous studies of Fe abundances during flare peaks with RHESSI spectra (sensitive to higher temperatures) showed abundances closer to coronal abundances (Phillips & Dennis, 2012) as opposed to photospheric abundances obtained from lower temperature lines (for e.g. Del Zanna & Woods, 2013). The explanation of observations of the Fe abundance in this work is consistent with these reports. It is also likely that some other factors may be responsible for this observed difference in the trend of Fe abundances. It can also be seen that the spectral fits, even with the multi-thermal models shown in Figure 6.8a, show small, but visible residuals near the Fe line complex. This aspect is investigated further in Chapter7.

The results presented in this chapter point towards a complex plasma heating process in solar flares. The observed bimodal temperature distribution and the evolution of abundances seem to support direct heating in the coronal loop top by magnetic reconnection and secondary heating by evaporated plasma. While the XSM spectra did provide insights into the broader temperature distribution, constraining the DEM over a wide range of temperatures require observations in different wavelengths sensitive to different temperatures. Further, for identification of the location of the origin of different temperature plasma, imaging observations are essential. For example, EUV observations with AIA are sensitive to lower temperatures than XSM and joint analysis of X-ray spectra and EUV fluxes can provide better constraints on the DEM, which we plan to take up in the future. Comparisons of model X-ray spectrum obtained from AIA DEM with the XSM observed spectrum of a B-class flare shown by Del Zanna et al. (2022) suggest that they agree with each other well and joint analysis would indeed be possible.

Further, the DEM at even higher temperatures and the distribution of non-thermal electrons accelerated by the flaring process is better constrained with observations at energies higher than the XSM energy band. Joint analysis of soft and hard X-ray spectra of flares provides the opportunity to simultaneously constrain the thermal and non-thermal populations and provide a better understanding of the energy partition in flares. In this context, we take up the joint analysis of X-ray spectroscopic observations with Chandrayaan-2 XSM in soft X-rays and Solar Orbiter STIX (Krucker et al., 2020) in hard X-rays in the next chapter.

Chapter 7

Multi-Scale Solar Flares: Thermal and Non-thermal Energies of Flares

The partition of energy into thermal and non-thermal particles in solar flares is key to understanding the flaring process. This study aims to investigate the thermal and non-thermal energies associated with a GOES C-class flare using broadband X-ray spectroscopy. We use spectroscopic observations in soft X-rays with Chandrayaan-2 XSM and hard X-rays with Solar Orbiter STIX. Time-resolved spectra during the flare from both instruments were analyzed independently first and then modeled jointly to infer the thermal and non-thermal parameters of the flare. We find that the spectra of both instruments are well-fitted with the same model consisting of a two-temperature thermal model and a thick target bremsstrahlung model. Flare volumes were estimated from the X-ray and EUV images from STIX and SDO AIA,respectively, which are used to obtain thermal energies. It is found that the energy of accelerated electrons is sufficient to explain plasma heating in this flare. We also examine the residuals observed in the Fe line complex and their origin from X-ray fluorescence from the photosphere.

7.1 Introduction

In the previous chapter, spectroscopic observations in soft X-rays were used to obtain the temperature structure of the multi-thermal plasma in solar flares.

Magnetic reconnection that causes the flares also accelerates electrons (and ions) to very high energies and forms a non-thermal population of particles that emit in hard X-rays (cf. Kontar et al., 2011).

Many studies of solar flares in X-rays relied on the observations with Reuven Ramaty High Energy Solar Spectroscopic Imager (RHESSI, Lin et al., 2002) that carried out hard X-ray imaging and spectroscopy of the Sun. While RHESSI observations provided unprecedented energy coverage to probe the non-thermal particle distribution, it had limited capability to probe the thermal plasma, particularly at low temperatures. X-ray spectra at higher energies, such as that with RHESSI, are biased to measure the highest temperatures of the multi-thermal plasma in the flares, and thus it is often difficult to discern the lower temperature components from the hard X-ray spectrum alone. Moreover, the total non-thermal energy critically depends on the low-energy cut-off of the electron distribution, which is a difficult parameter to measure as the emission from thermal plasma dominates in soft X-rays (Holman et al., 2011). Thus, better constraints on the thermal emission would provide improved estimates of the low energy cut-off and thereby, non-thermal energy.

Constraining the temperature structure of the thermal plasma requires observations in soft X-ray to EUV bands, as discussed in Chapter 6. Observations in EUV with spectrometers such as SDO EUV Variability Experiment (EVE, Woods et al., 2012) and imagers such as SDO Atmospheric Imaging Assembly (AIA, Lemen et al., 2012) are capable of deriving the differential emission measure (DEM) associated with the flaring plasma (Warren et al., 2013; Su et al., 2018). However, EUV observations are generally not sensitive to high temperatures, typically above $\sim$ 10 MK, and thus do not provide reasonable constraints at temperatures often present in flaring plasma. As discussed in Chapter 6, spectroscopic observations in soft X-rays complement the EUV and hard X-ray observations as soft X-rays have temperature responses between those of EUV and hard X-ray bands.

Joint analysis of flare observations in EUV/soft X-rays with hard X-ray observations can use their complementary sensitivities to obtain thermal and non-thermal parameters. There have been few attempts in this direction by combining the observations in EUV wavelengths from SDO EVE and hard X-ray observations by RHESSI. Caspi et al. (2014) have performed the joint fitting of EVE and RHESSI spectra with a model consisting of a DEM and non-thermal components. Similarly, Inglis & Christe (2014) analyzed a sample of microflares using observations with AIA and RHESSI and obtained estimates of thermal and non-thermal energies from the spectral fit parameters. Investigations have also been done to see if improved estimates of electron cut-off energy can be obtained by joint modeling of EUV and hard X-ray observations (McTiernan et al., 2019). More recently, Nagasawa et al. (2022) presented joint spectral fitting of soft to hard X-ray spectra of a solar flare using soft X-ray observation with MinXSS (Mason et al., 2016; Moore et al., 2018b) and hard X-ray observations with RHESSI. They showed the possibilities of such broad-band X-ray spectral studies of solar flares in deriving the evolution of thermal and non-thermal parameters.

In this work, we extend the studies in the previous chapter by combining X-ray spectroscopic observations in soft X-rays by Chandrayaan-2 XSM of a C-class flare with the hard X-ray spectroscopic observations with Solar Orbiter Spectrometer/Telescope for Imaging X-rays (STIX, Krucker et al., 2020). XSM observes the spectrum in the 1 − 15 keV band covering the thermal part of the solar flare spectrum, while STIX provides the spectrum in the complementary 4–150 keV energy range that covers the non-thermal part. STIX also provides images of the X-ray sources based on an indirect imaging method (cf. Massa et al., 2022). With the joint modeling of spectra from both instruments, we probe the evolution of the thermal and non-thermal plasma parameters throughout a solar flare to obtain improved estimates of the energetics of the flare.

Section 7.2 provides the details of the observations and data analysis, and the analysis results are presented in Section 7.3. The results are discussed in Section 7.4 followed by a summary in Section 7.5.

7.2 Observation of the Flare with XSM and STIX

In the present work, we analyze a GOES C-class flare on 08-Sep-2021 at ∼17:30 UTC observed by both XSM and STIX. Incidentally, it is one of the events in the sample considered for multi-thermal analysis with XSM observations in Chapter 6. This was one of the brightest events during the initial period of joint observation opportunity of XSM and STIX after the commissioning phase of STIX. Observations from both instruments are available for the entire flare duration, which also occurred in a favorable geometry for joint analysis, as discussed below.

7.2.1 Flare observation geometry

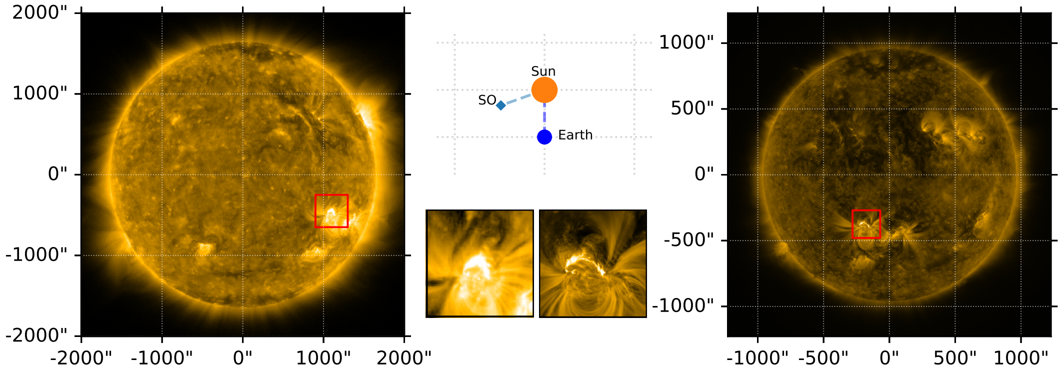

Figure 7.1: The Sun as observed from Solar Orbiter viewpoint (left) and from Earth viewpoint (right) during the early phase of the flare on 08-Sep-2021 at 17:25 UT. The relative location of SO with respect to the Sun and the Earth is shown in the middle panel. The image on the left is from SO EUI at 174 Å , and that on the right is from SDO AIA at 171 Å. Red boxes in the images mark the flaring active region, and the zoomed-in views of the same are shown in the middle.

The flaring event occurred in NOAA AR 12866, which was on-disk, as viewed from Earth. At the time of the event, the Solar Orbiter (SO) was at a heliocentric distance of $\sim$ 0.6 AU with the SO-Sun-Earth angle of 56 degrees[1]. The relative orientation of SO, Earth, and the Sun is shown in the middle top panel of Figure 7.1.

The Sun, as viewed from Earth's vantage point, which is very similar to

[1]Obtained from online tool at https://datacenter.stix.i4ds.net/view/ancillary

that seen from a lunar orbit by Chandrayaan-2 XSM, is shown in the image on the right panel from *Solar Dynamics Observatory/Atmospheric Imaging Assembly* (SDO/AIA, Lemen et al., 2012) in 171 Å band. The active region of interest is marked with a red box. The Sun as viewed from the SO vantage point is shown on the left in the figure using the image obtained with *Solar Orbiter/Extreme Ultraviolet Imager* (SO/EUI, Rochus et al., 2020) in 174 Å band and the active region is identified with the red box. Zoomed views of the AR from SDO/AIA and SO/EUI are shown in the lower middle panel of the figure. The same loops can be seen in both images from two different directions.

As the AR is on-disk for observations from Earth and SO, the flaring loops are observed without occultation from both vantage points. Thus, the thermal X-rays from the flare observed by CH-2/XSM and SO/STIX are expected to be identical as the emission is isotropic. On the other hand, the non-thermal X-ray emission from the flare can be anisotropic depending on the pitch angle distribution of the electrons (Kontar et al., 2011). It is possible that the non-thermal X-ray spectrum could depend on the viewing angle from the flare normal. Given the location of this flare on the solar disk ([-200”,-400”] as seen from Earth), the viewing angles from the flare normal for Earth and SO differ by only 18 degrees. Thus, directivity of non-thermal emission is expected not to cause a difference in the X-ray spectrum of this flare, as observed by XSM and STIX. Moreover, as the XSM energy range of 1–15 keV is expected to be dominated by thermal emission, any directivity effects in the non-thermal spectrum could have little impact on the joint analysis of X-ray spectra from both instruments.

Thus, the observation geometry of this flare is favorable to assume that the flare X-ray spectra incident on XSM and STIX are very similar, except for the light travel time and distance effects. After considering these two aspects, the observations from both instruments can be modeled jointly to obtain the flaring plasma characteristics. It may be noted that this may not be the case for all flares, and the effect of observing geometry in the X-ray spectra due to directivity or albedo effects needs to be considered in such cases while analyzing X-ray spectra from instruments observing from different vantage points.

7.2.2 Soft and hard X-ray light curves

Having established that the flare is suitable for simultaneous X-ray spectroscopic analysis with XSM and STIX, we examine the X-ray light curves in more detail. We generate XSM and STIX light curves for different energy bands. As SO was at a distance of 0.6 AU at the time of the flare, the light travel time difference between SO and Earth is 209.04 seconds, which is added to STIX time stamps so that the time stamps are that on Earth. Timestamps in XSM data already correspond to UTC on Earth and are thus kept the same. X-ray light curves thus obtained for different energy bands with a cadence of 1 minute are shown in Figure 7.2. The pre-flare background in the respective energy range is subtracted from the light curves. In the case of XSM, this pre-flare background is the quiescent solar emission. At the same time, for STIX, it is dominated by the background primarily arising from the radioactive source used for calibration. No flare emission is observed above 50 keV in STIX; thus, the energy bands for light curves are restricted up to 50 keV.

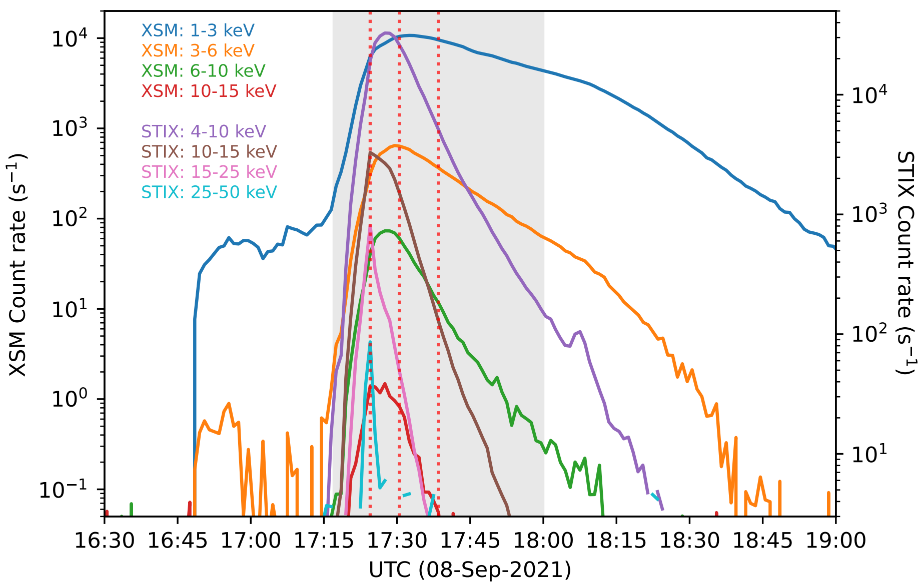

Figure 7.2: X-ray light curves of the flare in different energy bands observed by XSM and STIX. Grey-shaded duration is considered for joint analysis in the present work. The three vertical dotted lines correspond to the impulsive peak, thermal peak, and an instance during the decay phase.

The light curves exhibit the expected behavior of the highest energies peaking first, followed by progressively lower energies. The peak of emission in the highest energy band (STIX 25–50 keV) corresponding to the impulsive phase peak is observed at 17:24 – 17:25. The thermal phase peak is at 17:30 – 17:31, where the light curve in the lowest energy band (XSM 1–3 keV) attains maximum. Vertical dotted lines in the figure mark these times and an instance during the decay phase of the flare. It is interesting to note that the impulsive phase peak, as determined from the hard X-ray light curve from STIX for this event coincides with that determined from the soft X-ray light curve derivative in Chapter 6 shown in Figure 7.2. This shows that the flare follows the Neupert effect (Neupert, 1968).

From the figure, it can be seen that the light curves in the same or similar energy bands observed by XSM and STIX follow a similar trend. However, the light curve in the 4 – 10 keV band from STIX shows another secondary peak beyond 18:00 UT, which does not have a counterpart visible in the XSM light curves. It is likely that this secondary peak is associated with another flaring event occurring elsewhere on the Sun which is not observable from Earth. X-ray emission from the flare is observable in both instruments from around 17:17 UT. However, before that, we did observe some emission in the XSM 1–3 keV band and to some extent in the 3–6 keV band even after subtracting the average pre-flare quiescent emission. This could be associated with some pre-flaring activity observed only at lower energies, which we plan to investigate later. We also note that beyond $\sim$ 18:00 UT, no emission is observed in STIX at energies above 10 keV. For the present work, we consider the duration from 17:17 UT to 18:00 UT, shown in grey shade in the figure, for spectral analysis discussed in the next section.

7.2.3 X-ray Spectral Analysis

X-ray spectra of the solar flare observed with XSM and STIX are to be fitted with models to obtain thermal and non-thermal plasma parameters. OSPEX[2],

[2] https://hesperia.gsfc.nasa.gov/ssw/packages/spex/doc/ospex_explanation.htm

which is part of the Solarsoft package, is the widely used for modeling of X-ray spectra from RHESSI and for STIX as well. However, OSPEX presently does not have the capability to fit spectra from multiple instruments with the same model. Thus, instead, we use XSPEC (Arnaud, 1996) spectral fitting package that supports multi-instrument spectral fitting. Specifically, the Python interface to XSPEC, PyXSPEC, is used in the present work.

We generate time-resolved X-ray spectra and responses compatible with XSPEC for XSM and STIX for the duration of the flare. XSM observations are available at a constant cadence of 1 second while STIX records data nominally at 20 s cadence, which progressively reduces up to 0.5 s at the peak of the flare. However, to get good statistics in XSM spectra, it would be required to integrate spectra for longer durations. Thus, we generate spectra at a cadence of 60 s. STIX has a non-uniform time cadence, so we decide the time bins for spectra based on STIX data with bin sizes close to 60 s. Then, XSM spectra are also generated for the same time bins.

XSM spectra for the selected time intervals of the flare are generated using `xsmgenspec` task of the XSM Data Analysis Software version 1.1 (XSMDAS, Mithun et al., 2021a) with the latest version of calibration database (CALDB version 20210628). Apart from the statistical uncertainties, channel-wise systematic uncertainties are also included in the spectrum file. Along with the spectra, ancillary response files are also generated that are compatible with XSPEC. Non-solar background for XSM is obtained from observations when the Sun is out of the field of view, and this background spectrum is considered while fitting the spectra in XSPEC.

For STIX, the spectrogram data at full onboard resolution was available for this event, and this data is used for the spectral analysis, which adds up the counts in all 30 detectors. We generate X-ray spectra of STIX for the same time intervals using the routine `stx_convert_spectrogram.pro`, which is part of the STIX Ground Software (version 0.2.0)[3] available in SSWIDL. The standard response files generated by STIX data analysis software are in units compatible with OSPEX, which needed to be modified for analysis in XSPEC.

[3] https://github.com/i4Ds/STIX-GSW/tree/v0.2.0

OSPEX expects the response matrix file to have the normalized spectral redistribution function in units of counts keV^{-1} $\mathrm{photons}^{-1}$. The geometric area is included as a header keyword, which is read and interpreted by the OSPEX read routine. However, XSPEC requires a spectral response file (when provided as a single file) to have effective area in units of counts $\mathrm{photons}^{-1}$ cm^{-2}. Thus, the response matrix file had to be slightly modified to take care of the units so that they would be interpreted correctly. This has been incorporated into the STIX data analysis software to generate response files compatible with XSPEC. To create XSPEC-compatible spectrum and response files, the same routine `stx_convert_spectrogram.pro` should be run with the keyword `xspec` set. Additionally, as XSPEC can handle channel-wise systematic errors, energy-dependent systematic errors are included in the STIX spectra. Systematic errors of 7%, 5%, and 3% are included for spectra in the energy ranges of 4 – 8 keV, 8 – 11 keV, and 11 – 150 keV, respectively.

The calibration source dominates the background in STIX spectra and is stable over several hours (Battaglia et al., 2021). Thus, an average background spectrum is obtained from non-flaring periods of the same day and is then subtracted from the spectra during the flare. These background subtracted spectra are then used in spectral fitting. Another point to note is the distance factor for the STIX spectrum. As the observations were carried out when STIX was at a heliocentric distance of 0.6 AU , the effective area is multiplied with a factor of $1/\mathrm{distance}^2$ so that models providing flux at 1 AU can be used to fit STIX spectra.

Fitting the X-ray spectra in XSPEC requires models of thermal and non-thermal emission. For the thermal part, we use `chisoth`, which is a local model in XSPEC for ionized plasma emission that uses the CHIANTI atomic database, same as used in the analysis in Chapter 5 and Chapter 6. The model takes temperature, emission measure, and abundances of various elements as parameters and provides a spectrum that includes continuum and line emission. The non-thermal emission from solar flares arises from the bremsstrahlung of accelerated electrons having a power law spectrum (c.f. Kontar et al., 2011; Kepa et al., 2008). X-ray spectrum from this process can be modeled with an empirical broken power-law model, but this does not directly provide the characteristics of accelerated electrons. Physical models to explain the non-thermal spectrum include thick target bremsstrahlung (Brown, 1971) applicable for footprint emission and thin target bremsstrahlung for coronal emission (Kepa et al., 2008). The thick target model is considered because the footpoints are not occulted in the present case.

The model of thick target bremsstrahlung is readily available in OSPEX but not in XSPEC or PyXSPEC. Thus, we use the Python implementation of the thick target model in `sunxspex` package[4]. Additional functions are added in this package to use the thick target model as a local model in PyXSPEC[5]. This local model of thick target bremsstrahlung is used for spectral fitting.

7.2.4 Imaging Analysis

While XSM observes the Sun as a star and provides disk-integrated spectrum in soft X-rays, STIX is capable of providing images of the X-ray source regions on the Sun with its Fourier imaging technique. This is achieved by two sets of Tungsten grids that are placed in front of 32 coarsely pixellated CdTe detectors (Krucker et al., 2020). Each grid pair acts as a collimator that modulates the incoming X-rays so that a Moire pattern is formed on the detector. This pattern encodes one spatial Fourier component of the source brightness distribution. Combining the information from a larger number of detectors allows the reconstruction of the X-ray source with the help of various imaging algorithms (Massa et al., 2022) that are integrated into the STIX analysis software under SSWIDL.

To study the morphology of the thermal HXR source, we used the Maximum Entropy Method MEM_GE (Massa et al., 2020) to reconstruct STIX images in the energy range of 6–10 keV during the whole evolution of the flare. We used all subcollimators except the two finest groups, for which the calibration has not yet been completed. This results in an angular resolution of 14.6". An

[4] https://github.com/sunpy/sunxspex

[5] PyXSPEC local model implementation of thick target available at https://github.com/elastufka/sunxspex/blob/xspec_functions/sunxspex/xspec_models.py

integration time of 1 min was chosen for all images, the same as the time intervals used in the spectral analysis. To get quantitative estimates of the source size, we additionally fitted an elliptical Gaussian source to the data using the Visibility Forward Fit algorithm (Volpara et al., 2022). The advantage of this method is that it provides the uncertainties of the fitted geometric parameters.

We also use EUV observations from SDO AIA to study the morphology of the thermal plasma in the flaring region at lower temperatures, contributing to emission in the XSM range but not significantly to emission in STIX energy bands. AIA level-1 data were downloaded and processed using tasks from `aiapy` package[6], which included registering the image with updated pointing information and normalizing for the exposure times. Level 1.5 images thus generated are used for further analysis. Areas in AIA images where the counts are higher than the background level are identified, and the number of pixels of this flaring region is counted to obtain the area (A). The volume of the flaring region is estimated as $V = A^{3/2}$, similar to that in Chapter 5.

7.3 Analysis Results

7.3.1 Spectroscopy

First, we fit X-ray spectra observed with XSM and STIX using PyXSPEC independently to infer the plasma parameters. For XSM, we model the spectra with a two-temperature thermal model as the analysis of XSM spectra for this event presented in Chapter 6 has suggested the presence of two temperature components during the impulsive phase of the flare. Temperatures and emission measures of the two components are left as free parameters. Abundances of the two components are tied together, and abundances of those elements having prominent lines in the XSM spectra are also considered as free parameters in the fitting (see Section 6.3). Abundances of other elements are frozen to coronal abundances from Feldman (1992).

Figure 7.3 top panel shows XSM spectra at three instances during the

[6]https://aiapy.readthedocs.io/en/stable/

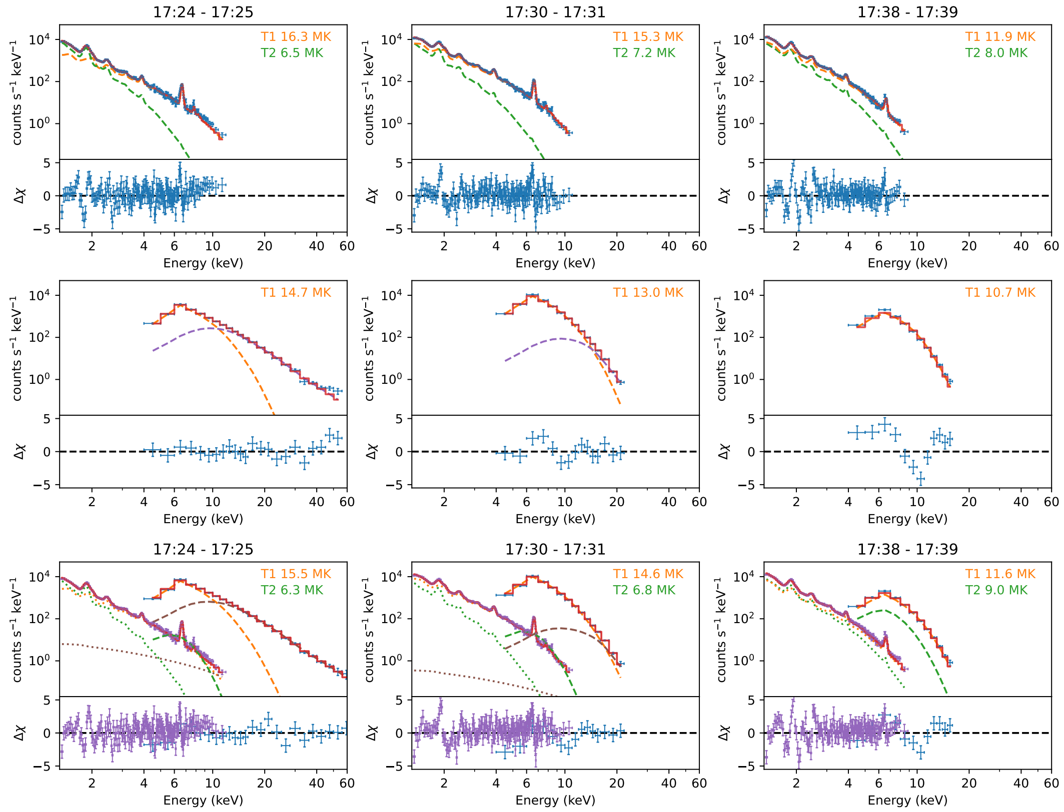

Figure 7.3: X-ray spectra at three phases of the solar flare with best fit models. Individual fits to XSM spectra are shown in top panel, individual fits to STIX spectra are shown in the middle panel and the bottom panel shows results of simultaneous fit to XSM and STIX spectra. Points with erro bars show observed spectra in all panels and red steps denote best fit model. Dashed/dotted lines correspond to individual model components.

flare (corresponding to the vertical dotted lines in Figure 7.2) along with the best-fit models. The dashed lines correspond to the emission from high temperature (orange) and low temperature (green) components and solid red steps show the total best-fit model. Temperatures obtained from the fit for both components are also marked in the figure. Temperature and emission measure for all one-minute intervals obtained from XSM spectral fits are shown in Figure 7.4 with faint orange and green open circles. One sigma errors obtained from MCMC analysis are also shown in the figure. It may be noted that beyond 17:40 UT, both components' temperatures were very similar, and thus, a single temperature model is fitted to spectra. The higher temperature component increases rapidly during the initial phase and peaks at the impulsive phase peak and then reduces gradually, while the lower temperature component shows a much gradual rise. We also note that the abundances obtained show the same trend as discussed in Chapter 6.

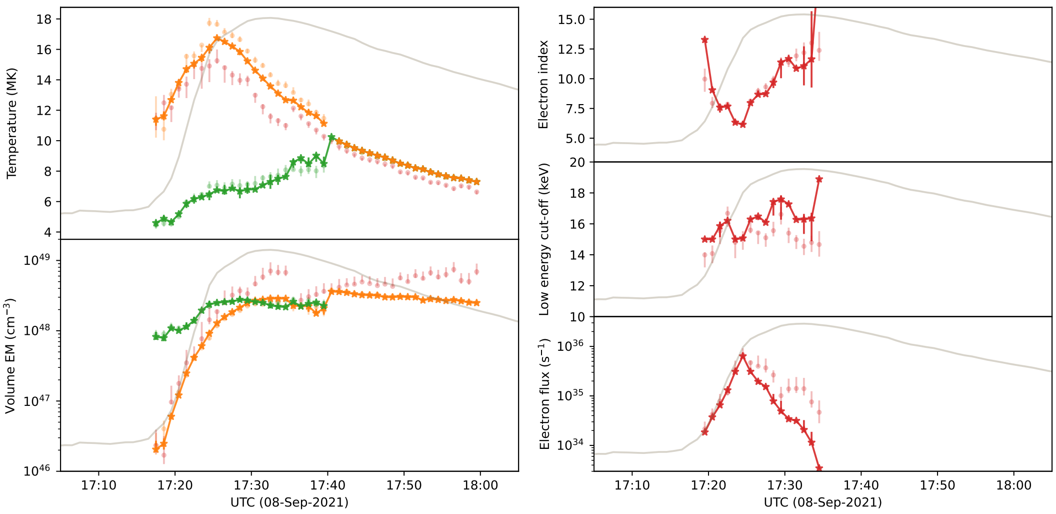

Figure 7.4: Thermal and non-thermal plasma parameters during the flare obtained from spectral fitting. Best fit parameters from simultaneous XSM and STIX spectra fitting are shown with a star symbol. Orange and green color points in temperature and emission measure correspond to the parameters of higher and lower temperature components, respectively. Results of the fit to the XSM spectrum alone are shown in faint orange and green points in panels of temperature and emission measure. Results of fit to STIX spectrum alone are shown in faint red points in all panels. Error bars correspond to one-sigma uncertainties. X-ray light curve in 1–15 keV band is shown in grey in the background for reference.

We then fitted the STIX spectra of the flare. Instead of a two-temperature thermal model, we consider the fitting model to be the sum of an isothermal component and a thick target bremsstrahlung component. The STIX spectrum is in wide energy bands with bin widths of 1 keV and higher, so the spectral lines are not well resolved. Thus, for the thermal component, the temperature and emission are the only free parameters, while the abundances of all elements are fixed at coronal abundances by Feldman (1992). For the non-thermal component, the electron distribution is considered a simple power law with a low energy cutoff, where the power law index, low energy cut-off, and the flux of electrons are the free parameters. The non-thermal component is set to zero beyond the impulsive phase, where the spectra are well-fitted with just the isothermal model. STIX spectra with best-fit models at the same three intervals as that of XSM spectra are shown in the middle panel of Figure 7.3. Orange and purple dashed lines correspond to the thermal and non-thermal components, respectively, and the total model is plotted with red steps. Best fit temperatures are shown in the figure, which is closer to the higher temperature component obtained with XSM spectra alone. Best fit parameters are shown with faint red-filled circles with error bars in Figure 7.4.

It can be seen from the figure that the temperature obtained from STIX closely follows the higher temperature component obtained from XSM observations. XSM and STIX temperatures are within error bars during the initial and decay phases. During the impulsive and thermal phase, the STIX temperatures are slightly lower than the XSM high temperatures. On the right panels of Figure 7.4, parameters of the accelerated electrons are shown, which is applicable only during the impulsive phase of the flare. It is also noted that temperature and emission measures show a discontinuity when the non-thermal component is excluded from the fitting model.

Now, we proceed to model the spectra of XSM and STIX jointly. For each one-minute time interval, we load both XSM and STIX spectra together in PyXSPEC. Based on the analysis of the individual spectra of both instruments, we consider a single model consisting of two isothermal components and a thick target bremsstrahlung component. The same model is applied to both spectra, and all parameters for both spectra are tied. To take into account any overall normalization difference between the instruments, we also consider a constant multiplication factor to the model, which is frozen to one for XSM and left as a free parameter for STIX.

Initial fitting of data showed that the constant factor is very close to one, showing that the cross-calibration factor between both instruments is close to unity within the systematic errors considered. Thus, we removed the constant factor between the instruments to obtain joint fit parameters. Lower panels of Figure 7.3 show the XSM and STIX spectra for three of the time bins with the best-fit models. Individual components of the spectral model convolved with respective instrument responses are shown in dotted (XSM) and dashed (STIX) lines with different colors. From the residuals, it can be inferred that the spectra of both instruments are well-fitted with the same model. The high-temperature component in the joint fit is between the temperatures from XSM and STIX separately. In contrast, the lower temperature component is very close to the low temperature obtained from XSM spectral fits. The best-fit spectral components in the figure show that the lower-temperature component has very little contribution to the STIX spectrum, which explains why it is constrained primarily by XSM alone. Similarly, the non-thermal component has little contribution in the XSM spectral range, and thus is determined primarily by the STIX spectrum.

Best fit spectral parameters obtained from simultaneous fits to XSM and STIX spectra are plotted with star symbols in Figure 7.4. It can be seen from the figure that the temperature and emission measures of the higher temperature component from joint fits are very close to that obtained from XSM observations alone. The only differences are during the impulsive phase, where the temperature gets adjusted taking into account the non-thermal component as well. This is also apparent from the difference in the accelerated electron parameters between the joint fitting and individual fit to STIX spectra. We also note that the errors on the non-thermal parameters are also slightly less for joint fits compared to the results obtained from STIX alone.

Comparison of XSPEC and OSPEX fit results

Spectral fitting package OSPEX, which is part of Solarsoft distribution, is widely used in solar X-ray spectral analysis. As OSPEX cannot be used for joint fitting of X-ray spectra from multiple instruments, so XSPEC was used in the above spectral analysis. Here, we compare the analysis results from fitting STIX spectra in XSPEC and OSPEX to understand any differences in results due to differences in analysis software.

OSPEX compatible STIX spectra and response matrices for the same intervals as in the analysis presented earlier are generated. Spectra are fitted in OSPEX with a model of `vth` and `thick2`. Spectral parameters obtained from XSPEC and OSPEX fits are overplotted in Figure 7.5. It can be seen that the parameters from both match closely. There are some differences (less than ten percent or so) near the impulsive peak caused by the differences in the best fit low energy cut-off.

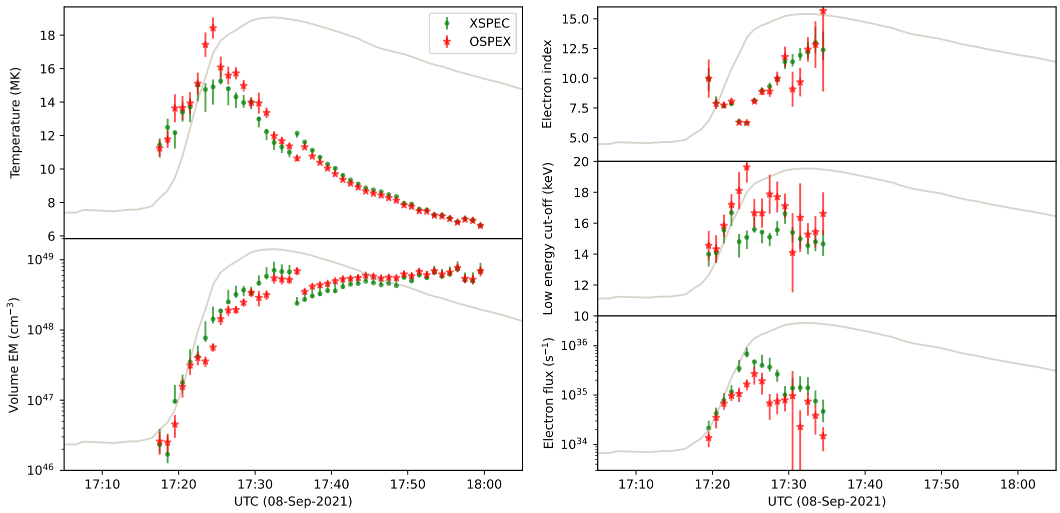

Figure 7.5: Thermal and non-thermal plasma parameters obtained from fitting STIX spectra in XSPEC (green filled circles) and OSPEX (red star).

7.3.2 Imaging

X-ray images obtained from STIX observations in the 6–10 keV band with MEM_GE method are shown in the top panels of Figure 7.6. The images correspond to the impulsive phase peak, thermal peak, and decay phase as marked by the vertical dotted lines in Figure 7.2. Respective AIA images from the 94 Å band are shown in the bottom panels of Figure 7.6. In the impulsive phase, the STIX image shows brightening at two locations, and the shape of the X-ray sources changes as the flare progresses. In AIA, the emission is predominantly in one region in the impulsive phase, which shifts to another location in the later part of the flare.

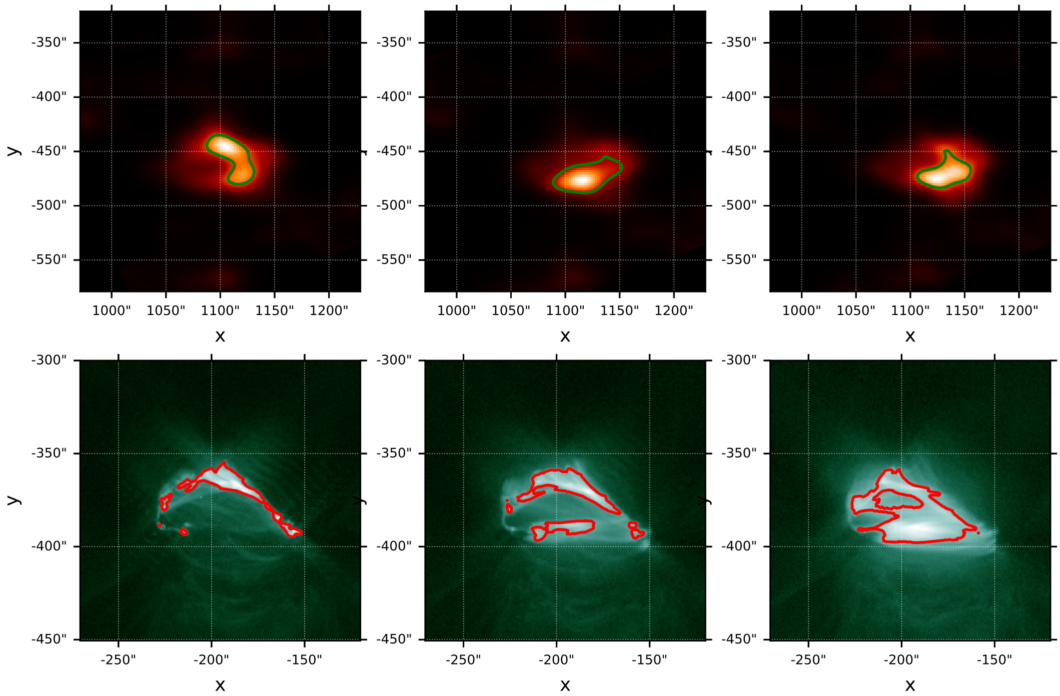

Figure 7.6: Images of the flaring region at three instances of flare, impulsive peak, thermal peak, and decay phase, marked by vertical lines in Figure 7.2. The upper panels show images obtained from STIX in the 6 – 10 keV energy range using the MEM_GE method and the lower panels show SDO AIA images in 94 Å band. For AIA, the contours overplotted on the images enclose the area considered for estimating the volume of the emission region.

Apart from understanding the location of the emission, the images were used to obtain the volume of the emission region. Volumes are estimates from STIX and AIA images in each time bin corresponding to the spectra, following the methods discussed in Section 7.2.4. Figure 7.7 shows the estimated volumes from the STIX X-ray images and AIA 94 Å images. It can be seen that the volumes estimated from STIX and AIA match each other in the early part of the flare, and towards the later part, they differ even though the trend remains similar. One possible reason for the difference is that both the images are tracing plasma at different temperatures and it is likely that the volume corresponding to the lower-temperature plasma observed by AIA may be higher than that of

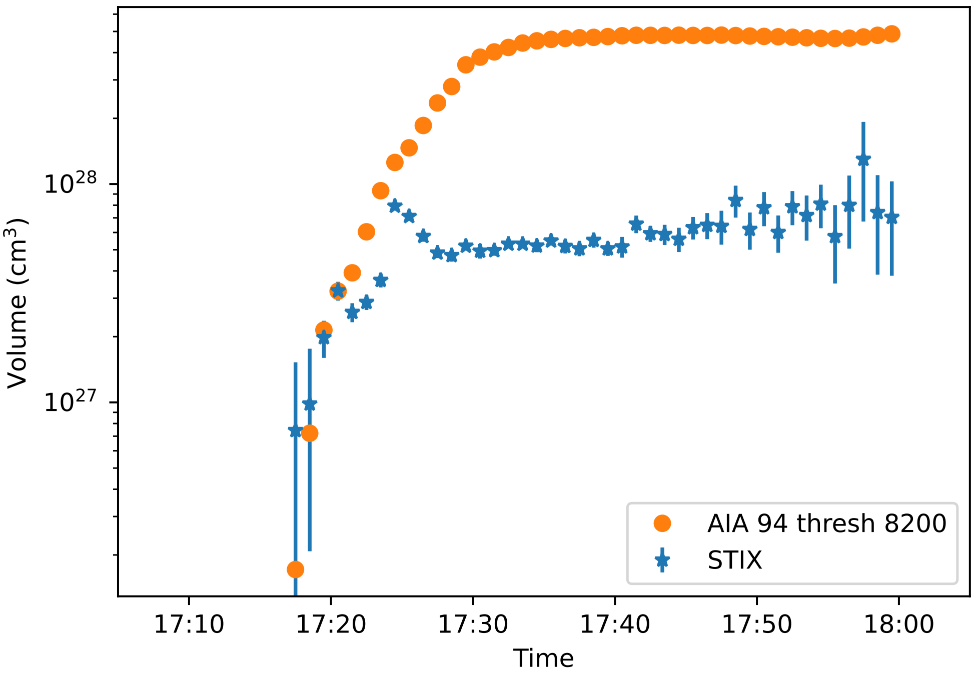

Figure 7.7: Volume of the plasma as estimated from STIX 6–10 keV images and AIA 94 Å band images.

the high-temperature plasma observed by STIX. It may also be noted that other methods (such as estimating loop lengths and getting their volumes considering them as cylinders) to derive volumes may result in slightly different results.

7.4 Discussion

We presented the analysis of X-ray spectra of a solar flare using observations with Chandrayaan-2 XSM and Solar Orbiter STIX. First, we independently fitted the spectra from both instruments for each one-minute time bin during the flare. A two-temperature model could describe XSM spectra, whereas the STIX spectra were fitted with an isothermal model and a non-thermal thick target model. Temperatures estimated from STIX were close to the higher temperature component inferred from the XSM spectra (see Figure 7.4). Further, we jointly modeled the spectra of both instruments to obtain the flare parameters consistent with both data sets. Joint fits resulted in slightly different values for the higher-temperature component and the non-thermal parameters, whereas the low-temperature component was very similar to that obtained from XSM alone. We also obtained the volume of emission region from X-ray images with STIX and EUV images with SDO AIA.

7.4.1 Thermal and Non-thermal Energy

Using the flare parameters obtained from spectral analysis and volume estimates from imaging analysis, we estimate thermal and non-thermal energies associated with the flare. Estimating thermal energy requires knowledge of the volumes associated with each thermal plasma component. The thermal plasma as inferred from spectroscopy, consists of two temperature components, and only the high-temperature component is dominant in the STIX energy range. Thus, we consider the STIX-derived volume to be the volume of the high-temperature component. Parameters of the low-temperature component are constrained primarily by the XSM spectra, and as imaging is not available, one cannot directly get the volume. From Figure 7.4, we can see that the temperatures of the cooler component are in the range of ~ 5-10 MK. AIA 94 Å band is sensitive to plasma at these temperatures, and thus, we consider the volume estimates from AIA 94 Å to be the volume of the low-temperature component. We estimate the thermal energy as

$$E_{th} \sim 3\ k_{\mathrm{B}} \times (T_1\ \sqrt{EM_1 \times V_1} + T_2\ \sqrt{EM_2 \times V_2}) \tag{7.1}$$

where T_i, EM_i, and V_i correspond to the temperature, emission measure, and volume of each thermal component. This assumes a unity filling factor for both components and thus would be an upper limit to the thermal energy.

The estimated thermal energies using the parameters obtained from joint analysis of XSM and STIX spectra are shown in Figure 7.8 with blue stars. Contribution to the total thermal energy from the high-temperature component (orange) and low-temperature component (green) are also shown separately. We also estimated the thermal energy from the STIX fit parameters, where only one thermal component was needed, as shown in the figure with grey stars. It can

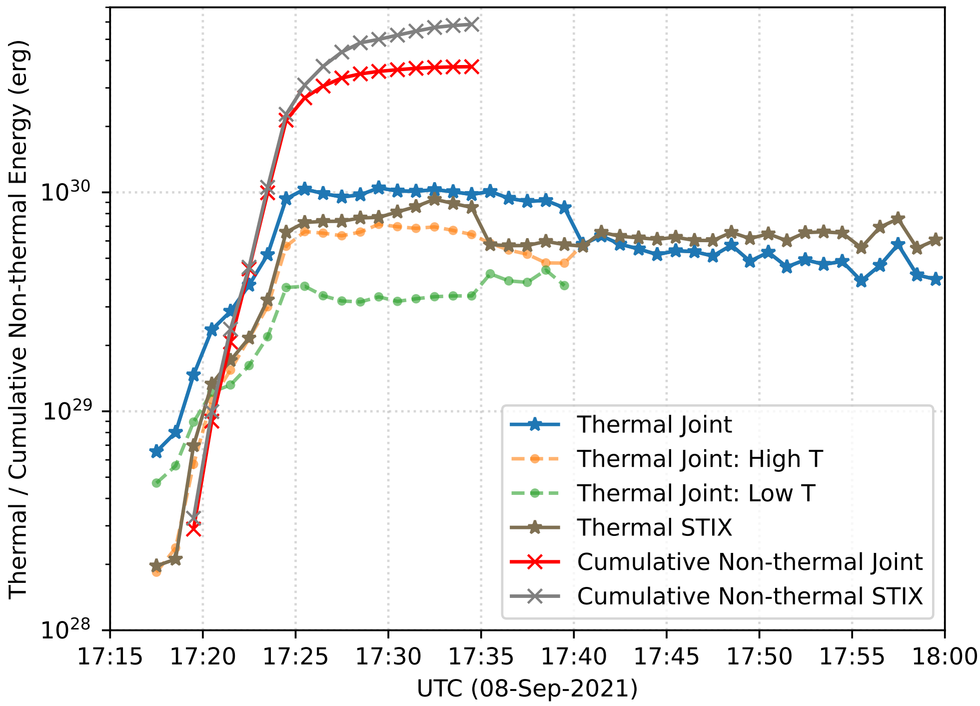

Figure 7.8: Thermal energy estimated using the plasma parameters from X-ray spectral fitting and volume estimates from STIX AIA images. The cumulative non-thermal energy of the accelerated electrons is overplotted. Energy estimates from joint fits of XSM and STIX spectra as well as individual fit to STIX spectra, are shown in different symbols, as noted in the figure.

be seen that the thermal energy estimates from STIX alone slightly underpredict the energies as one would expect.

Further, using the joint fit parameters of the thick target model, integrating over the electron power law distribution, we estimate the non-thermal energy. Cumulative non-thermal energy deposited by the accelerated electrons is shown with red crosses in Figure 7.8. Similar estimates using the parameters from fitting STIX spectra are shown with grey crosses, slightly higher than those from joint fits. In any case, it can be seen that the energy deposited by non-thermal electrons is a few times higher than the maximum thermal energy. This shows that the non-thermal electrons carry sufficient energy to explain the observed heating of plasma. It is important to note that the thermal energy in this case is estimated by considering the soft X-ray spectra as well and thus was a more accurate estimate as compared to that from the hard X-ray spectra alone.

Saqri et al. (2022) analyzed the AIA and STIX observations of two B-class flares to estimate thermal and non-thermal energies of the events, where thermal energies were estimated from DEMs derived from AIA images. They have shown the differences in thermal energy estimates when volumes are estimated from different methods. Similar uncertainties would exist in the thermal energy estimate due to uncertainties in volume, which would be applicable in this case as well. We estimated volumes from AIA images in 131 Å with different thresholds and compared it to the estimates from 94 Å band and find that they are not significantly different. Thus, the uncertainties in volume do not change the conclusion that cumulative non-thermal energy is higher than thermal energy.

We also note that in the present study, thermal energy is estimated from soft and hard X-ray observations. While the estimate would be more accurate than the estimation just from the hard X-ray spectra, it still does not account for the plasma at lower temperatures, which will be visible in EUV. Thus, modeling the EUV, soft X-ray, and hard X-ray observations simultaneously to obtain self-consistent thermal plasma distribution (DEM) and non-thermal particle distribution would provide more accurate estimates of the energy partition. DEM analysis also provides the opportunity for better estimates of volumes of plasma at different temperatures (e.g., Aschwanden et al., 2015b).

7.4.2 Fe line residuals and Fe fluorescence

A closer look at the spectral fits in Figure 7.3 shows the presence of systematic residuals around the Fe line complex at $\sim$6.5 keV and Si line complex around 1.8 keV. While the residuals near 1.8 keV could partly be arising from the uncertainties in the response being close to the Si K-edge, there is no such possibility for the residuals in the Fe line complex, and thus is more intriguing. In earlier work, Mithun et al. (2022) showed that broader multi-temperature differential emission measure distributions could not explain the additional flux seen in the

Fe line complex. We also explored the possibilities of unaccounted flux due to any satellite lines that are not included in the CHIANTI database, as well as the effect of electron densities and found both not sufficient to explain the observed excess flux.

High-resolution X-ray spectra of solar flares using crystal spectrometers on *SMM* and *Yokoh* missions have revealed the presence fluorescence lines of Fe Kα at $\sim$ 6.4 keV and Fe Kβ at $\sim$ 7.06 keV (e.g., Neupert et al., 1967; Doschek et al., 1971; Culhane et al., 1981; Parmar et al., 1984; Phillips, 2012). This emission is considered to be arising from the excitation of neutral or low ionization state Fe in the photosphere caused by either X-ray photons from the flaring plasma (Basko, 1979; Bai, 1979) or accelerated non-thermal electrons (Phillips & Neupert, 1973). Previous studies have shown that the excitation by X-ray photons might be the dominant process, but there is still a possibility of some contribution from non-thermal electrons (Emslie et al., 1986). Some evidence of Fe Kα flux being dependant on the location of the flare on the solar disk further supports the possibility of XRF being the dominant contributor (Parmar et al., 1984; Phillips et al., 1994).

To explore the possibility that the excess flux observed in XSM/STIX spectra in Fe line complex is due to Fe fluorescence emission, we add another line component at 6.4 keV to the spectral model. We then fitted the spectra, keeping other parameters of thermal and non-thermal components constant at their earlier best-fit values and obtained the excess flux at 6.4 keV.

Excess flux in the Fe line complex obtained from the spectral fits as a function of time is shown in Figure 7.9 with blue data points. To assess the possibility of this excess flux arising from X-ray fluorescence or particle-induced X-ray emission, we compare it with the flux of exciting X-ray and particle flux. X-rays from the solar flare having energies above the K-edge of Fe, 7.12 keV, can excite the Fe atoms in the photosphere and result in fluorescence emission. We compute the X-ray flux at energies above 7.12 keV from the best-fit spectral models, plotted with orange lines in the figure. The contribution from the thermal and non-thermal X-rays are shown with dashed and dotted lines, respectively. The solid orange line shows the total flux of X-rays that can cause Fe fluorescence

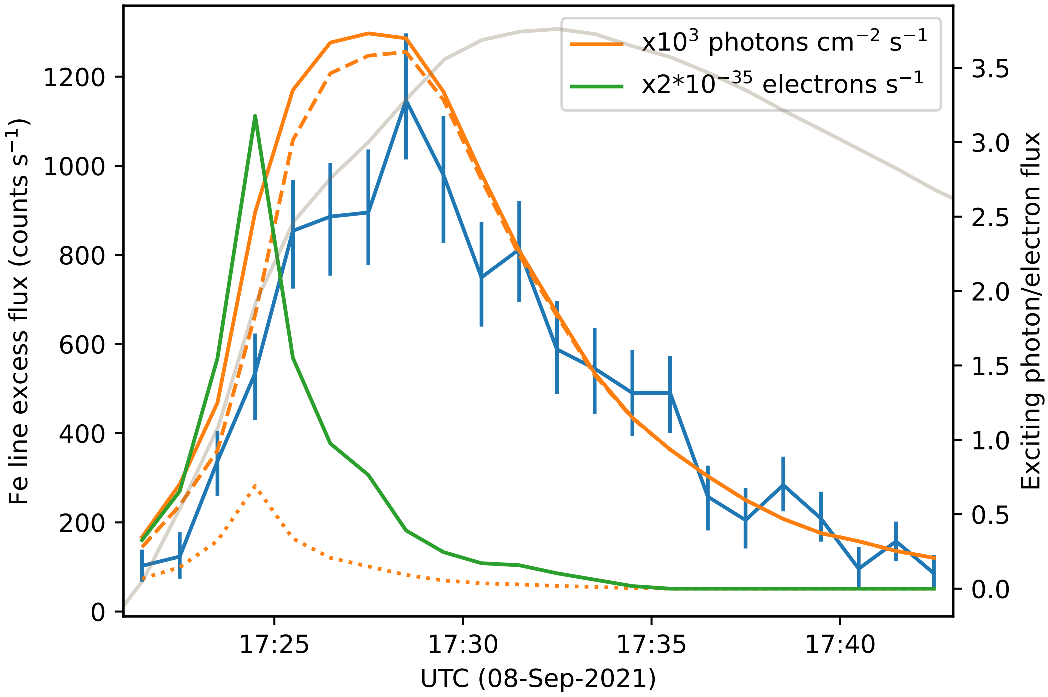

Figure 7.9: Excess flux in Fe line complex are shown in blue error bars. X-ray flux at energies above Fe K-edge at 7.12 keV obtained from the best fit spectral model is overplotted in orange. This consists of the flux from the thermal component (orange dashed line) and that from the non-thermal component (orange dotted line). Electron flux measured from X-ray spectra is shown with a green solid line. X-ray light curve (1–15 keV) is shown in the background in grey for reference.

emission. The flux of electrons, as obtained from the thick target model, is also overplotted in green.

It can be seen that the measured line excess closely follows the X-ray flux above Fe K-edge while showing no significant correlation with the non-thermal electron flux. This suggests that the excess flux observed in the Fe line complex arises from the Fe fluorescence has much of a contribution from X-ray fluorescence and little contribution from excitation by non-thermal electrons. We plan to explore this further with a sample of flares occurring at different locations on the solar limb observed by XSM and STIX and possibly other spectrometers.

It is also to be noted that the excess flux observed is not correlated with the total counts observed by XSM, which is shown in grey in Figure 7.9.

The excess flux peaks before the peak of the total light curve but coincides with the flux above 7.12 keV. Although it has been shown that the XSM instrument performance does not show any degradation to count rates above 80,000 counts/s (Mithun et al., 2021b), much higher than the count rates in this event, this further confirms that the residuals observed are not a result of any variation in the instrument characteristics at high count rates.

7.4.3 Directivity and Albedo effects

As discussed in Section 7.2.1, the flare was observed at similar angles with the flare normal from STIX and XSM vantage points. Thus, the directivity effect was not expected to be important. Moreover, from Figure 7.3, it can be seen that the non-thermal component has negligible contribution in the XSM energy band. Thus, the directivity of non-thermal X-rays did not impact the analysis presented here. Another aspect that needs to be considered is the Albedo effect. X-ray albedo can modify the high-energy spectrum. However, as the albedo model was not readily available for analysis in XSPEC, we did not consider this effect. To verify its impact, we carried out an analysis of just the STIX spectra in OSPEX with and without the albedo model. It was found that, for this flare, the derived parameters are not significantly different in both cases. Thus, excluding the albedo component has also not affected the results in the present work. However, we plan to examine the possibility of including the albedo effect in joint analysis of solar X-ray spectra in XSPEC as it would be essential to consider while attempting to measure hard X-ray directivity.

7.5 Conclusions and Summary

In this chapter, we have presented the joint spectral analysis of a GOES C-8 flare observed simultaneously with CH-2/XSM and SO/STIX. These instruments complement each other in terms of their energy range and sensitivity. This flare being observed with both these instruments at almost the same angle from the flare loop normal provided a very good opportunity to establish the joint spectral analysis over the broad energy range covered by the two instruments. The individual fits using both instruments resulted in similar plasma parameters, and joint fitting provided parameters consistent with both spectra. As XSM could constrain the thermal component better with the spectrum going down to lower energies, joint fits with STIX resulted in better constraints of the non-thermal electron parameters, including the low energy cut-off, providing more reliable estimates of thermal and non-thermal energy content.

Calculation of energies associated with the event showed that the cumulative energy associated with the electrons accelerated by reconnection is three to five times higher than the energy associated with the thermalized electrons. While it is likely that part of the thermal energy from lower-temperature plasma is missing in the energy estimates, which would be observable with emission at even lower energies in EUV, the energy from accelerated electrons is sufficient to explain the thermalized plasma. Excess energy suggests that part of the energy is possibly dissipated in other processes. By extending the framework for simultaneous modeling of X-ray spectra with XSM and STIX to include EUV observations from other missions, it would be possible to refine further the energy partition in solar flares.

Another interesting result concerns the excess flux observed in the Fe line complex, attributed to the Fe fluorescence emission due to X-ray fluorescence. While the presence of Fe K-α line in solar flare spectra has been confirmed with narrow-band high-resolution spectrographs in the 1970s, it was not possible to have good constraints of the exciting X-ray radiation or particles. Although the fluorescence line is not well resolved with XSM, joint observations with XSM and STIX provided the opportunity to compare the additional flux with the exciting radiation for X-ray fluorescence and electron-induced X-ray emission and show that the XRF is the dominant factor. While detailed modeling of the contribution due to fluorescence may not be warranted, any analysis of X-ray spectra of flares in this energy range needs to consider the contribution from fluorescence lines, which are not part of the models usually used in spectral fitting.

Finally, we emphasize that the present work showed that the two instruments, CH-2/XSM, and SO/STIX, despite having different types of detectors covering different energy ranges and operating on different spacecraft located at distant points in their orbit around the Sun, do provide consistent measurement of X-ray spectra for the same event when observed at a similar angle from the loop-normal. This suggests that any differences in the spectra for other flares observed at other angles, where there is a significant contribution from the non-thermal component in the XSM energy range, may be attributed to the directivity of the hard X-ray emission. The hard X-ray directivity measurements provide the opportunity to probe the beaming of accelerated electrons, which can break the degeneracies in the acceleration mechanisms. Since both these instruments are likely to be operational for the foreseeable future, our work paves the way for directivity studies in the future using STIX along with XSM, as well as other earth-bound instruments such as presently operational DAXSS on-board Inspiresat-1 or SoLEXS and HEL1OS spectrometers on the upcoming Adita-L1 mission.

While directivity measurement from stereoscopic X-ray spectroscopic observations is one way to probe the anisotropy of the electrons, the other method would be to go beyond X-ray spectroscopy and carry out measurements of the polarization of the hard X-ray emission from the solar flares. In the next chapter, we present a concept design for a hard X-ray spectro-polarimeter for solar observations and an extension of that for observations of other astrophysical sources.

Chapter 8

Beyond Spectroscopy: Prospects of X-ray Spectro-Polarimetry

So far in this thesis, the focus has been on X-ray spectroscopy. While spectroscopy is a powerful tool, there are cases where spectroscopy alone cannot disentangle various emission processes when different models predict similar spectral signatures. In such cases, additional parameters in observations can be helpful. The fraction of polarization and angle of polarization provide such independent parameters. Even for the models having the same spectral signatures, the polarization signatures need not be similar. This is the case for some of the properties of accelerated electrons in solar flares, such as its anisotropy. It is also true in several other scenarios for astrophysical sources such as black hole binaries and pulsars. Thus, going beyond spectroscopy, having X-ray spectro-polarimetric measurements is useful in breaking degeneracies in theoretical models.

The science case for the hard X-ray polarimetric observations of solar flares is discussed briefly in Section 8.1, and a conceptual design of an X-ray spectro-polarimeter and its expected performance is presented in Section 8.2. This concept is extended to the design capable of making polarimetric observations of other astrophysical sources, and the expected capabilities are determined, which is given in Section 8.3. Section 8.4 summarizes the chapter.

8.1 Case for X-ray Polarimetry of Solar Flares

Solar flares result from the reconnection of the magnetic field in the solar atmosphere. The energy released from the reconnection goes into the acceleration of electrons and ions, possibly heating the plasma, as well as coronal mass ejections. Accelerated electrons undergo non-thermal bremsstrahlung and emit power law-like spectrum in hard rays (Chapter 4, Chapter 7). Although it is established that solar flares are efficient in accelerating the particles, the exact mechanism and site of acceleration are not well constrained (Benz, 2017). Hard X-ray spectrum provides the diagnostics of the accelerated electron population by measuring the index of the power-law distribution. However, the X-ray spectrum alone is insufficient to probe properties such as the direction distribution and high energy cutoff of the electron population, as the spectra are practically insensitive to these parameters, except when observed from two viewpoints (Section 7.5). However, the electron anisotropy and high energy cutoff are two important quantities that are required to constrain the underlying acceleration mechanisms (Kontar et al., 2011).

Hard X-ray polarization measurements provide a unique opportunity to probe the electron direction distribution (see Jeffrey & Kontar, 2011 and references therein). In addition to the direct hard X-ray emission from bremsstrahlung, the observed X-rays include a significant contribution from the albedo effect, which is Compton backscattering of photons from the photosphere, and this alters the polarization signatures (Bai & Ramaty, 1978). Thus, the polarization properties depend on the flare location and viewing angle as well.

Figure 8.1 left panel shows the simulated polarization fraction (top) and spectrum (bottom) as a function of energy for different electron anisotropy distributions from an isotropic distribution to fully beamed distribution, taken from Jeffrey et al. (2020). Except for the anisotropy, all other plasma parameters are kept constant in the simulations that also take into account the electron transport within the corona, and the spectrum includes the albedo component as well as the thermal emission. It can be seen that while the spectra are practically insensitive to anisotropy, the energy-dependant polarization degree above 20 keV

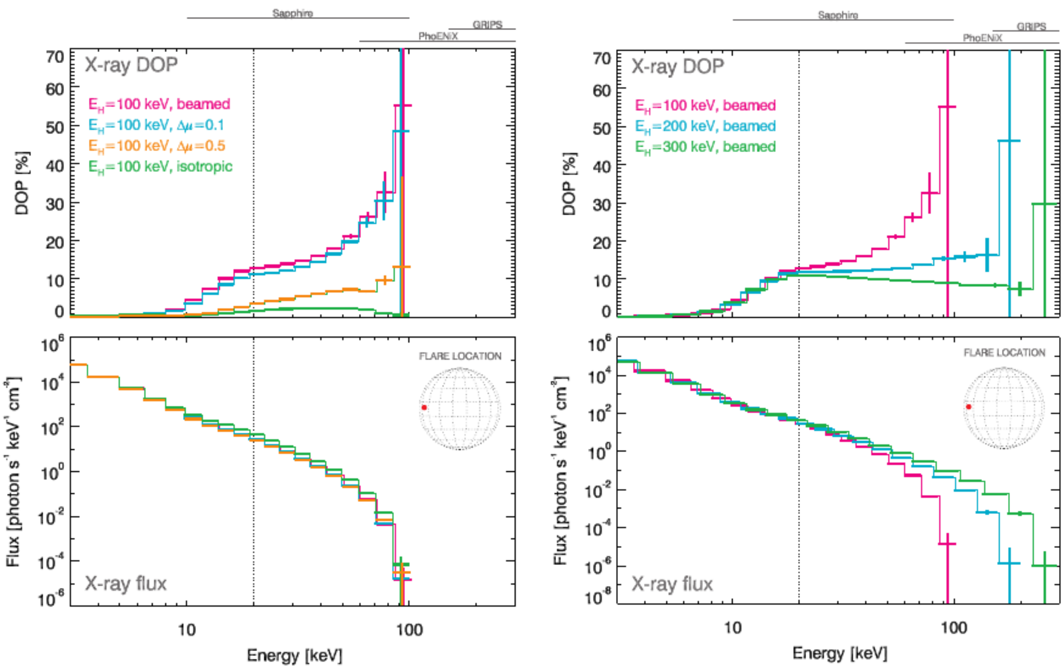

Figure 8.1: Simulations results taken from Jeffrey et al. (2020) showing the expected energy dependant polarization fraction (top panels) for different electron anisotropy (left) and high energy cutoff (right). Lower panels show respective energy spectra.

increases from less than a few percent for isotropic case to 10-30% for beamed case, showing the diagnostic potential of energy-dependant X-ray polarization measurements at energies >20 keV.

Another factor that alters the energy-dependent polarization properties is the high energy cutoff of the electron distribution, i.e., the highest energy electrons produced by the acceleration process. Figure 8.1 right panel shows the energy dependant polarization degree and spectra for three different high energy cut off for fully beamed electron distribution taken from Jeffrey et al. (2020). It can be seen the polarization degree reduces as the higher energy cutoff increases, and thus, measurement of flare X-ray polarization as a function of energy can also constrain the high energy cut-off of the accelerated electrons.

While the measurements of hard X-ray polarization of solar flares are very rewarding, there haven't been many successful measurements. The first measurements of X-ray polarization from solar flares date back to 1970s (Tindo et al., 1970, 1972, 1976). However, they were met with significant skepticism.

There have been a few more attempts since then, but not many have resulted in very significant measurements. There have also been some measurements with RHESSI. However, as RHESSI is not optimized for polarimetric observations, there have been only limited measurements of low significance. A brief history of X-ray polarization observations of solar flares, including those with RHESSI, is given by Kontar et al. (2011).

In the recent past, there have been several developments and concepts of X-ray polarimeters with different configurations being planned for observations of the solar flares such as PING-M (Kotov et al., 2016), PhoENiX (Narukage, 2019), SAPPHIRE (Saint-Hilaire et al., 2019), GRIPS (Saint-Hilaire et al., 2020), CUSP (Fabiani et al., 2022), and PADRE (Martinez Oliveros et al., 2023). While some of them are still under active development and consideration for flight, they are yet to materialize to a mission. In this context, the development of X-ray polarimeters for solar flare observations is of significance, and we provide an instrument concept in the subsequent section.

8.2 Conceptual Design of Flare Polarimeter

As the polarization from solar flares would also be affected by the photospheric albedo effects, ideal measurements would be imaging polarimetry, which could possibly segregate the direct emission component and scattered component (Jeffrey & Kontar, 2011). However, imaging polarimetry in hard X-rays, even in the case of the Sun, is going to be extremely challenging. Hard X-ray polarimeters typically do not have any position sensitivity, and even if such an instrument is conceived, the sensitivity will be poor due to the inherent inefficiency of the polarimeter as well as that of the reflectivity of mirrors at high-energy X-rays. Indirect imaging methods such as those employed in STIX also is not compatible with polarization measurements. Compton telescopes are one possibility where the incident direction and polarization can be recorded simultaneously; however, the angular resolutions are much poorer than those required for imaging of extended sources like the Sun.

On the other hand, the basic requirement of energy-dependent polarization measurement can be met with non-imaging polarimetry. As discussed in the previous section, disk-integrated energy-dependent measurements of the polarization of the solar flares can also provide diagnostics of the electron population. Thus, the basic requirement is to have an instrument capable of measuring polarization in the hard X-ray band (typically above 20 keV where the non-thermal emission dominates), at least over a few energy bins, and sensitive enough to make measurements of at least a few tens of flares over the mission duration.

8.2.1 Compton X-ray polarimetry

Various techniques are employed for the measurement of X-ray polarization in different energy bands. Photo-electric polarimetry is best suited for soft X-rays, while Rayleigh and Compton scattering polarimetry work best at medium and high energy X-rays (Section 1.2.3). In scattering polarimetry, incident X-rays from the source get scattered from a scatterer, and the azimuthal distribution of the scattered photons is used to measure the polarization properties. If the scattering is incoherent (Compton) and the scatterer is an active detector (ideally low-Z materials), that interaction can be recorded. The scattered photons are recorded by absorber detectors surrounding the scatterer. Then, the real scattering events can be identified by simultaneous detection of events in the scatterer and one of the absorber detectors, which will reduce the background significantly. As the Compton interaction probability increases at higher energies, Compton polarimetry with an active scatterer is best suited for polarization measurements in hard X-rays.

In a Compton polarimeter, the azimuthal scattering angle distribution will be uniform if the incident X-rays are unpolarized. When the incident X-rays are polarized, the azimuthal scattering angle distribution follows a sinusoidal pattern following the Klein-Nishina cross-section formula. Most photons get scattered in a direction perpendicular to the direction of polarization. The amplitude of the modulation provides the measure of the degree of polarization, whereas the phase provides the measurement of the angle of polarization. The degree of polarization is obtained as the ratio of measured modulation amplitude to the modulation amplitude for 100% polarized X-rays, denoted as μ_{100}. Geometry and other configuration details of the polarimeter decide its μ_{100} and is, in general, energy dependent.

The minimum detectable polarization (MDP) by a polarimeter depends on the μ_{100} and is given by:

$$MDP = \frac{4.29}{\mu_{100} R_s} \left[\frac{R_s + R_b}{T} \right]^{1/2} \tag{8.1}$$

where R_s is the source count rate, R_b is the background count rate, and T is the exposure time (see Weisskopf et al., 2010a and references therein). As the source count rate is R_s is proportional to the effective area of the polarimeter, for zero background case, the MDP is related to μ_{100} and effective area as:

$$MDP \propto \frac{1}{\mu_{100} * \sqrt{\text{effArea}}} \tag{8.2}$$

Thus, a polarimeter with the maximum figure of merit, defined as $\mu_{100} * \sqrt{\text{effArea}}$, would provide the best performance.

8.2.2 A prototype focal plane Compton polarimeter

Figure 8.2 left panel shows a close-to-ideal geometry for a Compton polarimeter. At the center is a scatterer rod, which is surrounded by several absorber detectors arranged in a cylindrical manner that measures the azimuthal angle distribution of scattered photons. A prototype of a Compton polarimeter in this configuration to be used as a focal plane detector to a hard X-ray focusing telescope has been developed in PRL (Chattopadhyay et al., 2013, 2014b, 2016b). In this prototype, the central scatterer is a plastic scintillator detector read out by a photo-multiplier tube, whereas the absorber detectors are CsI scintillators read out by Si-photo-multipliers (SiPM). The low energy limit for the instrument is dictated by the detection of energy deposition in the plastic scintillator, which is shown to be possible at energies above 20 keV (Chattopadhyay et al., 2014b). The high energy range of this configuration was 80 keV, which is limited by the effective area of hard X-ray focusing telescopes, assumed to be similar to *NuSTAR*.

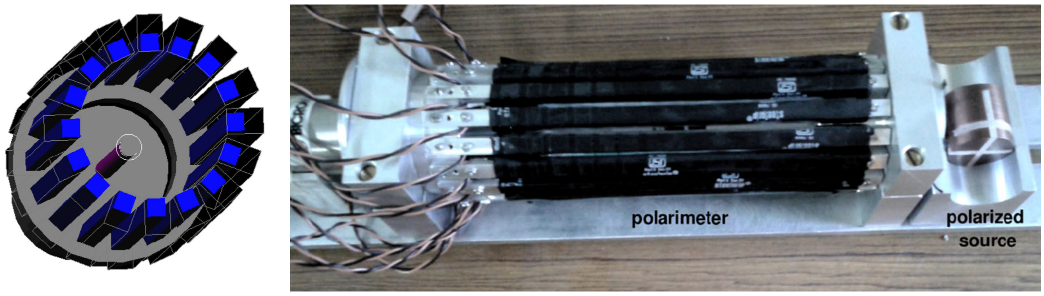

Figure 8.2: Focal plane hard X-ray Compton polarimeter concept (left) and prototype focal plane polarimeter (right) taken from Chattopadhyay et al. (2016b)

The developed prototype of the focal plane Compton polarimeter is shown in the right panel of Figure 8.2 (taken from Chattopadhyay et al., 2016b). Experiments with unpolarized and partially polarized X-rays and comparisons of the measurements with simulations were used to demonstrate the proof-of-concept of this polarimeter configuration (Chattopadhyay et al., 2016b). In this configuration, the hard X-ray focusing optics is used as a photon collection system, and no imaging polarimetry is feasible as the instrument does not have such capabilities. It is best suited for observations of fainter astrophysical sources, where the flux collection provides a significant advantage; however, for observations of solar flares, this prototype concept can be modified to a collimated instrument.

8.2.3 Spectro-Polarimeter Configuration and Geant4 Simulations

Figure 8.3 shows the proposed configuration of the collimated hard X-ray polarimeter for observations of solar flares. It consists of a plastic scintillator surrounded by 12 NaI (Tl) scintillator detectors arranged in a cylindrical fashion similar to the focal plane polarimeter prototype.

In the focal plane polarimeter prototype, CsI scintillators were used as absorber detectors primarily due to the ease of handling. NaI scintillators have much faster scintillation decay times (250 ns) compared to CsI scintillators (1000 ns) and thus provide better signal-to-noise when read out by SiPMs. Thus, NaI detectors are considered in the proposed configuration. One of the important

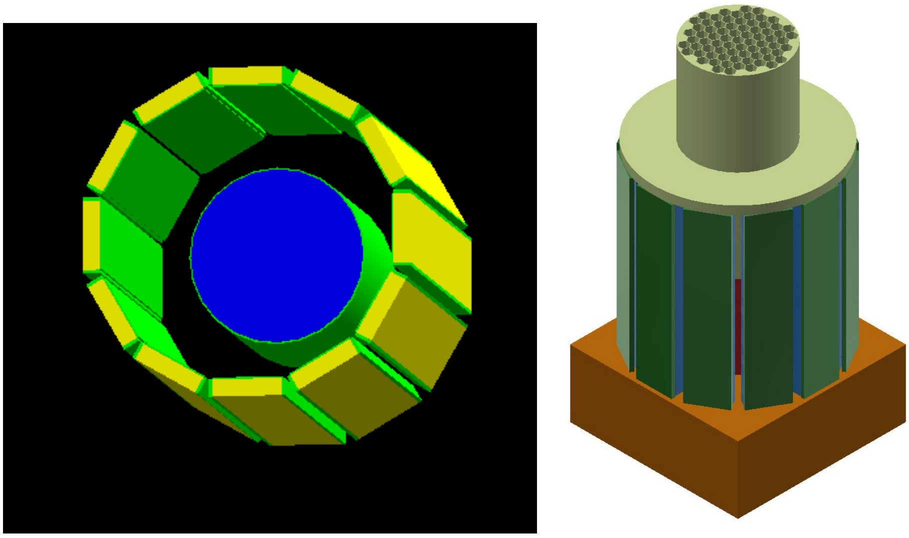

Figure 8.3: Left: Geant4 rendering of the polarimeter configuration with a central plastic scatterer and surrounding NaI scintillator detectors. Right: Schematic CAD model of the polarimeter with the collimator and electronic box. CAD courtesy: Neeraj K. Tiwari and Hitesh L. Adalja.

learnings from the focal plane polarimeter prototype development was that the absorber detectors read by SiPMs on one end are not capable of detecting X-rays over their entire length. Typically, detection of X-rays of 20 keV was possible only up to a distance of 50 mm from the SiPM end of the scintillator. Thus, in the proposed configuration, the NaI detectors are 100 mm long and are read out by SiPMs from both ends. The width of NaI detectors is tentatively 20 mm so that four SiPMs can be accommodated along each end. The thickness of the detector is 5 mm, which provides good detection efficiency up to energies beyond 100 keV. The SiPMs at both ends of NaI can be read with a Citiroc ASIC having 32 channels. The number of absorber detectors is decided to be 12 so that 24 of the readout chains of the ASIC will be used for NaI detectors while the rest can be used for the plastic scintillator.

The plastic scintillator is collimated to a small field of view of about 2 degrees with the help of the collimator shown in the figure. Unlike the Compton polarimeter in focal plane configuration, the plastic scintillator needs to have a larger diameter so that a reasonably high effective area can be achieved. However, increasing the diameter reduces the modulation amplitude of the polarimeter due to multiple scatterings within the scatterer.

To identify the optimum geometrical parameters for the plastic scatterer, we carried out simulations using the Geant4 toolkit. Figure 8.3 left panel is the rendering from Geant4 of the geometry of the polarimeter. Simulations were done with different radii and lengths of the plastic scintillator, and the modulation amplitude for 100% polarised X-rays (μ_{100}) for each configuration was obtained. The figure of merit of the polarimeter, defined as $\mu_{100} * \sqrt{\text{effArea}}$, for different configurations are shown in Figure 8.4. The maximum value of this figure of merit corresponds to the least Minimum Detectable Polarization if the background is ignored (Equation 8.2). From Figure 8.4, it can be seen that the configurations with a length of 70 mm and radius of 30/35 mm provide the best performance (marked by cyan stars). Among the two options, the one with a 30 mm radius is preferred as it would reduce the mass, and thus, the plastic scintillator with a radius of 30 mm and length of 70 mm is chosen for the proposed configuration of the polarimeter. It may be noted that simulations were also carried out considering different offsets between the placement of the scatterer and the absorber detectors; however, the configuration where the scatterer is aligned with the bottom end of the absorber is found to have the best performance and the same configuration is considered for further analysis.

In this Compton polarimeter configuration, the energy recorded by the absorber detectors is of the scattered photons, which will be less than the energy of the incident X-ray photon. While the deposition of energy in the plastic scatterer is detected, its energy resolution is rather poor to use the measurement in plastic to compute the incident photon energy. However, if the polar scattering angle is known, using the energy deposition in the NaI detectors, the incident photon energy can be estimated, making it possible to provide spectro-polarimetric observations. NaI scintillators read out from both ends provide the added advantage of the measurement of interaction position along the NaI detector, which can be used to measure the polar scattering angle. The polar angle can be estimated with better accuracy if the position of interaction within the plastic scintillator is also known. For this purpose, instead of a single plastic scintillator rod of 70 mm in length, smaller segments, having lengths of $\sim$10 mm,

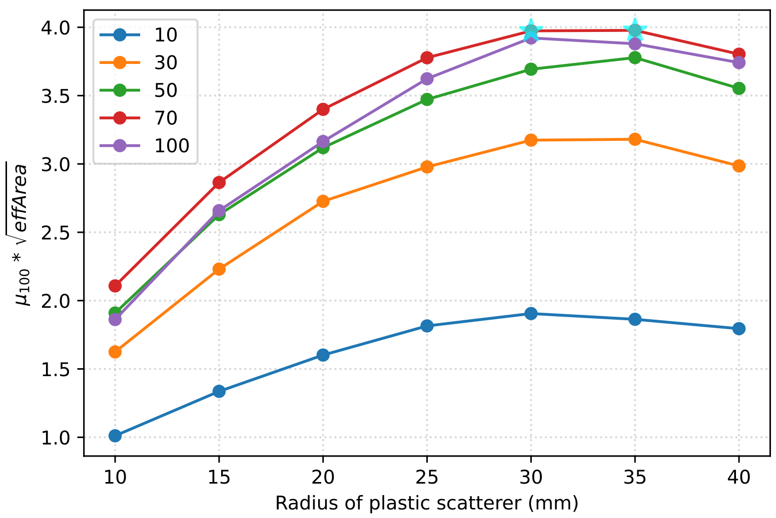

Figure 8.4: Figure of merit of the polarimeter configuration defined as ($\mu_{100} * \sqrt{\text{effArea}}$) for different radii and lengths of the plastic scatterer. Each color corresponds to different lengths of the scatterer, as noted in the figure. Cyan stars represent the most optimal configurations with nearly the same performance.

stacked together are to be used as the scatter. Each of these segments is read out by SiPMs from their sides, using the remaining readout chains of the Citiroc ASIC. With this, the interaction position in the plastic is also known, which gives better estimates of the polar angle and, hence, the incident photon energy to provide modest spectroscopic capabilities, allowing polarization measurements in different energy bands.

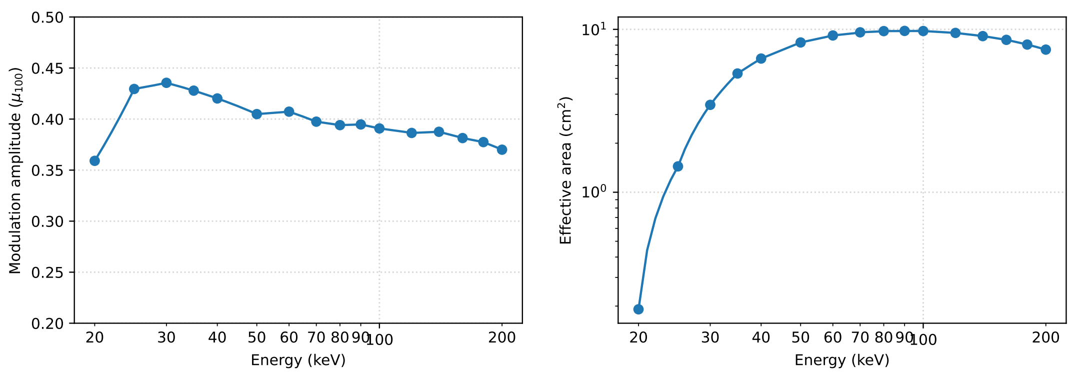

Figure 8.5: Modulation amplitude for 100% polarized X-rays (μ_{100}) and effective area as a function of energy for the optimal configuration of the polarimeter with a 70 mm long plastic scatterer having 30 mm radius.

Figure 8.5 shows the modulation amplitude for 100% polarized X-rays as a function of energy as well as the effective area for the arrived optimal configuration of the Compton spectro-polarimeter. It may be noted that the efficiency and modulation amplitude at lower energies would depend on the achieved low-energy threshold in the plastic scatterer, which is considered to be 1 keV in these calculations based on previous experiments with plastic scintillator (Chattopadhyay et al., 2014b). Further, to compute the effective area, a collimator open fraction of 90% is considered. From the figure, it can be seen that the modulation amplitude is about 0.4 for most parts of the energy range, and a maximum effective area of about 10 cm^2 is achievable with this configuration.

The proposed configuration is estimated to have a mass of $\sim$ 5 kg, including the detectors, readout electronics, and support structures. The power requirement is estimated to be about 15 W. These resource requirements match with the typical availability on small satellite platforms such as CubeSats and ISRO's PSLV Orbital Experimental Module (POEM) platform. Thus, the proposed configuration can be planned to be flown in such platforms.

8.2.4 Expected Performance

We now examine the expected performance of the proposed Compton polarimeter for observations of solar flares. For this purpose, we consider typical model spectra of solar flares of different classes as shown in Figure 8.6 left panel. Thermal components of the spectra were estimated considering the temperature emission measure correlation with GOES class given by Feldman et al. (1995). The non-thermal components were considered as powerlaws whose index and normalization are obtained from correlations of these parameters with GOES class given in Saint-Hilaire et al. (2008). Considering the effective area of the proposed polarimeter configuration, the expected spectra for each class of flare are shown in the right panel of Figure 8.6. The dotted lines in the figure correspond to the contribution from the non-thermal component, which is expected to be polarized. It can be seen that the measurements above 30 keV would be probing primarily the non-thermal component alone in all cases.

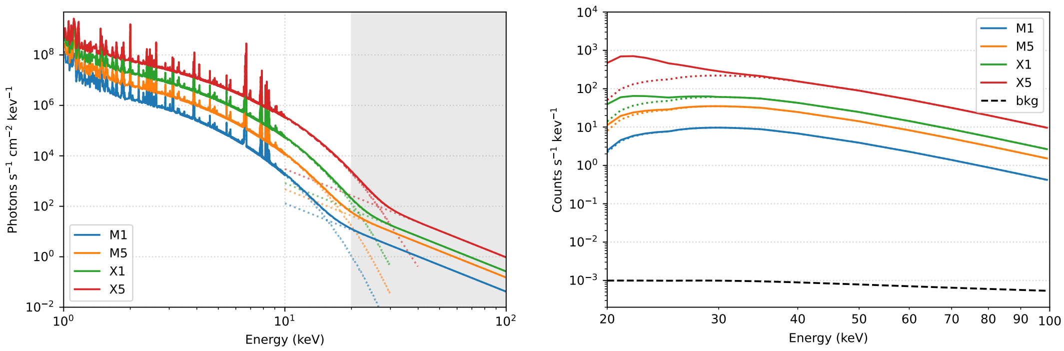

Figure 8.6: Left: Typical model spectra of few classes of flares including thermal and non-thermal components. Right: Expected count spectra for each flare with the proposed polarimeter configuration. The dotted lines correspond to the contribution from the non-thermal component alone. The Black dashed line corresponds to the estimated background spectrum.

The background spectrum is estimated as the sum of the Cosmic X-ray Background (CXB) component (CXB scattered from plastic and detected in NaI) and particle background component (chance coincidence between plastic and NaI events). CXB component is estimated using the CXB models from Türler et al. (2010) (broken power law model in Table 3). For particle background, we consider a power law with an index of 0.4 and total particle counts to be 0.56 per cc (10-200 keV). This is estimated from the actual measured background in AstroSat CZTI veto detectors scaled by a factor of two. It maybe noted that this is applicable only for low inclination orbits like AstroSat, which would be the preferred orbit for the polarimeter as it would provide low and relatively stable background. To estimate chance coincidence rates, the coincidence time window is considered to be 10 μs. The estimated background spectrum is shown in Figure 8.6 right panel with the black dashed line, which is considerably less than the counts expected from the solar flares.

Using the expected count rates for different classes of solar flares and the background rates, MDP is computed for each flare class in the entire energy range of 20 – 100 keV, which is shown in Figure 8.7. The figure shows MDPs considering exposures of 60 s and 300 s. It can be seen that the MDP for flares of M1 class and higher is less than 10% considering even 60 s exposure at the

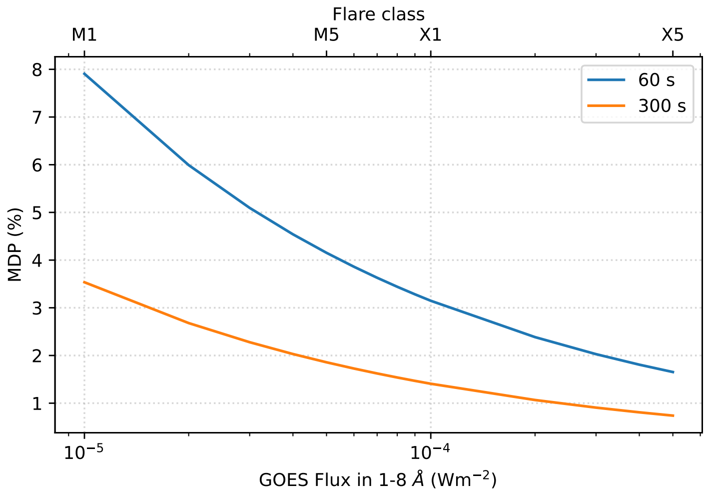

Figure 8.7: Minimum Detectable Polarization (MDP) for different flare classes assuming 60 s and 300 s durations. MDP shown is for the 20 – 100 keV energy range.

flare non-thermal peak, and thus polarization measurements in the entire energy range are feasible for M1 class flares and higher.

While the energy-integrated polarization measurements for several flares would be a useful measurement, better diagnostics of electron anisotropy is the energy dependence of polarization. To check whether observations with the proposed polarimeter can distinguish between the energy-dependant polarization signatures of beamed electron distribution against the isotropic electron distribution, simulations are carried out. Beamed electrons are expected to cause increasing polarization with energy, while the isotropic distribution would result in close to zero polarization over the entire energy range (Figure 8.1). Figure 8.8 shows the expected measurements of polarization for the case if the polarization were increasing with energy for an M5 class flare and an X1 class flare. The red dashed line corresponds to the assumed trend in polarization, and the data points with error bars are the expected measurements. The green dashed line corresponds to the low polarization case, and the MDP for each energy bin is shown with the black lines. It can be seen that if the polarization of flares were low due to the isotropic distribution of electrons, the polarimeter would not detect polarization from observations, while clear detection of polarization that increases with energy can be expected if the electrons were beamed. Thus, the proposed configuration of the instrument is capable to discern between the expected polarization signatures from beamed and isotropic electron populations, for flares of M5 class and higher.

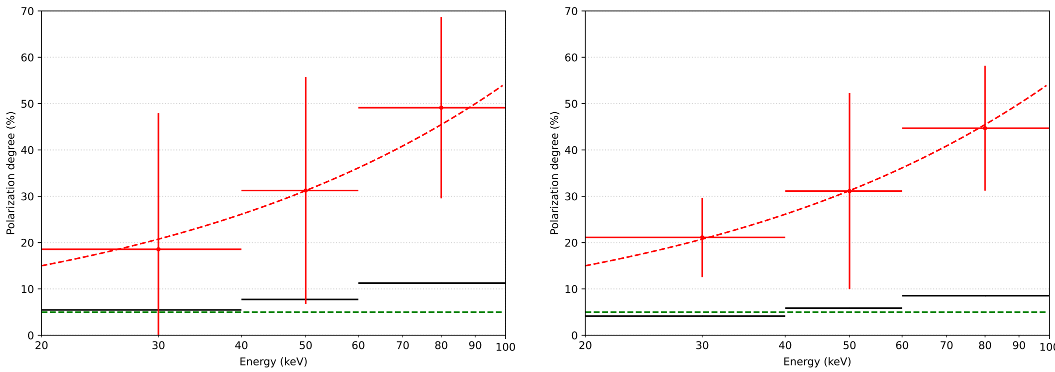

Figure 8.8: The red data points with errors show the expected polarization measurements for an M5 flare (left) and an X1 flare (right) if the inherent polarization were increasing with energy (red dashed line) as in the case of beamed electron distribution as opposed to very low polarization that does not change much with energy (green dashed line) in the case of isotropic electrons (see Figure 8.1). Black lines correspond to the MDP for the respective energy bin. Simulations consider an observing duration of 60 s.

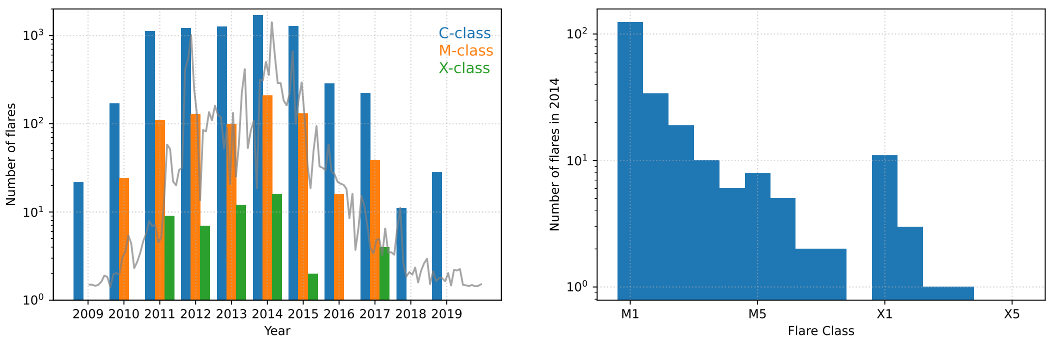

Figure 8.9: Left: Number of different classes of flares in each year during the last Solar Cycle from HEK database. The grey line in the background shows the monthly average number of Sunspots. Right: Number of M1-X5 flares during the maximum in 2014.

The small satellite platforms that can accommodate the proposed polarimeter typically have a nominal mission life of six months, and being in low earth orbit, observing efficiency would be approximately 50%. To maximize the opportunities for polarization measurements of flares with such a short-term mission, it should be planned during the solar maximum. To estimate the number of flare events expected to be observable with the proposed polarimeter within typical mission life, we use the statistics of number of flares observed in the last Solar Cycle. Figure 8.9 left panel shows the number of flares of C, M, and X classes observed during the last Solar Cycle. The solar activity peaked in 2014, and the right panel of Figure 8.9 shows the number of flares in 2014 greater than the M1 class that can be observed with the polarimeter. Assuming the polarimeter carries out observations for six months with an efficiency of 50% during a solar maximum similar to that in 2014, it is expected to observe ~ 55 flares of M1 class and higher for which polarization measurements will be possible. It is expected that ~ 10 flares of M5 class or higher would be observable in this period, for which energy-dependent measurements will be feasible.

Thus, the proposed configuration flown on a small satellite platform can indeed provide new insights into the acceleration mechanisms in solar flares and an impetus to the area of solar X-ray polarimetry. Such a mission would also be a pathfinder for hard X-ray polarimetry missions for observations of other astrophysical sources.

8.3 Polarimetry of Other Astrophysical Sources

Until recently, X-ray polarimetry of astrophysical sources has remained a largely unexplored field, unlike imaging, spectroscopy, and timing in X-rays, despite its potential to add another dimension to our understanding of the physics of sources such as black hole binaries, AGNs, and pulsars. The first successful measurement of X-ray polarization dates back to 1970s (Weisskopf et al., 1976, 1978), not much later than the birth of X-ray astronomy. However, the difficulties in building sensitive X-ray polarimeters hampered the field's continued growth. With the advent of polarimeter concepts such as the photo-electric polarimeter (Costa et al., 2001) in the early 2000s, interest in X-ray polarimetry gained momentum over the last two decades (Marin, 2018). It resulted in developments and proposals of various instrument configurations for X-ray polarimetry.

With the launch of the Imaging X-ray Polarimetry Experiment (IXPE, Weisskopf et al., 2022), the first dedicated space mission for X-ray polarimetry carrying out measurements in the soft X-ray band of 2-8 keV, the field of X-ray polarimetry has entered a new era with measurements of polarization for a number of sources for the first time. POLIX (Paul et al., 2016), a Thomson X-ray polarimeter experiment very recently launched with the Indian XPoSat mission, would extend the polarization measurements to higher energies by providing measurements in the 8-30 keV energy band.

However, at present, no approved missions or instruments are planned for polarimetric observations in the hard X-rays beyond the POLIX energy range. The hard X-ray energy range is dominated by the emission from different processes compared to the processes responsible for soft X-ray emission in several classes of sources. Thus, observations in hard X-rays provide complementary information to soft X-ray measurements. Moreover, in many cases, the hard X-ray spectra can be modeled with several physical processes, but the predictions of the degree of polarization for them are different, similar to the scenario in the case of solar flares as discussed in Section 8.1.

Several groups are pursuing the development of hard X-ray polarimeters. Different generations of instruments such as POGOLite & POGO+ (Chauvin et al., 2016c, 2017a, 2016b) and X-Calibur & XL-Calibur (Abarr et al., 2022, 2021) have been developed and had few observations from balloon platform. There have also been some measurements made in the hard X-ray to soft gamma-ray energies with instruments that were not purpose-built polarimeters, such as INTEGRAL IBIS & SPI, AstroSat CZTI, and Hitomi HXD. However, these are limited to very bright sources such as Crab and Cygnus X-1. See Table 8.1 for a summary of recent and near-future missions in X-ray polarimetry, including the balloon missions (only narrow FOV instruments meant for on-axis sources). While there have been proposals such as the X-ray Polarimetry Probe mission (Krawczynski et al., 2019) to take the developments of balloon-borne polarimeters into a satellite mission, there are no active developments for po-

Instrument	Energy Range	Remarks	Reference
IXPE	2–10 keV	Launched in Dec 2021	Weisskopf et al. (2022)
XPoSat POLIX	8–30 keV	Launched in Jan 2024	Paul et al. (2016)
X-Calibur	15–50 keV	Balloon flight in 2018/19	Abarr et al. (2022)
XL-Calibur	15–50 keV	Short Balloon flight in 2022, long Antarctica flight in 2023	Abarr et al. (2021)
POGOLite	25–150 keV	Balloon flight in 2013	Chauvin et al. (2016c)
POGO+	20-150 keV	Balloon flight in 2016	Chauvin et al. (2017a, 2016b)
Integral IBIS	200 – 800 keV	Launched in 2002	Forot et al. (2008)
Integral SPI	130 keV - 1 MeV	Launched in 2002	Dean et al. (2008); Chauvin et al. (2013)
AstroSat CZTI	100–380 keV	Launched in 2015	Vadawale et al. (2015)
Hitomi SGD	60–160 keV	Operated for short period	Hitomi Collaboration et al. (2018)

Table 8.1: Summary of recent X-ray Polarimeters including dedicated satellite missions, balloon-borne instruments and instruments

larimetry missions in the hard X-ray regime and thus presents a niche area.

The configuration of the collimated hard X-ray polarimeter presented in Section 8.2 for observations of solar flares can be extended to suit observations of bright astrophysical sources. First, we briefly review the science cases of hard X-ray polarimetry of astrophysical sources other than the Sun and then we present an instrument concept and discuss its expected performance.

8.3.1 Science Cases of Hard X-ray Polarimetry

Black hole binaries

X-ray polarimetric observations of the black hole binaries in different spectral states such as hard state and soft state (Remillard & McClintock, 2006) provide the opportunity to probe different aspects. In the hard state, where the emission in the hard X-ray energy range is dominated by the emission from the corona and the reflected component, hard X-ray polarization measurements allow us to probe the geometry of the corona (Schnittman & Krolik, 2010). For example, Schnittman & Krolik (2010) has shown the model predictions of energy-dependent X-ray polarization for different coronal geometries observed at different inclinations.

In the soft state where the accretion disk dominates the emission, polarization measurement can probe the black hole's mass and spin (Schnittman & Krolik, 2009). Even though the expected polarization is much higher in hard X-rays above 20 keV, as the flux is expected to be low, this may not be achievable with collimated X-ray polarimeters and would require focusing telescopes.

In the hard or intermediate hard state where there is the presence of a jet, the emission in hard X-rays above 100 keV may also include a contribution from the synchrotron emission from the jet. There has been spectroscopic evidence for such contribution of jet emission in X-rays (Vadawale et al., 2001; Markoff et al., 2001). Moreover, this is consistent with the very high polarization measurements by INTEGRAL for Cygnus X-1(Laurent et al., 2011; Jourdain et al., 2012). However, this hypothesis also has been met with criticism and contradictory evidence(Zdziarski et al., 2014) as the polarization measurements with INTEGRAL have limited credibility due to a lack of dedicated ground calibration excercise for polarimetry. Our recent report of state-dependant polarization measurements in the 100-380 keV of Cygnus X-1 with *AstroSat* CZTI showed an increasing trend of polarization within this energy band, confined only to the intermediate hard state, pointing to contribution from the jet component (Chattopadhyay et al., 2023). Extending such measurements of energy-dependent polarization in the intermediate energy bands would allow making definitive statements on the jet contribution.

Neutron stars

In the case of rotation-powered pulsars, polarization measurement as a function of the pulse phase allows to discern between various emission models (Harding, 2019). The predictions of pulse phase resolved polarization properties for different emission models, such as the two-pole caustic model, polar cap model, outer gap model, and striped wind model, show distinctions that are not present in the predictions of pulse profiles or spectra. Our earlier report of phase-resolved polarization measurement of the Crab pulsar in 100-380 keV showed swings in polarization degree and angle, ruling out the classic variants of the polar cap and outer gap models (Vadawale et al., 2018). The observed swings in polarization properties in the off-pulse phase, however, are not explained by any of the existing models (Vadawale et al., 2018). Extending such measurements to lower energy bands and to other rotation-powered pulsars would provide further insights.

In the case of accretion-powered pulsars, the X-ray polarization allows us to probe the accretion geometry, i.e., fan beam or pencil beam. Phase-dependant polarization signatures for these two geometries show distinguishable features (Meszaros et al., 1988). It is also to be noted that these signatures are more pronounced near the cyclotron resonant feature, which usually falls in the hard X-ray energy band.

AGNs

Bright Blazars are possibly the best class of AGNs that could be targeted with collimated polarimeters. X-ray polarization measurements would be able to break the degeneracy between the two main leptonic models that attempt to explain the blazar jet emission (Zhang, 2017).

8.3.2 Instrument Concept and Expected Performance

A single unit of the collimated Compton polarimeter presented in Section 8.2 for observations of solar flares does not have sufficient effective area for observations of other astrophysical sources. However, by using multiple units of such instruments, required sensitivities can be achieved. Taking into consideration the typical mass and power resources available on the IMS-2 spacecraft bus[1] of ISRO (used in the *XPoSat* mission), we arrive at the hard X-ray polarimeter instrument consisting of a 7 x7 array of individual polarimeter units on a spacecraft as shown in the Figure 8.10 left panel.

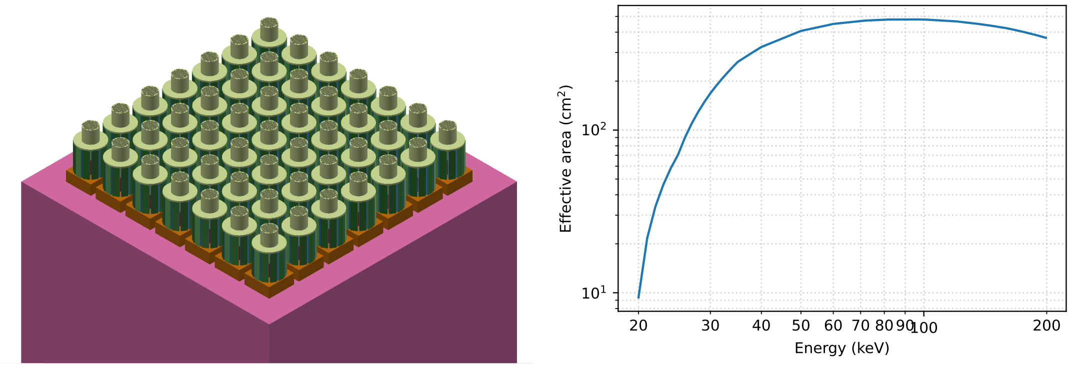

Figure 8.10: Left: CAD model of the concept of an array of collimated hard X-ray polarimeter units. Right: Effective area of the full instrument. CAD courtesy: Neeraj K. Tiwari and Hitesh L. Adalja.

With this configuration of the instrument, we estimate the effective area for the hard X-ray polarimeter, similar to that done in the previous section for one unit. Figure 8.10 right panel shows the effective area of the Compton polarimeter array with 49 modules. The instrument has a peak effective area of about 500 cm^2.

Using modulation amplitudes and effective area estimates obtained from Geant4 simulations as well as estimates of background as in Section 8.2.4, MDP of the polarimeter array as a function of flux in 20-200 keV are computed for different exposures as shown in Figure 8.11. This assumes a power law of index 2.1 as the source spectrum. It can be seen from the figure that with the proposed

[1] https://acadpubl.eu/jsi/2018-118-16-17/articles/17/18.pdf

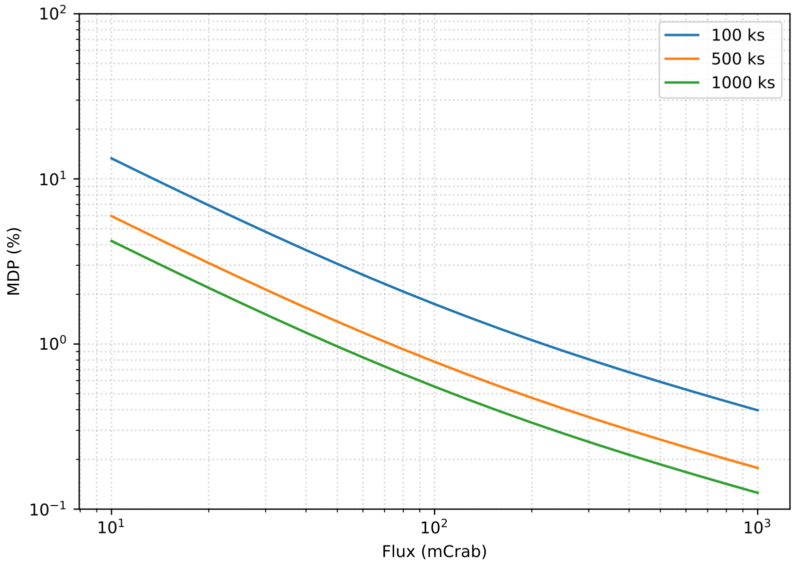

Figure 8.11: Minimum Detectable Polarization as a function of the source flux in mCrab units. Each line corresponds to a different exposure time, as mentioned in the figure.

instrument, a few percent MDP can be achieved with exposures of 500 ks - 1 Ms for a 10 mCrab source. For sources brighter than 100 mCrab, an MDP of less than 1% can be achieved with exposures of 500 ks, while for sources having flux higher than 500 mCrab, exposure of 100 ks is sufficient to reach an MDP of less than 1%. Thus, the proposed instrument configuration is capable of measuring the X-ray polarization of astrophysical sources with flux above 10 mCrab.

While the energy-integrated polarization measurements are useful in some cases, in most cases, the measurement of energy-dependent polarization is what allows distinction between various theoretical models. In Figure 8.12, MDP as a function of energy is shown for a 1 Crab source and a 100 mCrab source. Count spectra for both sources (not including the spectral redistribution) are also shown in the lower panels along with the background spectra. Counts from the source dominate over the background in the case of the 1 Crab source, while the background dominates at lower energies and at energies above $\sim$ 80 keV for the 100 mCrab source. For the 1 Crab source, energy-dependent polarization measurements of a few percent are feasible with exposures of 100 ks or higher. For the 100 mCrab source, MDP is less than 10% for broad energy bins at energies

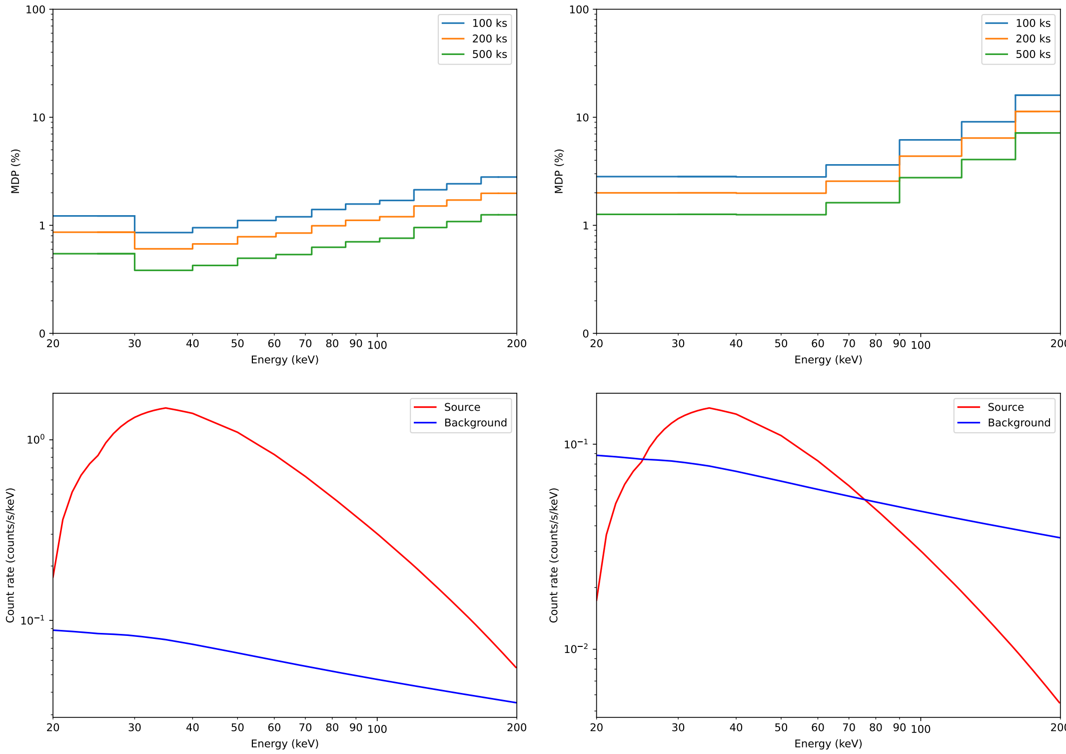

Figure 8.12: Top: Minimum Detectable Polarization as a function of energy for a source having flux of 1 Crab (left) and 100 mCrab (right). Bottom: Expected source count spectra with background spectra for 1 Crab (left) and 100 mCrab (right) source.

less than 100 keV. Thus, energy-dependent polarization measurements with at least a few energy bins are feasible with the proposed instrument for sources having fluxes of 100 mCrab as well.

As an example, to demonstrate the capability of the proposed instrument to distinguish between different energy dependencies of polarization, we show the expected performance for polarimetry of the persistent high-mass X-ray binary Cygnus X-1. Figure 8.13 top panel shows the available measurements of Cygnus X-1 polarization below 10 keV and above 100 keV from previous reports (Krawczynski et al., 2022; Chauvin et al., 2018; Jourdain et al., 2012; Chattopadhyay et al., 2023). The two dashed lines in the figure show possible trends of energy-dependent polarization as constant with energy and increasing as a power law with energy, both of which are close to being consistent with the measurements in a few energy bins below 10 keV with IXPE. The proposed

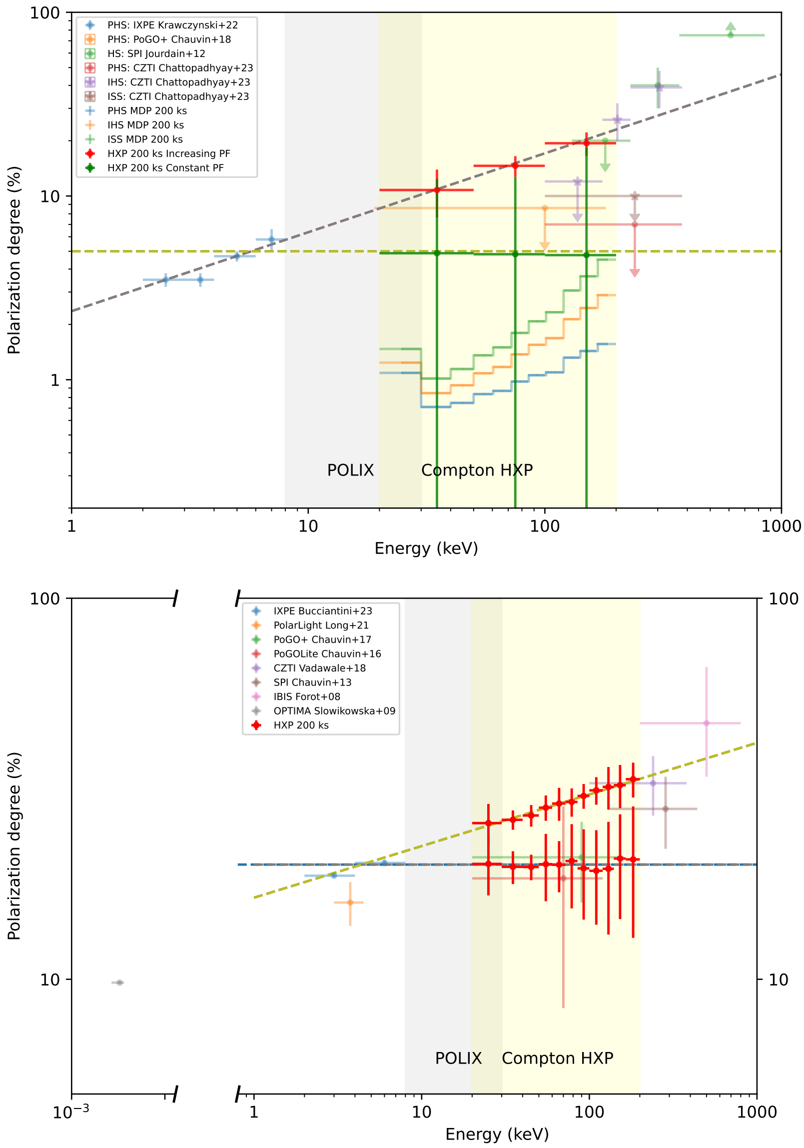

Figure 8.13: Capability of the proposed instrument to distinguish between constant and power law energy dependence of polarization degree for observations of Cygnus X-1 (top) and Crab (bottom). Previously reported measurements in other energy ranges are shown (see text), and the dashed lines show two potential energy dependence trends. Red/green data points with error bars are expected measurements with the proposed instrument. The yellow-shaded energy range corresponds to that covered by the proposed hard X-ray polarimeter instrument, while the grey-shaded region corresponds to the POLIX energy range.

instrument covers the yellow-shaded energy range, and the MDP for Cygnus X-1 observation of 200 ks in High Soft State (HSS), Intermediate Hard State (IHS), and Pure Hard State (PHS) are shown as steps. It may be noted that measurements in this energy range would provide crucial evidence to confirm whether the polarization is increasing with energy or remains constant. Red points show the expected measured polarization degree with error bars if the source was following an increasing energy dependence in a pure hard state, and the green points with error bars correspond to constant polarization with energy. Both correspond to observations with an exposure of 200 ks. It is apparent from the figure that it would be possible to discern if the polarization fraction remains constant or it is increasing with energy with the measurements from the proposed instrument.

The lower panel of Figure 8.13 shows the expected measurements of the energy-dependent polarization degree of the crab pulsar, assuming a constant or increasing trend of polarization degree with energy. The two trends (shown by dashed lines) are considered based on previously available measurements at lower and higher energies (Bucciantini et al., 2023; Long et al., 2021; Chauvin et al., 2016a, 2017b; Vadawale et al., 2018; Chauvin et al., 2013; Forot et al., 2008; Słowikowska et al., 2009). The red points correspond to the expected polarization degree measured as a function of energy for an observation of 200 ks exposure with the proposed hard X-ray polarimeter, which shows that the observations with this instrument would be able to clearly distinguish between the two models of energy dependant of polarization.

Another measurement of interest is that of polarization degree at each phase interval for the Crab pulsar and nebula. Vadawale et al. (2018) reported variations in the polarization degree during the off-pulse phases in the 100 – 380 keV energy band, which was unexpected. However, the variations were not highly statistically significant, and measurements with IXPE at energies below 10 keV did not show any significant variations in the polarization properties in the off-pulse phase. While spectroscopic measurements with pulse phase would throw some light on the potential energy dependence of such a variation and its origin (Section 2.10), further measurements in other energy ranges would provide more insights. Here, we consider the variations observed by CZTI to be real and simulated if the proposed instrument can discern the variations if they exist at lower energies in the 20 – 200 keV energy band. Figure 8.14 shows the

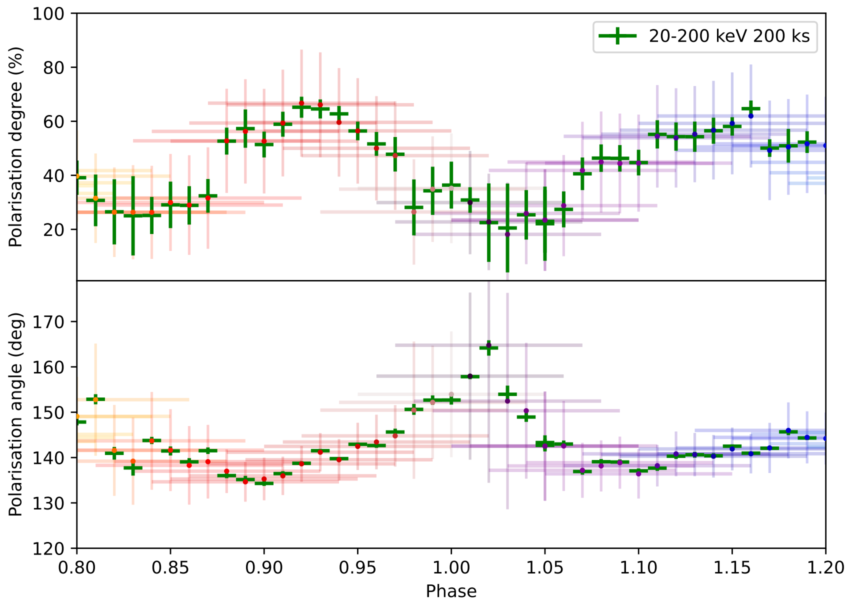

Figure 8.14: Expected capability of the instrument to measure any variations in off-pulse polarization degree and angle as observed by AstroSat CZTI. CZTI reported measurements from Vadawale et al. (2018) are shown as error bars in the background. Expected measurements with errors assuming CZTI measurements to be the actual values of polarization properties are shown in green error bars.

expected polarization measurements in the off-pulse phase with an exposure of 200 ks. In the background are the CZTI measurements for broader phase bins. The simulations show that it would be possible to have statistically significant measurements of the variations, if they are real, with the proposed instrument.

The proposed configuration of the hard X-ray Compton polarimeter is expected to have sufficient sensitivity to measure polarization of sources brighter than 10 mCrab. It is also shown that these measurements are capable of discerning between different possible models of energy-dependence of polarization.

8.4 Summary

X-ray polarization measurements add another dimension to understanding the physical processes in astrophysical sources obtained with spectroscopic and timing observations. In this chapter, we presented a concept design of an instrument for spectro-polarimeteric observations of solar flares in the hard X-ray band to probe the properties of the flare-accelerated electron population, such as its anisotropy and high-energy cutoff, which in turn points to the underlying acceleration mechanism. The concept is extended from a prototype focal plane Compton polarimeter to a collimated polarimeter. It uses plastic scintillators surrounded by NaI scintillator detectors to measure the azimuthal scattering angle distribution to infer polarization properties in different energy bands. With the optimized configuration of the polarimeter, a minimum detectable polarization of less than 10% is achievable for flares of M1 class and higher, with modest resource requirements that can be matched with small satellite platforms. If the instrument is flown on a small satellite mission with a nominal life of six months during solar maximum, the instrument is expected to make polarization measurements for $\sim$ 55 flares and energy-dependant polarization measurements for $\sim$ 10 flares. Thus, the proposed instrument is expected to provide insights into the acceleration mechanism in flares.

Further, we extend this concept of the collimated polarimeter unit to a larger mission with an array of polarimeter units for observations of other astrophysical sources. This configuration provides an MDP of less than 10% for a 10 mCrab source with exposures of a few 100 ks. It is also shown that the observations with the proposed configuration can provide crucial measurements in the hard X-ray band of 20 – 200 keV in the energy-dependent polarization of the black hole binary Cyg X-1 and the Crab pulsar and nebula, complementing the existing measurements and having the potential to discern between increasing trend or constancy of polarization degree with energy.

While some aspects of the Compton polarimeter, such as the NaI detectors readout by SiPMs at two ends, have been demonstrated, other aspects, such as the readout of segmented plastic scintillator, need to be taken up in the future. We plan to take up the development of one unit of the Compton polarimeter and propose for flight in a suitable small satellite platform for observations of solar flares. This would provide first-of-its-kind measurements of X-ray polarization of the flares and, at the same time, would prove to be a pathfinder for a mission proposal for a hard X-ray polarimeter for observations of other astrophysical sources.

Chapter 9

Summary and Future Prospects

9.1 Summary

Continuum X-ray spectroscopy is a powerful technique to decipher the emission mechanisms and physical conditions in astrophysical sources such as the solar corona, black hole binaries, and neutron stars that harbor matter in extreme conditions. Inferring the source characteristics from the observed X-ray spectrum requires an accurate model of the spectroscopic response of the instruments. While some aspects of the instrument response can be obtained by laboratory characterization, in almost all cases, significant improvements are required to be done using in-flight observations so that accurate measurements of the characteristics of astrophysical sources are possible.

Among the celestial X-ray sources, the brightest one is the solar corona. X-ray emission from the Sun includes quiescent emission as well as sudden enhancements during solar flares. While there is consensus that magnetic reconnection is the driver of solar flares, details of the acceleration and heating mechanisms still remain elusive, and they are best probed with observations in X-rays. Aside from the large solar flares, weak events are also of interest as they offer possibilities to probe the contribution of nanoflares to coronal heating.

This thesis presented the improvements in different aspects of the spectroscopic response of *AstroSat* Cadmium Zinc Telluride Imager (CZTI) and Chandrayaan-2 Solar X-ray Monitor (XSM). In the second part, solar flares of different scales were analyzed primarily using X-ray spectroscopic observations with XSM to address specific questions on the contribution of small-scale events to coronal heating as well as mechanisms of plasma heating and acceleration in solar flares. Further, instrument concepts for polarimetric observations of solar flares and other astrophysical sources in hard X-rays were presented, which offers possibilities to break degeneracies in models that cannot be resolved with spectroscopy alone. The key results from this thesis are summarised below.

- CZTI is the hard X-ray spectroscopic instrument onboard *AstroSat* consisting of pixelated CZT detectors. Using in-flight observations over six years, response parameters of individual detector pixels, such as gain, are refined. With an improved understanding of the background, a new background subtraction algorithm is developed, which is shown to be statistically limited for typical exposures of CZTI observations. Further, the effective area of the instrument is refined by using measured alignments of individual detectors with the mask and calibration against the standard source Crab. With the improved response, CZTI is shown to be sensitive to carrying out spectroscopic analysis of sources of a few tens of milliCrab.

- XSM carried out disk-integrated soft X-ray spectral measurements of the Sun. With slight updates in the gain parameters, XSM is shown to have a stable detector response over the four years of in-flight operations. Corrections to the effective area at different angles were derived, and the resultant refined effective area is shown to have relative uncertainties of less than 1%. The low background levels in XSM make it sensitive to X-ray flux levels of order of magnitude lower than GOES A level, and slight variations in the background are well understood. The adequacy of the calibration is demonstrated with spectral fitting, establishing the capabilities of XSM.

- Using XSM observations during the solar minimum, the largest sample of X-ray microflares occurring outside the active regions in the quiet Sun are detected. Using flare parameters obtained with X-ray spectroscopy and volume estimates from EUV images, we estimate the thermal energies of the events to be in the range of $\sim 3 \times 10^{26}$ - 6×10^{27} erg. It was shown to be difficult to conclude whether the nanoflare frequencies obtained from extrapolation of the flare frequency distribution are sufficient to heat the corona. However, the X-ray microflares are much less in number compared to the extrapolated frequencies of EUV transients observed at lower energies, suggesting different origins of some EUV transients and X-ray microflares.

– With time-resolved spectral analysis of a sample of three C-class flares, it is found that the X-ray emitting plasma during the impulsive phase of intense flares is not consistent with the isothermal assumption. Rather, the temperature distributions follow a bimodal distribution. The observed bimodal temperature distribution and the evolution of abundances seem to support direct heating in the coronal loop top by magnetic reconnection and secondary heating by evaporated plasma.

– By combining the soft X-ray spectra obtained with XSM with the hard X-ray spectra with Solar Orbiter STIX, improved constraints on the parameters of thermal plasma and non-thermal particles in a flare are obtained. From the estimated energetics, it is found that the cumulative non-thermal energy is higher than the energy content of the thermal plasma, which is consistent with the standard flare model picture. We also showed that the residuals near the Fe line complex arise from the fluorescence emission from the photosphere, suggesting that it would be important to consider this process in the analysis of X-ray spectra of flares.

– An instrument concept for collimated hard X-ray Compton polarimeter for observations of solar flares is presented. It is shown that, in a nominal mission life of six months, the instrument would be capable of measuring the polarization of $\sim$ 55 flares and would also be able to provide energy-dependant measurements of $\sim$ 10 flares which would allow the distinction between beamed and isotropic distributions of accelerated electrons. This concept is extended to a larger instrument that would be capable of measuring the X-ray polarization of other astrophysical sources brighter than 10 mCrab.

9.2 Future Prospects

The work presented in this thesis opens up various avenues to explore in the related areas, and some of them are briefly discussed here.

- In Chapter 2, a methodology for obtaining background subtracted spectrum with *AstroSat* CZTI employing mask-weighting has been presented, which is shown to provide statistically limited results. CZTI is also capable of measurement of X-ray polarisation of bright sources such as Crab and Cygnus X-1. At present, the background subtraction technique employed is limited to sources with dedicated background observations, and thus, it is difficult to carry out polarimetric analysis for some of the other bright black hole transients observed with CZTI having sufficient flux at energies above 100 keV (Table 2.5). In that context, extending the mask-weighting technique for polarimetric analysis would prove extremely useful, which is planned to be taken up in the near future.

- Section 2.10 presented initial results on the spectroscopic context of the variations in polarization properties in the off-pulse phases of the Crab pulsar. We plan to take this up further by utilizing observations with CZTI and NuSTAR. The medium energy X-ray polarimeter on the recently launched XpoSat would be observing the Crab in the early phases of its mission, and it would also be interesting to explore the off-pulse polarization variations with POLIX.

- In Chapter 3, the corrections to effective area of *Chandrayaan-2* XSM at energies above 1.3 keV were presented. At present, there are some uncertainties in the response in the energy range of 1 – 1.3 keV in XSM. Dual-zone Aperture X-ray Solar Spectrometer (DAXSS) (Woods et al., 2023) flown on Inspiresat-1 uses similar Silicon Drift Detectors as that of XSM for observations of the Sun. Simultaneous observations of solar X-rays at different intensity levels with both XSM and DAXSS are available now, which can be used to understand the low energy response of XSM better and make comparisons of both instruments.

– At high count rates when observing intense solar flares, *Chandrayaan-2* XSM suffers the effects of pulse pileup in addition to the dead time effects discussed in Chapter 3. It is estimated that the pileup effect is of the order of a few percent (Mithun et al., 2021b); however, a detailed pileup model can provide how it would affect the measurements of flare plasma parameters and possibly also be used in the analysis of several M class flares now observed with XSM.

– The analysis presented in Chapter 5 concluded that the frequency distribution of X-ray microflares is lower than the extrapolated frequencies of previously observed EUV transients in the quiet Sun. One possibility is that not all EUV transients are arising from reconnection events reaching flare-like temperatures. A comprehensive analysis of EUV transients with observed X-ray counterparts, like the events presented in this thesis and other EUV transients observed in the same period without any counterparts, can possibly shed some light on this. Further investigations, such as the photospheric magnetic field structures and corresponding extrapolated coronal magnetic field topology for some of the events from both classes, would also provide insights into their origin from magnetic reconnection.

– We showed that the X-ray emitting plasma in the impulsive phase of intense flares is multi-thermal (Chapter 6). Temperature and emission measure derived from GOES XRS instruments, under isothermal assumptions, are widely used due to the continuous availability of the data. However, these are approximations and do not provide correct results, especially when they are used in deriving some other parameters. For example, elemental abundances of the lunar surface derived from the X-ray fluorescence emission observed by Chandrayaan-2 CLASS show discrepancies when GOES-derived temperature and emission measures are used instead of spectroscopically determined values (Narendranath et al., 2024). Thus, it is worthwhile to explore the possibilities of any correction factors to GOES fluxes as well as the derived temperature and emission measure by using available simultaneous observations with XSM.

– Chapter 7 demonstrated the power of combining observations in soft X-rays and hard X-rays to consistently determine the properties of thermal and non-thermal particle populations in solar flares and their energies. Observations in EUV can probe temperatures even lower than that by soft X-rays. A joint modeling of EUV, soft X-ray, and hard X-ray observations would provide a more complete picture of the flaring plasma and provide more accurate energy estimates. Thus, extending the efforts of joint spectroscopy of soft and hard X-ray spectra to include EUV narrow-band imaging data such as from AIA would prove useful.

– In Chapter 7, analysis of the residuals of Fe line complex revealed the contribution from Fe fluorescence emission. Preliminary analysis of spectra from another spectrometer, Inspiresat-1 DAXSS (Woods et al., 2023), also has shown similar results. As the photospheric fluorescence is expected to be dependent on the location of the flare on the solar disk, investigations of Fe line residuals for flares occurring at different locations on the disk using XSM and DAXSS would provide further insights.

– Recent studies of X-ray observations of the flares with GOES XRS by Hudson et al. (2021) and with Solar Orbiter STIX by Battaglia et al. (2023) have shown the presence of plasma at elevated temperatures before the start of the impulsive energy release, which they call as the hot onset in flares. In XSM observations of some flares, enhanced emission has been observed before the impulsive energy release, and such flares are good candidates for exploring the presence of hot onsets. XSM, being more sensitive to lower-temperature plasma than STIX and having the advantage of spectroscopic observations compared to GOES, would provide further insights into the flare hot onset investigations.

– Recently launched Aditya-L1 mission includes two X-ray spectrometers covering the soft X-rays and hard X-rays named SoLEXS and HEL1OS, respectively (Sankarasubramanian et al., 2017). SoLEXS has very similar capabilities as the *Chandrayaan-2* XSM, and combined with HEL1OS, these instruments provide wide-band X-ray spectroscopic capabilities, advantages of which were demonstrated by the analysis of a flare with XSM and STIX observations presented in Chapter 7. As Aditya-L1 is observing the Sun from the L1 point, continuous coverage of the Sun is available, and thus, its X-ray spectrometers provide the opportunity to extend the work presented in this thesis for a larger sample of flares.

– In Chapter 8, an instrument concept for a hard X-ray spectro-polarimeter for solar flare observations was presented. In the near future, we plan to demonstrate experimentally the proposed scatterer configuration of stacked plastic scintillators read out by SiPMs, followed by the development of the complete instrument. As the polarimeter can be accommodated on a small satellite platform, a proposal for such a mission during the solar maximum of the present cycle should also be pursued.

– Simulations of expected polarization from solar flares suggest an increasing trend (Figure 8.1), and thus, extending polarization measurements to energies above 100 keV certainly provides further constraints on electron anisotropy and high energy cutoff. *Daksha* is a proposed high energy transient mission (Bhalerao et al., 2022a) with the primary objective of investigations of electromagnetic counterparts to gravitational wave sources and gamma-ray bursts (Bhalerao et al., 2022b). The medium energy (ME) CZT detectors in *Daksha* are also capable of measuring X-ray polarization of bright transients like GRBs in the 100-380 keV energy range, beyond its spectral energy range (Bala et al., 2023). Present *Daksha* configuration includes an array of ME detectors in the sunward direction that can provide hard X-ray observations of solar flares. For bright solar flares, the sensitivity may be sufficient to measure the X-ray polarization of solar flares at energies above 100 keV, and it is worthwhile to explore this possibility as another added science objective for *Daksha*.

– This thesis discussed small-scale nanoflare events fainter than observable microflares in the quiet Sun that could be contributing to the coronal heating (Chapter 5) and the non-thermal emission from solar flares (Chapter 7). If nanoflares are ubiquitously present and follow a similar process as the larger flares, non-thermal emission in higher energy X-rays at much fainter levels should be present in the quiet Sun. Constraints on the hard X-ray emission from quiet Sun were provided first with RHESSI observations (Hannah et al., 2010). More recently, using a few minutes of observations with the focusing X-ray telescope rocket mission FOXSI, stringent constraints could be provided for non-thermal emission from the quiet Sun (Buitrago-Casas et al., 2022). Chandrayaan-2 XSM has observed the quiet Sun in the disk-integrated mode for several days during the solar minimum, and there were significant durations when no observable flares were present (Chapter 5). These observations can, in principle, be used to probe non-thermal emissions from the quiet Sun, although it is important to consider the background in this case. Characteristics of background in XSM are well understood with the work presented in this thesis (Chapter 3), and it is possible to use these to build a background model with which statistically limited background subtraction can be attempted like that achieved in the case of CZTI (Chapter 2). With a well-established background model, XSM observations of the quiet Sun could be used to probe the non-thermal emission expected from the nanoflares, and it may provide more stringent constraints than the previous reports.

Appendix A

List of observations with source detections in CZTI

Table A.1 provides the list of CZTI observations for which sources are tentatively detected at 3 sigma level, with the analysis using the updated pipeline as discussed in Section 2.9. The source coordinates are matched against the Swift BAT catalogue and for cases where the BAT counter part could be identified, those details are also included in the catalogue. While most of these are positive detections, there are a handful of cases such as Obsid `20170423_G07_060T01_9000001200`, the obtained counts are significant although there are no sources in the field. However, such cases become obvious once the spectra are examined.

Sl No	Obsid	Source	Exp(ks)	Count Rate	Sigma	BAT Source	SrcType	AngDist(')
1	20171109_A04_021T03_9000001678	M31 Field No. 4	34.784	0.46796	6.07	SWIFT J0042.7+4111	multiple	22.000
2	20171111_A04_021T04_9000001682	M31 Field No. 5	26.509	0.50188	5.61	SWIFT J0042.7+4111	multiple	25.000
3	20171112_A04_021T05_9000001686	M31 Field No. 6	32.644	0.29967	3.74	SWIFT J0042.7+4111	multiple	23.000
4	20171113_A04_021T06_9000001688	M31 Field No. 7	34.483	0.32090	4.13	SWIFT J0042.7+4111	multiple	26.000
5	20200721_A09_033T02_9000003762	NGC262	37.013	0.35035	4.64	Mrk348	Beamed AGN	0.000
6	20200821_A09_038T06_9000003832	SMC-06	12.577	9.08453	66.01	RX J0053.8-7226	HMXB	20.000
7	20220710_T05_041T01_9000005234	SMC X-2	72.522	0.36501	6.90	RX J0052.1-7319	HMXB	29.000
8	20180402_A04_193T01_9000002004	SMC X-1	47.948	1.39071	21.41	SMC X-1	HMXB	0.000
9	20191214_T03_168T01_9000003368	RX J0209.6-7427	102.738	2.22461	48.84	RX J0209.6-7427	HMXB	8.000
10	20171007_T01_193T01_9000001590	Swift J0243.6+6124	42.821	13.83380	192.13	LS I +61 303	HMXB	24.000
11	20171026_T01_202T01_9000001640	Swift J0243.6+6124	36.838	103.91800	968.34	LS I +61 303	HMXB	24.000
12	20170901_A03_126T01_9000001512	A3223	73.237	0.42170	7.70	-	-	-
13	20171029_A04_144T01_9000001652	3C 111	81.370	0.34996	6.97	3C111	Sy1.2	0.000
14	20201126_A10_049T01_9000004032	1H 0419-577	44.820	0.22112	3.20	RBS542	Sy1.5	0.000
15	20200826_T03_220T01_9000003842	AT2019wey	22.305	0.72769	7.30	-	-	-
16	20160829_G05_115T01_9000000634	LMC X-4	39.599	0.86445	12.66	LMC X-4	HMXB	2.000
17	20181014_C04_008T01_9000002434	Crab Offset	18.369	15.28840	127.46	Crab	Pulsar	11.000
18	20151008_P01_120T01_9000000006	Crab offset1	5.021	1.71681	9.37	Crab	Pulsar	0.000
19	20151114_P01_141T01_9000000100	Crab	14.099	16.38060	145.49	Crab	Pulsar	0.000
20	20151114_P01_141T01_9000000104	Crab	19.550	16.19330	167.94	Crab	Pulsar	0.000
21	20160822_G05_237T01_9000000620	Crab	72.915	28.15010	477.57	Crab	Pulsar	0.000
22	20171027_C03_012T01_9000001642	Crab offset	16.750	0.75230	6.08	SWIFT J0538.3+2147	multiple	45.000
23	20151123_P01_156T01_9000000114	Crab	4.429	6.15780	31.71	Crab	Pulsar	0.000
24	20151124_P01_156T01_9000000118	Crab	21.010	14.27010	151.88	Crab	Pulsar	0.000
25	20151125_P01_156T01_9000000122	Crab	7.955	12.76000	83.36	Crab	Pulsar	0.000
26	20160201_T01_052T01_9000000308	Crab	45.975	5.68068	95.21	Crab	Pulsar	0.000

27	20160203_T01_052T01_9000000312	Crab	54.408	12.14520	209.28	Crab	Pulsar	0.000
28	20160207_T01_052T01_9000000316	Crab	42.615	10.48780	160.54	Crab	Pulsar	0.000
29	20161108_A02_090T01_9000000778	Crab	53.498	28.14710	408.06	Crab	Pulsar	0.000
30	20170114_G06_029T01_9000000964	Crab	71.441	27.11250	449.80	Crab	Pulsar	0.000
31	20170118_A02_090T01_9000000970	Crab	104.701	27.12260	550.86	Crab	Pulsar	0.000
32	20170219_T01_155T01_9000001042	Crab	2.592	26.98450	86.22	Crab	Pulsar	0.000
33	20170927_A03_086T01_9000001568	Crab	103.120	27.91950	558.78	Crab	Pulsar	0.000
34	20180115_A04_174T01_9000001850	Crab	148.366	27.57420	657.04	Crab	Pulsar	0.000
35	20180129_A04_174T01_9000001876	Crab	186.467	27.95380	747.28	Crab	Pulsar	0.000
36	20180313_T02_013T01_9000001976	Crab	29.898	28.05370	304.63	Crab	Pulsar	0.000
37	20180315_T02_014T01_9000001980	Crab	2.567	29.01430	88.35	Crab	Pulsar	0.000
38	20180408_T02_039T01_9000002026	Crab	6.775	27.89130	134.46	Crab	Pulsar	0.000
39	20180830_T02_058T01_9000002338	crab	12.705	29.92450	208.40	Crab	Pulsar	0.000
40	20180912_T02_090T01_9000002360	Crab	47.804	20.42930	282.64	Crab	Pulsar	0.000
41	20180913_T02_090T01_9000002364	Crab	22.032	30.07740	268.10	Crab	Pulsar	0.000
42	20180914_T02_091T01_9000002368	Crab	41.633	28.49910	354.59	Crab	Pulsar	0.000
43	20181029_T03_024T01_9000002472	Crab	60.236	28.22690	418.57	Crab	Pulsar	0.000
44	20190126_A05_159T01_9000002678	Crab	101.320	27.39820	529.14	Crab	Pulsar	0.000
45	20200821_A09_120T02_9000003834	Crab	1.852	27.54350	70.40	Crab	Pulsar	0.000
46	20200822_C05_017T01_9000003836	Crab	45.215	28.58020	365.09	Crab	Pulsar	0.000
47	20200829_A09_145T01_9000003848	Crab	212.340	28.52920	794.37	Crab	Pulsar	0.000
48	20200909_A09_145T01_9000003854	Crab	7.069	27.53140	138.15	Crab	Pulsar	0.000
49	20200913_A09_145T01_9000003866	Crab	45.615	28.61630	370.19	Crab	Pulsar	0.000
50	20200915_A09_145T01_9000003870	Crab	1.352	25.58410	54.52	Crab	Pulsar	0.000
51	20200923_A09_145T01_9000003900	Crab	101.619	28.31780	537.51	Crab	Pulsar	0.000
52	20200926_A09_120T02_9000003904	Crab	121.868	28.56530	593.26	Crab	Pulsar	0.000
53	20151019_P01_161T01_9000000040	Crab	3.479	15.95790	70.09	Crab	Pulsar	0.000
54	20171116_T01_206T01_9000001694	B0531+21	12.954	28.25750	194.29	Crab	Pulsar	0.000

55	20181005_C04_007T01_9000002408	Crab	9.216	29.94080	176.73	Crab	Pulsar	0.000
56	20181014_C04_007T02_9000002432	Crab	4.733	29.81960	127.37	Crab	Pulsar	0.000
57	20181014_C04_007T03_9000002436	Crab	8.899	30.09580	173.48	Crab	Pulsar	0.000
58	20220219_C07_014T01_9000004950	Crab	42.321	26.41660	327.24	Crab	Pulsar	0.000
59	20210314_A10_094T08_9000004252	LMC-08	1.604	1.25696	3.46	LMC X-1	HMXB	50.000
60	20201112_T03_263T01_9000003990	A0535+262	40.971	108.99400	1025.76	1A 0535+262	HMXB	0.000
61	20180828_A04_100T01_9000002336	UGC 3374	80.584	0.21624	4.33	UGC3374	Sy1.5	0.000
62	20191017_A07_100T03_9000003242	Mrk 3	106.108	0.23485	5.36	Mrk3	Sy1.9	0.000
63	20161210_A02_175T01_9000000874	4U 0614+09	10.127	0.56661	4.29	4U 0614+091	LMXB	0.000
64	20170123_A02_175T01_9000000976	4U 0614+09	9.294	0.50122	3.43	4U 0614+091	LMXB	0.000
65	20191121_T03_159T01_9000003328	MAXI J0637-430	22.984	0.40880	4.34	LEDA549777	Sy2	54.000
66	20210911_A10_057T01_9000004692	UGC 3698	82.207	0.17178	3.40	-	-	-
67	20190304_A05_188T01_9000002756	Vela Pulsar	48.829	0.24690	3.85	Vela Pulsar	Pulsar	0.000
68	20151125_P01_171T01_9000000126	Vela X-1	18.946	1.41092	16.11	Vela X-1	HMXB	0.000
69	20181106_A05_140T01_9000002496	Vela X-1	37.981	9.79303	127.99	Vela X-1	HMXB	0.000
70	20181224_A05_140T01_9000002596	Vela X-1	38.877	2.62682	36.11	Vela X-1	HMXB	0.000
71	20190312_T03_091T01_9000002790	Vela X1	23.384	11.58970	117.80	Vela X-1	HMXB	0.000
72	20190315_T03_091T01_9000002798	Vela X1	21.482	3.88318	39.32	Vela X-1	HMXB	0.000
73	20190707_A05_140T01_9000003016	Vela X-1	36.716	14.01370	173.81	Vela X-1	HMXB	0.000
74	20181115_A05_206T01_9000002518	MAXI J0911-655	42.990	0.20335	3.01	2MASXJ09172716-6456271	Sy2	34.000
75	20210714_T04_025T01_9000004538	MAXI J0911-655	51.403	0.29942	4.68	2MASXJ09172716-6456271	Sy2	34.000
76	20170404_A03_103T01_9000001132	NGC 2808	35.599	0.36861	5.03	2MASXJ09172716-6456271	Sy2	34.000
77	20171107_A04_024T04_9000001670	GRO J1008-57	44.151	7.65487	111.32	GRO J1008-57	HMXB	0.000
78	20180203_G08_021T01_9000001880	GRO J1008-57	46.338	2.25398	35.06	GRO J1008-57	HMXB	0.000
79	20170103_A02_005T01_9000000948	Mrk421	50.585	0.22041	3.56	Mrk421	Beamed AGN	0.000
80	20180119_T01_218T01_9000001852	Mrk 421	39.712	0.21410	3.07	Mrk421	Beamed AGN	0.000
81	20180203_A04_130T04_9000001878	Mrk 421	9.690	0.82375	5.75	Mrk421	Beamed AGN	0.000
82	20190423_A05_204T01_9000002856	Mrk421	156.855	0.40150	11.09	Mrk421	Beamed AGN	0.000

83	20200508_T03_200T01_9000003654	NGC 3516	139.366	0.19303	5.06	NGC3516	Sy1.2	0.000
84	20160703_G05_213T01_9000000534	Cen X-3	3.280	1.03711	4.21	Cen X-3	HMXB	0.000
85	20161212_G06_091T01_9000000880	Cen X-3	45.188	4.19582	64.22	Cen X-3	HMXB	0.000
86	20161219_A02_111T01_9000000900	Cen X-3	14.912	3.40378	30.24	Cen X-3	HMXB	0.000
87	20170109_A02_111T01_9000000954	Cen X-3	17.365	1.51725	14.68	Cen X-3	HMXB	0.000
88	20170127_A02_111T01_9000000986	Cen X-3	14.134	1.67535	14.38	Cen X-3	HMXB	0.000
89	20180223_A04_216T01_9000001916	Cen X-3	85.887	0.60910	12.83	Cen X-3	HMXB	0.000
90	20180308_A04_216T01_9000001968	Cen X-3	68.252	0.85356	16.02	Cen X-3	HMXB	0.000
91	20160315_T01_103T01_9000000374	NGC4151	69.508	1.05049	20.79	NGC4151	Sy1.5	0.000
92	20170207_G06_117T01_9000001012	NGC4151	23.297	0.73017	7.98	NGC4151	Sy1.5	0.000
93	20170221_G06_117T01_9000001046	NGC4151	54.704	0.70784	12.01	NGC4151	Sy1.5	0.000
94	20170316_G06_117T01_9000001086	NGC4151	53.078	0.44472	7.40	NGC4151	Sy1.5	0.000
95	20180103_G08_064T01_9000001814	NGC4151	74.991	0.71364	14.09	NGC4151	Sy1.5	0.000
96	20180501_G08_064T01_9000002070	NGC4151	44.359	0.53929	8.04	NGC4151	Sy1.5	0.000
97	20170423_G07_060T01_9000001200	Mrk766	201.717	1.34298	39.51	NGC4253	Sy1.5	1.000
98	20160503_G05_104T01_9000000440	GX 301-2	59.567	11.98640	194.86	2GX 301-2	LMXB	0.000
99	20160912_G05_104T01_9000000656	GX 301-2	45.464	2.25326	34.36	2GX 301-2	LMXB	0.000
100	20181219_T03_067T01_9000002582	GX 301-2	56.493	1.90746	31.86	2GX 301-2	LMXB	0.000
101	20160302_T01_040T01_9000000354	GX 301-2	14.111	0.87103	7.38	2GX 301-2	LMXB	0.000
102	20160504_G05_221T01_9000000442	GX 301-2	46.066	8.52960	130.11	2GX 301-2	LMXB	0.000
103	20190520_A05_013T01_9000002944	CenA southmidlob	88.571	0.95732	19.93	CenA	Beamed AGN	8.000
104	20190731_A05_013T01_9000003070	CenA southmidlob	199.805	0.61496	18.82	CenA	Beamed AGN	8.000
105	20180107_A04_048T01_9000001820	Cen A	39.945	0.79778	11.49	CenA	Beamed AGN	0.000
106	20180212_A04_048T01_9000001890	Cen A	30.209	0.93886	11.65	CenA	Beamed AGN	0.000
107	20180329_A04_048T01_9000001992	Cen A	26.284	0.95846	10.99	CenA	Beamed AGN	0.000
108	20180524_A04_048T01_9000002114	Cen A	29.361	0.53314	6.37	CenA	Beamed AGN	0.000
109	20180618_A04_048T01_9000002176	Cen A	40.576	0.88963	12.32	CenA	Beamed AGN	0.000
110	20170516_G07_087T01_9000001228	centaurus A	44.310	0.59433	8.91	CenA	Beamed AGN	0.000

111	20180314_G08_023T01_9000001978	centaurus A	47.131	0.37425	5.79	CenA	Beamed AGN	14.000
112	20170216_A02_134T01_9000001036	4U1323-62	54.646	0.31534	5.35	4U 1323-619	LMXB	0.000
113	20180319_A04_103T01_9000001988	MCG-6-30-15	391.624	0.11235	4.97	MCG-6-30-15	Sy1.9	0.000
114	20190219_T03_083T01_9000002722	MAXI J1348-630	2.234	10.95200	33.16	-	-	-
115	20190222_T03_083T01_9000002728	MAXI J1348-630	18.371	10.47860	95.83	-	-	-
116	20190228_T03_083T01_9000002742	MAXI J1348-630	18.578	8.37588	76.95	-	-	-
117	20190614_T03_120T01_9000002990	MAXI J1348-630	37.826	26.81360	318.24	-	-	-
118	20190508_T03_112T01_9000002896	MAXI J1348-630	12.129	3.07421	23.31	-	-	-
119	20170203_A02_178T01_9000001006	IC4329A	47.730	0.29373	4.62	IC4329A	Sy1.5	0.000
120	20170223_A02_178T01_9000001048	IC4329A	38.968	0.24832	3.53	IC4329A	Sy1.5	0.000
121	20170329_A02_178T01_9000001118	IC4329A	41.598	0.26044	3.80	IC4329A	Sy1.5	0.000
122	20170625_A02_178T01_9000001340	IC4329A	36.656	0.32070	4.44	IC4329A	Sy1.5	0.000
123	20180627_A04_218T01_9000002194	SWIFT J1349.3-3018	49.383	0.36210	5.54	IC4329A	Sy1.5	0.000
124	20210802_A10_123T01_9000004620	BCD_T1	33.453	0.28580	3.59	-	-	-
125	20160731_G05_233T10_9000000570	M 101	115.484	1.17614	26.17	-	-	-
126	20200128_A07_100T02_9000003470	Circinus Galaxy	50.817	0.45149	7.02	CircinusGalaxy	Sy2	0.000
127	20200131_A07_100T02_9000003476	Circinus Galaxy	20.221	0.57108	5.65	CircinusGalaxy	Sy2	0.000
128	20210125_A10_121T01_9000004134	2S 1417-624	105.440	2.44933	54.79	4U 1416-62	HMXB	0.000
129	20170126_G06_083T01_9000000984	Cir X-1	44.666	0.23727	3.62	Cir X-1	LMXB	0.000
130	20170912_T01_191T01_9000001536	MAXIJ1535-571	201.629	47.71120	1240.38	IRAS15318-5740	star	36.000
131	20170712_A02_198T01_9000001376	4U 1538-52	43.354	0.65967	9.79	H 1538-522	HMXB	0.000
132	20210831_T04_046T01_9000004680	4U 1543-47	56.394	0.86375	13.90	-	-	-
133	20210904_T04_051T01_9000004686	4U 1543-47	112.566	0.65756	15.10	-	-	-
134	20210923_T04_059T01_9000004704	4U 1543-47	72.916	1.26364	24.10	-	-	-
135	20200823_C05_019T04_9000003838	Blank Sky-8	12.999	21.30230	154.65	LEDA2730634	Sy2	53.000
136	20210223_T03_272T01_9000004204	2S 1553-542	31.007	0.39842	4.86	H 1553-542	HMXB	2.000
137	20160828_G05_140T01_9000000628	4U 1608-52	20.880	0.62010	6.42	4U 1608-522	LMXB	0.000
138	20200714_T03_214T01_9000003758	4U 1608-52	27.357	0.52546	5.72	4U 1608-522	LMXB	0.000

139	20190730_A05_063T03_9000003066	UGC10420	18.973	0.96559	8.51	IRAS16288+3929	Sy2	21.000
140	20170414_A03_009T01_9000001160	IGR J16318-4848	7.655	0.51424	3.11	IGR J16318-4848	HMXB	0.000
141	20170519_A03_009T01_9000001234	IGR J16318-4848	12.812	0.83317	6.78	IGR J16318-4848	HMXB	0.000
142	20170708_A03_009T01_9000001366	IGR J16318-4848	11.000	0.73686	5.31	IGR J16318-4848	HMXB	0.000
143	20160826_G05_021T01_9000000624	4U 1626-67	38.451	0.82228	11.81	4U 1626-67	LMXB	0.000
144	20170702_G07_049T01_9000001352	4U 1626-67	91.119	1.10832	24.08	4U 1626-67	LMXB	0.000
145	20180515_G08_084T01_9000002100	4U 1626-67	77.535	0.78370	15.24	4U 1626-67	LMXB	0.000
146	20160827_G05_157T01_9000000626	4U 1630-472	43.185	0.38429	5.72	4U 1630-47	LMXB	0.000
147	20180804_T02_076T01_9000002274	4U1630-472	39.309	0.25765	3.56	4U 1630-47	LMXB	0.000
148	20180911_T02_100T01_9000002354	4u1630-472	5.694	1.29807	6.73	4U 1630-47	LMXB	0.000
149	20180917_T02_101T01_9000002372	4u1630-472	9.659	2.88672	19.62	4U 1630-47	LMXB	0.000
150	20170704_G07_049T02_9000001354	Sky_4u1626	22.262	1.18767	11.88	-	-	-
151	20160215_P01_175T03_9000000322	4U 1636-536	30.858	0.86988	12.54	4U 1636-536	LMXB	0.000
152	20160702_G05_195T01_9000000530	4U 1636-536	36.434	0.49497	6.97	4U 1636-536	LMXB	0.000
153	20170621_G07_040T01_9000001326	4U 1636-536	19.728	1.36742	13.83	4U 1636-536	LMXB	0.000
154	20171002_A04_055T01_9000001574	4U 1636-536	51.177	0.40027	6.48	4U 1636-536	LMXB	0.000
155	20180509_G08_033T01_9000002084	4U 1636-536	8.821	1.01127	6.51	4U 1636-536	LMXB	0.000
156	20180806_G08_033T01_9000002278	4U 1636-536	9.065	1.42134	9.23	4U 1636-536	LMXB	0.000
157	20180818_T02_086T01_9000002316	4U 1636-536	105.595	1.46473	33.17	4U 1636-536	LMXB	0.000
158	20170730_G07_016T01_9000001420	GX 340+0	38.349	0.21804	3.08	GX 340+0	LMXB	0.000
159	20180506_G08_022T01_9000002078	GX 340+0	75.126	0.70871	13.49	GX 340+0	LMXB	0.000
160	20190501_A06_009T02_9000002882	GX 340+0	5.306	0.66482	3.34	GX 340+0	LMXB	0.000
161	20190629_A06_009T02_9000003006	GX 340+0	2.733	1.05883	3.65	GX 340+0	LMXB	0.000
162	20190719_A06_009T02_9000003044	GX 340+0	4.589	0.68368	3.24	GX 340+0	LMXB	0.000
163	20190917_A06_009T02_9000003170	GX 340+0	5.950	0.71876	3.85	GX 340+0	LMXB	0.000
164	20190923_A06_009T02_9000003194	GX 340+0	9.441	0.99157	6.67	GX 340+0	LMXB	0.000
165	20200919_A09_134T01_9000003896	GX 340+0	4.019	0.71766	3.18	GX 340+0	LMXB	0.000
166	20210812_A10_059T02_9000004636	GX 340+0	20.408	0.60434	5.94	GX 340+0	LMXB	0.000

167	20200302_A07_101T02_9000003544	Mrk 501	62.406	0.21392	3.65	Mrk501	Beamed AGN	0.000
168	20170315_A02_027T01_9000001084	Her X-1	58.785	0.87320	15.11	Her X-1	LMXB	0.000
169	20170629_A03_005T01_9000001348	Her X-1	24.889	6.71837	72.82	Her X-1	LMXB	0.000
170	20180120_A04_230T01_9000001854	Her X-1	44.229	5.45899	78.96	Her X-1	LMXB	0.000
171	20180405_G08_038T01_9000002018	Her X-1	38.226	0.45375	6.12	Her X-1	LMXB	0.000
172	20180917_A04_230T01_9000002374	Her X-1	41.619	5.95117	82.99	Her X-1	LMXB	0.000
173	20180921_T02_092T01_9000002384	HER X-1	41.005	3.30695	46.41	Her X-1	LMXB	0.000
174	20200220_A07_113T01_9000003526	Her X-1	108.932	5.25468	116.25	Her X-1	LMXB	0.000
175	20200428_T03_197T01_9000003626	Hercules X-1	72.649	2.72333	50.50	Her X-1	LMXB	0.000
176	20210917_A10_005T01_9000004700	Her X-1	128.528	0.83518	21.00	Her X-1	LMXB	0.000
177	20180920_T02_094T01_9000002380	Hercules X-1	35.746	6.25745	80.82	Her X-1	LMXB	0.000
178	20180220_T02_004T01_9000001910	Swift J1658.2-4242	17.074	3.45163	31.45	AX J1700.2-4220	HMXB	31.000
179	20180328_T02_020T01_9000001990	Swift J1658.2-4242	27.579	2.51744	28.20	AX J1700.2-4220	HMXB	31.000
180	20180303_T02_011T01_9000001940	Swift J1658.2-4242	29.932	3.58064	42.67	AX J1700.2-4220	HMXB	31.000
181	20190331_A05_205T01_9000002824	OAO 1657-415	53.029	0.35678	5.69	2MASS J17004888-4139214	HMXB	0.000
182	20190704_A05_205T01_9000003012	OAO 1657-415	52.861	2.15038	34.11	2MASS J17004888-4139214	HMXB	0.000
183	20171004_A04_109T01_9000001578	GX 339-4: Rising HS	31.701	0.52572	6.73	GX 339-4	LMXB	0.000
184	20190922_A05_166T01_9000003192	GX339-4	28.285	2.89371	32.67	GX 339-4	LMXB	0.000
185	20210213_T03_275T01_9000004180	GX339-4	25.290	9.64238	101.30	GX 339-4	LMXB	0.000
186	20210302_T03_279T01_9000004218	GX339-4	78.892	11.14470	205.51	GX 339-4	LMXB	0.000
187	20210330_T03_291T01_9000004278	GX_339-4	269.708	1.17873	41.66	GX 339-4	LMXB	0.000
188	20210305_T03_280T01_9000004222	gx339-4_1	2.617	5.18125	17.07	GX 339-4	LMXB	11.000
189	20210305_T03_282T01_9000004226	gx339-4_3	1.076	6.01871	12.53	GX 339-4	LMXB	13.000
190	20210305_T03_281T01_9000004224	gx339-4_2	0.719	7.84958	13.15	GX 339-4	LMXB	11.000
191	20160923_G05_106T01_9000000678	4U 1700-37	42.717	1.37473	20.09	4U 1700-377	HMXB	0.000
192	20170814_A03_133T01_9000001464	4U 1700-37	50.575	10.79320	163.82	4U 1700-377	HMXB	0.000
193	20170418_G07_053T01_9000001186	4U 1700-377	6.555	6.27307	34.25	4U 1700-377	HMXB	0.000
194	20170927_G07_053T01_9000001566	4U 1700-377	9.333	12.34470	79.12	4U 1700-377	HMXB	0.000

195	20170312_A02_071T01_9000001078	GX 349+2	82.399	0.62684	12.78	GX 349+2	LMXB	0.000
196	20170714_A03_029T01_9000001384	GX 349+2	50.939	0.76108	12.03	GX 349+2	LMXB	0.000
197	20190910_A06_009T05_9000003154	GX 349+2	15.790	0.79009	6.79	GX 349+2	LMXB	0.000
198	20190916_A06_009T05_9000003164	GX 349+2	1.707	1.19539	3.27	GX 349+2	LMXB	0.000
199	20190923_A06_009T05_9000003196	GX 349+2	8.333	0.90163	5.62	GX 349+2	LMXB	0.000
200	20180427_A04_225T01_9000002062	4U 1702-429	61.826	0.35982	6.19	4U 1702-429	LMXB	0.000
201	20190808_A06_002T03_9000003080	4U 1702-429	70.551	1.43773	25.87	4U 1702-429	LMXB	0.000
202	20170302_G06_064T01_9000001066	4U 1705-44	113.101	0.27432	6.59	4U 1705-440	LMXB	0.000
203	20170829_A03_073T01_9000001498	4U 1705-44	41.877	0.26173	3.77	4U 1705-440	LMXB	0.000
204	20220401_T05_020T01_9000005050	IGR J17091-3624	31.538	0.27471	3.36	IGR J17091-3624	LMXB	0.000
205	20220319_T05_010T01_9000005016	IGR J17091-3624	90.262	1.86296	37.03	IGR J17091-3624	LMXB	0.000
206	20160426_T01_118T01_9000000430	IGR J17091-3624	55.711	0.42780	7.42	IGR J17091-3624	LMXB	4.000
207	20170215_T01_156T01_9000001034	GRS 1716- 249	40.614	13.95900	182.67	-	-	-
208	20170406_T01_164T01_9000001140	GRS 1716- 249	10.807	9.51901	65.86	-	-	-
209	20170713_T01_176T01_9000001378	GRS 1716-249	8.935	5.71710	37.57	-	-	-
210	20170715_A02_029T01_9000001386	4U 1724-30	20.816	0.36001	3.62	4U 1722-30	LMXB	0.000
211	20160805_G05_190T01_9000000578	4U 1728-34	22.526	0.44685	4.81	4U 1728-34	LMXB	0.000
212	20180219_G08_035T01_9000001904	4U 1728-34	10.709	0.82756	6.12	4U 1728-34	LMXB	0.000
213	20180717_G08_035T01_9000002234	4U 1728-34	8.415	0.88632	5.77	4U 1728-34	LMXB	0.000
214	20180801_G08_035T01_9000002268	4U 1728-34	9.145	1.65498	11.23	4U 1728-34	LMXB	0.000
215	20190829_A06_002T01_9000003134	4U 1728-34	71.592	0.44691	8.29	4U 1728-34	LMXB	0.000
216	20190725_A05_229T02_9000003060	4U 1728-34	83.322	2.32976	45.56	4U 1728-34	LMXB	0.000
217	20160804_G05_154T01_9000000576	GX1+4	48.384	0.62541	9.98	GX 1+4	HMXB	0.000
218	20170813_A03_039T01_9000001462	4U 1735-44	38.260	0.33315	4.63	4U 1735-44	LMXB	0.000
219	20180731_A04_126T01_9000002262	4U 1735-44	52.162	0.29481	4.79	4U 1735-44	LMXB	0.000
220	20190506_A05_062T01_9000002892	4U 1735-44	18.289	0.46030	4.32	4U 1735-44	LMXB	0.000
221	20190828_A05_062T01_9000003132	4U 1735-44	15.829	0.47983	4.20	4U 1735-44	LMXB	0.000
222	20210812_A10_059T01_9000004634	4U 1735-44	8.700	0.51783	3.23	4U 1735-44	LMXB	0.000

223	20210824_A10_059T01_9000004656	4U 1735-44	9.621	0.49715	3.22	4U 1735-44	LMXB	0.000
224	20200219_T03_180T01_9000003524	XTE J1739-285	37.340	0.67129	8.71	XTE J1739-285	LMXB	0.000
225	20160828_G05_158T01_9000000630	1E 1740.7-2942	43.751	0.20869	3.09	1E 1740.7-2942	LMXB	0.000
226	20161006_A02_086T01_9000000714	1E 1740.7-2942	31.654	1.42961	18.18	1E 1740.7-2942	LMXB	0.000
227	20180225_G08_045T01_9000001920	1E 1740.7-29	33.448	2.12142	26.93	1E 1740.7-2942	LMXB	0.000
228	20180511_G08_045T01_9000002092	1E 1740.7-29	31.835	1.99872	24.17	1E 1740.7-2942	LMXB	0.000
229	20180512_A04_229T01_9000002096	1E 1740.7-2942	52.914	1.95734	30.69	1E 1740.7-2942	LMXB	0.000
230	20160309_T01_045T01_9000000364	H 1743-332	14.613	2.60334	22.30	XTE J17464-3213	LMXB	0.000
231	20170808_G07_039T01_9000001444	H 1743-322	16.823	4.87460	43.34	XTE J17464-3213	LMXB	0.000
232	20170812_A03_116T01_9000001460	1E 1743.1-2843	48.447	0.45979	6.98	2E 1743.1-2842	LMXB	0.000
233	20220430_T05_028T01_9000005100	SAX J1747.0-2853	34.682	0.25751	3.26	SAX J1747.0-2853	LMXB	0.000
234	20180827_T02_088T01_9000002332	IGR J17591-2342	38.840	0.51299	7.05	-	-	-
235	20170226_G06_114T01_9000001056	GX 5-1	20.134	0.84506	8.58	GX 5-1	LMXB	0.000
236	20171005_G08_068T01_9000001580	GX 5-1	5.952	0.70626	3.66	GX 5-1	LMXB	0.000
237	20180226_G08_068T01_9000001922	GX 5-1	21.143	0.84032	8.59	GX 5-1	LMXB	0.000
238	20180510_G08_068T01_9000002090	GX 5-1	9.381	1.24094	8.25	GX 5-1	LMXB	0.000
239	20190805_A06_009T03_9000003072	GX 5-1	5.862	1.00933	5.26	GX 5-1	LMXB	0.000
240	20190817_A06_009T03_9000003098	GX 5-1	5.458	1.17895	6.04	GX 5-1	LMXB	0.000
241	20190825_A06_009T03_9000003122	GX 5-1	13.399	1.37883	10.98	GX 5-1	LMXB	0.000
242	20190828_A06_009T03_9000003128	GX 5-1	4.050	1.56161	6.98	GX 5-1	LMXB	0.000
243	20190924_A06_009T03_9000003198	GX 5-1	1.540	1.37519	3.44	GX 5-1	LMXB	0.000
244	20170728_A03_053T01_9000001410	GRS 1758-258	25.295	1.77170	20.13	GRS 1758-258	LMXB	0.000
245	20170919_A03_053T01_9000001542	GRS 1758-258	49.531	1.44788	22.96	GRS 1758-258	LMXB	0.000
246	20180408_G08_070T01_9000002028	GRS1758-58	73.776	1.72554	31.86	GRS 1758-258	LMXB	0.000
247	20190502_A05_221T01_9000002888	GX 9+1	69.853	0.29736	5.43	GX 9+1	LMXB	0.000
248	20210511_T04_003T01_9000004368	MAXI J1803-298	18.991	3.20897	30.14	-	-	-
249	20210511_T04_006T01_9000004370	MAXI J1803-298	46.164	3.28639	46.94	-	-	-
250	20190814_T03_131T01_9000003090	SAX J1808-3658	45.550	0.81772	11.96	SAX J1808.4-3658	LMXB	0.000

251	20180726_A04_223T01_9000002258	4U 1812-12	49.230	0.62676	9.75	4U 1812-12	LMXB	0.000
252	20170822_A03_072T01_9000001484	GX 17+2	40.844	0.75403	10.69	GX 17+2	LMXB	0.000
253	20171006_G08_037T01_9000001588	GX 17+2	22.822	0.38719	4.17	GX 17+2	LMXB	0.000
254	20180228_G08_037T01_9000001928	GX 17+2	17.137	0.58612	5.45	GX 17+2	LMXB	0.000
255	20180726_G08_037T01_9000002256	GX 17+2	14.610	0.78303	6.53	GX 17+2	LMXB	0.000
256	20180801_G08_037T01_9000002264	GX 17+2	16.567	0.65570	5.79	GX 17+2	LMXB	0.000
257	20180910_T02_087T01_9000002352	GX 17+2	46.306	1.37301	20.67	GX 17+2	LMXB	0.000
258	20190901_A05_062T02_9000003138	GX 17+2	13.084	1.78803	14.00	GX 17+2	LMXB	0.000
259	20200814_A09_044T02_9000003814	GX 17+2	11.360	1.00431	7.24	GX 17+2	LMXB	0.000
260	20200908_A09_044T02_9000003852	GX 17+2	6.538	0.94591	5.12	GX 17+2	LMXB	0.000
261	20160511_G05_112T01_9000000452	GX 17+2	106.179	0.58497	13.92	GX 17+2	LMXB	0.000
262	20180710_T02_060T01_9000002216	Maxi J1820+070	92.878	5.92885	123.57	-	-	-
263	20180330_T02_038T01_9000001994	MAXI J1820+070	36.818	106.14500	977.77	-	-	-
264	20170526_A03_107T01_9000001246	4U 1820-30	12.535	0.60444	4.98	4U 1820-30	LMXB	0.000
265	20170909_A03_107T01_9000001530	4U 1820-30	18.530	0.66452	6.43	4U 1820-30	LMXB	0.000
266	20161017_A02_098T01_9000000736	4U 1820-30	76.915	0.55959	11.15	4U 1820-30	LMXB	0.000
267	20170731_G07_047T01_9000001424	4U 1820-30	39.479	0.37639	5.39	4U 1820-30	LMXB	0.000
268	20171003_A04_055T02_9000001576	4U 1820-30	47.491	0.82541	12.79	4U 1820-30	LMXB	0.000
269	20171005_G08_036T01_9000001584	4U 1820-30	10.083	0.94228	6.88	4U 1820-30	LMXB	0.000
270	20180809_G08_036T01_9000002290	4U 1820-30	10.944	0.80233	5.91	4U 1820-30	LMXB	0.000
271	20160924_G05_021T02_9000000680	3A 1822-371	34.518	0.48223	6.56	4U 1822-371	LMXB	0.000
272	20170809_G07_072T01_9000001452	4U 1822-37	12.421	0.77791	6.07	4U 1822-371	LMXB	0.000
273	20200818_A09_056T01_9000003824	3C 380	9.857	7.64654	50.19	3C380	Beamed AGN	0.000
274	20160425_G05_214T01_9000000428	GRS 1915+105	37.860	0.26638	7.09	GRS 1915+105	LMXB	0.000
275	20160427_G05_167T02_9000000432	GRS1915+105	15.027	1.47938	13.46	GRS 1915+105	LMXB	0.000
276	20160611_G05_189T01_9000000492	GRS 1915+105	126.981	1.16366	30.16	GRS 1915+105	LMXB	0.000
277	20160910_G05_214T01_9000000652	GRS 1915+105	89.244	0.19686	4.24	GRS 1915+105	LMXB	0.000
278	20160925_G05_214T01_9000000684	GRS 1915+105	81.176	0.34020	7.04	GRS 1915+105	LMXB	0.000

279	20161027_G06_033T01_9000000760	GRS 1915+105	45.231	5.70554	84.11	GRS 1915+105	LMXB	0.000
280	20161102_G06_027T01_9000000770	GRS1915+105	11.892	7.48524	57.08	GRS 1915+105	LMXB	0.000
281	20161112_G06_033T01_9000000792	GRS 1915+105	43.686	0.56781	8.61	GRS 1915+105	LMXB	0.000
282	20170328_G06_033T01_9000001116	GRS 1915+105	42.468	4.84441	68.21	GRS 1915+105	LMXB	0.000
283	20170401_G07_046T01_9000001124	GRS 1915+105	17.434	4.28435	39.02	GRS 1915+105	LMXB	0.000
284	20170414_G07_046T01_9000001162	GRS 1915+105	22.750	3.95818	41.92	GRS 1915+105	LMXB	0.000
285	20170415_G07_028T01_9000001166	GRS 1915+105	10.520	5.00150	36.30	GRS 1915+105	LMXB	0.000
286	20170518_G07_028T01_9000001232	GRS 1915+105	8.994	4.14635	28.16	GRS 1915+105	LMXB	0.000
287	20170519_G07_046T01_9000001236	GRS 1915+105	20.885	2.55101	25.24	GRS 1915+105	LMXB	0.000
288	20170605_G07_028T01_9000001272	GRS 1915+105	7.266	1.68527	10.26	GRS 1915+105	LMXB	0.000
289	20170605_G07_046T01_9000001274	GRS 1915+105	18.865	1.42298	13.86	GRS 1915+105	LMXB	0.000
290	20170727_G07_028T01_9000001406	GRS 1915+105	8.297	1.13285	7.46	GRS 1915+105	LMXB	0.000
291	20170727_G07_046T01_9000001408	GRS 1915+105	14.482	1.57977	13.31	GRS 1915+105	LMXB	0.000
292	20170830_G07_028T01_9000001500	GRS 1915+105	10.471	1.81047	12.41	GRS 1915+105	LMXB	0.000
293	20170911_G07_046T01_9000001534	GRS 1915+105	14.874	1.84252	15.85	GRS 1915+105	LMXB	0.000
294	20171015_G08_028T01_9000001618	GRS 1915+105	17.298	1.78862	16.94	GRS 1915+105	LMXB	0.000
295	20171019_A04_180T01_9000001622	grs1915+105	18.530	1.08551	10.47	GRS 1915+105	LMXB	0.000
296	20171031_G08_028T01_9000001656	GRS 1915+105	15.202	1.05329	9.29	GRS 1915+105	LMXB	0.000
297	20180401_A04_180T01_9000002000	grs1915+105	16.318	10.97400	91.70	GRS 1915+105	LMXB	0.000
298	20180403_G08_028T01_9000002006	GRS 1915+105	16.053	10.43050	89.09	GRS 1915+105	LMXB	0.000
299	20180508_G08_028T01_9000002080	GRS 1915+105	14.953	8.34051	66.03	GRS 1915+105	LMXB	0.000
300	20180521_G08_078T01_9000002110	GRS 1915+105	88.362	5.95862	121.26	GRS 1915+105	LMXB	0.000
301	20180524_G08_028T01_9000002112	GRS 1915+105	15.148	6.03346	51.89	GRS 1915+105	LMXB	0.000
302	20180626_G08_028T01_9000002190	GRS 1915+105	10.459	5.27401	36.67	GRS 1915+105	LMXB	0.000
303	20180713_G08_028T01_9000002220	GRS 1915+105	39.419	5.25297	71.78	GRS 1915+105	LMXB	0.000
304	20180814_G08_028T01_9000002306	GRS 1915+105	15.640	4.94197	41.81	GRS 1915+105	LMXB	0.000
305	20180828_G08_028T01_9000002334	GRS 1915+105	16.387	4.52316	39.94	GRS 1915+105	LMXB	0.000
306	20190515_T03_116T01_9000002916	GRS 1915+105	33.314	6.01246	74.71	GRS 1915+105	LMXB	0.000

307	20190613_T03_117T01_9000002988	GRS 1915+105	32.704	2.91274	35.31	GRS 1915+105	LMXB	0.000
308	20190626_T03_123T01_9000003000	V1487 Aql	32.743	1.89617	23.55	GRS 1915+105	LMXB	0.000
309	20201001_T03_231T01_9000003910	GRS 1915+105	51.512	0.44465	7.01	GRS 1915+105	LMXB	0.000
310	20160304_T01_030T01_9000000358	GRS 1915+105	83.550	5.52282	109.57	GRS 1915+105	LMXB	0.000
311	20171021_A04_042T01_9000001630	GRS 1915+105	20.219	1.16238	12.07	GRS 1915+105	LMXB	0.000
312	20190321_A05_173T01_9000002812	GRS 1915+105	76.774	4.08393	77.06	GRS 1915+105	LMXB	0.000
313	20180609_G08_055T02_9000002148	XTE J1946+274	55.892	2.19465	35.79	XTE J1946+275	HMXB	0.000
314	20180724_T02_073T01_9000002252	Cyg X-1	24.541	3.49170	37.62	Cyg X-1	HMXB	1.000
315	20180728_T02_073T01_9000002260	Cyg X-1	98.493	3.58668	77.62	Cyg X-1	HMXB	1.000
316	20151007_P01_140T01_9000000004	Cyg X-1	8.762	1.57099	12.83	Cyg X-1	HMXB	1.000
317	20151115_P01_147T01_9000000106	Cyg X-1	28.420	7.37421	99.28	Cyg X-1	HMXB	1.000
318	20160108_G02_016T01_9000000258	Cyg X-1	36.297	15.93100	229.25	Cyg X-1	HMXB	1.000
319	20160422_G05_237T03_9000000426	Cyg X-1	97.782	19.11640	399.38	Cyg X-1	HMXB	0.000
320	20151023_P01_161T03_9000000054	Cyg X-1	4.326	1.30793	7.41	Cyg X-1	HMXB	0.000
321	20151127_P01_161T03_9000000178	Cyg X-1	27.171	7.51053	94.92	Cyg X-1	HMXB	0.000
322	20160214_P01_161T03_9000000320	Cyg X-1	2.438	11.63630	42.53	Cyg X-1	HMXB	0.000
323	20160429_G05_127T01_9000000436	Cyg X-1	52.857	11.00100	170.38	Cyg X-1	HMXB	0.000
324	20160515_G05_167T01_9000000456	Cyg X-1	129.716	20.86270	490.90	Cyg X-1	HMXB	0.000
325	20160519_G05_245T01_9000000460	Cyg X-1	76.624	1.51388	30.83	Cyg X-1	HMXB	0.000
326	20160601_G05_191T01_9000000476	Cyg X-1	30.832	20.33590	231.56	Cyg X-1	HMXB	0.000
327	20160617_G05_167T01_9000000500	Cyg X-1	9.059	16.62550	106.18	Cyg X-1	HMXB	0.000
328	20160701_G05_191T01_9000000524	Cyg X-1	31.793	21.85590	248.03	Cyg X-1	HMXB	0.000
329	20160702_G05_167T01_9000000528	Cyg X-1	20.509	22.21890	206.26	Cyg X-1	HMXB	0.000
330	20160703_G05_245T01_9000000532	Cyg X-1	5.850	20.53570	97.41	Cyg X-1	HMXB	0.000
331	20160718_G05_167T01_9000000542	Cyg X-1	11.982	24.06030	172.34	Cyg X-1	HMXB	0.000
332	20160724_G05_245T01_9000000554	Cyg X-1	4.726	22.38940	94.99	Cyg X-1	HMXB	0.000
333	20160803_G05_191T01_9000000572	Cyg X-1	30.222	26.50210	286.20	Cyg X-1	HMXB	0.000
334	20160807_G05_167T01_9000000584	Cyg X-1	11.729	23.65570	163.13	Cyg X-1	HMXB	0.000

335	20160817_G05_245T01_9000000606	Cyg X-1	3.620	20.43150	78.95	Cyg X-1	HMXB	0.000
336	20161009_G06_034T01_9000000722	Cyg X-1	22.378	17.62480	171.98	Cyg X-1	HMXB	0.000
337	20161101_G06_028T01_9000000768	Cyg X-1	14.758	25.74100	199.98	Cyg X-1	HMXB	0.000
338	20161128_G06_028T01_9000000834	Cyg X-1	16.186	23.93160	193.64	Cyg X-1	HMXB	0.000
339	20161216_G06_028T01_9000000890	Cyg X-1	14.350	31.61610	233.18	Cyg X-1	HMXB	0.000
340	20170320_G06_028T01_9000001094	Cyg X-1	13.021	18.21280	131.67	Cyg X-1	HMXB	0.000
341	20170331_G06_028T01_9000001122	Cyg X-1	13.809	20.32320	152.91	Cyg X-1	HMXB	0.000
342	20170417_G07_027T01_9000001180	Cyg X-1	9.058	21.15570	131.98	Cyg X-1	HMXB	0.000
343	20170508_G07_027T01_9000001210	Cyg X-1	10.098	16.61820	108.32	Cyg X-1	HMXB	0.000
344	20170530_G07_027T01_9000001258	Cyg X-1	6.374	22.50750	114.35	Cyg X-1	HMXB	0.000
345	20170705_G07_027T01_9000001358	Cyg X-1	9.041	21.11370	123.42	Cyg X-1	HMXB	0.000
346	20170705_G07_042T01_9000001360	Cyg X-1	31.394	22.69240	253.16	Cyg X-1	HMXB	0.000
347	20170729_G07_027T01_9000001414	Cyg X-1	8.641	16.60270	103.55	Cyg X-1	HMXB	0.000
348	20170817_G07_027T01_9000001470	Cyg X-1	11.384	6.82310	50.78	Cyg X-1	HMXB	0.000
349	20170905_G07_027T01_9000001516	Cyg X-1	7.302	9.00237	53.74	Cyg X-1	HMXB	0.000
350	20170917_A03_097T01_9000001540	Cyg X-1	92.878	5.80416	123.62	Cyg X-1	HMXB	0.000
351	20171008_G08_030T01_9000001592	Cyg X-1	7.645	10.27860	58.80	Cyg X-1	HMXB	0.000
352	20171014_G08_075T01_9000001616	Cyg X-1	18.729	3.64708	34.35	Cyg X-1	HMXB	0.000
353	20171024_G08_075T01_9000001636	Cyg X-1	19.434	1.74212	17.45	Cyg X-1	HMXB	0.000
354	20171101_G08_062T01_9000001660	Cyg X-1	103.965	3.06861	70.36	Cyg X-1	HMXB	0.000
355	20171127_G08_075T01_9000001726	Cyg X-1	24.017	4.46122	48.86	Cyg X-1	HMXB	0.000
356	20180407_G08_075T01_9000002024	Cyg X-1	20.696	6.35529	62.07	Cyg X-1	HMXB	0.000
357	20180412_G08_062T01_9000002038	Cyg X-1	109.555	12.39540	267.90	Cyg X-1	HMXB	0.000
358	20180422_G08_030T01_9000002044	Cyg X-1	10.326	10.52010	70.40	Cyg X-1	HMXB	0.000
359	20180526_G08_075T01_9000002120	Cyg X-1	13.666	14.31090	108.09	Cyg X-1	HMXB	0.000
360	20180813_G08_030T01_9000002302	Cyg X-1	32.207	4.34827	53.59	Cyg X-1	HMXB	0.000
361	20180825_G08_030T01_9000002326	Cyg X-1	8.188	7.23178	45.02	Cyg X-1	HMXB	0.000
362	20190612_A05_180T01_9000002986	Cyg X-1	37.914	33.28150	377.89	Cyg X-1	HMXB	0.000

363	20190615_A05_180T01_9000002992	Cyg X-1	189.086	26.00360	683.40	Cyg X-1	HMXB	0.000
364	20210627_A10_109T01_9000004492	Cyg X-1	114.454	18.82560	398.04	Cyg X-1	HMXB	0.000
365	20210813_A10_109T01_9000004638	Cyg X-1	34.741	24.98820	280.81	Cyg X-1	HMXB	0.000
366	20210816_A10_109T01_9000004646	Cyg X-1	137.308	21.01710	479.48	Cyg X-1	HMXB	0.000
367	20210829_A10_109T01_9000004678	Cyg X-1	203.384	12.42220	362.75	Cyg X-1	HMXB	0.000
368	20211103_A11_080T01_9000004756	Cyg X-1	22.118	17.89500	168.50	Cyg X-1	HMXB	0.000
369	20220515_A11_080T01_9000005146	Cyg X-1	283.983	33.28080	1060.95	Cyg X-1	HMXB	0.000
370	20171025_T01_200T01_9000001638	ES 1959+650	98.615	0.36826	8.44	QSOB1959+650	Beamed AGN	0.000
371	20170723_A03_134T01_9000001400	WR 133	30.997	0.33148	4.01	SWIFT J200622.36+364140.9	U2	58.000
372	20210814_T04_041T01_9000004642	EXO 2030+375	33.870	11.74620	138.03	EXO 2030+375	HMXB	0.000
373	20210913_T04_054T01_9000004694	EXO 2030+375	35.972	11.65860	143.23	EXO 2030+375	HMXB	0.000
374	20211014_T04_063T01_9000004724	EXO 2030+375	38.872	8.94534	116.62	EXO 2030+375	HMXB	0.000
375	20211125_T04_071T01_9000004782	EXO 2030+375	36.461	1.13349	14.94	EXO 2030+375	HMXB	0.000
376	20210514_A10_121T02_9000004378	EXO 2030+375	86.482	0.88626	17.15	EXO 2030+375	HMXB	0.000
377	20180909_G08_081T01_9000002350	EXO 2030+375	26.769	0.56002	6.44	EXO 2030+375	HMXB	0.000
378	20151022_P01_161T05_9000000050	Cyg X-3	0.670	2.46287	5.24	Cyg X-3	HMXB	0.000
379	20151023_P01_161T05_9000000058	Cyg X-3	13.466	1.95834	19.78	Cyg X-3	HMXB	0.000
380	20151113_P01_147T02_9000000098	Cyg X-3	40.253	1.88991	32.37	Cyg X-3	HMXB	0.000
381	20151127_P01_161T05_9000000180	Cyg X-3	21.450	0.86243	10.45	Cyg X-3	HMXB	0.000
382	20160306_T01_028T01_9000000360	Cyg X-3	28.803	3.24991	39.31	Cyg X-3	HMXB	0.000
383	20160521_G05_192T01_9000000466	Cyg X-3	27.971	4.28365	50.63	Cyg X-3	HMXB	0.000
384	20160622_G05_170T01_9000000510	Cyg X-3	10.856	3.61048	27.69	Cyg X-3	HMXB	0.000
385	20160630_G05_192T01_9000000522	Cyg X-3	10.739	3.03469	22.62	Cyg X-3	HMXB	0.000
386	20160701_G05_192T01_9000000526	Cyg X-3	9.963	3.16295	22.40	Cyg X-3	HMXB	0.000
387	20160812_G05_192T01_9000000594	Cyg X-3	22.600	2.73304	27.83	Cyg X-3	HMXB	0.000
388	20161120_G06_103T01_9000000812	Cyg X-3	45.035	4.46145	67.36	Cyg X-3	HMXB	0.000
389	20170401_G07_043T01_9000001126	Cyg X-3	43.813	0.27974	4.24	Cyg X-3	HMXB	0.000
390	20171110_G08_032T01_9000001680	Cyg X-3	15.674	5.58420	48.07	Cyg X-3	HMXB	0.000

391	20180331_G08_032T01_9000001998	Cyg X-3	14.492	3.92789	33.01	Cyg X-3	HMXB	0.000
392	20190430_T03_105T01_9000002876	Cyg X-3	11.652	1.76021	13.30	Cyg X-3	HMXB	0.000
393	20190513_T03_115T01_9000002914	Cyg X-3	66.358	3.52837	62.33	Cyg X-3	HMXB	0.000
394	20190410_T03_098T01_9000002836	GRO J2058+42	65.806	6.17331	107.83	-	-	-
395	20180528_A04_186T01_9000002126	SAX J2103.5+4545	17.603	0.93704	8.87	SAX J2103.5+4545	HMXB	0.000
396	20180702_T02_055T01_9000002206	Cep X-4	38.070	0.87076	12.12	-	-	-
397	20180708_T02_057T01_9000002212	Cep X-4	56.008	0.46340	7.86	-	-	-
398	20180529_G08_025T01_9000002130	Cyg X-2	129.590	0.62749	15.96	Cyg X-2	LMXB	0.000
399	20190609_A06_002T02_9000002982	Cyg X-2	67.579	0.37103	6.67	Cyg X-2	LMXB	0.000
400	20190928_A06_002T02_9000003206	Cyg X-2	90.137	0.26262	5.57	Cyg X-2	LMXB	0.000
401	20160228_T01_058T01_9000000348	Cyg X-2	56.949	0.63124	10.42	Cyg X-2	LMXB	0.000
402	20160906_G05_105T01_9000000644	4U 2206+54	44.715	1.23678	17.41	4U 2206+54	HMXB	0.000
403	20161008_A02_081T01_9000000720	4U 2206+54	46.283	0.22135	3.47	4U 2206+54	HMXB	0.000
404	20220725_C07_010T01_9000005246	SSM3 -- Sco X1	56.246	0.23563	3.80	-	-	-

Table A.1: List of CZTI observations with signifcant detection of sources.

Bibliography

Abarr, Q., Awaki, H., Baring, M. G., et al. 2021, Astroparticle Physics, 126, 102529 [Cited on pages 272 and 273.]

Abarr, Q., Beheshtipour, B., Beilicke, M., et al. 2022, Astroparticle Physics, 143, 102749 [Cited on pages 272 and 273.]

Acton, L., Tsuneta, S., Ogawara, Y., et al. 1992, Science, 258, 618 [Cited on page 164.]

Agostinelli, S., Allison, J., Amako, K., et al. 2003, Nuclear Instruments and Methods in Physics Research A, 506, 250 [Cited on page 60.]

Agostinelli, S., Allison, J., Amako, K., et al. 2003, Nuclear Instruments and Methods in Physics Research Section A: Accelerators, Spectrometers, Detectors and Associated Equipment, 506, 250 [Cited on pages 37 and 41.]

Agrawal, P. C. 2017, Journal of Astrophysics and Astronomy, 38, 27 [Cited on page 53.]

Agrawal, P. C., Yadav, J. S., Antia, H. M., et al. 2017, Journal of Astrophysics and Astronomy, 38, 30 [Cited on pages 21 and 53.]

Alha, L., Huovelin, J., Nygård, K., et al. 2009, Nuclear Instruments and Methods in Physics Research A, 607, 544 [Cited on page 120.]

Alston, W., Giustini, M., & Petrucci, P.-O. 2023, in Handbook of X-ray and Gamma-ray Astrophysics. Edited by Cosimo Bambi and Andrea Santangelo, 135 [Cited on page 10.]

Antia, H. M., Agrawal, P. C., Katoch, T., et al. 2022, ApJS, 260, 40 [Cited on pages 46, 80, and 84.]

Antia, H. M., Yadav, J. S., Agrawal, P. C., et al. 2017, ApJS, 231, 10 [Cited on page 46.]

Arnaud, K. A. 1996, in Astronomical Society of the Pacific Conference Series, Vol. 101, Astronomical Data Analysis Software and Systems V, ed. G. H. Jacoby & J. Barnes, 17 [Cited on pages 25, 158, 181, 190, 208, and 238.]

Aschwanden, M. J. 2001, ApJ, 560, 1035 [Cited on page 200.]

Aschwanden, M. J., Boerner, P., Caspi, A., et al. 2015a, Sol. Phys., 290, 2733 [Cited on page 220.]

Aschwanden, M. J., Boerner, P., Ryan, D., et al. 2015b, ApJ, 802, 53 [Cited on page 251.]

Aschwanden, M. J., Nightingale, R. W., Tarbell, T. D., & Wolfson, C. J. 2000a, ApJ, 535, 1027 [Cited on page 184.]

Aschwanden, M. J., Tarbell, T. D., Nightingale, R. W., et al. 2000b, ApJ, 535, 1047 [Cited on pages 175, 184, 199, and 201.]

Asplund, M., Grevesse, N., Sauval, A. J., & Scott, P. 2009, ARA&A, 47, 481 [Cited on pages 225 and 226.]

Athiray, P. S., Vievering, J., Glesener, L., et al. 2020, ApJ, 891, 78 [Cited on pages 202 and 207.]

Awasthi, A. K., Sylwester, B., Sylwester, J., & Jain, R. 2016, ApJ, 823, 126 [Cited on page 207.]

Ayzenberg, D., & Bambi, C. 2022, in Handbook of X-ray and Gamma-ray Astrophysics, 81 [Cited on page 8.]

Bai, T. 1979, Sol. Phys., 62, 113 [Cited on page 252.]

Bai, T., & Ramaty, R. 1978, ApJ, 219, 705 [Cited on page 258.]

Bala, S., Mate, S., Mehla, A., et al. 2023, Journal of Astronomical Telescopes, Instruments, and Systems, 9, 048002 [Cited on page 289.]

Barbera, M., Lo Cicero, U., & Sciorino, L. 2022, in Handbook of X-ray and Gamma-ray Astrophysics, 116 [Cited on page 19.]

Basko, M. M. 1979, Soviet Ast., 23, 224 [Cited on page 252.]

Battaglia, A. F., Saqri, J., Massa, P., et al. 2021, A&A, 656, A4 [Cited on page 239.]

Battaglia, A. F., Hudson, H., Warmuth, A., et al. 2023, A&A, 679, A139 [Cited on pages 168 and 288.]

Battaglia, M., Fletcher, L., & Benz, A. O. 2009, A&A, 498, 891 [Cited on page 168.]

Bautz, M. W., Holland, A. D., & Lumb, D. H. 2022, in Handbook of X-ray and Gamma-ray Astrophysics. Edited by Cosimo Bambi and Andrea Santangelo, 11 [Cited on page 21.]

Becker, P. A., & Wolff, M. T. 2007, ApJ, 654, 435 [Cited on page 17.]

Benz, A. O. 2017, Living Reviews in Solar Physics, 14, 2 [Cited on pages 168, 169, 170, 171, 172, 202, 206, and 258.]

Benz, A. O., & Krucker, S. 2002, ApJ, 568, 413 [Cited on pages 175 and 184.]

Bhalerao, V. 2012, PhD thesis, California Institute of Technology [Cited on page 39.]

Bhalerao, V., Kasliwal, M. M., Bhattacharya, D., et al. 2017a, ApJ, 845, 152 [Cited on page 61.]

Bhalerao, V., Bhattacharya, D., Vibhute, A., et al. 2017b, Journal of Astrophysics and Astronomy, 38, 31 [Cited on pages 24, 49, 54, and 55.]

Bhalerao, V., Vadawale, S., Tendulkar, S., et al. 2022a, arXiv e-prints, arXiv:2211.12055 [Cited on page 289.]

Bhalerao, V., Sawant, D., Pai, A., et al. 2022b, arXiv e-prints, arXiv:2211.12052 [Cited on page 289.]

Bhardwaj, A. 2022, in Handbook of X-ray and Gamma-ray Astrophysics, ed. C. Bambi & A. Sangangelo, 85 [Cited on page 11.]

Biltzinger, B., Kunzweiler, F., Greiner, J., Toelge, K., & Burgess, J. M. 2020, A&A, 640, A8 [Cited on page 42.]

Blake, R. L., Chubb, T. A., Friedman, H., & Unzicker, A. E. 1963, ApJ, 137, 3 [Cited on page 163.]

Bohlin, J. D., Frost, K. J., Burr, P. T., Guha, A. K., & Withbroe, G. L. 1980, Sol. Phys., 65, 5 [Cited on page 164.]

Brandt, W. N., & Yang, G. 2022, in Handbook of X-ray and Gamma-ray Astrophysics, 78 [Cited on page 31.]

Brown, J. C. 1971, Sol. Phys., 18, 489 [Cited on pages 164, 177, and 240.]

Bucciantini, N., Ferrazzoli, R., Bachetti, M., et al. 2023, Nature Astronomy, 7, 602 [Cited on page 280.]

Buitrago-Casas, J. C., Glesener, L., Christe, S., et al. 2022, A&A, 665, A103 [Cited on pages 173 and 290.]

Burnight. 1949, Phys. Rev., 76, 160 [Cited on pages 8 and 162.]

Campana, R. 2022, in Handbook of X-ray and Gamma-ray Astrophysics, 39 [Cited on pages 31 and 32.]

Carmichael, H. 1964, in NASA Special Publication, Vol. 50, 451 [Cited on page 168.]

Carrington, R. C. 1859, MNRAS, 20, 13 [Cited on page 166.]

Carter, C., Karovska, M., Jerius, D., Glotfelty, K., & Beikman, S. 2003, in Astronomical Society of the Pacific Conference Series, Vol. 295, Astronomical Data Analysis Software and Systems XII, ed. H. E. Payne, R. I. Jedrzejewski, & R. N. Hook, 477 [Cited on page 39.]

Caspi, A., & Lin, R. P. 2010, ApJ, 725, L161 [Cited on pages 172, 219, and 227.]

Caspi, A., McTiernan, J. M., & Warren, H. P. 2014, ApJ, 788, L31 [Cited on pages 207, 220, 227, and 233.]

Chand, V., Chattopadhyay, T., Iyyani, S., et al. 2018, ApJ, 862, 154 [Cited on page 62.]

Chattopadhyay, T., Vadawale, S. V., & Pendharkar, J. 2013, Experimental Astronomy, 35, 391 [Cited on page 262.]

Chattopadhyay, T., Vadawale, S. V., Rao, A. R., et al. 2016a, in Society of Photo-Optical Instrumentation Engineers (SPIE) Conference Series, Vol. 9905, Space Telescopes and Instrumentation 2016: Ultraviolet to Gamma Ray, 99054D [Cited on page 66.]

Chattopadhyay, T., Vadawale, S. V., Rao, A. R., Sreekumar, S., & Bhattacharya, D. 2014a, Experimental Astronomy, 37, 555 [Cited on page 61.]

Chattopadhyay, T., Vadawale, S. V., Shanmugam, M., & Goyal, S. K. 2014b, ApJS, 212, 12 [Cited on pages 262 and 267.]

Chattopadhyay, T., Vadawale, S. V., Goyal, S. K., et al. 2016b, Experimental Astronomy, 41, 197 [Cited on pages 262 and 263.]

Chattopadhyay, T., Vadawale, S. V., Aarthy, E., et al. 2019, ApJ, 884, 123 [Cited on page 61.]

Chattopadhyay, T., Gupta, S., Sharma, V., et al. 2021, Journal of Astrophysics and Astronomy, 42, 82 [Cited on pages 61 and 76.]

Chattopadhyay, T., Gupta, S., Iyyani, S., et al. 2022, ApJ, 936, 12 [Cited on page 61.]

Chattopadhyay, T., Kumar, A., Rao, A. R., et al. 2023, The Astrophysical Journal Letters, 960, L2 [Cited on pages 274 and 278.]

Chattopadhyay, T., Kumar, A., Rao, A. R., et al. 2024, ApJ, 960, L2 [Cited on pages 61 and 112.]

Chauvin, M., Roques, J. P., Clark, D. J., & Jourdain, E. 2013, ApJ, 769, 137 [Cited on pages 273 and 280.]

Chauvin, M., Florén, H. G., Jackson, M., et al. 2016a, MNRAS, 456, L84 [Cited on page 280.]

Chauvin, M., Jackson, M., Kawano, T., et al. 2016b, Astroparticle Physics, 82, 99 [Cited on pages 272 and 273.]

Chauvin, M., Florén, H. G., Jackson, M., et al. 2016c, Experimental Astronomy, 41, 17 [Cited on pages 272 and 273.]

Chauvin, M., Friis, M., Jackson, M., et al. 2017a, Nuclear Instruments and Methods in Physics Research A, 859, 125 [Cited on pages 272 and 273.]

Chauvin, M., Florén, H. G., Friis, M., et al. 2017b, Scientific Reports, 7, 7816 [Cited on page 280.]

—. 2018, Nature Astronomy, 2, 652 [Cited on page 278.]

Cheung, M. C. M., Boerner, P., Schrijver, C. J., et al. 2015, ApJ, 807, 143 [Cited on page 206.]

Choudhary, R. K., Bindu, K. R., Harshit, K., et al. 2020, Current Science, 118, doi:10.18520/cs/v118/i2/210-218 [Cited on page 119.]

Chowdhury, A. R., Saxena, M., Kumar, A., et al. 2019, Current Science, 117, doi:10.18520/cs/v118/i4/560-565 [Cited on page 119.]

Chowdhury, A. R., Banerjee, A., Joshi, S. R., et al. 2020a, Current Science, 118, doi:10.18520/cs/v118/i3/368-375 [Cited on page 119.]

Chowdhury, A. R., Patel, V., Joshi, S. R., et al. 2020b, Current Science, 118, doi:10.18520/cs/v118/i4/566-572 [Cited on page 119.]

Christe, S., Hannah, I. G., Krucker, S., McTiernan, J., & Lin, R. P. 2008, ApJ, 677, 1385 [Cited on page 174.]

Christe, S., Krucker, S., Glesener, L., et al. 2017, arXiv e-prints, arXiv:1701.00792 [Cited on page 170.]

Christensen, F. E., & Ramsey, B. D. 2022, in Handbook of X-ray and Gamma-ray Astrophysics, 112 [Cited on page 19.]

Cooper, K., Hannah, I. G., Grefenstette, B. W., et al. 2020, ApJ, 893, L40 [Cited on page 197.]

Costa, E., Soffitta, P., Bellazzini, R., et al. 2001, Nature, 411, 662 [Cited on pages 24 and 271.]

Cranmer, S. R. 2009, Living Reviews in Solar Physics, 6, 3 [Cited on page 165.]

Culhane, J. L., & Acton, L. W. 1974, ARA&A, 12, 359 [Cited on page 164.]

Culhane, J. L., Rapley, C. G., Bentley, R. D., et al. 1981, ApJ, 244, L141 [Cited on page 252.]

Das, T. P., Thampi, S. V., Dhanya, M. B., et al. 2020, Current Science, 118, doi:10.18520/cs/v118/i2/202-209 [Cited on page 119.]

de Vries, C. P., Lowes, P., den Herder, J. W., et al. 2012, in Society of Photo-Optical Instrumentation Engineers (SPIE) Conference Series, Vol. 8443, Space Telescopes and Instrumentation 2012: Ultraviolet to Gamma Ray, ed. T. Takahashi, S. S. Murray, & J.-W. A. den Herder, 844353 [Cited on page 43.]

Dean, A. J., Clark, D. J., Stephen, J. B., et al. 2008, Science, 321, 1183 [Cited on page 273.]

Del Monte, E., Fabiani, S., & Pearce, M. 2023, in Handbook of X-ray and Gamma-ray Astrophysics. Edited by Cosimo Bambi and Andrea Santangelo, 127 [Cited on page 24.]

Del Zanna, G. 2013, A&A, 558, A73 [Cited on pages 189, 225, and 226.]

Del Zanna, G., Andretta, V., Cargill, P. J., et al. 2021a, Frontiers in Astronomy and Space Sciences, 8, 33 [Cited on page 206.]

Del Zanna, G., Dere, K. P., Young, P. R., & Landi, E. 2021b, ApJ, 909, 38 [Cited on page 176.]

Del Zanna, G., & Mason, H. E. 2018, Living Reviews in Solar Physics, 15, 5 [Cited on pages 14, 120, 168, 175, 215, 216, and 218.]

Del Zanna, G., Tripathi, D., Mason, H., Subramanian, S., & O'Dwyer, B. 2015, A&A, 573, A104 [Cited on page 173.]

Del Zanna, G., & Woods, T. N. 2013, A&A, 555, A59 [Cited on pages 207 and 228.]

Del Zanna, G., Mondal, B., Rao, Y. K., et al. 2022, ApJ, 934, 159 [Cited on pages 160 and 229.]

Dennis, B. R., Phillips, K. J. H., Schwartz, R. A., et al. 2015, ApJ, 803, 67 [Cited on page 120.]

Diebold, S. 2022, in Handbook of X-ray and Gamma-ray Astrophysics, 60 [Cited on page 21.]

Dong, W.-D., Zhang, X., Li, Y., et al. 2019, Sol. Phys., 294, 120 [Cited on page 120.]

Doschek, G. 2021, Sol. Phys., 296, 123 [Cited on page 164.]

Doschek, G. A. 1972, Space Sci. Rev., 13, 765 [Cited on pages 163 and 164.]

—. 1990, ApJS, 73, 117 [Cited on page 206.]

Doschek, G. A., Meekins, J. F., Kreplin, R. W., Chubb, T. A., & Friedman, H. 1971, ApJ, 170, 573 [Cited on page 252.]

Drake, J. J., & Stelzer, B. 2023, in Handbook of X-ray and Gamma-ray Astrophysics. Edited by Cosimo Bambi and Andrea Santangelo, 132 [Cited on page 11.]

Dunn, W. R. 2022a, in Handbook of X-ray and Gamma-ray Astrophysics, ed. C. Bambi & A. Sangangelo, 109 [Cited on page 11.]

—. 2022b, in Handbook of X-ray and Gamma-ray Astrophysics, ed. C. Bambi & A. Sangangelo, 110 [Cited on page 11.]

Emslie, A. G., Phillips, K. J. H., & Dennis, B. R. 1986, Sol. Phys., 103, 89 [Cited on page 252.]

Fabiani, S., Baffo, I., Bonomo, S., et al. 2022, in Society of Photo-Optical Instrumentation Engineers (SPIE) Conference Series, Vol. 12181, Space Telescopes and Instrumentation 2022: Ultraviolet to Gamma Ray, ed. J.-W. A. den Herder, S. Nikzad, & K. Nakazawa, 121810J [Cited on page 260.]

Fano, U. 1947, Physical Review, 72, 26 [Cited on page 27.]

Feldman, U. 1992, Phys. Scr, 46, 202 [Cited on pages 210, 225, 226, 241, and 244.]

—. 1996, Physics of Plasmas, 3, 3203 [Cited on page 206.]

Feldman, U., Doschek, G. A., Mariska, J. T., & Brown, C. M. 1995, ApJ, 450, 441 [Cited on page 267.]

Fenimore, E. E., & Cannon, T. M. 1978, Appl. Opt., 17, 337 [Cited on page 57.]

Fletcher, L., Dennis, B. R., Hudson, H. S., et al. 2011, Space Sci. Rev., 159, 19 [Cited on pages 168 and 175.]

Forman, W., Jones, C., Cominsky, L., et al. 1978, ApJS, 38, 357 [Cited on page 8.]

Forot, M., Laurent, P., Grenier, I. A., Gouiffès, C., & Lebrun, F. 2008, ApJ, 688, L29 [Cited on pages 273 and 280.]

Foster, A. R., Ji, L., Smith, R. K., & Brickhouse, N. S. 2012, ApJ, 756, 128 [Cited on page 176.]

Frank, J., King, A., & Raine, D. J. 2002, Accretion Power in Astrophysics: Third Edition [Cited on page 14.]

Freeman, P., Doe, S., & Siemiginowska, A. 2001, in Society of Photo-Optical Instrumentation Engineers (SPIE) Conference Series, Vol. 4477, Astronomical Data Analysis, ed. J.-L. Starck & F. D. Murtagh, 76–87 [Cited on page 25.]

Friedman, H. 1963a, in The Solar Corona, ed. J. W. Evans, Vol. 16, 45 [Cited on page 163.]

Friedman, H. 1963b, ARA&A, 1, 59 [Cited on page 164.]

Friedman, H., Lichtman, S. W., & Byram, E. T. 1951, Physical Review, 83, 1025 [Cited on pages 8 and 163.]

Gburek, S., Sylwester, J., Kowalinski, M., et al. 2013, Sol. Phys., 283, 631 [Cited on page 121.]

Giacconi, R., Gursky, H., Kellogg, E., Schreier, E., & Tananbaum, H. 1971, ApJ, 167, L67 [Cited on page 8.]

Giacconi, R., Gursky, H., Paolini, F. R., & Rossi, B. B. 1962, Phys. Rev. Lett., 9, 439 [Cited on pages 8 and 155.]

Gilfanov, M. 2010, in Lecture Notes in Physics, Berlin Springer Verlag, ed. T. Belloni, Vol. 794, 17 [Cited on page 17.]

Glesener, L., Krucker, S., Hannah, I. G., et al. 2017, ApJ, 845, 122 [Cited on page 197.]

Glesener, L., Krucker, S., Duncan, J., et al. 2020, ApJ, 891, L34 [Cited on page 202.]

Goldwurm, A., & Gros, A. 2022, in Handbook of X-ray and Gamma-ray Astrophysics, 15 [Cited on page 18.]

Golub, L., Krieger, A. S., Silk, J. K., Timothy, A. F., & Vaiana, G. S. 1974, ApJ, 189, L93 [Cited on page 195.]

Golub, L., Deluca, E., Austin, G., et al. 2007, Sol. Phys., 243, 63 [Cited on pages 180, 187, and 189.]

Goryaev, F. F., Parenti, S., Urnov, A. M., et al. 2010, A&A, 523, A44 [Cited on page 206.]

Gottardi, L., & Smith, S. 2022, in Handbook of X-ray and Gamma-ray Astrophysics, 103 [Cited on page 23.]

Grefenstette, B. W., Madsen, K. K., Miyasaka, H., & Zoglauer, A. 2022, Journal of Astronomical Telescopes, Instruments, and Systems, 8, 047001 [Cited on pages 82 and 85.]

Grimm, H. J., McDowell, J., Fabbiano, G., & Elvis, M. 2009, ApJ, 690, 128 [Cited on page 26.]

Gryciuk, M., Siarkowski, M., Sylwester, J., et al. 2017, Sol. Phys., 292, 77 [Cited on page 197.]

Guainazzi, M., David, L., Grant, C. E., et al. 2015, Journal of Astronomical Telescopes, Instruments, and Systems, 1, 047001 [Cited on page 43.]

Gupta, R., Gupta, S., Chattopadhyay, T., et al. 2022, MNRAS, 511, 1694 [Cited on page 62.]

Gursky, H., Solinger, A., Kellogg, E. M., et al. 1972, ApJ, 173, L99 [Cited on page 9.]

Hannah, I. G., Christe, S., Krucker, S., et al. 2008, ApJ, 677, 704 [Cited on pages 174, 196, 197, and 198.]

Hannah, I. G., Hudson, H. S., Battaglia, M., et al. 2011, Space Sci. Rev., 159, 263 [Cited on pages 173 and 198.]

Hannah, I. G., Hudson, H. S., Hurford, G. J., & Lin, R. P. 2010, ApJ, 724, 487 [Cited on pages 173 and 290.]

Hannah, I. G., Kleint, L., Krucker, S., et al. 2019, ApJ, 881, 109 [Cited on page 197.]

Harding, A. K. 2019, in Astrophysics and Space Science Library, Vol. 460, Astronomical Polarisation from the Infrared to Gamma Rays, ed. R. Mignani, A. Shearer, A. Słowikowska, & S. Zane, 277 [Cited on page 275.]

Harrison, F. A., Craig, W. W., Christensen, F. E., et al. 2013, ApJ, 770, 103 [Cited on pages 19 and 121.]

Hathaway, D. H. 2015, Living Reviews in Solar Physics, 12, 4 [Cited on page 165.]

Hecht, K. 1932, Zeitschrift fur Physik, 77, 235 [Cited on page 66.]

Hinode Review Team, Al-Janabi, K., Antolin, P., et al. 2019, PASJ, 71, R1 [Cited on page 173.]

Hirayama, T. 1974, Sol. Phys., 34, 323 [Cited on page 168.]

Hitomi Collaboration, Aharonian, F., Akamatsu, H., et al. 2016, Nature, 535, 117 [Cited on page 23.]

—. 2018, PASJ, 70, 113 [Cited on page 273.]

Hodgson, R. 1859, MNRAS, 20, 15 [Cited on page 166.]

Holman, G. D., Aschwanden, M. J., Aurass, H., et al. 2011, Space Sci. Rev., 159, 107 [Cited on page 232.]

Houck, J. C., & Denicola, L. A. 2000, Astronomical Society of the Pacific Conference Series, Vol. 216, ISIS: An Interactive Spectral Interpretation System for High Resolution X-Ray Spectroscopy, ed. N. Manset, C. Veillet, & D. Crabtree, 591 [Cited on page 25.]

Hudson, H. S. 1991, Sol. Phys., 133, 357 [Cited on pages 173 and 201.]

Hudson, H. S., Simões, P. J. A., Fletcher, L., Hayes, L. A., & Hannah, I. G. 2021, MNRAS, 501, 1273 [Cited on page 288.]

Hulburt, E. O. 1938, Physical Review, 53, 344 [Cited on page 162.]

Huovelin, J., Alha, L., Andersson, H., et al. 2002, Planet. Space Sci., 50, 1345 [Cited on page 120.]

Huovelin, J., Vainio, R., Andersson, H., et al. 2010, Planet. Space Sci., 58, 96 [Cited on page 120.]

Inglis, A. R., & Christe, S. 2014, ApJ, 789, 116 [Cited on page 233.]

Iyudin, A. F., Labanti, C., & Roberts, O. J. 2022, in Handbook of X-ray and Gamma-ray Astrophysics. Edited by Cosimo Bambi and Andrea Santangelo, 66 [Cited on page 21.]

Jackson, J. D. 1998, Classical Electrodynamics, 3rd Edition [Cited on page 11.]

Jahoda, K., Markwardt, C. B., Radeva, Y., et al. 2006, ApJS, 163, 401 [Cited on pages 42, 45, and 47.]

Jain, R., Dave, H., Shah, A. B., et al. 2005, Sol. Phys., 227, 89 [Cited on page 121.]

Janardhan, P., Bisoi, S. K., Ananthakrishnan, S., Tokumaru, M., & Fujiki, K. 2011, Geophys. Res. Lett., 38, L20108 [Cited on page 185.]

Janardhan, P., Bisoi, S. K., Ananthakrishnan, S., et al. 2015, Journal of Geophysical Research (Space Physics), 120, 5306 [Cited on page 185.]

Jeffrey, N. L. S., & Kontar, E. P. 2011, A&A, 536, A93 [Cited on pages 258 and 260.]

Jeffrey, N. L. S., Saint-Hilaire, P., & Kontar, E. P. 2020, A&A, 642, A79 [Cited on pages 258 and 259.]

Jourdain, E., & Roques, J. P. 2009, ApJ, 704, 17 [Cited on page 107.]

—. 2020, ApJ, 899, 131 [Cited on page 107.]

Jourdain, E., Roques, J. P., Chauvin, M., & Clark, D. J. 2012, ApJ, 761, 27 [Cited on pages 274 and 278.]

Kaastra, J. S., Mewe, R., & Nieuwenhuijzen, H. 1996, in UV and X-ray Spectroscopy of Astrophysical and Laboratory Plasmas, 411–414 [Cited on page 25.]

Kaastra, J. S., Paerels, F. B. S., Durret, F., Schindler, S., & Richter, P. 2008, Space Sci. Rev., 134, 155 [Cited on pages 14 and 15.]

Kalemci, E., Kara, E., & Tomsick, J. A. 2022, in Handbook of X-ray and Gamma-ray Astrophysics, 9 [Cited on page 10.]

Kasliwal, M. M., Nakar, E., Singer, L. P., et al. 2017, Science, 358, 1559 [Cited on page 61.]

Katsuda, S., Enoto, T., Lommen, A. N., et al. 2023, Journal of Geophysical Research (Space Physics), 128, e2022JA030797 [Cited on page 30.]

Kayal, A., Singh, V., Ricci, C., et al. 2023, MNRAS, 522, 4098 [Cited on page 112.]

Kepa, A., Sylwester, B., Siarkowski, M., & Sylwester, J. 2008, Advances in Space Research, 42, 828 [Cited on pages 227, 239, and 240.]

Kepa, A., Sylwester, B., Sylwester, J., Gryciuk, M., & Siarkowski, M. 2018, Journal of Atmospheric and Solar-Terrestrial Physics, 179, 545 [Cited on page 206.]

Kilbourne, C. A., Adams, J. S., Brekosky, R. P., et al. 2018, Journal of Astronomical Telescopes, Instruments, and Systems, 4, 011214 [Cited on page 22.]

Kirsch, M. G., Briel, U. G., Burrows, D., et al. 2005, in Society of Photo-Optical Instrumentation Engineers (SPIE) Conference Series, Vol. 5898, UV, X-Ray, and Gamma-Ray Space Instrumentation for Astronomy XIV, ed. O. H. W. Siegmund, 22–33 [Cited on page 47.]

Kitaguchi, T., Grefenstette, B. W., Harrison, F. A., et al. 2011, in Society of Photo-Optical Instrumentation Engineers (SPIE) Conference Series, Vol. 8145, Society of Photo-Optical Instrumentation Engineers (SPIE) Conference Series, 814507 [Cited on page 26.]

Klimchuk, J. A. 2006, Sol. Phys., 234, 41 [Cited on page 173.]

Knoll, G. F. 2000, Radiation detection and measurement [Cited on pages 20, 34, and 35.]

Kontar, E. P., Brown, J. C., Emslie, A. G., et al. 2011, Space Sci. Rev., 159, 301 [Cited on pages 168, 179, 232, 235, 239, 258, and 260.]

Kopp, R. A., & Pneuman, G. W. 1976, Sol. Phys., 50, 85 [Cited on page 168.]

Kosugi, T., Matsuzaki, K., Sakao, T., et al. 2007, Sol. Phys., 243, 3 [Cited on pages 164 and 180.]

Kotov, Y. D., Yurov, V. N., Glyanenko, A. S., et al. 2016, Advances in Space Research, 58, 635 [Cited on page 260.]

Krawczynski, H., Matt, G., Ingram, A. R., et al. 2019, arXiv e-prints, arXiv:1904.09313 [Cited on page 272.]

Krawczynski, H., Muleri, F., Dovčiak, M., et al. 2022, Science, 378, 650 [Cited on page 278.]

Krucker, S., & Benz, A. O. 1998, ApJ, 501, L213 [Cited on pages 175, 184, 199, and 201.]

Krucker, S., Benz, A. O., Bastian, T. S., & Acton, L. W. 1997, ApJ, 488, 499 [Cited on pages 184 and 192.]

Krucker, S., Battaglia, M., Cargill, P. J., et al. 2008, A&A Rev., 16, 155 [Cited on pages 168, 171, 206, and 227.]

Krucker, S., Hurford, G. J., Grimm, O., et al. 2020, A&A, 642, A15 [Cited on pages 121, 179, 202, 229, 233, and 240.]

Kuhar, M., Krucker, S., Glesener, L., et al. 2018, ApJ, 856, L32 [Cited on pages 175, 184, 192, 196, and 197.]

Laming, J. M., Adams, J., Alexander, D., et al. 2010, arXiv e-prints, arXiv:1011.4052 [Cited on page 206.]

Laurent, P., Rodriguez, J., Wilms, J., et al. 2011, Science, 332, 438 [Cited on page 274.]

Leibacher, J., Sakurai, T., Schrijver, C. J., & van Driel-Gesztelyi, L. 2010, Sol. Phys., 263, 1 [Cited on page 192.]

Lemen, J. R., Title, A. M., Akin, D. J., et al. 2012, Sol. Phys., 275, 17 [Cited on pages 164, 180, 187, 232, and 235.]

Lin, R. P., Schwartz, R. A., Kane, S. R., Pelling, R. M., & Hurley, K. C. 1984, ApJ, 283, 421 [Cited on page 173.]

Lin, R. P., Dennis, B. R., Hurford, G. J., et al. 2002, Sol. Phys., 210, 3 [Cited on pages 17, 18, 121, 164, and 232.]

Long, X., Feng, H., Li, H., et al. 2021, ApJ, 912, L28 [Cited on page 280.]

Longair, M. S. 2011, High Energy Astrophysics [Cited on page 13.]

Madjarska, M. S. 2019, Living Reviews in Solar Physics, 16, 2 [Cited on pages 165 and 195.]

Madsen, K. K., Beardmore, A. P., Forster, K., et al. 2017a, AJ, 153, 2 [Cited on page 47.]

Madsen, K. K., Forster, K., Grefenstette, B., Harrison, F. A., & Miyasaka, H. 2022, Journal of Astronomical Telescopes, Instruments, and Systems, 8, 034003 [Cited on pages 30, 47, and 107.]

Madsen, K. K., Forster, K., Grefenstette, B. W., Harrison, F. A., & Stern, D. 2017b, ApJ, 841, 56 [Cited on pages 47 and 107.]

Madsen, K. K., Reynolds, S., Harrison, F., et al. 2015a, ApJ, 801, 66 [Cited on pages 116 and 117.]

Madsen, K. K., Harrison, F. A., Markwardt, C. B., et al. 2015b, ApJS, 220, 8 [Cited on pages 47 and 107.]

Mandel'Štam, S. L. 1965, Space Sci. Rev., 4, 587 [Cited on pages 163 and 164.]

Marin, F. 2018, Galaxies, 6, 38 [Cited on page 272.]

Markoff, S., Falcke, H., & Fender, R. 2001, A&A, 372, L25 [Cited on page 274.]

Martinez Oliveros, J. C., Christe, S., Saint-Hilaire, P., et al. 2023, in AAS/Solar Physics Division Meeting, Vol. 55, AAS/Solar Physics Division Meeting, 302.05 [Cited on page 260.]

Mason, J. P., Woods, T. N., Caspi, A., et al. 2016, Journal of Spacecraft and Rockets, 53, 328 [Cited on page 233.]

Massa, P., Schwartz, R., Tolbert, A. K., et al. 2020, ApJ, 894, 46 [Cited on page 240.]

Massa, P., Battaglia, A. F., Volpara, A., et al. 2022, Sol. Phys., 297, 93 [Cited on pages 233 and 240.]

Masterson, R. A., Chodas, M., Bayley, L., et al. 2018, Space Sci. Rev., 214, 48 [Cited on page 120.]

Masuda, S., Kosugi, T., Hara, H., Tsuneta, S., & Ogawara, Y. 1994, Nature, 371, 495 [Cited on pages 168 and 170.]

Mate, S., Chattopadhyay, T., Bhalerao, V., et al. 2021, Journal of Astrophysics and Astronomy, 42, 93 [Cited on pages 41 and 61.]

Matthews, S. A., Reid, H. A. S., Baker, D., et al. 2021, Experimental Astronomy, doi:10.1007/s10686-021-09798-6 [Cited on page 206.]

McTiernan, J. M., Caspi, A., & Warren, H. P. 2019, ApJ, 881, 161 [Cited on pages 207 and 233.]

McTiernan, J. M., Kane, S. R., Loran, J. M., et al. 1993, ApJ, 416, L91 [Cited on page 168.]

Meszaros, P., Novick, R., Szentgyorgyi, A., Chanan, G. A., & Weisskopf, M. C. 1988, ApJ, 324, 1056 [Cited on page 275.]

Meuris, A., Nagazawa, K., Kuvvetli, I., & Caroli, E. 2022, in Handbook of X-ray and Gamma-ray Astrophysics. Edited by Cosimo Bambi and Andrea Santangelo, 10 [Cited on page 22.]

Mihara, T., Nakajima, M., Sugizaki, M., et al. 2011, PASJ, 63, S623 [Cited on page 21.]

Mitchell, A. M. W., & Gelfand, J. 2022, in Handbook of X-ray and Gamma-ray Astrophysics, 61 [Cited on page 10.]

Mitchell, R. J., Culhane, J. L., Davison, P. J. N., & Ives, J. C. 1976, MNRAS, 175, 29P [Cited on page 23.]

Mithun, N. P. S., Vadawale, S. V., Sarkar, A., et al. 2020, Sol. Phys., 295, 139 [Cited on pages 50 and 122.]

Mithun, N. P. S., Vadawale, S. V., Patel, A. R., et al. 2021a, Astronomy and Computing, 34, 100449 [Cited on pages 158, 185, 208, and 238.]

Mithun, N. P. S., Vadawale, S. V., Shanmugam, M., et al. 2021b, Experimental Astronomy, 51, 33 [Cited on pages 37, 38, 42, 49, 129, 134, 145, 254, and 287.]

Mithun, N. P. S., Vadawale, S. V., Zanna, G. D., et al. 2022, ApJ, 939, 112 [Cited on pages 51, 205, and 251.]

Modi, M., Gupta, R., Kane, S., et al. 2019, in AIP Conference Proceedings, Vol. 2054, 060022 [Cited on page 37.]

Mondal, B., Vadawale, S. V., Del Zanna, G., et al. 2023a, ApJ, 955, 146 [Cited on page 160.]

Mondal, B., Vadawale, S. V., Mithun, N. P. S., et al. 2021a, Astronomy and Computing, 34, 100446 [Cited on page 39.]

Mondal, B., Sarkar, A., Vadawale, S. V., et al. 2021b, ApJ, 920, 4 [Cited on pages 160, 181, 190, 207, 210, 211, 225, and 227.]

Mondal, B., Klimchuk, J. A., Vadawale, S. V., et al. 2023b, ApJ, 945, 37 [Cited on page 160.]

Moore, C. S., Caspi, A., Woods, T. N., et al. 2018a, Sol. Phys., 293, 21 [Cited on page 121.]

—. 2018b, Sol. Phys., 293, 21 [Cited on page 233.]

Mushtukov, A., & Tsygankov, S. 2022, in Handbook of X-ray and Gamma-ray Astrophysics, ed. C. Bambi & A. Santangelo (Singapore: Springer Nature Singapore), 1–72 [Cited on page 10.]

Nagasawa, S., Kawate, T., Narukage, N., et al. 2022, ApJ, 933, 173 [Cited on page 233.]

Nama, L., Mondal, B., Narendranath, S., & Paul, K. T. 2023, Sol. Phys., 298, 55 [Cited on page 160.]

Nandy, D., Martens, P. C. H., Obridko, V., Dash, S., & Georgieva, K. 2021, Progress in Earth and Planetary Science, 8, 40 [Cited on page 84.]

Narendranath, S., Sreekumar, P., Alha, L., et al. 2014a, Sol. Phys., 289, 1585 [Cited on pages 120 and 210.]

Narendranath, S., Tadeppalli, S. P., Athiray, P. S., Misra, A., & Sreekumar, P. 2014b, in Lunar and Planetary Science Conference, Lunar and Planetary Science Conference, 2199 [Cited on page 152.]

Narendranath, S., Pillai, N. S., Bhatt, M., et al. 2024, Icarus, 410, 115898 [Cited on page 287.]

Narukage, N. 2019, in AGU Fall Meeting Abstracts, Vol. 2019, SH31C–3311 [Cited on page 260.]

Nättilä, J., & Kajava, J. J. E. 2022, in Handbook of X-ray and Gamma-ray Astrophysics, 30 [Cited on page 8.]

Navalgund, K. H., Suryanarayana Sarma, K., Gaurav, P. K., Nagesh, G., & Annadurai, M. 2017, Journal of Astrophysics and Astronomy, 38, 34 [Cited on page 53.]

Neupert, W. M. 1968, ApJ, 153, L59 [Cited on pages 208 and 237.]

Neupert, W. M., Gates, W., Swartz, M., & Young, R. 1967, ApJ, 149, L79 [Cited on page 252.]

Odaka, H., Asai, M., Hagino, K., et al. 2018, Nuclear Instruments and Methods in Physics Research A, 891, 92 [Cited on pages 41 and 85.]

Parker, E. N. 1988, ApJ, 330, 474 [Cited on page 173.]

Parmar, A. N., Culhane, J. L., Rapley, C. G., et al. 1984, ApJ, 279, 866 [Cited on page 252.]

Parnell, C. E., & Jupp, P. E. 2000, ApJ, 529, 554 [Cited on pages 175, 184, 199, and 201.]

Paul, B. 2022, in 44th COSPAR Scientific Assembly. Held 16-24 July, Vol. 44, 1853 [Cited on page 24.]

Paul, B., Gopala Krishna, M. R., & Puthiya Veetil, R. 2016, in 41st COSPAR Scientific Assembly, Vol. 41, E1.15–8–16 [Cited on pages 272 and 273.]

Pauluhn, A., & Solanki, S. K. 2007, A&A, 462, 311 [Cited on page 173.]

Pesnell, W. D., Thompson, B. J., & Chamberlin, P. C. 2012, Sol. Phys., 275, 3 [Cited on pages 164 and 180.]

Phillips, K. J. H. 2012, MNRAS, 421, 1757 [Cited on page 252.]

Phillips, K. J. H., & Dennis, B. R. 2012, ApJ, 748, 52 [Cited on page 228.]

Phillips, K. J. H., & Neupert, W. M. 1973, Sol. Phys., 32, 209 [Cited on page 252.]

Phillips, K. J. H., Pike, C. D., Lang, J., Watanbe, T., & Takahashi, M. 1994, ApJ, 435, 888 [Cited on page 252.]

Plucinsky, P. P., Beardmore, A. P., Foster, A., et al. 2017, A&A, 597, A35 [Cited on page 43.]

Priest, E. R., Parnell, C. E., & Martin, S. F. 1994, ApJ, 427, 459 [Cited on page 195.]

Prigozhin, G., Gendreau, K., Doty, J. P., et al. 2016, in Society of Photo-Optical Instrumentation Engineers (SPIE) Conference Series, Vol. 9905, Space Telescopes and Instrumentation 2016: Ultraviolet to Gamma Ray, 99051I [Cited on page 144.]

Putrevu, D., Das, A., Vachhani, J. G., Trivedi, S., & Misra, T. 2016, Advances in Space Research, 57, 627 [Cited on page 119.]

Putrevu, D., Trivedi, S., Das, A., et al. 2020, Current Science, 118, doi:10.18520/cs/v118/i2/226-233 [Cited on page 119.]

Radhakrishna, V., Tyagi, A., Narendranath, S., et al. 2020, Current Science, 118, 219 [Cited on page 119.]

Ramadevi, M. C., Ravishankar, B. T., Sitaramamurthy, N., et al. 2017, Journal of Astrophysics and Astronomy, 38, 32 [Cited on pages 21 and 54.]

Rao, A. R., Bhattacharya, D., Bhalerao, V. B., Vadawale, S. V., & Sreekumar, S. 2017a, Current Science, 113, 595 [Cited on page 54.]

Rao, A. R., Naik, S., Patil, M., Malkar, J. P., & Kalyan Kumar, R. P. S. 2010, Nuclear Instruments and Methods in Physics Research A, 616, 55 [Cited on page 57.]

Rao, A. R., Chand, V., Hingar, M. K., et al. 2016, ApJ, 833, 86 [Cited on page 60.]

Rao, A. R., Patil, M. H., Bhargava, Y., et al. 2017b, Journal of Astrophysics and Astronomy, 38, 33 [Cited on page 54.]

Ratheesh, A., Rao, A. R., Mithun, N. P. S., et al. 2021, Journal of Astrophysics and Astronomy, 42, 37 [Cited on pages 59 and 79.]

Reale, F. 2014, Living Reviews in Solar Physics, 11, 4 [Cited on page 164.]

Remillard, R. A., & McClintock, J. E. 2006, ARA&A, 44, 49 [Cited on pages 10, 13, and 274.]

Remillard, R. A., Loewenstein, M., Steiner, J. F., et al. 2022, AJ, 163, 130 [Cited on pages 42 and 45.]

Rochus, P., Auchère, F., Berghmans, D., et al. 2020, A&A, 642, A8 [Cited on page 235.]

Rothschild, R. E., Blanco, P. R., Gruber, D. E., et al. 1998, ApJ, 496, 538 [Cited on page 43.]

Rybicki, G. B., & Lightman, A. P. 1979, Radiative processes in astrophysics [Cited on pages 12 and 13.]

Saint-Hilaire, P., Krucker, S., & Lin, R. P. 2008, Sol. Phys., 250, 53 [Cited on page 267.]

Saint-Hilaire, P., Shih, A. Y., Hurford, G. J., & Dennis, B. 2022, in Handbook of X-ray and Gamma-ray Astrophysics. Edited by Cosimo Bambi and Andrea Santangelo, 37 [Cited on page 18.]

Saint-Hilaire, P., Shih, A. Y., Zoglauer, A., et al. 2020, in AGU Fall Meeting Abstracts, Vol. 2020, SH048–0015 [Cited on page 260.]

Saint-Hilaire, P., Jeffrey, N. L. S., Martinez Oliveros, J. C., et al. 2019, in AGU Fall Meeting Abstracts, Vol. 2019, SH31C–3310 [Cited on page 260.]

Sakurai, T. 2017, Proceeding of the Japan Academy, Series B, 93, 87 [Cited on page 173.]

Salvo, T. D., Papitto, A., Marino, A., Iaria, R., & Burderi, L. 2022, in Handbook of X-ray and Gamma-ray Astrophysics, ed. C. Bambi & A. Santangelo (Singapore: Springer Nature Singapore), 1–73 [Cited on page 10.]

Sankarasubramanian, K., Sudhakar, M., Nandi, A., et al. 2017, Current Science, 113, 625 [Cited on page 288.]

Santangelo, A., Madonia, R., & Piraino, S. 2023, in Handbook of X-ray and Gamma-ray Astrophysics. Edited by Cosimo Bambi and Andrea Santangelo, 124 [Cited on page 9.]

Saqri, J., Veronig, A. M., Warmuth, A., et al. 2022, A&A, 659, A52 [Cited on page 251.]

Scherrer, P. H., Schou, J., Bush, R. I., et al. 2012, Sol. Phys., 275, 207 [Cited on page 189.]

Schlemm, C. E., Starr, R. D., Ho, G. C., et al. 2007, Space Sci. Rev., 131, 393 [Cited on page 120.]

Schnittman, J. D., & Krolik, J. H. 2009, ApJ, 701, 1175 [Cited on page 274.]

—. 2010, ApJ, 712, 908 [Cited on page 274.]

Schwab, B. D., Sewell, R. H. A., Woods, T. N., et al. 2020, ApJ, 904, 20 [Cited on page 145.]

Shakura, N. I., & Sunyaev, R. A. 1973, A&A, 24, 337 [Cited on page 10.]

Shanmugam, M., Vadawale, S. V., Patel, A. R., et al. 2020, Current Science, 118, 45 [Cited on pages 49, 119, 122, and 184.]

Shaposhnikov, N., Jahoda, K., Markwardt, C., Swank, J., & Strohmayer, T. 2012, ApJ, 757, 159 [Cited on page 48.]

Sharma, V., Iyyani, S., Bhattacharya, D., et al. 2019, ApJ, 882, L10 [Cited on page 62.]

Shibata, K., & Magara, T. 2011, Living Reviews in Solar Physics, 8, 6 [Cited on page 168.]

Shimizu, T. 1995, PASJ, 47, 251 [Cited on page 173.]

Singh, K. P., Tandon, S. N., Agrawal, P. C., et al. 2014, in Society of Photo-Optical Instrumentation Engineers (SPIE) Conference Series, Vol. 9144, Space Telescopes and Instrumentation 2014: Ultraviolet to Gamma Ray, ed. T. Takahashi, J.-W. A. den Herder, & M. Bautz, 91441S [Cited on page 53.]

Singh, K. P., Stewart, G. C., Westergaard, N. J., et al. 2017, Journal of Astrophysics and Astronomy, 38, 29 [Cited on page 53.]

Słowikowska, A., Kanbach, G., Kramer, M., & Stefanescu, A. 2009, MNRAS, 397, 103 [Cited on page 280.]

Smith, D. M., Hurford, G. J., & Boggs, S. E. 2004, New A Rev., 48, 209 [Cited on page 18.]

Sturrock, P. A. 1966, Nature, 211, 695 [Cited on page 168.]

Su, Y., Veronig, A. M., Hannah, I. G., et al. 2018, ApJ, 856, L17 [Cited on pages 206 and 232.]

Su, Y., Veronig, A. M., Holman, G. D., et al. 2013, Nature Physics, 9, 489 [Cited on page 170.]

Swings, P. 1943, ApJ, 98, 116 [Cited on page 162.]

Sylwester, B., Sylwester, J., Kepa, A., et al. 2006, Solar System Research, 40, 125 [Cited on page 227.]

Sylwester, B., Sylwester, J., Phillips, K. J. H., Kępa, A., & Mrozek, T. 2014, ApJ, 787, 122 [Cited on page 206.]

Sylwester, B., Sylwester, J., Siarkowski, M., et al. 2019, Sol. Phys., 294, 176 [Cited on pages 184, 192, 196, and 197.]

Tajima, H., & Hagino, K. 2022, in Handbook of X-ray and Gamma-ray Astrophysics. Edited by Cosimo Bambi and Andrea Santangelo, 70 [Cited on page 22.]

Tandon, S. N., Hutchings, J. B., Ghosh, S. K., et al. 2017, Journal of Astrophysics and Astronomy, 38, 28 [Cited on page 53.]

Tatischeff, V., Ubertini, P., Mizuno, T., & Natalucci, L. 2022, in Handbook of X-ray and Gamma-ray Astrophysics, 53 [Cited on page 32.]

Testa, P., & Reale, F. 2023, in Handbook of X-ray and Gamma-ray Astrophysics. Edited by Cosimo Bambi and Andrea Santangelo, 134 [Cited on page 9.]

Tindo, I. P., Ivanov, V. D., Mandel'stam, S. L., & Shuryghin, A. I. 1970, Sol. Phys., 14, 204 [Cited on page 259.]

—. 1972, Sol. Phys., 24, 429 [Cited on page 259.]

Tindo, I. P., Shurygin, A. I., & Steffen, W. 1976, Sol. Phys., 46, 219 [Cited on page 259.]

Tiwari, M., Gupta, P., Sinha, A., et al. 2013, Journal of synchrotron radiation, 20, 386 [Cited on page 37.]

Tolbert, K., & Schwartz, R. 2020, OSPEX: Object Spectral Executive, Astrophysics Source Code Library, record ascl:2007.018, ascl:2007.018 [Cited on page 25.]

Toriumi, S., & Wang, H. 2019, Living Reviews in Solar Physics, 16, 3 [Cited on page 164.]

Tripathi, D., Klimchuk, J. A., & Mason, H. E. 2011, ApJ, 740, 111 [Cited on page 173.]

Trombka, J. I., Nittler, L. R., Starr, R. D., et al. 2001, Meteoritics and Planetary Science, 36, 1605 [Cited on page 120.]

Tuo, Y.-L., Ge, M.-Y., Song, L.-M., et al. 2019, Research in Astronomy and Astrophysics, 19, 087 [Cited on page 115.]

Türler, M., Chernyakova, M., Courvoisier, T. J. L., et al. 2010, A&A, 512, A49 [Cited on pages 32, 148, and 268.]

Upendran, V., Tripathi, D., Mithun, N. P. S., Vadawale, S., & Bhardwaj, A. 2022, ApJ, 940, L38 [Cited on pages 160 and 173.]

Vacchi, A. 2022, in Handbook of X-ray and Gamma-ray Astrophysics. Edited by Cosimo Bambi and Andrea Santangelo, 68 [Cited on pages 22 and 124.]

Vadawale, S. V., Chattopadhyay, T., Rao, A. R., et al. 2015, A&A, 578, A73 [Cited on pages 61 and 273.]

Vadawale, S. V., Rao, A. R., & Chakrabarti, S. K. 2001, A&A, 372, 793 [Cited on page 274.]

Vadawale, S. V., Shanmugam, M., Purohit, S., Acharya, Y. B., & Sudhakar, M. 2012, in Society of Photo-Optical Instrumentation Engineers (SPIE) Conference Series, Vol. 8453, High Energy, Optical, and Infrared Detectors for Astronomy V, ed. A. D. Holland & J. W. Beletic, 84532K [Cited on page 66.]

Vadawale, S. V., Shanmugam, M., Acharya, Y. B., et al. 2014, Advances in Space Research, 54, 2021 [Cited on pages 119 and 184.]

Vadawale, S. V., Rao, A. R., Bhattacharya, D., et al. 2016, in Society of Photo-Optical Instrumentation Engineers (SPIE) Conference Series, Vol. 9905, Space Telescopes and Instrumentation 2016: Ultraviolet to Gamma Ray, 99051G [Cited on pages 49 and 55.]

Vadawale, S. V., Chattopadhyay, T., Mithun, N. P. S., et al. 2018, Nature Astronomy, 2, 50 [Cited on pages 61, 114, 275, 280, and 281.]

Vadawale, S. V., Mondal, B., Mithun, N. P. S., et al. 2021, ApJ, 912, L12 [Cited on pages 160 and 190.]

Vadawale, Mithun, S., Mondal, B., Sarkar, A., et al. 2021, ApJ, 912, L13 [Cited on pages 51, 184, 192, and 194.]

Vaiana, G. S., Krieger, A. S., & Timothy, A. F. 1973, Sol. Phys., 32, 81 [Cited on page 163.]

Vibhute, A., Bhattacharya, D., Mithun, N. P. S., et al. 2021, Journal of Astrophysics and Astronomy, 42, 76 [Cited on pages 57, 98, and 99.]

Volpara, A., Massa, P., Perracchione, E., et al. 2022, A&A, 668, A145 [Cited on page 241.]

Wang, Y., Zhao, Z., Hou, D., et al. 2023, Experimental Astronomy, 55, 427 [Cited on page 37.]

Warmuth, A., & Mann, G. 2016a, A&A, 588, A115 [Cited on page 172.]

—. 2016b, A&A, 588, A116 [Cited on page 172.]

Warren, H. P. 2014, ApJ, 786, L2 [Cited on page 207.]

Warren, H. P., Mariska, J. T., & Doschek, G. A. 2013, ApJ, 770, 116 [Cited on pages 206, 227, and 232.]

Weisskopf, M. C., Cohen, G. G., Kestenbaum, H. L., et al. 1976, ApJ, 208, L125 [Cited on page 271.]

Weisskopf, M. C., Elsner, R. F., & O'Dell, S. L. 2010a, in Society of Photo-Optical Instrumentation Engineers (SPIE) Conference Series, Vol. 7732, Space Telescopes and Instrumentation 2010: Ultraviolet to Gamma Ray, ed. M. Arnaud, S. S. Murray, & T. Takahashi, 77320E [Cited on page 262.]

Weisskopf, M. C., Guainazzi, M., Jahoda, K., et al. 2010b, ApJ, 713, 912 [Cited on page 47.]

Weisskopf, M. C., Silver, E. H., Kestenbaum, H. L., Long, K. S., & Novick, R. 1978, ApJ, 220, L117 [Cited on page 271.]

Weisskopf, M. C., Soffitta, P., Baldini, L., et al. 2022, Journal of Astronomical Telescopes, Instruments, and Systems, 8, 026002 [Cited on pages 24, 272, and 273.]

Wolter, H. 1952, Annalen der Physik, 445, 94 [Cited on page 19.]

Woods, T. N., Eparvier, F. G., Hock, R., et al. 2012, Sol. Phys., 275, 115 [Cited on page 232.]

Woods, T. N., Schwab, B., Sewell, R., et al. 2023, ApJ, 956, 94 [Cited on pages 145, 286, and 288.]

Wright, P. J., Hannah, I. G., Grefenstette, B. W., et al. 2017, ApJ, 844, 132 [Cited on page 197.]

Yu, Y.-W., Gao, H., Wang, F.-Y., & Zhang, B.-B. 2022, in Handbook of X-ray and Gamma-ray Astrophysics, 31 [Cited on page 11.]

Zdziarski, A. A., Pjanka, P., Sikora, M., & Stawarz, Ł. 2014, MNRAS, 442, 3243 [Cited on page 274.]

Zhang, H. 2017, Galaxies, 5, 32 [Cited on page 275.]

Zharkova, V. V., Arzner, K., Benz, A. O., et al. 2011, Space Sci. Rev., 159, 357 [Cited on page 168.]